INTELLIGENT CONTROL AND SYSTEM AGGREGATION TECHNIQUES FOR IMPROVING ROTOR-ANGLE STABILITY OF LARGE-SCALE POWER SYSTEMS

A Dissertation
Presented to
The Academic Faculty

By

Diogenes Molina

In partial Fulfillment
of the Requirements for the Degree
Doctor of Philosophy in the
School of Electrical and Computer Engineering

Georgia Institute of Technology
December, 2013

INTELLIGENT CONTROL AND SYSTEM AGGREGATION TECHNIQUES FOR IMPROVING ROTOR-ANGLE STABILITY OF LARGE-SCALE POWER SYSTEMS

Approved by:

Dr. Ronald G. Harley, Advisor
School of Electrical and Computer Engineering
Georgia Institute of Technology

Dr. Thomas Michaels
School of Electrical and Computer Engineering
Georgia Institute of Technology

Dr. Santiago Grijalva
School of Electrical and Computer Engineering
Georgia Institute of Technology

Dr. J. Rhett Mayor
School of Mechanical Engineering
Georgia Institute of Technology

Dr. Thomas Habetler
School of Electrical and Computer Engineering
Georgia Institute of Technology

Dr. G. Kumar Venayagamoorthy
Department of Electrical and Computer Engineering
Clemson University

Date Approved: September 10, 2013

This dissertation is dedicated to
my wife Tara, my mother Rosynella, and my father Diogenes

ACKNOWLEDGEMENTS

The path that has taken me to this point has been long and arduous. Thankfully, I have been fortunate to have a strong support network. My friends and family have given me the strength to endure the many low points I have encountered throughout my academic studies. The importance of the patience and understanding that my wife Tara has shown cannot be overstated. I would be lost without her. Cliché, I know, but true nonetheless. The open communication channel, advice, and encouragement provided by my mother Rosynella have also been instrumental. She always knew how to push me to try and be the best I can be. My dad Diogenes was always my source of inspiration. His example has been a constant reminder that I can push through and overcome adversity even when there seems to be no light at the end of the tunnel.

I also owe special thanks to a number of professionals that have molded my career. They have shown me how challenging and enjoyable electrical engineering can be. Prof. Ronald Harley, my current advisor, really knew when to lead me to success and when to let me fail and learn. He provided countless opportunities for me to grow as a professional. Similar thanks are due to Prof. G. Kumar Venayagamoorthy, from Clemson University. It has been an honor and a pleasure to attend talks and lectures by Profs. Harley, Habetler, Grijalva, Meliopoulos, Divan, and Begovic. I want to express special gratitude to all the members of the dissertation committee. Their feedback during the PhD proposal and dissertation process has been invaluable.

Lastly, I want to thank the students in the power group. Being in the trenches with such a smart and fun group of people has made my graduate student experience memorable and enjoyable.

TABLE OF CONTENTS

LIST OF TABLES

LIST OF FIGURES

LIST OF ABBREVIATIONS

AB-ILADC	Aggregation-Based Local-Area Damping Control
AB-IWADC	Aggregation-Based Intelligent Wide-Area Damping Control
AB-LQR	Aggregation-Based Linear Quadratic Regulator
ACD	Adaptive Critic Design
ADP	Approximate Dynamic Programming
AN	Action Network or Actor Network (used interchangeably)
ANN	Artificial Neural Network
AVR	Automatic Voltage Regulator
CN	Critic Network
DHP	Dual Heuristic Programming
FSHC	Full-Simulation Hierarchical Clustering
HDP	Heuristic Dynamic Programming
IWADC	Intelligent Wide-Area Damping Control
GRNN	Globally Recurrent Neural Network
MN	Model Network
MSE	Mean Square Error
MLP	Multi-layer perceptron
NDFM	Nearly Decentralized Fixed Modes
ONS	Brazilian Independent System Operator
PMU	Phasor Measurement Unit
PSO	Particle Swarm Optimization
PSS	Power System Stabilizer

RAS	Rotor-Angle Stability
RNN	Recurrent Neural Network
SCG	Scaled Conjugate Gradient
SIN	Brazilian National Interconnected System
WADC	Wide-Area Damping Control
VG	Virtual Generator

SUMMARY

A variety of factors such as increasing electrical energy demand, slow expansion of transmission infrastructures, and electric energy market deregulation, are forcing utilities and system operators to operate power systems closer to their design limits. Operating under stressed regimes can have a detrimental effect on the rotor-angle stability of the system. This stability reduction is often reflected by the emergence or worsening of poorly damped low-frequency electromechanical oscillations. Without appropriate measures these can lead to costly blackouts. To guarantee system security, operators are sometimes forced to limit power transfers that are economically beneficial but that can result in poorly damped oscillations. Controllers that damp these oscillations can improve system reliability by preventing blackouts and provide long term economic gains by enabling more extensive utilization of the transmission infrastructure.

Previous research in the use of artificial neural network-based intelligent controllers for power system damping control has shown promise when tested in small power system models. However, these controllers do not scale-up well enough to be deployed in realistically-sized power systems. The work in this dissertation focuses on improving the scalability of intelligent power system stabilizing controls so that they can significantly improve the rotor-angle stability of large-scale power systems.

A framework for designing effective and robust intelligent controllers capable of scaling-up to large scale power systems is proposed. Extensive simulation results on a large-scale power system simulation model demonstrate the rotor-angle stability improvements attained by controllers designed using this framework.

CHAPTER 1 INTRODUCTION AND OBJECTIVES

1.1 MOTIVATION AND OVERVIEW

A variety of factors such as increasing electrical energy demand, slow expansion of transmission infrastructures, and electric energy market deregulation, are forcing utilities and system operators to operate power systems closer to their design limits [1]-[2]. Operating under stressed regimes can have a detrimental effect on the rotor-angle stability of the system. This stability reduction is often reflected by the emergence or worsening of poorly damped low-frequency electromechanical oscillations. Several power systems are experiencing an increase in the number of events involving these oscillations [3]-[4]. Without appropriate measures these can lead to costly blackouts. The 1996 North American blackout that led to the loss of 31 GW of load and affected 7.49 million customers clearly demonstrated the potential impact of rotor-angle instability [5].

To guarantee system security, operators are sometimes forced to limit power transfers that are economically beneficial but that can result in poorly damped oscillations [6]-[7]. Controllers that damp these oscillations can improve system reliability by preventing blackouts and provide long term economic gains by enabling more extensive utilization of the transmission infrastructure [7].

Researchers have recognized that conventional stabilizing technology might not be effective enough to damp these oscillations, so more advanced control technology is needed. Previous research in the use of computational intelligence for power system damping control has shown promise when tested in small power system models [8]-[10]. Comparisons have shown that intelligent damping controllers can match or surpass the

performance of other advanced damping controllers in terms of robustness and effectiveness [11]. However, results in [12] demonstrate that the state-of-the-art Artificial Neural Network topologies typically used for implementing the intelligent controllers of [8]-[11] do not scale-up well enough and their training becomes intractable once system sizes grow to realistic proportions. Consequently, there is no clear path for scaling intelligent controllers up to handle the unparalleled size and complexity of real power systems.

The research presented in this dissertation focuses on improving the scalability of intelligent power system stabilizing controls such that they can significantly improve the rotor-angle stability of large-scale power systems.

The scalability issue is approached by means of system aggregation techniques. The core idea is to generate abstract representations of the system that, while significantly reducing the size and complexity of the system as "seen" by the controllers, still preserve the behavioral features needed for effective damping control. These representations can be generated online in real-time and allow intelligent damping controllers to treat large areas of a power system as single equivalent "virtual generators" [13].

An intelligent damping controller capable of significantly improving the rotor-angle stability of a realistic large-scale power system model is developed to validate the ideas introduced throughout the dissertation. A detailed model of the South, Southeast, and Midwest portions of the Brazilian power system serves as the testing bench to evaluate the scalability, performance, and robustness of the intelligent control and system aggregation techniques developed in the dissertation.

1.2 MAIN OBJECTIVES

A framework is needed for designing controllers capable of significantly improving rotor-angle stability by damping low-frequency electromechanical oscillations in large-scale power systems. In addition to being scalable, the framework must result in controllers that can handle the non-linear, time-varying, stochastic, and complex nature of power systems. These controllers must be evaluated on a large-scale power system model to reveal whether scalability, performance, and robustness requirements are met. The core objective of this work is to develop and evaluate such a control design framework. This is accomplished by completing five specific objectives.

The first specific objective is to evaluate the potential improvements in rotor-angle stability that can be achieved utilizing relatively conventional control technology. These evaluations will shed light on the potential benefits of intelligent control and provide insights into the specific needs that have not been met by conventional technology.

The second specific objective is to investigate the importance of scalability and the ability of state-of-the-art intelligent damping controllers to scale-up to handle the size and complexity of large-scale power systems. The results will determine whether the research efforts in the dissertation are justified, and guide the development of a new control design framework.

The first and second specific objectives are geared towards demonstrating the importance of developing a more advanced and scalable control approach for improving large-scale power system damping.

The third specific objective is to develop aggregation based intelligent damping controls with improved scalability. The goal is to provide the capabilities needed to

overcome some of the limitations of state-of-the-art intelligent damping controls such that this technology becomes suitable for implementation in realistic large-scale power systems.

The fourth specific objective is to develop a large-scale power system model that can be used as the testing environment to evaluate whether the approaches proposed meet the core objective of the dissertation.

The fifth specific objective is to demonstrate how the ideas developed throughout the dissertation can be integrated into a framework for designing wide-area damping controllers for large-scale power systems. The improvements attained by applying the proposed framework must be substantiated by exhaustive simulation studies on a large-scale power system model.

1.3 OUTLINE

The organization of the dissertation closely follows the specific objectives outlined in the previous section. Chapter 2 provides a brief introduction to the rotor-angle stability problem in power systems, describes the techniques commonly used to analyze rotor-angle stability, and presents a review of a representative sample of the literature dedicated to the design of closed-loop controls for enhancing rotor-angle stability in power systems.

Chapter 3 attacks the first specific objective of the dissertation. The advantages and limitations of classical and more modern approaches for improving rotor angle stability are illustrated by means of design examples. A heuristic optimization-based tuning technique for coordinated design of multiple stabilizers is presented. Also, a technique is developed for selecting adequate sets of linearized models to use for multi-model control design. These two techniques are then used to design robust linear damping controllers

for a medium-size power system model. Extensive small-signal studies illustrate how the complex tradeoff between robustness and performance can prevent linear controllers from attaining more significant improvements in rotor-angle stability.

Chapter 4 addresses the second specific objective of the dissertation. The focus is on exploring the importance of scalability for large-scale power system damping, and on investigating the ability of present day Artificial Neural Network topologies to scale-up. This chapter provides insights into the limitations of state-of-the-art intelligent damping control approaches in terms of scalability.

Chapter 5 focuses on developing aggregation-based intelligent controllers with improved scalability properties to address the requirements of the third specific objective. The concept of a "virtual generator" is introduced to generate simplified representations of the power system in real-time. These representations allow intelligent controllers to treat large portions of the system as single machines without losing information critical for effective damping control. This results in large dimensionality reductions that significantly improve scalability. A design example using a medium-size power system model illustrates the ideas in the chapter. Comparisons are made against state-of-the-art stabilizing technology currently deployed in real power systems to demonstrate the potential improvements offered by intelligent aggregation-based controls. While the results are encouraging, the size and complexity of the system utilized in this chapter are not representative of a realistic power system. Therefore, the results do not imply scalability.

Chapter 6 meets the needs imposed by the fourth specific objective. The chapter is dedicated to the development of a large-scale power system model of the South,

Southeast, and Midwest portions of the Brazilian power system. The chapter also includes extensive small-signal stability studies aimed at determining the specific needs of this system model in terms of rotor-angle stability. The resulting model provides an adequate testing platform for evaluating the ideas presented throughout the dissertation.

Chapter 7 enhances the approach presented in chapter 5 in order to address the needs imposed by the fifth specific objective. An aggregation-based intelligent controller is deployed in the realistic large-scale simulation model of chapter 6. Extensive simulations illustrate the stability improvements attained over a large set of challenging operating conditions. The results in this clearly demonstrate that the ideas of the dissertation allow the development of intelligent controllers that significantly improve the rotor-angle stability of realistic large-scale power systems. These ideas then integrated into a cohesive framework for wide-area damping controller design.

Chapter 8 provides conclusions, summarizes the contributions of the dissertation, and outlines potential directions for future research.

CHAPTER 2 LITERATURE REVIEW

2.1 ORIGIN AND HISTORY OF THE PROBLEM

The dependence of modern society on electrical energy imposes high reliability standards on power systems. To operate reliably, power systems must remain stable when subjected to a wide variety of disturbances and operating conditions. Maintaining stability in power systems has been recognized as an important problem to maintain secure operation since the 1920s, when large blocks of power began to be transmitted from distant locations to large load centers [15].

A widely accepted definition of power system stability proposed by the IEEE/CIGRE Joint Task Force on Stability Terms and Definitions is repeated below [14]:

"Power system stability is the ability of an electric power system, for a given initial operating condition, to regain a state of operating equilibrium after being subjected to a physical disturbance, with most system variables bounded so that practically the entire system remains intact."

Three main classifications of the power system stability problem are identified in [14] and illustrated in Figure 2.1: rotor-angle, frequency, and voltage stability. All three must be maintained. The research in this dissertation focuses on improving rotor-angle stability.

This section provides a high level overview of rotor-angle stability for readers unfamiliar with the topic.

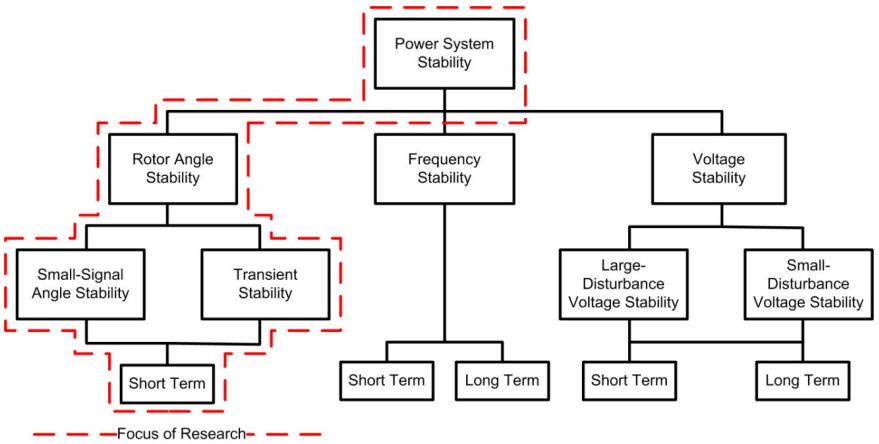

Figure 2.1 Focus of the proposed research

2.1.2 Overview of Basic Concepts on Rotor-Angle Stability

Rotor-angle stability refers to the ability of synchronous machines in an interconnected power system to remain in synchronism after being subjected to a disturbance. A comprehensive historical overview of the developments in the study of rotor-angle stability problems is provided in [16]. The interested reader is pointed to power system analysis textbooks such as [16]-[18] for in-depth explanations of the causes, nature, characteristics, and methods for analyzing this phenomenon. Only a brief discussion of that material is repeated here to avoid unnecessary explanations that can be easily found elsewhere.

Figure 2.2 shows an abstracted view of a 68-bus/16-machine benchmark power system model introduced in [18] for studying rotor-angle stability in power systems. A modified version of this system is used here to illustrate some basic concepts regarding small-signal and transient stability analysis. Detailed descriptions of the model are unnecessary at this point and are postponed until later chapters. Rotor-angle stability

encompasses small-signal and transient stability. Brief descriptions and examples of the two are provided next.

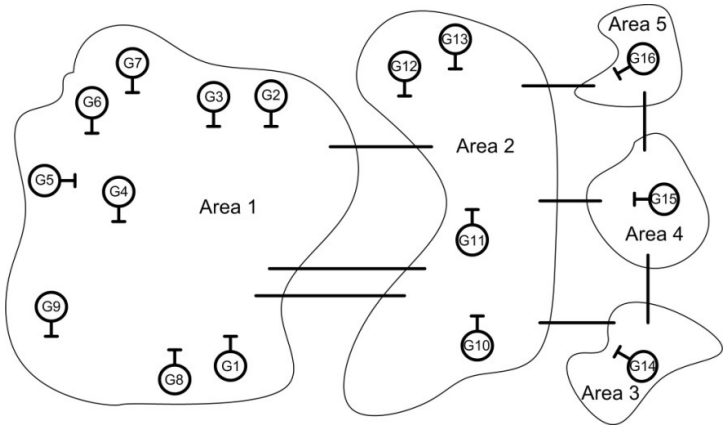

Figure 2.2 Abstracted view of 68-bus/16-machine benchmark system

2.1.2.2 Small-Signal Stability – Response to Small Disturbances

Small disturbances due to load and generation variations are continuously affecting power systems. The system's ability to withstand these disturbances is studied using small-signal stability analysis. This is typically completed by calculating the eigenvalues of a linearized power system model obtained at a particular steady-state operating condition. The system is small-signal stable inside a small region around that operating condition if all of its eigenvalues lie on the left side of the complex plane.

An example of small-signal stability analysis for the 68-bus/16-machine system in Figure 2.2 at four operating conditions is shown in Figure 2.3. The system is small-signal stable for three of the operating conditions and unstable for the fourth. The drastic change of some of the eigenvalues in Figure 2.3 illustrates why the use of linear analysis is only justified when disturbances are small. Also, the destabilizing effect of the fourth

operating condition serves as evidence of the steady-state operational constraints that the small-signal stability phenomenon can impose on a power system.

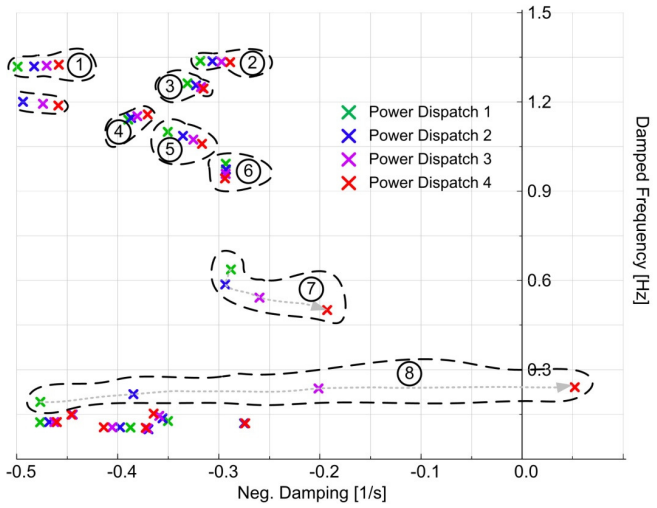

Figure 2.3 Results of small-signal analysis at different operating conditions

In addition to determining small-signal stability, eigenvalues also determine the frequency and decay rate of the oscillations in the system. Two types of oscillatory problems associated with electromechanical oscillations are of concern when analyzing small-signal stability: local and global.

Local problems involve small portions of the system and the oscillations usually lie in the 0.7-2 Hz frequency range. These oscillations typically involve machines at a single generating plant oscillating against the rest of the system and are called local plant oscillations. Other types of local oscillations such as inter-plant, torsional, and control mode oscillations do exist but the technologies used to address them are mature and effective, so these types of oscillations are not explored further in this dissertation.

The oscillatory pattern of the generators when a particular eigenvalue (or mode) is excited can be analyzed using mode shapes extracted from the eigenvalue's right

eigenvector. This is illustrated by Figure 2.4, which plots the normalized right eigenvector (mode shape) corresponding to eigenvalue 2 in Figure 2.3. The relatively large magnitude of the eigenvector component corresponding to G10 indicates that mode 2 is a local plant mode characterized by generator G10 oscillating against the rest of the system.

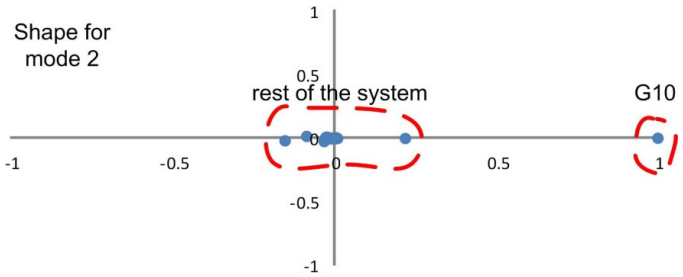

Figure 2.4 Normalized right eigenvector for local plant mode 2

Global problems have a significant impact on the system's overall rotor-angle stability. They consist of oscillations that typically lie in the 0.1-0.7 Hz frequency range, and that involve large groups of machines in one area of the system oscillating against other groups of machines in other areas. These are called inter-area oscillations. The low-frequency electromechanical oscillations discussed in the introductory section are of this type. As discussed earlier, these can have devastating effects on the system's operation if their damping is insufficient [5].

Figure 2.5 provides the mode shape for the highly sensitive and eventually unstable mode 8 in Figure 2.3. This low-frequency mode is clearly an inter-area mode involving virtually every machine in the system. Generators G1-G9 (Area 1 in Figure 2.2) can be expected to oscillate the most due to the higher relative magnitude of the eigenvector components corresponding to them. The mode shape also indicates that generators G10-

G13 (Area 2 in Figure 2.2) can be expected to oscillate less than and almost in phase with generators in Area 1.

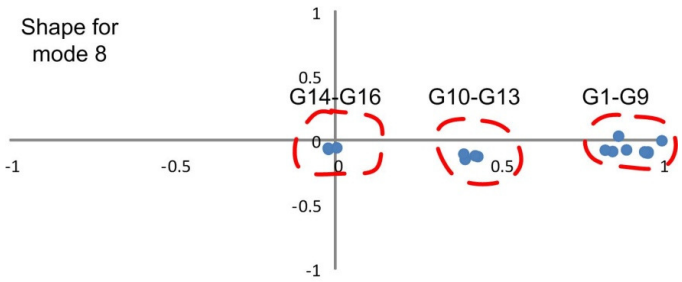

Figure 2.5 Normalized right eigenvector for inter-area mode 8

2.1.2.3 Transient Stability – Response to Large Disturbances

Power systems are often affected by large stochastic disturbances such as short-circuit faults, disconnection of transmission lines, loss of large amounts of load and generation, equipment failures, etc. The system's ability to withstand these disturbances is studied using transient stability analysis. A common approach to study transient stability is to use numerical integration of the non-linear power system model to obtain its time-domain response to a particular disturbance. The variables in the model are initialized to a particular steady-state operating condition. The system is transient-stable for that disturbance and initial operating condition if the definition of stability provided before is satisfied. The pre and post-disturbance system configurations and operating conditions are often not the same. Typically 3-5 seconds of simulation time are enough to determine whether a system is transient-stable, but studies might have to extend to 10-20 seconds in larger systems. Instabilities are often due to insufficient synchronizing torque and result in first-swing instability; however, instability can also occur after the first swing due to

the superposition of multiple oscillatory modes, or due to a small-signal unstable post-disturbance condition [16].

Figure 2.6 illustrates stable and unstable transient behaviors of the 68-bus/16-machine system in response to the same disturbance applied at two different initial operating points. The speeds for machines in areas 1 and 2 in Figure 2.2 are plotted in black and red respectively. In the unstable case, the areas loose synchronism after the first swing due to poorly damped inter-area oscillations in the post-disturbance system.

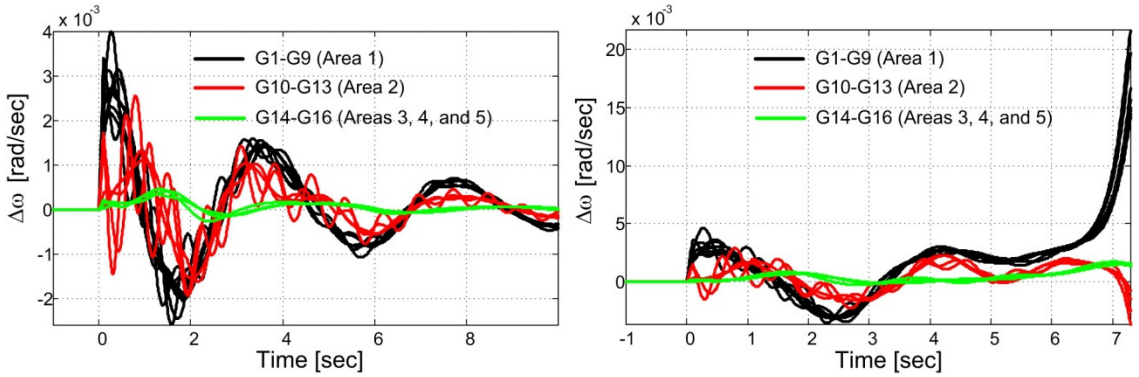

Figure 2.6 Examples of transient stable (left) and unstable system (right)

The small-signal analysis results are also evident in Figure 2.6. The low frequency mode is mostly observable on the machines in Area 1 (black waveforms) and to a lesser degree on the machines in Area 2 (red waveforms). As predicted, the oscillations in the two areas are almost in phase. A higher frequency oscillation is also noticeable in one of the machines in Area 2. Closer inspection reveals that this oscillation corresponds to G10 and that its frequency corresponds to that of mode 2 in Figure 2.3. These observations point to the complementary role of small-signal and transient stability analysis.

Clearly, rotor-angle stability is critical for the safe and reliable operation of power systems. Small-signal and transient stability analysis provide effective tools to evaluate

the dynamic response of power systems when subjected to a wide variety of small and large disturbances.

Poorly damped local and inter-area oscillations have a detrimental effect on small-signal and transient stability and often impose operational constraints. In modern power systems, small-signal stability problems are usually the result of insufficient damping of oscillations, so enhancing the damping of these oscillations has obvious advantages for the performance of power systems. The next section reviews classical and state-of-the-art technologies for improving the damping of oscillations.

2.2 ROTOR-ANGLE STABILITY IMPROVEMENT VIA CLOSED-LOOP CONTROL

The rotor-angle stability of a power system (both transient and small-signal) can be enhanced using closed-loop controllers that damp electromechanical oscillations [19]. The most commonly used damping controllers inject supplementary control signals to synchronous generators, HVDC links, SVCs, and other FACTS devices. Among them, supplementary excitation control for synchronous generators is the most cost effective form of damping control and has been widely adopted as the standard approach [20]. The classical damping controller for synchronous generators is the power system stabilizer (PSS). Conventional and modern PSS designs and their limitations are reviewed next.

2.2.1 Power System Stabilizer-Based Damping

Power system stabilizers (PSSs) are closed-loop control devices that utilize local feedback measurements to produce an electrical torque component in the generator that mitigates electromechanical oscillations. A diagram illustrating the connection of a PSS to a generic synchronous generator in a power system appears in Figure 2.7.

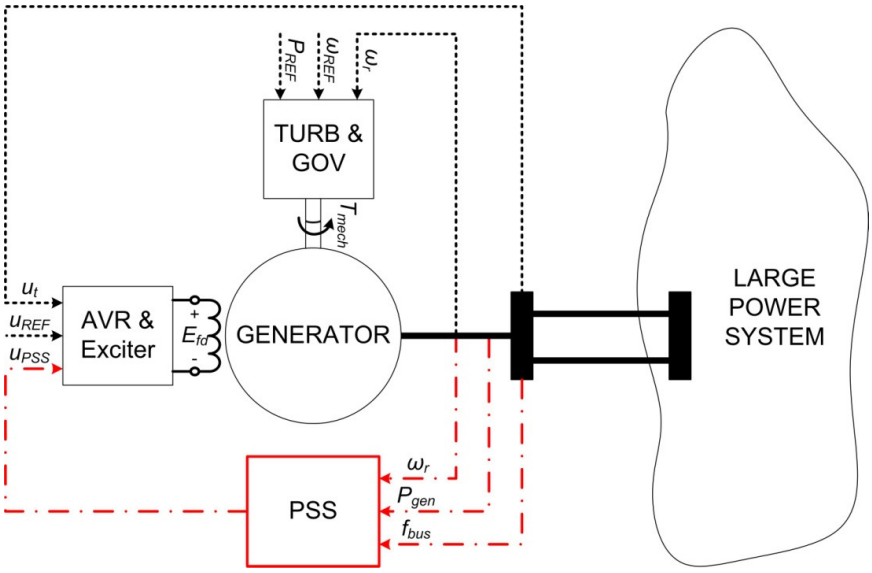

Figure 2.7 Connection of a PSS to a generic synchronous generator

The literature addressing the design and implementation of PSSs is extensive and dates back to the 1960s [21]-[22]. A detailed analysis of the effects of excitation systems on rotor-angle stability and evaluations of the requirements for effective supplementary stabilizing controls for synchronous generators is given in [23]. The three-part paper series in [24]-[26] provides a thorough summary of the classical approach to PSS design and implementation. The approach is based on linearized models of a single-machine-infinite-bus system, and views PSSs as phase compensation networks for which appropriate time constants and gains need to be determined. An example of a simple yet frequently used PSS topology is shown in Figure 2.8, but more advanced and flexible ones are also used in practice [27].

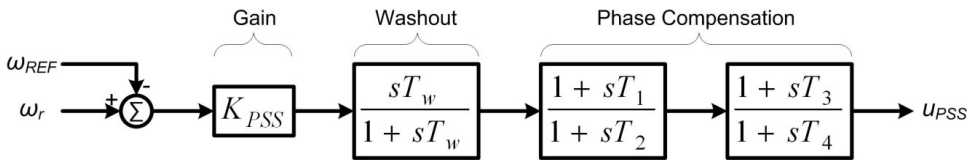

Figure 2.8 Generic speed input PSS model

The block diagram in Figure 2.9 introduced by Heffron and Phillips in [28] is commonly used for classical PSS design. The effects of the turbine and governor dynamics shown in Figure 2.7 are ignored due to their slow response. The magnitudes and signs of the K1-K6 constants in this model are determined by the parameters and operating conditions of the system and change as the system operates. The time-varying nature of these parameters complicates the PSS design problem.

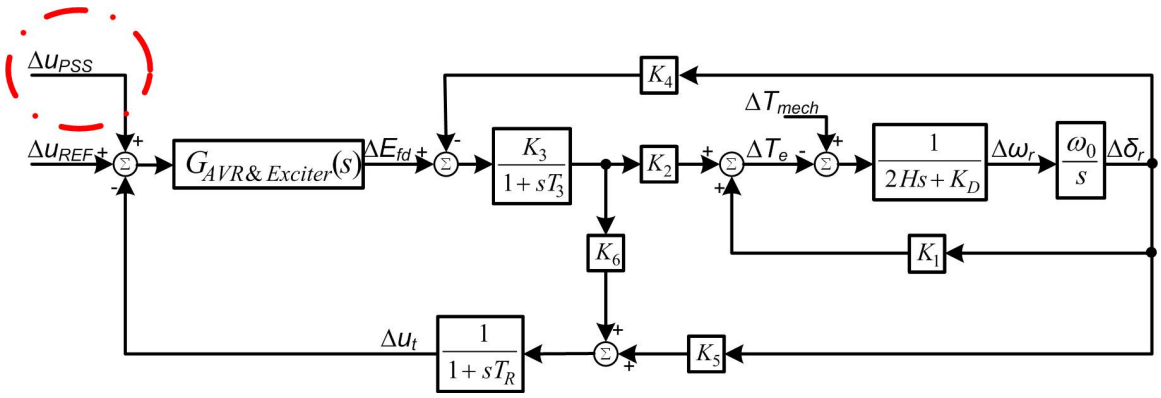

Figure 2.9 Linearized model of SMIB system for classical PSS design

Techniques have evolved over time to deal with the time-varying nature of power systems. Engineering judgment and experience has resulted in relatively simple, practical, and intuitive approaches that are robust enough to provide reasonable performance over a wide range of operating conditions [19]. These have gained popularity in real power system applications [29]. Nevertheless, more powerful stabilizer design methodologies have been explored by the research community. Examples include: robust control, adaptive control, optimal control, state feedback control, and intelligent control.

Robust control techniques such as μ-synthesis and H∞ control have been applied to design PSSs that perform well under a wide variety of operating conditions [30]-[32].

These approaches view the variations in the dynamic behavior of power systems as parametric uncertainties with known upper and lower bounds (think of bounded changes in the K1-K6 constants in Figure 2.9). PSSs are designed to guarantee stability and some degree of performance in the face of these parametric uncertainties. Linear Matrix Inequalities (LMI)-based pole placement approaches to robust control have also been used to accomplish this task [33].

Adaptive PSSs designs and implementations have been reported to offer improved performance when compared to classical PSS designs [34]-[35]. PSS parameter adaptation provides the ability to maintain high damping performance even as the operating conditions of the system change.

Optimization methods such as particle swarm optimization [36], simulated annealing [37], genetic algorithms [38]-[39], conic programming [40], bacterial foraging [41], etc., have been used to design PSSs that minimize eigenvalue or time series-based objective functions, i.e. optimal PSSs. These objective functions are often minimized over multiple operating points to push the PSSs to achieve a sort of robust optimum. Also, these techniques are often used to tune multiple PSSs simultaneously to ensure more appropriate controller coordination.

State-feedback controllers for voltage regulation and oscillation damping have been utilized by the Electricite de France (EDF) for the last few decades. These controllers and their design methodologies are compared against more conventional techniques in [42]. One of the advantages of these approaches is an inherent coordination between automatic voltage regulators (AVRs) and PSSs.

Nonlinear intelligent control has also been shown to be effective for damping control. Intelligent controllers based on fuzzy logic [43]-[45] and artificial neural networks [46]-[49] have been shown to outperform classical PSSs in simulations and experimentally. The robustness of these controllers is achieved by online adaptation or by training/designing them to perform well over a wide range of operating conditions.

The classical and modern PSSs described so far are effective in damping local modes involving a limited number of generators. However, they are less effective in damping inter-area modes which involve large groups of generators from distant areas across the system. The concept of nearly decentralized fixed modes (NDFM) is introduced in [50] to describe oscillatory modes that cannot be "appreciably" shifted using any permissible local feedback gains, i.e., local controllers cannot improve their damping significantly. In practice, inter-area modes are often not as highly controllable and observable using local signals at generators as local modes [51]. Interactions among multiple PSSs which lack knowledge of global states can also have a detrimental effect on the damping of inter-area oscillations, further degrading the performance of local PSSs [52].

It is not clear that local damping controllers such as the PSSs in this section will be effective enough to adequately damp low-frequency oscillations in the highly stressed power networks of the future. An example of a power system affected by poorly damped oscillations even after the addition of a large number of PSSs is discussed in [53].

Thankfully, power systems are currently being modernized with the installation of phasor measurement units (PMUs) and more advanced communication infrastructures capable of providing time-synchronized signals at high sampling rates from distant locations across the system [54]. These enhancements will enable the implementation of

more advanced monitoring and closed-loop control algorithms known as wide-area controllers (WACs). A representative sample of wide-area damping controller designs for improving rotor-angle stability is reviewed next.

2.2.2 Wide-Area Damping Controller-Based Damping

Past research has shown that wide-area damping controllers (WADCs) that make use of global signals can damp inter-area oscillations more effectively than conventional PSSs [50]-[51], [55]. Generic WADCs are illustrated in Figure 2.10. Global input and output signals can provide higher controllability and observability of the inter-area dynamics and improve damping control. This technology is still in its infancy and has not gained wide-spread acceptance by the electric power industry.

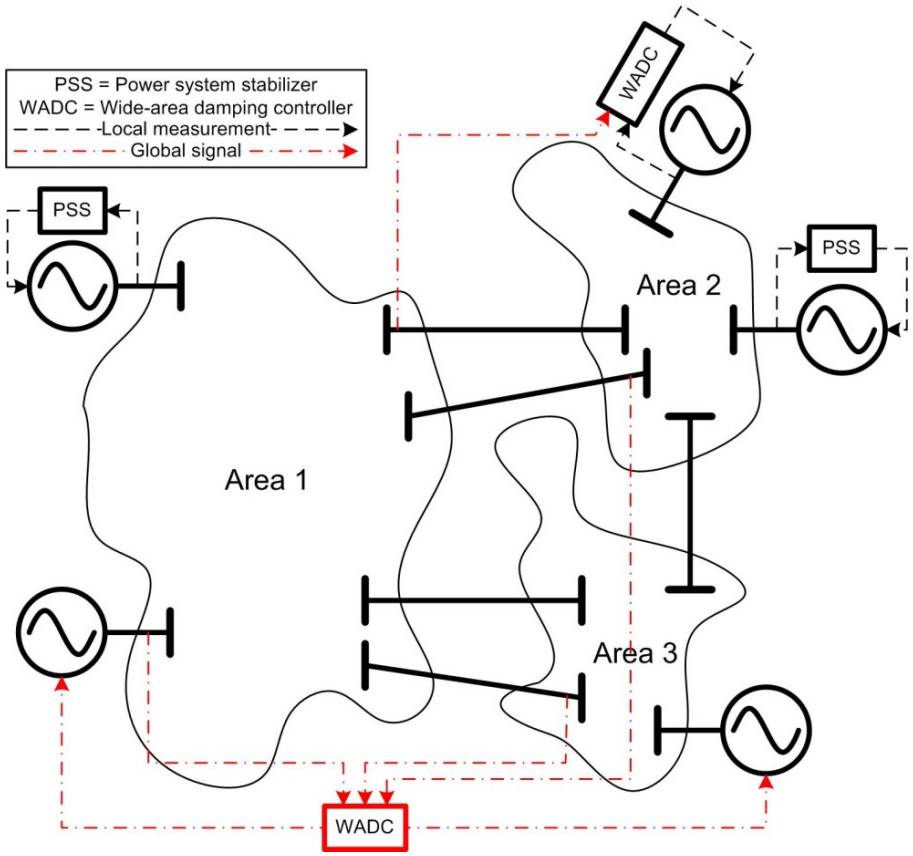

Figure 2.10 Generic local and wide-area controllers in a power system

Two broad types of WADC approaches have emerged over time and are illustrated in Figure 2.10. The first type consists of enhancing the capabilities of conventional devices such as PSSs by providing them with a few carefully selected global signals as shown in the top-right corner of Figure 2.10. The second broad type consists of more ambitious designs that measure and inject signals at multiple locations across the system, making the WADC more of a supervisory controller as shown at the bottom of Figure 2.10. In both approaches the global input and output signals and the local devices they are connected to are carefully selected using linear analysis tools such as residues, participation factors, geometric measures of observability and controllability, etc., [56]-[57].

The work in [58] presents a decentralized/hierarchical approach for the coordinated design of local and WADC to improve the damping of low-frequency oscillations in the Hydro-Quebec system. The lower hierarchical level implements conventional PSSs and the higher level is based on a WADC. The approach relies on linear system identification to obtain reduced-order multiple-input-multiple-output (MIMO) models of the power system. Often used geometric measures of controllability and observability introduced in [57] allow the selection of the most effective global input and output signals to reduce communication requirements. The local PSSs and WADCs are tuned sequentially using generic optimization algorithms. Simulations demonstrate that noticeable damping improvements can be achieved with minimal control effort. However, the tuning procedure only considers a single operating condition and therefore the performance of the controllers can be expected to degrade if operating conditions change significantly.

The design is completed for five WADC loops and demonstrated on a large-scale model of the Hydro-Quebec grid under a number of operating conditions and contingencies.

An inter-area mode pole-shifting approach for coordinating the design of multiple WADCs is proposed in [59]. The approach is capable of tuning multiple WADCs over many operating conditions to ensure that the system's eigenvalues are located within a certain region in the complex plane. Special attention is given to allocating the control effort among the different controllers and to ensuring that the limited control resources available are utilized to improve the damping of inter-area modes and not of local ones. The tuning process is framed as a two-stage optimization problem that is solved using sequential quadratic programming. An application example for tuning two WADCs (10 tunable parameters) for a 68-bus/16-machine power system model demonstrates the effectiveness of the method. However, the scalability of the method to handle a large number of WADCs for more realistically sized systems is yet to be tested. Computational requirements and convergence might become problematic in such cases.

A centralized robust WADC is proposed in [60]. Mixed sensitivity output-feedback control with regional pole placement is applied to design the WADC for a reduced order linear model of a 39-bus/10-machine power system. The goal is to achieve a controller that maintains good robust performance in the presence of model uncertainties while guaranteeing good transient behavior in response to disturbances. The design problem is formulated as a linear matrix inequalities system and solved using tools available in MATLAB. Considerable additional tuning is required to achieve acceptable performance once the controller (designed using a reduced-order linear model) is evaluated on the full non-linear model of the power system. A single input signal is injected into the power

system, but a larger number of them are likely needed to improve the performance of a more realistically sized system.

A combination of robust control techniques and multi-agent theory for WADC is proposed in [61]. Robust local PSSs are designed to damp local modes and to work in collaboration with a higher level WADC. An adaptive neuro-fuzzy inference system and measurements from all generators in the system are used to determine the system's operating condition. A robust WADC designed a-priori for that same operating condition is then recalled from a database of robust designs. This allows the WADC to modify its own behavior to match the system conditions and maintain its performance even as those conditions change. However, the many operating conditions and possibly multiple WADCs needed for large-scale power systems would likely make this approach impractical.

A two-level control approach is proposed in [62]. Local PSSs on the bottom level are used to damp local oscillations and to ensure generator stability. A WADC at the top level is used to enhance the performance of each local controller by compensating for the effects of interactions among the different generators and inter-area oscillations. In essence, the WADC decouples the dynamics of all generators such that conventional local controllers become more effective. The WADC is equipped with an adaptation mechanism based on gain scheduling to ensure that acceptable decoupling is achieved even when the operating conditions of the system change. Effectiveness is demonstrated in simulations of a 4-machine system. Implementing the approach in more realistically sized systems would make the higher level controller implementation difficult since it

would have to compensate for the interactions of hundreds or even thousands of generators to achieve the desired generator decoupling.

Intelligent WADCs based on approximate dynamic programming are proposed in [10]-[11] and [63]. Heuristic dynamic programming (HDP) from the theory of adaptive critic designs (ACD) is used to implement WADCs that approach optimal damping performance over time as they gain experience trough interactions with power system simulation models. Comparisons against state-feedback and robust control-based WADC for a 68-bus/16-machine power system in [11] demonstrate the effectiveness of intelligent control. However, the artificial neural networks (ANNs) used to implement these intelligent controllers are difficult to scale up [12], so these approaches cannot be easily extended to realistically sized systems.

WADC depend on the use of global signals to and from distant locations across the system. These signals must travel trough communication networks which introduce random communication delays. The effects of these delays and methods to mitigate them are reviewed next.

2.2.3 Wide-Area Damping Control and Time Delays

Figure 2.11 illustrates the nature of communication delays in a generic power system with WADCs. These delays can vary from tens to hundreds of milliseconds depending on the communication infrastructure in place. They have been found to have a noticeable destabilizing effect on the performance of WADCs. WADC design methodologies must be capable of addressing these delays effectively.

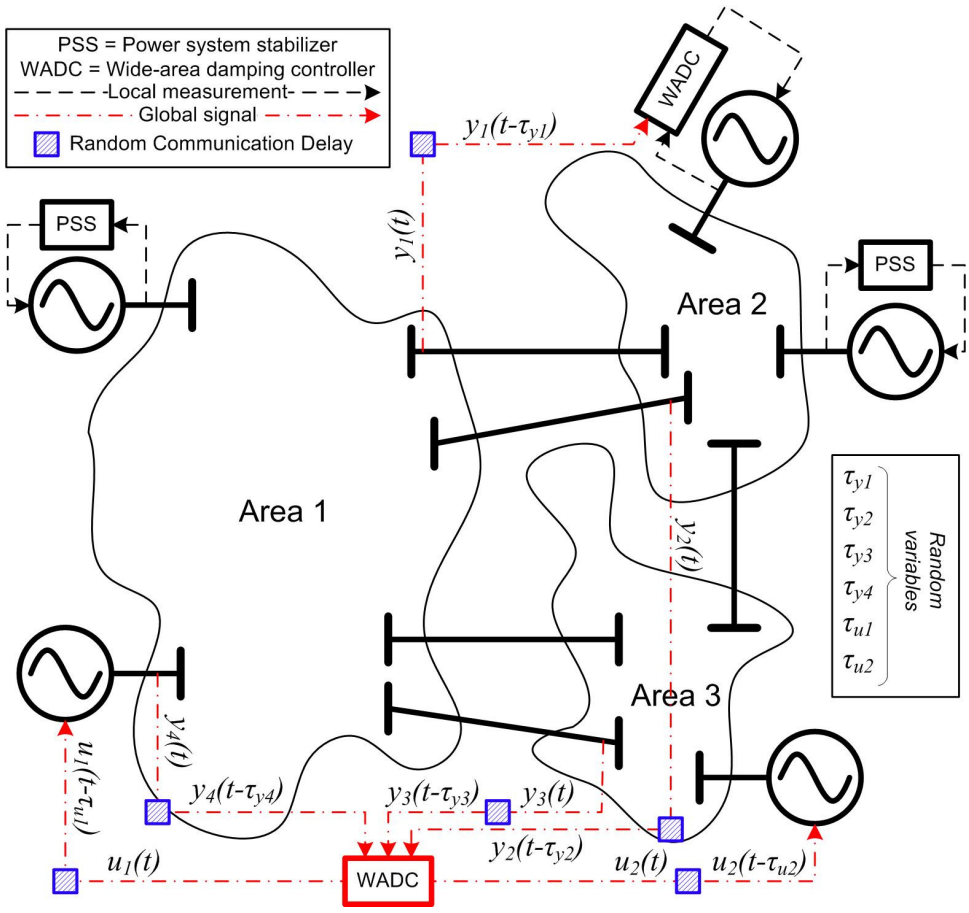

Figure 2.11 Generic local and wide-area controllers including signal delays

A robust WADC design methodology with H_∞ norm-based stability and performance guarantees and gain scheduling is proposed in [64]. A family of controllers is designed over a discrete set of delay values. Each design ensures appropriate performance inside a range of delays. The actual delay is measured in real-time and used as the scheduling variable to switch smoothly among designs. The need to switch between multiple designs stems from the finding that high damping performance and high robustness to random delays are conflicting design requirements. A 4-machine system is used to illustrate the effectiveness of the approach. The desired performance is obtained for delay values ranging from 50-250 milliseconds.

A network control system model that allows the design of linear optimal controllers capable of acceptable performance in spite of delayed global signals is proposed in [65]. The controllers proposed are full-state feedback controllers and require measurements or estimation of all state-variables in a system, making them impractical even for medium sized power systems. The different mechanisms responsible for the existence of random delays in global power system measurements are described in this reference.

A centralized WADC designed using multi-variable optimal control design techniques while considering communications delays is proposed in [66]. The effects of time delays are included in a reduced order linear state-space model of a small equivalent representation of a portion of the Brazilian power system. The controller tuning problem is framed as a structurally constrained optimal control problem with a quadratic cost function. Manipulations allow the controller to be an output-feedback controller and avoid the need for full-state feedback or a state-observer to estimate the unmeasured states. Acceptable results were obtained for time delays of up to 400 milliseconds.

The effect of signal loss on controller performance is also of high importance but has received less attention in the literature. In [58], the authors allude to the availability of highly reliable communications technology, the possibility of utilizing redundancy when designing critical components, and the potential to implement rigorous maintenance policies, to provide low communication outage rates. However, even with such technologies, the potential for signal loss is still latent. Consequently, designing wide-area damping controls capable of acceptable performance under situations of diminished communications performance remains important. When carefully designed, ANN-based

intelligent damping control has been shown to provide acceptable performance in spite of communication delays and signal loss [10].

2.3 OPPORTUNITIES FOR IMPROVED DAMPING

Most of the literature addressing the design and implementation of WADCs has focused on "minimalist" designs that require a reduced number of input and output global signals. Minimalist designs are illustrated in the left side of Figure 2.12. Researchers have turned to linear system analysis techniques to pinpoint locations where supplementary control signals can have the highest impact on particularly troublesome oscillatory modes, and locations where the maximum amount of information can be gathered for such modes, i.e., signals at locations with the highest controllability and observability. However, this dissertation argues that injecting only a small number of control signals into a large-scale system is bound to limit the potential benefits that WADCs can provide. These limitations are aggravated by the fact that only a small amount of control effort can be exerted at each input location in order to ensure that supplementary damping signals do not interfere with the primary functions of the equipment they are injected to.

Minimalist designs have some obvious advantages: lower complexity, lower communication and implementation costs, possibly higher reliability, and easier controller design. In spite of this, the benefits of utilizing "holistic" controllers with high input and output signal count need to be evaluated. These evaluations would establish if the performance gains provided by more ambitious schemes as illustrated on the right side of Figure 2.12 are sufficient to justify their deployment even after the known drawbacks are accounted for. The research in this dissertation is geared towards holistic control.

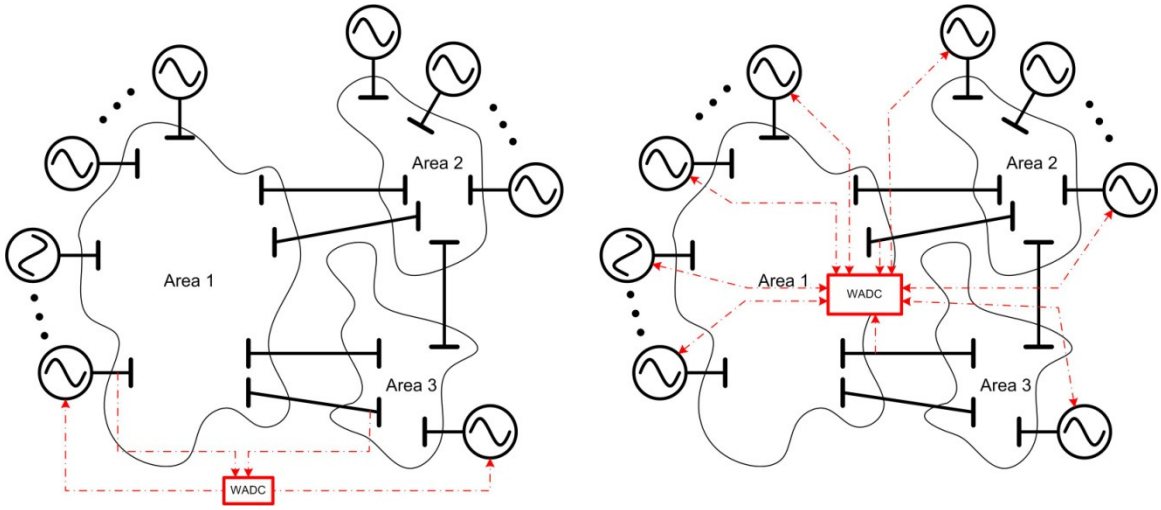

Figure 2.12 Minimalist vs. holistic WADC

As a side note, the reader is cautioned that the definitions of "minimalist" and "holistic" wide-area damping controls are not taken from the broader literature in this subject, where distinctions between minimalist and holistic damping controls have not been made at this time.

2.4 Relation of the Dissertation to Larger Research Project

The research presented in this dissertation has been completed as a portion of a larger project funded by the Office of Emerging Frontiers in Research and Innovation (EFRI) at the National Science Foundation under the topic Cognitive Optimization and Prediction: From Neural Systems to Neurotechnology (COPN). The title of the award is "EFRI-COPN: Neuroscience and Neural Networks for Engineering the Future Intelligent Electric Power Grid". This is a multi-disciplinary research project involving the areas of neuro-biology, neuro-engineering, and electrical engineering. The overarching goal is to infuse more neuro-biology into control systems to make them more brain-like and be able to carry out real-time control of complex systems. Power system models and

experimental setups are used as testing platforms to evaluate novel biologically-inspired control, optimization, and prediction algorithms.

Neuro-biologists participating in the project will draw inspiration from biological brains to develop novel optimization, monitoring, and control algorithms that can scale up to meet the demands of large-scale power systems.

The research in this dissertation focuses on evaluating state-of-the-art intelligent control approaches and on improving them as needed for control of large-scale power systems. Realistic power system simulations are developed for this task. Emphasis is given here to the fact that there is no neuro-biology or neuro-engineering component to this dissertation.

2.5 SUMMARY

It is clear that rotor-angle stability must be maintained for power systems to operate properly. Improvements to rotor-angle stability are regularly achieved using local damping controllers such as PSSs. These have become the standard in the electric power industry. However, it is not clear that they will be effective for damping inter-area oscillations in the highly stressed power networks of the future. These oscillations can impose limits on the steady-state operation of the system and have caused costly wide-spread blackouts in the recent past.

Wide-area damping controllers (WADCs) that make use of global signals can circumvent the limitations of local controls at the expense of higher complexity and cost. However, features such as controller robustness, controller resilience to communication delays and signal loss, reliable communication infrastructures, etc, must be addressed before WADCs can be deployed in real power systems.

Most of the literature addressing the design and implementation of WADCs takes minimalist approaches that require a reduced number of input and output global signals. These have some obvious advantages: lower complexity, lower communication and implementation costs, possibly higher reliability, simpler design, etc. In spite of these, the benefits of utilizing more powerful holistic controllers might be significant enough to justify their deployment and need to be evaluated.

A representative sample of conventional and state-of-the-art approaches to improve rotor-angle stability using closed-loop control has been reviewed. Intelligent control was identified as one of the promising technologies for WADC. However, the ability of intelligent controllers to scale up to meet the demands of large-scale power systems has not been demonstrated and remains an open question.

The next chapter explores relatively conventional stabilizing technology. A new method to tune local and wide-area damping controllers simultaneously while ensuring robustness is provided. The results are then used to highlight the limitations of more conventional technologies and to point to areas where intelligent controls can help.

CHAPTER 3 COORDINATED DESIGN OF CONVENTIONAL LOCAL AND WIDE-AREA DAMPING CONTROLS

3.1 INTRODUCTION

Prior to embarking into the development of intelligent damping controllers, it is important to evaluate the limitations of more conventional stabilizing technology for power systems. This chapter explores some of those limitations by means of design examples. The developments in this chapter were recently reported in [67] and [68].

The next section provides an overview of the power system model used throughout the chapter. Local and wide-area stabilizing controllers are then designed using linearized power system models to illustrate some of the advantages of wide-area control over conventional local controls. A method for coordinating the design of multiple local and wide-area controllers is introduced. The importance of robustness is then illustrated by observing the performance of the resulting damping controllers using small-signal analysis over a large number of power system operating conditions. The results highlight the inadequacy of considering a single operating point during control design.

As was mentioned in Chapter 2, one of the typical approaches used to improve controller robustness is to consider multiple operating conditions during control design. The analysis in this chapter illustrates that selecting the right set of operating conditions to consider is critical and not trivial. In addition, the literature does not provide an adequate method to make this selection. A new gap-metric and hierarchical clustering-based method for automating the selection process is introduced. The method allows the selection of a set of operating conditions that is relatively small, yet rich enough to result in truly robust controller designs.

Small-signal analysis using controllers designed via the improved set of operating conditions then point to the complex tradeoff between robustness and performance. This tradeoff limits the potential rotor-angle stability improvements offered by relatively conventional damping controllers.

3.2 68-BUS POWER SYSTEM MODEL

The power system in Figure 3.1 represents a reduced order model of the New England/New York interconnection of more than 30 years ago. More details on the parameters of this model can be found in Appendix A. The system is composed of 16 machines, 68 buses, 68 lines, 35 loads, and 20 transformers. Generators G14-G16 represent adjacent areas to the NY side of the system as large equivalent machines. The control designs in this chapter assume that supplementary damping signals cannot be added to these three equivalent machines. Each generator is equipped with an excitation system modeled as a simplified IEEE type ST1A static excitation system with transient gain reduction in the feedback path and ignoring under/over excitation limiters (UEL and OEL) as shown in Figure 3.2. This excitation system model follows guidelines defined in [69]. No governors have been added. Local stabilizing controls in the form of power system stabilizers (PSSs) are to be added to generators G1-G13. Wide-area stabilizing controls are also added if and when needed. Each generator is simulated using 6th order synchronous machine models, electromagnetic transients in the transmission system are neglected, and loads are modeled as constant impedances. Simulations are completed using DIgSILENT PowerFactory [70].

Multiple linear models of the system at different operating conditions are obtained after some manipulation using PowerFactory's small-signal analysis capabilities

following the approach described in Appendix B. These models are used for analysis and control design throughout the paper. Each model is of 144th order with structure given as in (3.1).

$$\begin{aligned} \dot{x} &= Ax + Bu \\ y &= Cx \end{aligned} \tag{3.1}$$

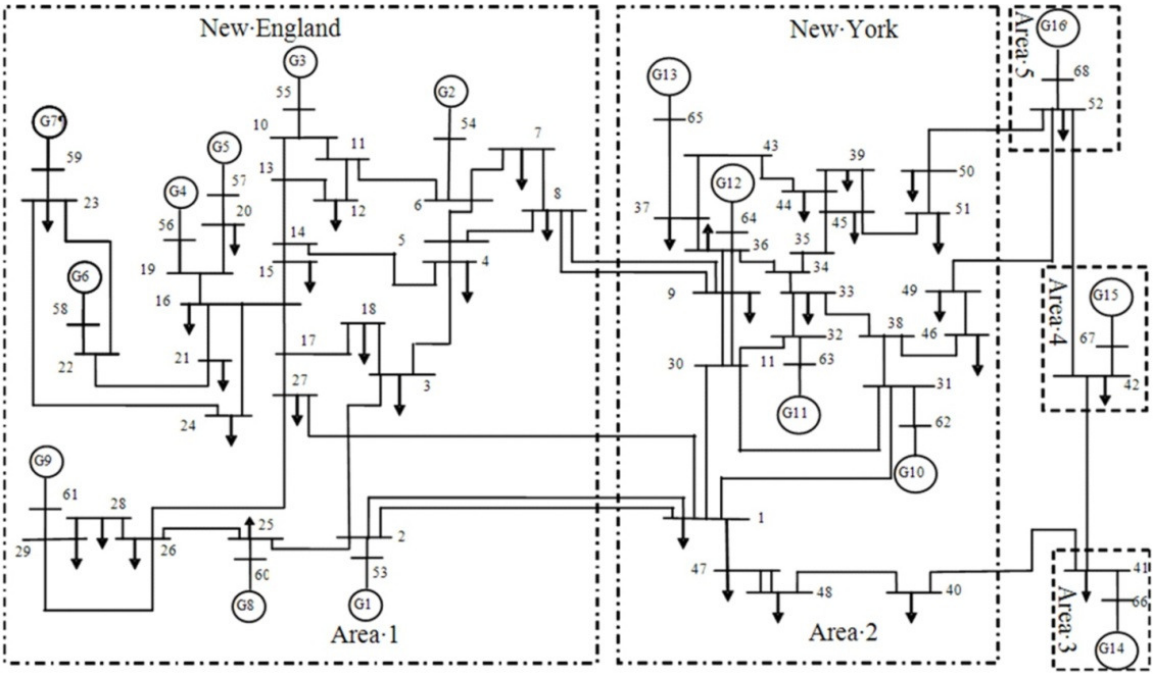

Figure 3.1 Single-line diagram of the 68-bus New England/New York benchmark system

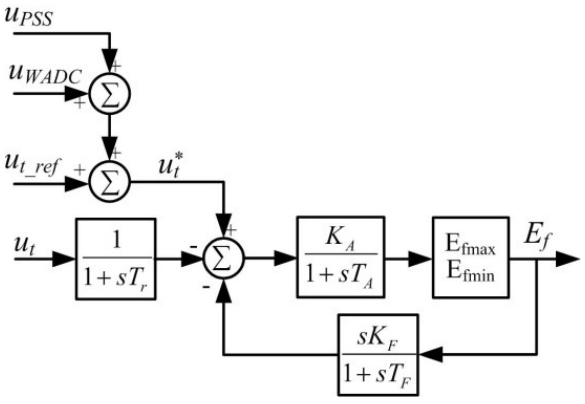

Figure 3.2 Excitation system model

The inputs into the system are the local and wide-area supplementary signals into the AVRs at G1-G13. The outputs are the rotor-speed deviations of G1-G16 as defined in (3.2).

$$u = \begin{bmatrix} u_{PSS}^{G1} + u_{WADC}^{G1} & \cdots & u_{PSS}^{G13} + u_{WADC}^{G13} \end{bmatrix}^T$$
$$y = \begin{bmatrix} \Delta\omega^{G1} & \cdots & \Delta\omega^{G16} \end{bmatrix}^T \tag{3.2}$$

This system exhibits multiple poorly damped local and inter-area modes as illustrated in Figure 3.3. The shaded region (Ω) in Figure 3.3 indicates the region of eigenvalues with damping ratios lower than 10%.

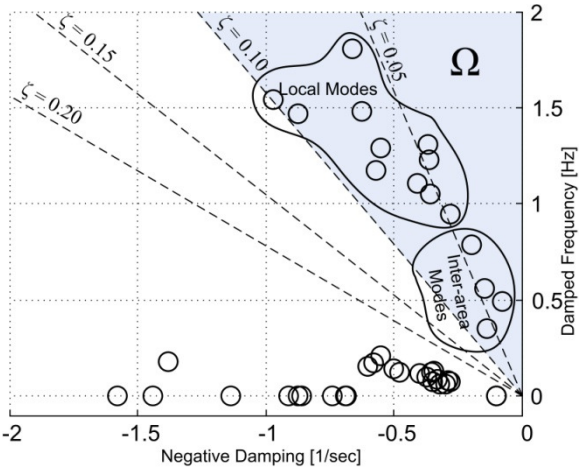

Figure 3.3 Open loop modes for the linearized base-case system

The inter-area mode shapes are presented in Figure 3.4 to provide a better insight into the oscillatory patterns in the system. Interested readers are pointed to Appendix C for a primer on how mode shapes are calculated and interpreted in a power systems setting. The equivalent areas 4-6 in the system are heavily involved in two of the modes (the 0.79 and the 0.49 Hz modes). No control inputs exist for these areas. This will reduce the effectiveness of local controllers and complicate the control task.

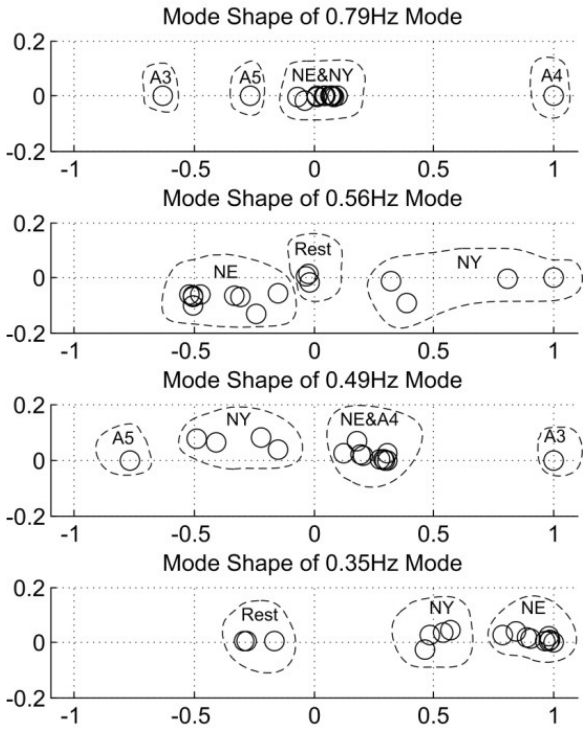

Figure 3.4 Inter-area mode shapes

Local and wide-area damping controllers are to be designed to improve the stability of the system by enhancing the damping of all electromechanical modes. The goal is to push all eigenvalues inside shaded region (Ω) Figure 3.3 towards the left of the complex plane such that their damping ratio is increased to 10% or higher. A PSO-based method of stabilizer design is described next.

3.3 PSO-BASED DAMPING CONTROLLER DESIGN

3.3.1 Overview of Particle Swarm Optimization

Particle swarm optimization (PSO) is an evolutionary optimization technique first introduced by Eberhart and Kennedy in 1995 [71]. The algorithm utilizes a "population" of particles, where each particle represents a candidate solution to the optimization problem. Particles travel across the solution hyperspace with velocities defined by their

own previous experience, as well as the experience of their neighbors. The positions and velocities of the population are updated iteratively until a maximum number of iterations is reached or until a satisfactory stopping criterion is met. A comprehensive survey of the different variations of PSO and its applications to power systems is presented in [72]. The use of PSO for damping controller design was demonstrated in [36], [41], and [73]. However, none of the approaches in the literature provide the capabilities to coordinate the design of multiple PSSs and WADCs while considering all critical electromechanical modes in a power system over a wide range of operating conditions.

3.3.2 Controller Optimization Objectives

The PSSs and WADCs to be designed have the structure given in Figure 3.5 and Figure 3.6 respectively. These structures were defined by loosely following guidelines defined in [69]. Generators G1-G13 in Figure 3.1 are to be equipped with one PSS each. Controllability and observability measures calculated in section 3.5 will show that appropriate input points for WADC signals are G9, G11, and G13 and that appropriate measurements points are the speeds of G15 and G16. Input and output signals of each controller are in per unit. The time constant for all washout stages is chosen as T_w = 10 sec, which is in agreement with common practice. The washout stage keeps stabilizers from reacting to changes in the system's steady state operating condition, which would be undesirable. The gain and phase compensation time constants for each controller, $\theta_i = \left[K_{PSS}^i \; T_1^i \;\; T_2^i \;\; T_3^i \;\; T_4^i\right]$, are to be optimized. Each PSS has one set of five parameters and each WADC has two sets for this scenario, but may have more or less depending on the number of wide-area measurements used. For "p" local PSSs and "w" WADCs, there

are a total of $(5 \times p + 2 \times 5 \times w)$ parameters to be optimized using PSO. The decision vector $\theta = [\theta_1 \cdots \theta_{p+w}]$ is composed of these parameters.

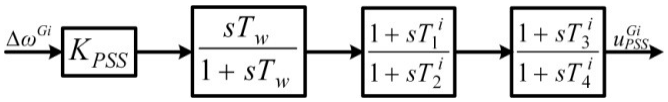

Figure 3.5 Speed-input power system stabilizer

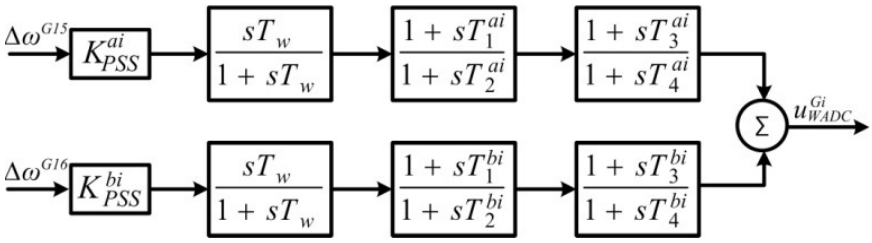

Figure 3.6 Wide-area damping controller

The outputs of the PSSs and WADCs are connected to the excitation system at the u_{PSS} and u_{WADC} points in Figure 3.2 respectively.

The fitness function (or objective function) to be minimized is defined as (3.3). The part of this function shown in (3.4) assigns higher priority to eigenvalues with small real parts which correspond to oscillations that decay slowly. The function in (3.5) penalizes eigenvalues that have real parts greater than $\overline{\sigma}$, in a linear manner by the scalar k_p in order to prioritize unstable and near unstable modes and guide them back towards the left half plane. The λ_i's (3.4) and (3.5) refer to the closed-loop eigenvalues of the linearized system after adding the stabilizing controls. Function (3.6) penalizes any parameters that result in transfer function magnitudes greater than $\overline{H}$. This ensures the gains of the resulting controllers are bounded to acceptable levels. The regions $\mathbb{N}$ and $\mathbb{M}$ are shown in Figure 3.7 and $\mathbb{O}$ is the set of parameters that result in $\left\|H_{PSS,o}(j\omega)\right\| > \overline{H}$. Eigenvalues

outside the region $N \cup M$ have no effect on the value of J. PSO is used to solve the optimization problem defined by (3.7).

$$J(\theta) = J_1(\theta) + J_2(\theta) + J_3(\theta) \tag{3.3}$$

$$J_1(\theta) = \sum_n \left(\frac{1}{|re(\lambda_n)|} \right) \forall n : \lambda_n \in N \tag{3.4}$$

$$J_2(\theta) = \sum_m k_p \left(re(\lambda_n) + \frac{1}{k_p |\overline{\sigma}|} + \overline{\sigma} \right) \forall m : \lambda_m \in M \tag{3.5}$$

$$J_3(\theta) = \sum_o \left(\frac{10 \max \left(H_{PSS_o}(j\omega) \right)}{\overline{H}} \right) \forall o : \theta_o \in O \tag{3.6}$$

$$\theta^* = \underset{\theta}{\operatorname{argmin}} \{ J(\theta) \} \tag{3.7}$$

Figure 3.7 also shows that stable eigenvalues with very low frequencies (less than 0.01 Hz) are ignored, since they do not correspond to the range of frequencies associated with electromechanical oscillations.

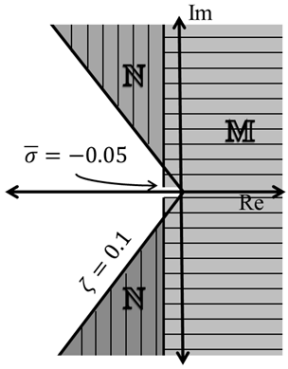

Figure 3.7 Definition of eigenvalue regions used to define the controller optimization problem

3.4 EXAMPLE OF LIMITATIONS OF LOCAL DAMPING CONTROLS

The first set of stabilizers considering only local control loops is designed using PSO to minimize (3.3) by tuning the gains and time constants of the 13 PSSs connected to G1-G13. The behavior of (3.3) during the optimization process for 5 trials is depicted in

Figure 3.8. The fact that each optimization run ends at the same final value of $J(\theta)$ indicates that it is likely that a global minimum has been reached.

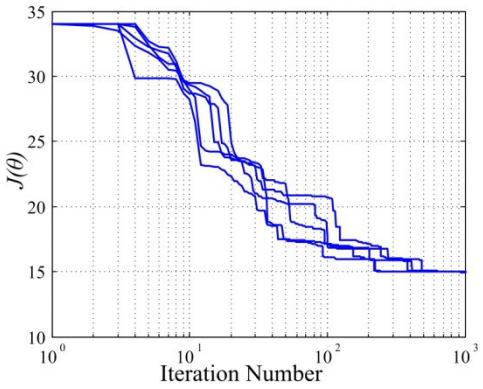

Figure 3.8 PSS optimization results for 5 trials

Figure 3.9 illustrates the eigenvalues of the linearized system before and after adding the optimized PSSs. The optimized local controllers significantly improve the damping of nearly all eigenvalues. However, two inter-area modes remain almost completely unaffected and their open and closed loop values overlap. These are known as nearly decentralized fixed modes (NDFMs), which are defined as modes that cannot be appreciably shifted using permissible local controls. The causes of this behavior are explored next.

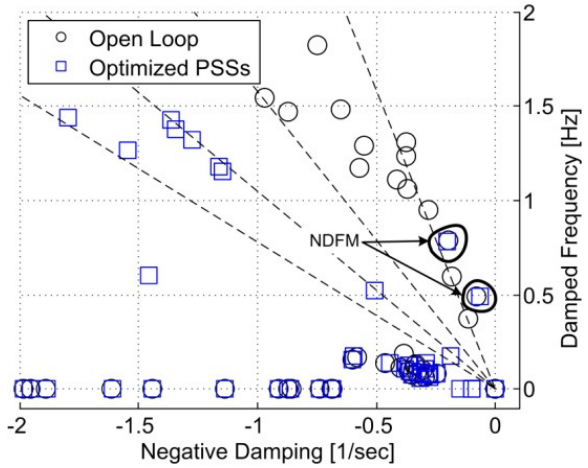

Figure 3.9 Eigenvalues of the system before and after adding local controls

The existence of NDFMs highlights some of the limitations of local damping controls. The next section illustrates the causes behind the emergence of NDFMs and demonstrates the ability of controllers based on wide-area signals to overcome these limitations.

3.5 OVERCOMING THE LIMITATIONS OF LOCAL DAMPING CONTROLS

3.5.1 Observability and Controllability Analysis for Selection of Input-Output Locations

This section analyzes the causes of the inability of the local controllers to improve the damping of the two poorly damped inter-area modes in Figure 3.9. The results provide the starting point for the design of multiple wide-area controllers that can overcome the limitations of the local controllers.

Residue-based linear observability and controllability measures defined by (3.8)-(3.9) are calculated for all electromechanical modes [55]. They provide a measure of the relative effectiveness of available inputs and outputs to control and observe a particular mode. Results are relative to the set of inputs and outputs used for the analysis, i.e., adding a new input/output signal can dramatically change these measures.

$$R_k = Ce_k f_k^T B \tag{3.8}$$

$$\begin{cases} \overline{m}_{ci}(k) = \left\| R_k(:,i) \right\| \Big/ \left\| R_k \right\| \quad (i = 1,...,13) \\ \overline{m}_{oj}(k) = \left\| R_k(j,:) \right\| \Big/ \left\| R_k \right\| \quad (j = 1,...,16) \\ \overline{m}_{ji}(k) = \overline{m}_{ci}(k) \times \overline{m}_{oj}(k) \end{cases} \tag{3.9}$$

The results for the two inter-area modes that can be shifted by local controls are illustrated in Figure 3.10, while the ones for the NDFMs are given in Figure 3.11.

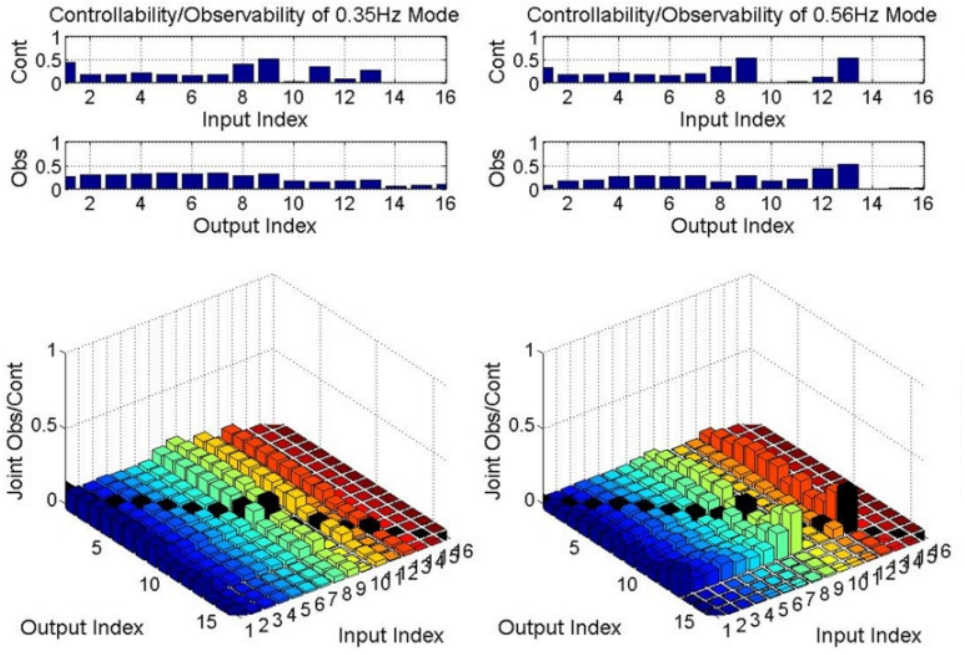

Figure 3.10 Observability and controllability analysis of inter-area modes that can be influenced by local controls

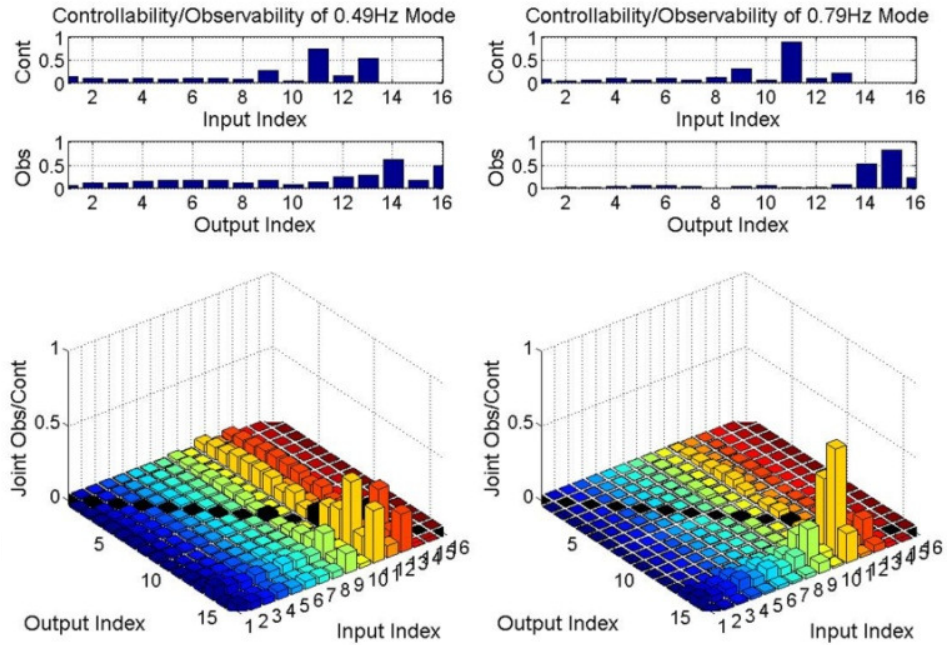

Figure 3.11 Observability and controllability analysis of nearly decentralized fixed inter-area modes

A mode can be damped effectively using local controls if it is both controllable and observable from the same location, giving a high joint controllability/observability measure for local signals. The joint controllability/observability for local controllers is given by the diagonal terms marked in black in the 3D plots of Figure 3.10 and Figure 3.11. Figure 3.11 shows that the 0.49 Hz and 0.79 Hz modes are not observable from G1-G13 (locations with PSSs installed). This explains the inability of the local PSSs of the previous section to improve the damping of these two modes. These limitations could be lifted by enabling input signals into the excitation systems of G14-G16. However, G14-G16 represent large aggregated areas potentially composed of many generators, loads, etc, so inputting signals into them would not be realizable in practice and is considered infeasible in this chapter.

Signals with the highest observability and controllability for the NFDM are selected. The observability measures point to the speed deviations of G15 and G16 as effective output signals for controlling the NDFM. The controllability measures point to G9, G11, and G13 as the most effective input locations. This analysis justifies the input-output configuration chosen in section 3.3.2.

3.5.2 Coordinated Design of Local and Wide-Area Damping Controls

A second set of stabilizers is designed using PSO. The parameters of the 13 PSSs connected to G1-G13 and of the 3 WADCs connected to G9, G11, and G13 are tuned simultaneously to achieve a coordinated design. Figure 3.12 illustrates eigenvalues of the system before and after adding the stabilizing controls. All eigenvalues, including the NDFMs, exhibit a damping ratio of 10% or higher and serve as a clear demonstration of the additional damping improvements that can be achieved using WADCs.

The designs are further evaluated using time-domain simulations of the full non-linear model of the power system. This validation step is needed since the controllers were designed using a linearized power system model. Figure 3.13 demonstrates the effectiveness of the controllers for a three phase fault in the New York side of the system. Similar results are obtained with other fault locations.

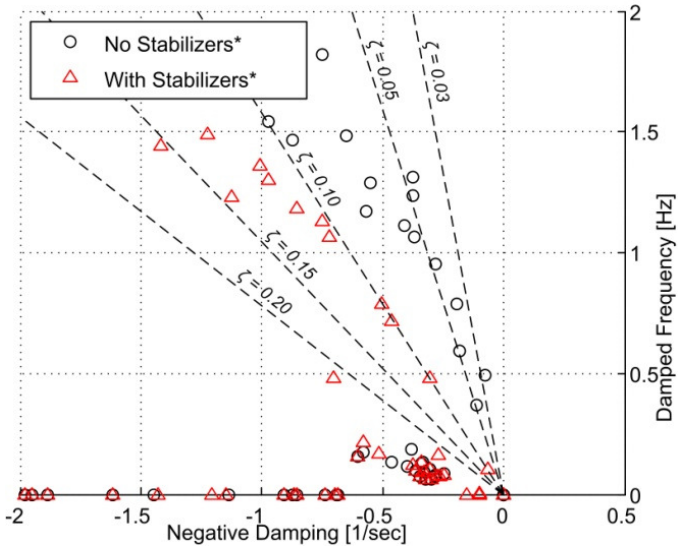

Figure 3.12 Eigenvalues of the linearized model before and after adding stabilizing controls optimized for a single operating point

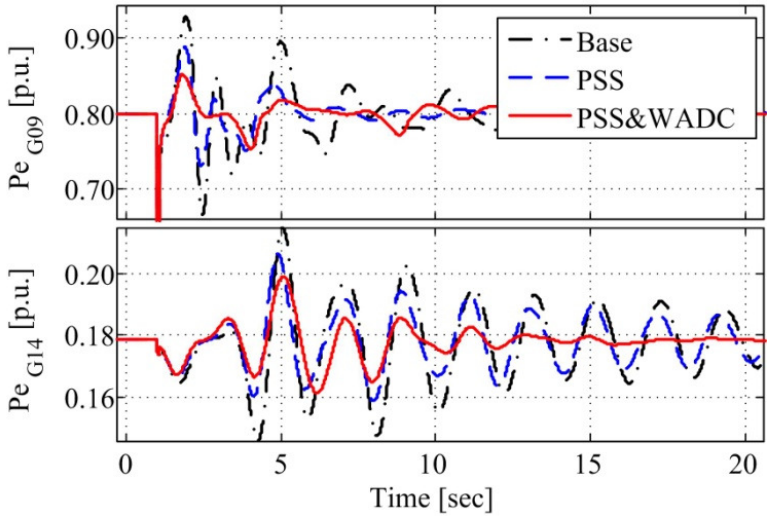

Figure 3.13 Time-domain simulation

The stabilizer designs obtained so far appear to be effective. However, as was mentioned in Chapter 2, robustness to changes in operating conditions is paramount for effective designs. The next section evaluates controller robustness and provides a multi-model approach to enhance it.

3.6 DESIGNS CONSIDERING ROBUSTNESS

This section evaluates the performance and robustness of the stabilizing controllers developed so far. The evaluations consist of extensive small-signal analysis. The goal is to observe the behavior of the closed-loop system over a wide array of operating conditions. An approach is presented and validated to enhance robustness incorporating the idea of using multiple linearized models for control design coupled with a new method to select those models.

3.6.1 Approach to Analyze Eigenvalue Movements

Inter-area oscillations tend to emerge or worsen as the transmission system weakens and as power transfers among distant areas increase. The movement of the eigenvalues under a wide variety of operating conditions is analyzed using the approach given by the flow chart in Figure 3.14. Note that the approach involves calculating a large set of linearized models of the power system under study, where each linearized model corresponds to a different operating condition. Custom software was developed to automate the linearization process and store the resulting models in a model bank for analysis. This model bank can be useful for other tasks beyond eigenvalue movement analysis as will become clear in sections 3.6.3 and 3.6.4.

A set of all N-1 transmission line contingencies is considered. Also, the inter-area active power interchange from NE to NY (see Figure 3.1) is varied by ±500 MW in step increments of 25 MW from its base level of 720 MW. Loads are held constant for all cases. Power interchange variations are implemented by increasing/decreasing the power output of all generators in NE evenly (in per unit). Power balance is achieved by decreasing/increasing the output of generators in NY evenly (in per unit). Disconnection of the equivalent lines interconnecting areas 4, 5, and 6 is not considered.

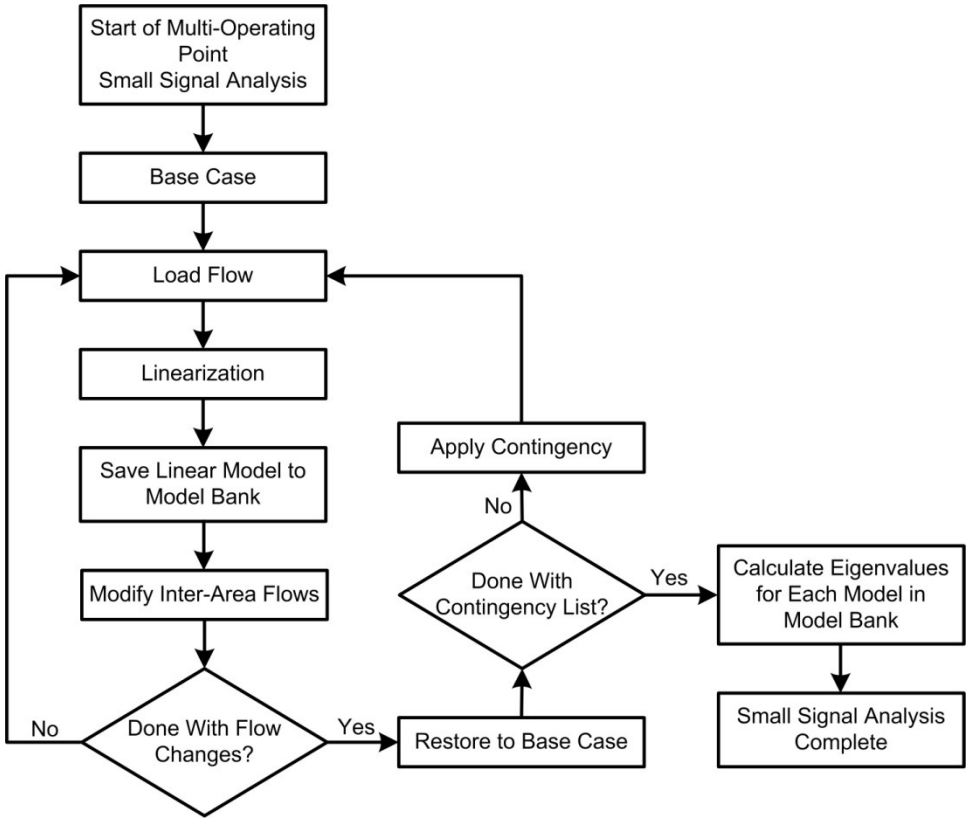

Figure 3.14 Flow chart of approach to multi-operating point small signal analysis

Figure 3.15 illustrates the movement of the system eigenvalues over the resulting operating conditions. The base case eigenvalues are shown in yellow, contingency cases with no interchange variation are shown in black, and the red and green circles

correspond to progressive increases and decreases in the NE/NY interchange before and after contingencies. A total of 1736 operating conditions are examined.

There is a clear trend in Figure 3.15: as the NE/NY interchange increases, the damping of some of the low-frequency inter-area modes decreases until stability is lost. With an N-1 contingency criterion, i.e. the system must remain small-signal stable for all N-1 contingencies considered, the additional interchange from NE to NY has to be limited to 200 MW just to guarantee the system remains critically stable (point where eigenvalues cross to the right side of the complex plane) at all post-contingency states.

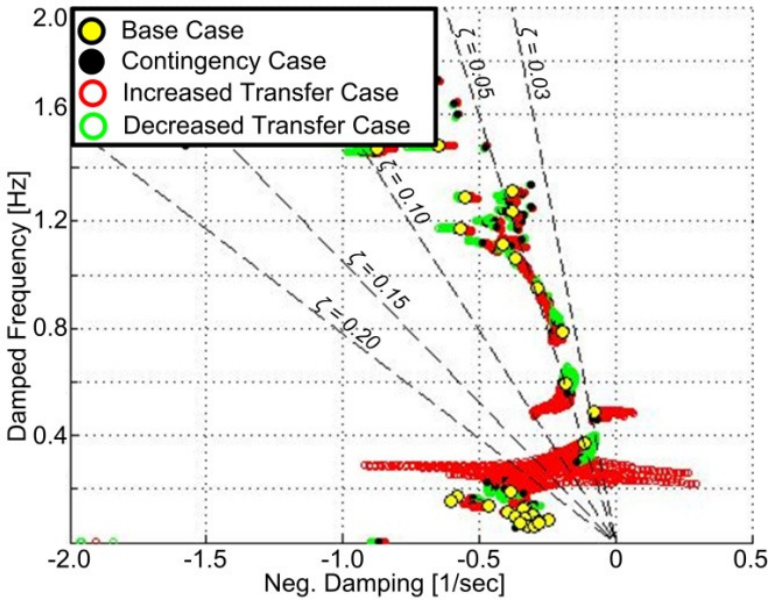

Figure 3.15 Eigenvalue movements with changes in operating conditions and no supplementary stabilizing controls

3.6.2 Evaluating Robustness of PSO-Based Stabilizer Designs

The eigenvalue movement analysis from the previous section is completed here after adding the WADCs designed in section 3.5. The results are depicted by Figure 3.16. Some of the operating conditions result in system instability and limit the inter-area

active power interchange from NE to NY. However, the maximum power transfer considering an N-1 contingency criterion is now 430 MW (up from 200 MW). This is a substantial improvement. In spite of these improvements, it is possible to design controllers with enhanced robustness that can increase the transfer capabilities even further. A method to do so is explored next.

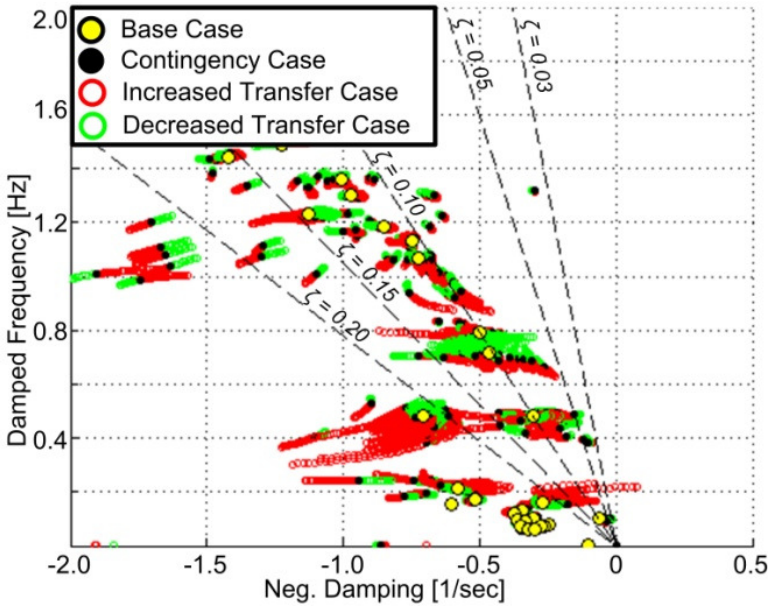

Figure 3.16 Eigenvalue movements after adding stabilizers designed using 1 operating point

3.6.3 Enhancing Robustness by Heuristic Multi-Operating Point Design

One of the methods often proposed in the literature to enhance robustness is to utilize linearized models obtained around multiple operating points for control design. The core idea is that accounting for the "worst case scenarios" during the design stage results in stabilizers that perform well over a much larger set of operating conditions. The selection of the operating conditions to use is heuristic and based on the designer's experience. This heuristic approach is taken here.

The base-case scenario and 4 operating conditions nearing instability are selected. Five linearized models obtained at these 5 conditions are then used for multi-model control design. The coordinated PSS and WADC optimization approach is identical to that used in section 3.5. The eigenvalues of the linearized models for all 5 operating conditions before and after adding the stabilizing controls are depicted in **Error! Reference source not found.**. Clearly, the design objectives have been met and the damping ratios of all eigenvalues with closed loop control and for all 5 operating conditions are above 10%. However, this does not imply robustness improvements over the wider set of operating conditions.

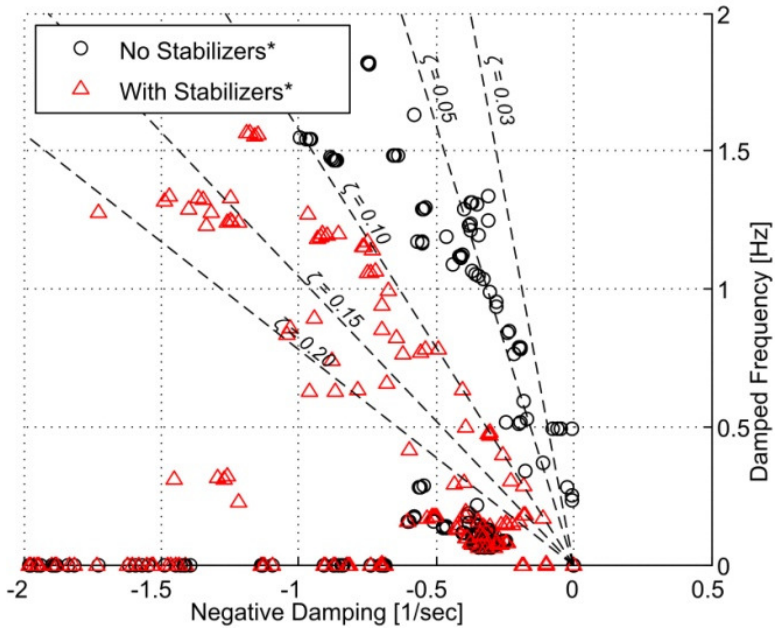

Figure 3.17 Eigenvalues of the linearized models before and after adding stabilizing controls optimized for 5 operating points

Figure 3.18 illustrates the eigenvalue movements of the closed-loop system with the controller parameters for "improved robustness". Unexpectedly, the system now becomes unstable over a larger set of operating conditions. This can be inferred by the larger

number of eigenvalues crossing into the right hand side of the complex plane in comparison to Figure 3.16. This indicates that the initial attempt at improving robustness using multi-model control design has failed.

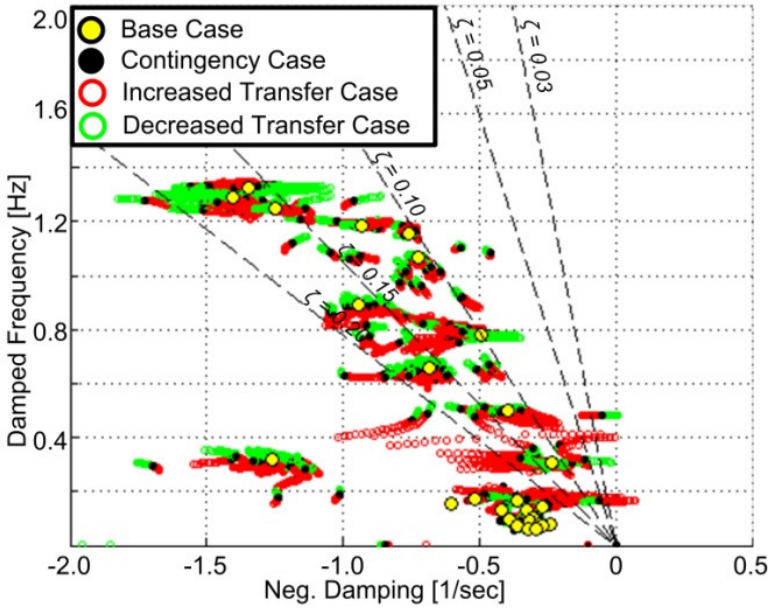

Figure 3.18 Eigenvalue movements after adding stabilizers designed using 5 operating points

These results point to the need for an effective mechanism to select an appropriate set of operating conditions to consider during control design. Making this selection is critical and not straightforward. In fact, Figure 3.18 demonstrates that selecting the wrong set can actually degrade robustness and degrade overall rotor-angle stability. However, the literature does not offer a straightforward and effective method to make this selection. The next section presents such a method.

3.6.4 Enhancing Robustness Using Advanced Operating Point Selection

An appropriate set of operating conditions for control design is one that is rich enough to allow for robust controller development, but small enough to make the

parameter optimization process computationally tractable. The goal is to eliminate redundancy while maintaining diversity such that the conditions selected for control design span all expected system behaviors.

A measure of operating point similarity is needed for determining redundancy or diversity. The concept of the gap metric introduced in [74] provides such a measure. The gap metric can be seen as a measure of "distance" between two dynamical systems. The distance (or gap) between two models varies between 0 and 1. When the gap between two models is close to 1, they are not similar; when it is close to 0, the models are similar.

In [75], the gap metric was used in the context of multi-linear model-based control for selecting a small set of linear models that accurately represent the different modes of operation of a non-linear system. A similar approach is used here after incorporating hierarchical clustering to simplify the selection process.

The model selection and stabilizer optimization procedure follows the steps outlined in Figure 3.19. Prior to starting this process, a linearized model of the system is calculated for each operating condition under consideration following the automated approach presented in Figure 3.14. A bank of linear power system models is thus available for analysis. These linear models are then compared against each other using the gap metric as implemented in MATLAB's Robust Control Toolbox. If needed, the models in the bank can be reduced using balanced realization truncation to minimize the computational burden of calculating the gap metric. Hierarchical clustering is then applied using the gap metric as the distance measure. The dendrogram in Figure 3.20 illustrates the clustering results. The vertical axis corresponds to the value of the gap

metric. The horizontal axis corresponds to an arbitrary identification number assigned to each linear time-invariant (LTI) power system model for easy indexing.

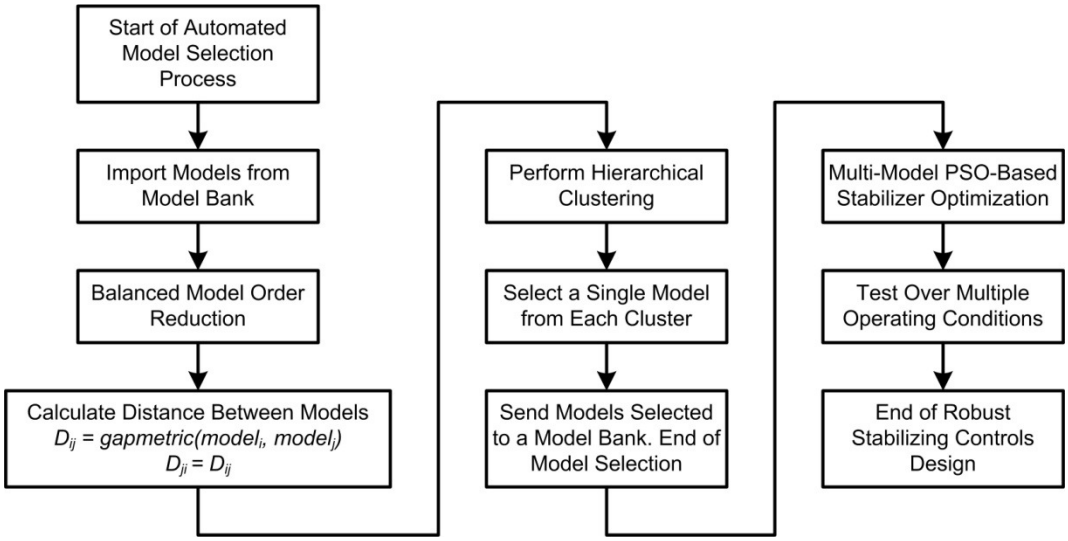

Figure 3.19 Robust stabilizer design using automated selection of multiple operating points

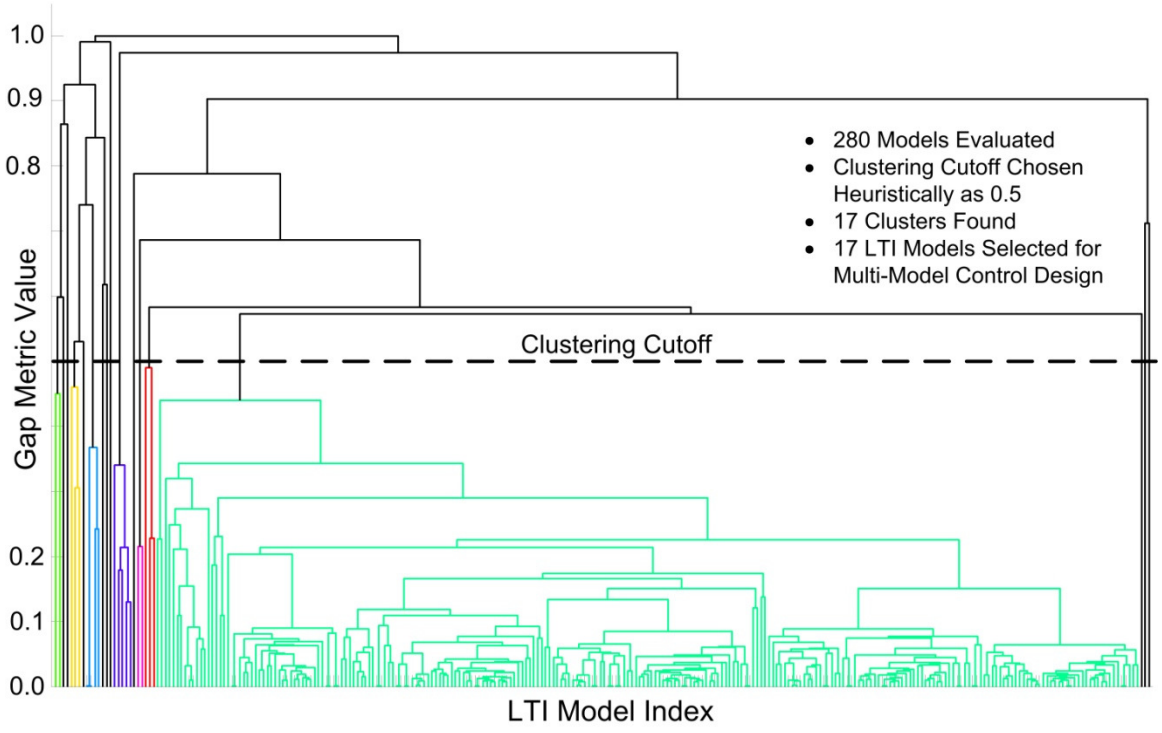

Figure 3.20 Dendrogram of operating points under consideration

A total of 17 operating conditions are selected. Each operating condition is represented using a separate linearized model. PSS and WADC parameters are then optimized using the same PSO-based mechanism used thus far.

Figure 3.21 depicts the objective function during the parameter optimization process for 5 trials. Each of the trials achieves the same value of $J(\theta)$ indicating that it is likely that a global minimum has been reached.

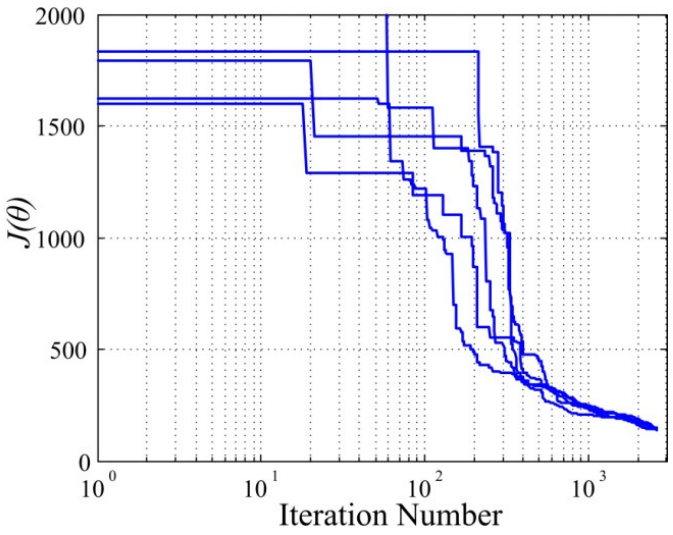

Figure 3.21 PSS and WADC optimization results for 5 trials when considering 17 operating conditions

The eigenvalues of the linearized models for all 17 operating conditions before and after adding the stabilizing controls are depicted in Figure 3.22. In contrast with the past examples, this time the optimization step does not push all eigenvalues to have a damping ratio of 10% or higher, and therefore the performance objectives are not met. In fact, some of the critical inter-area modes are still poorly damped with damping ratios slightly lower than 3%.

Figure 3.23 shows the eigenvalue movements with the new controller parameters. In spite of the poor damping improvements for some modes, none of the operating

conditions in the study results in instability, and the eigenvalue movement analysis closely matches the results observed during control design as depicted in Figure 3.22.

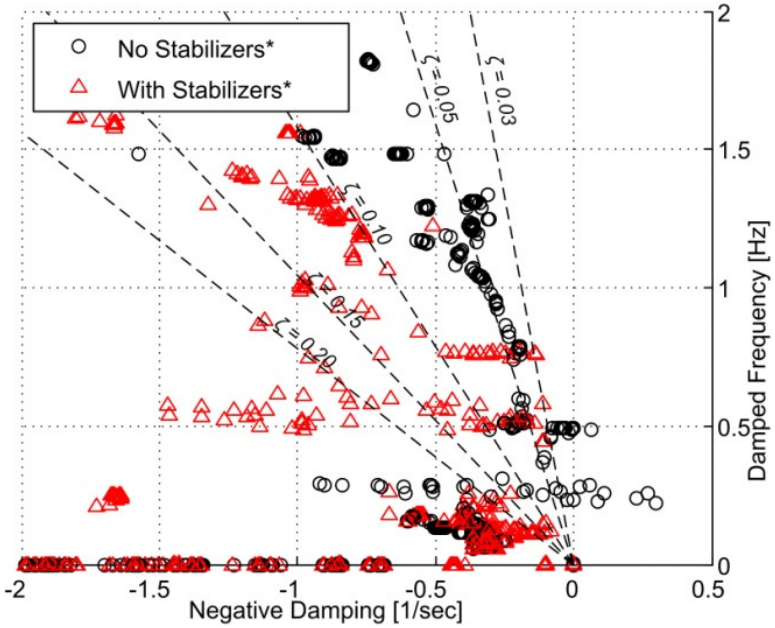

Figure 3.22 Eigenvalues of the linearized models before and after adding stabilizing controls optimized for 17 operating points

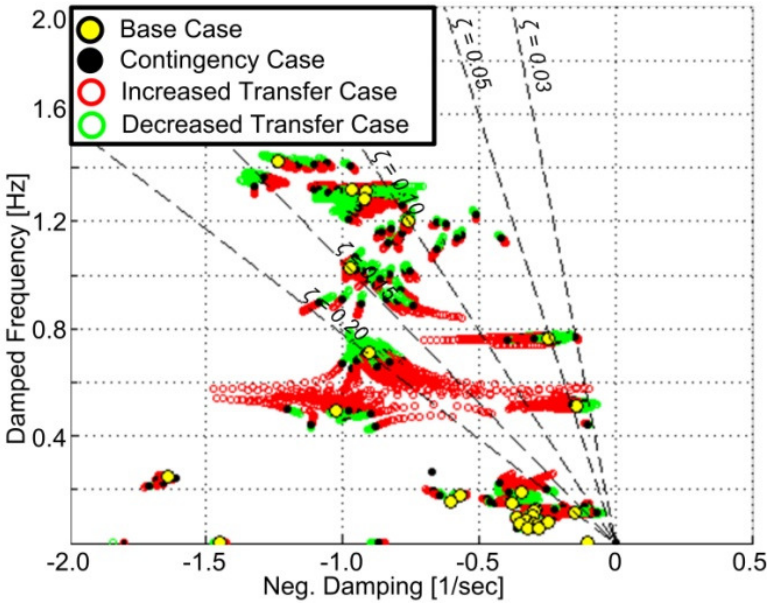

Figure 3.23 Eigenvalue movements after adding stabilizers designed using 17 operating points

These results illustrate the tradeoff between robustness and performance when designing damping controls for power systems. The results suggest that imposing stringent robustness requirements limits the rotor-angle stability improvements that linear local and wide-area damping controls can provide to a power system.

Intelligent controllers offer the possibility to circumvent these limitations, achieve a better tradeoff, and provide significant rotor-angle stability enhancements over a wider range of operating conditions without sacrificing robustness.

3.7 SUMMARY

This chapter illustrated some of the limitations of conventional power system stabilizing technology used to enhance rotor-angle stability in power systems. Two new tools for designing linear stabilizers were provided.

The first enables the coordinated design of multiple PSSs and WADCs and is based on PSO and linearized power system models.

The second automates the selection of an appropriate set of operating conditions to consider for robust multi-model control design. This selection is critical and, until now, not straightforward. The resulting set allows controllers to become robust to a large set of operating conditions as demonstrated by extensive small-signal analysis throughout the chapter.

The complex tradeoff between robustness and performance was illustrated. The studies show that imposing stringent robustness demands on linear stabilizing controllers can limit their contribution to rotor-angle stability. Intelligent controllers offer the possibility to enhance performance when compared to conventional linear controls due to their non-linear nature and adaptation capabilities. This potential grants the exploration of

intelligent controls for power system damping purposes. This exploration begins in Chapter 5.

As mentioned in Chapter 2, this dissertation is focused on developing holistic WADC. These are controls with high input-output count when compared to the minimalist designs of the majority of the literature. The next chapter investigates the importance of scalability for enhancing power system damping control. It also explores the capabilities of artificial neural network topologies typically used to implement power system damping controls to scale-up. Good scalability is paramount for holistic control of large-scale power systems.

CHAPTER 4 IMPORTANCE AND CHALLENGES OF SCALING-UP

4.1 INTRODUCTION

Real power systems are composed of hundreds or even thousands of generators, transmission lines, transformers, loads, etc. These systems are also non-linear and are subject to incessant stochastic operating condition and structural variations. Therefore, control algorithms and methodologies to improve the rotor-angle stability of these systems in a holistic way as described in Chapter 2 need to be both robust and scalable.

The next section probes into the advantages of holistic approaches over minimalist ones. Mode observability/controllability measures and mode sensitivities are calculated for a small set of local and inter-area oscillatory modes of a sample system over a number of different operating conditions. The value of developing holistic controls is substantiated by the observations. The reader is reminded that a minimalist approach is one that utilizes a relatively low input/output signal count in an attempt to provide acceptable performance with minimal communication requirements. In contrast, a holistic approach utilizes a higher input/output signal count in order to achieve superior performance enhancements. These definitions were first introduced in section 2.3.

The implementation of holistic controllers demands good algorithm scalability. However, the ability of intelligent wide-area damping controllers (IWADC) to scale-up has not been demonstrated and remains an open question. An investigation into the scalability of IWADCs is thus completed. This investigation shows that state-of-the-art IWADCs do not meet the needs of holistic control of large-scale systems.

4.2 Consequences of Minimalist Designs on Modal Controllability and Observability

The limitations of minimalist designs are explored in this section using the 68-bus/16-machine benchmark model from Chapter 3. The simplified diagram of the system is repeated in Figure 4.1 for convenience. Recall that generators G14, G15, and G16 are large equivalent machines used to represent large areas of the system. As such, the analysis assumes that inputs cannot be added to these 3 machines.

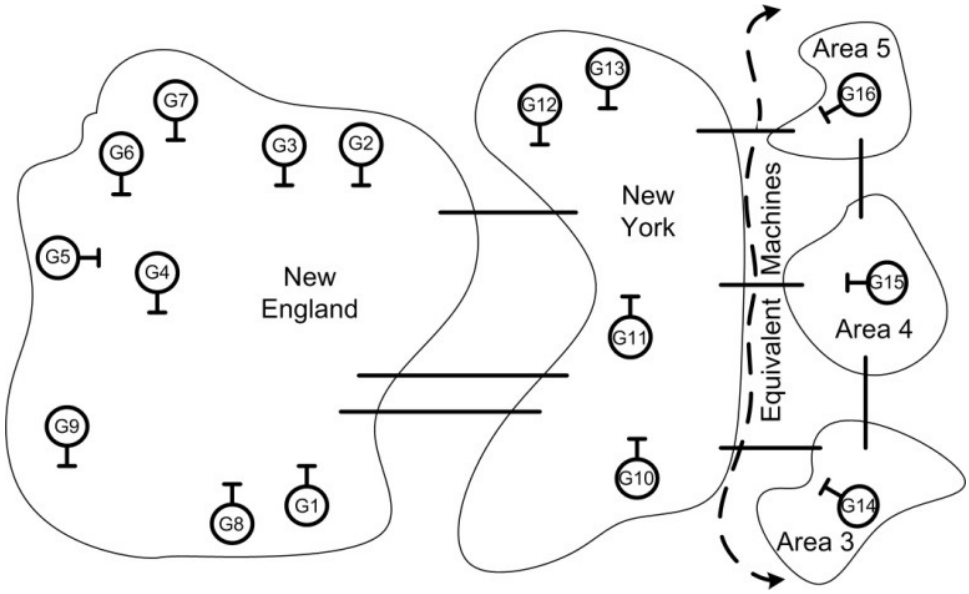

Figure 4.1 Abstracted view of 68-bus New England/New York benchmark system

Figure 4.2 illustrates the system's eigenvalues over the set of 17 operating conditions determined in Chapter 3. Recall that this relatively small set spans the behaviors of the system over a set of operating conditions much larger than 17 (1736 operating conditions described in Chapter 3). Three different modes are given special attention. The locations and movements of these 3 modes, labeled A, B, and C respectively, are encircled by the red/dashed lines in Figure 4.2.

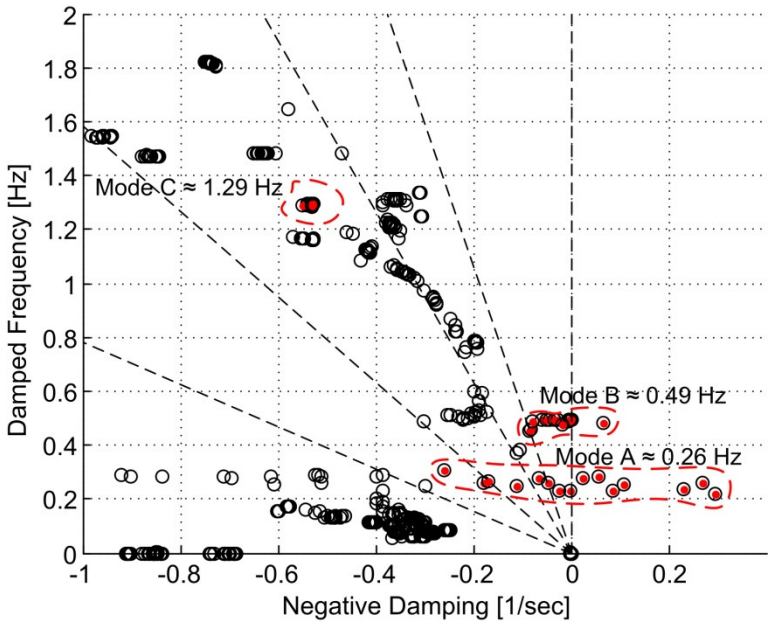

Figure 4.2 System eigenvalues over 17 different operating conditions

As mentioned in Chapter 3 , interested readers can refer to Appendix C for a primer on how mode shapes are calculated and interpreted in a power systems setting. Recall that eigenvalue plots illustrate the frequency and decay rates of oscillations in a system. Speed mode shapes depict the magnitude and phase displacement of the rotor speed of generators when a particular oscillatory mode is excited. Speed mode shapes are thus calculated here to understand the oscillatory behavior of the 68-bus system over multiple operating conditions.

The mode shapes for modes A, B, and C are depicted in Figure 4.3. The shape of mode A indicates that this mode involves the New England side of the system oscillating against Areas 3-4-5, and to a lesser extent against the New York side. The shape of mode B indicates that this mode involves Area 3 oscillating against Area 5, and also against the New York side of the system. From these shapes it can determined that modes A and B are inter-area modes, since they involve large groups of machines in different areas of the

system oscillating against each other. These two modes are found to be very sensitive to changes in operating conditions, as made clear by their significantly different locations in the complex plane of Figure 4.2 at different operating conditions. Recall that mode B was found to be a nearly decentralized fixed mode (NDFM) in Chapter 3 . This was determined since, at least at the nominal operating condition, this mode could not be appreciably shifted using any permissible local controls.

The shape of mode C indicates that this mode is a local mode, since it involves only two machines within the same area oscillating against each other (both G2 and G3 are inside of the New England side of the system). The similarity of the locations of mode C at different operating conditions in Figure 4.2 demonstrates that this mode is not significantly sensitive to changes in the system's operating point.

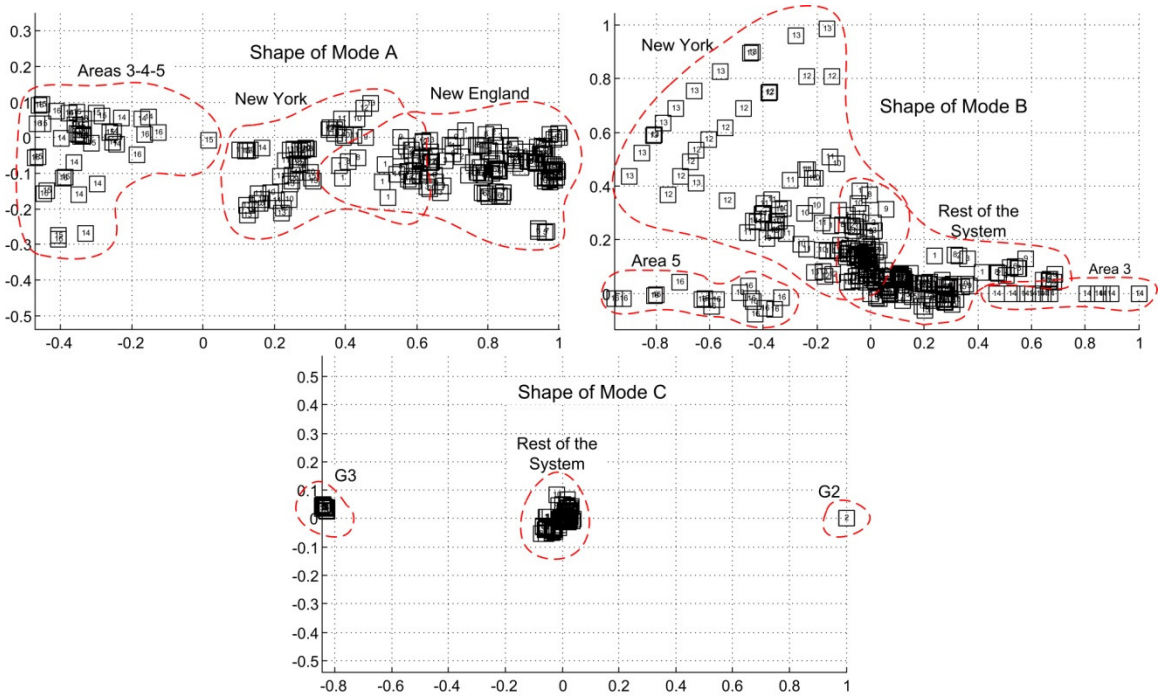

Figure 4.3 Shapes of modes A, B, and Cover 17 different operating conditions

An extensive numerical analysis of modes A, B, and C can provide insights into the characteristics of local and inter-area oscillations over a wide set of operating conditions. Such an analysis in terms of controllability, observability, and sensitivity is presented next. The observations will likely be applicable to other power systems, and will be used to draw conclusions expected to extend beyond the sample system of this chapter.

A more fundamental (not numerical) analysis would be desirable since it would be more conclusive and perhaps more insightful, but the complexity of such an analysis would likely require mathematical developments beyond the scope of this dissertation. Also, fundamental studies of power system oscillations [76] are often completed using numerical studies of the form given next.

4.2.2 Modal Controllability, Observability, and Sensitivity Analysis

A typical minimalist damping controller design approach relies on selecting a small number of input/output locations. These locations are selected so as to maximize the controllability/observability of critical oscillatory modes in need of additional damping.

Two of the measures of relative mode controllability and observability that can be used for input and output signal selection [55] were provided in Chapter 3 and are repeated in (4.1)- (4.3) for convenience. An input/output location with high relative controllability/observability (value close to 1) for a particular mode is a good candidate for adding a control/measurement signal to damp that mode.

$$R_k = Ce_k f_k^T B \tag{4.1}$$

$$\overline{m}_{ci}(k) = \left\| R_k(:,i) \right\| \Big/ \left\| R_k \right\| \quad (i = 1,...,13) \tag{4.2}$$

$$\overline{m}_{oj}(k) = \left\| R_k(j,:) \right\| \Big/ \left\| R_k \right\| \quad (j = 1,...,16) \tag{4.3}$$

In (4.1), f_k and e_k are the left and right eigenvectors corresponding to mode k respectively. These eigenvectors are orthogonal and normalized and satisfy (4.4).

$$\begin{cases} Ae_k = \lambda_i e_k \\ A^T f_k = \lambda_i f_k \\ f_i^T e_j = 1 \forall (i = j) \\ f_i^T e_j = 0 \forall (i \neq j) \end{cases} \tag{4.4}$$

The relative controllability and observability measures for modes A, B, and C at the 17 operating conditions are summarized in Figure 4.4 and Figure 4.5. Clearly, the controllability and observability measures for mode C are not affected by changes in the system's operating condition. Both measures are high for the inputs and outputs at locations 2 and 3. This is expected since the mode shapes in Figure 4.3 showed that G2 and G3 are the only generators swinging in this mode.

The controllability and observability measures for modes A and B vary significantly with changes in the system's operating condition. Close inspection of the measures over the different operating conditions reveals that there is no single input or output location that emerges as the best candidate at all times. This is particularly noticeable for the controllability measures. Some of the locations that exhibit high relative controllability at some operating condition also exhibit low relative controllability at other operating conditions.

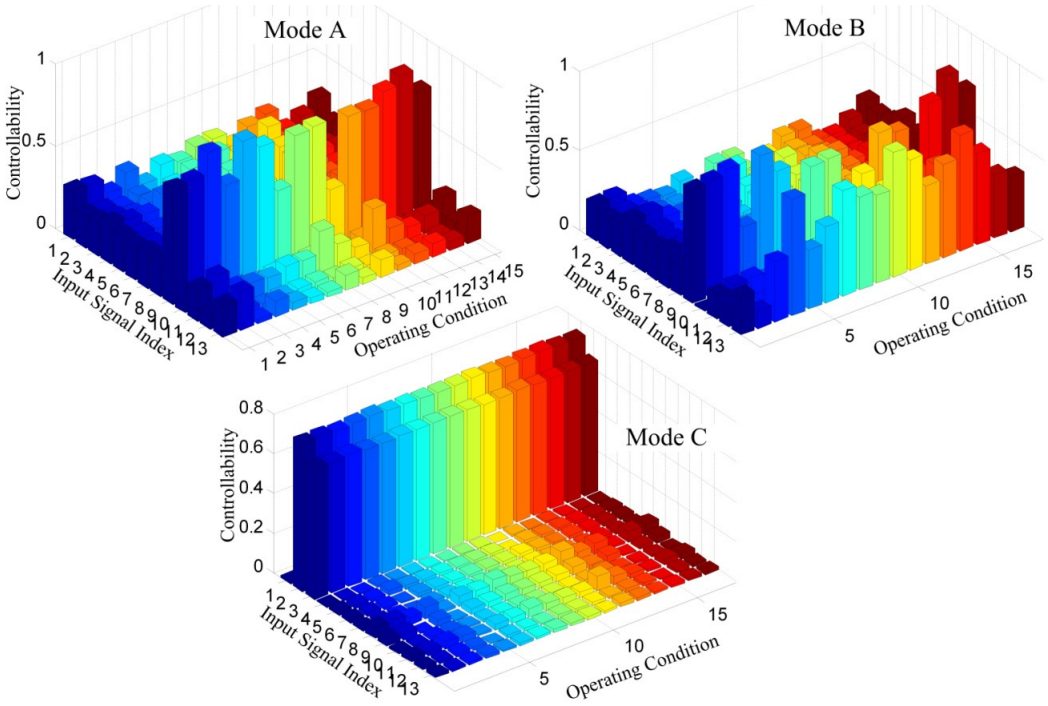

Figure 4.4 Controllability measures for modes A, B, and C

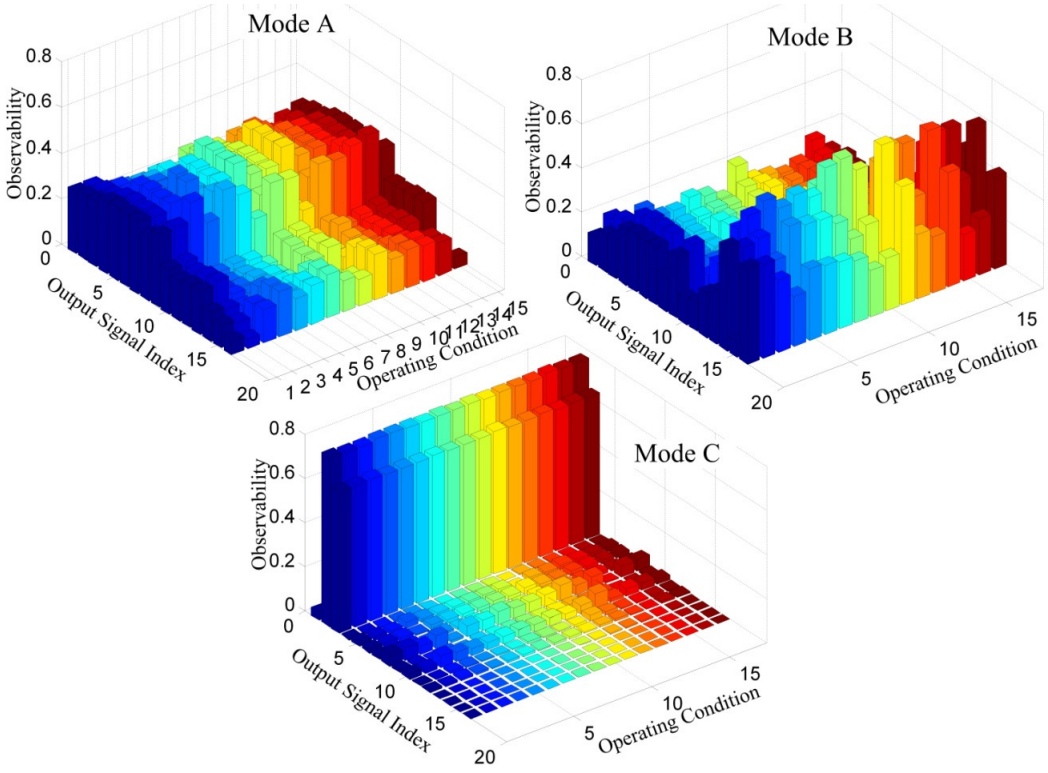

Figure 4.5 Observability measures for modes A, B, and C

A damping controller expected to enhance system stability at all credible operating conditions must be able to affect the damping of the critical modes at all operating conditions, not just some of them.

The observability/controllability calculations completed so far provide a measure of input/output channel effectiveness relative to each other. However, they do not provide an absolute indication of the effectiveness of an input/output signal pairing to shift a particular eigenvalue of interest. This means that a controller that uses input/output signals with large controllability/observability measures does not necessarily have the potential to significantly shift a given mode. A more descriptive indication of potential controller effectiveness can be obtained by calculating the sensitivity of an eigenvalue of interest to changes in the gain of a particular controller input/output configuration. A possible controller configuration is illustrated by Figure 4.6 for a static output-feedback controller.

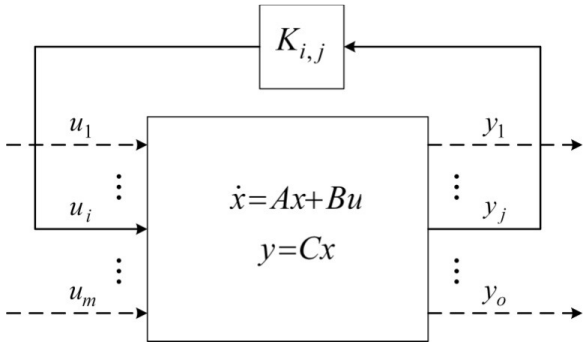

Figure 4.6 System configuration for sensitivity calculation

The potential effectiveness of a controller closing the loop from output y_j to input u_i to improve the damping of a particular mode λ_k can be obtained by calculating the sensitivity of that mode to changes in the gain $K_{i,j}$. For a linear system of the form in Figure 4.6 and defined as in (4.5), this sensitivity can be obtained using (4.6).

$$\begin{aligned} \dot{x} &= Ax + Bu \\ y &= Cx \\ u &= Ky \\ \dot{x} &= A_c x \\ A_c &= A + BKC \end{aligned} \tag{4.5}$$

$$\frac{\partial \lambda_k}{\partial K_{i,j}} = f_k^T B \frac{\partial K}{\partial K_{i,j}} Ce_k \tag{4.6}$$

The derivation of (4.6) is well known and is provided in Appendix D for completeness. In general, the result of (4.6) for a particular mode λ_k and output-feedback gain $K_{i,j}$ is a complex number. The magnitude of that number gives the amount of shift of an eigenvalue given a particular change in gain, while its phase gives the direction of movement of the eigenvalue in the complex plane. The magnitudes of the eigenvalue sensitivities for modes A, B, and C for different input and output configurations and at different operating conditions are given in Figure 4.7 to Figure 4.9.

There are multiple operating conditions for which the sensitivities of modes A and B are low for all input locations. This indicates that there is no single input/output pairing that can provide significant damping at all operating conditions. The sensitivities of mode B in particular are very low at a number of operating conditions and for all input locations (about 1 and 2 orders of magnitude compared to the sensitivities of modes A and C respectively). This suggests that minimalist designs which select a low number of input locations would not be able to provide significant damping improvements without resorting to significantly large feedback gains. In contrast, the sensitivities of mode C clearly point to input and output signals at G2 and G3as the ideal places to install a damping controller. Controllers at those locations can shift mode C regardless of the

operating condition, and so would always be effective. These results reinforce the tendency of inter-area oscillations to be more difficult to damp compared to local ones.

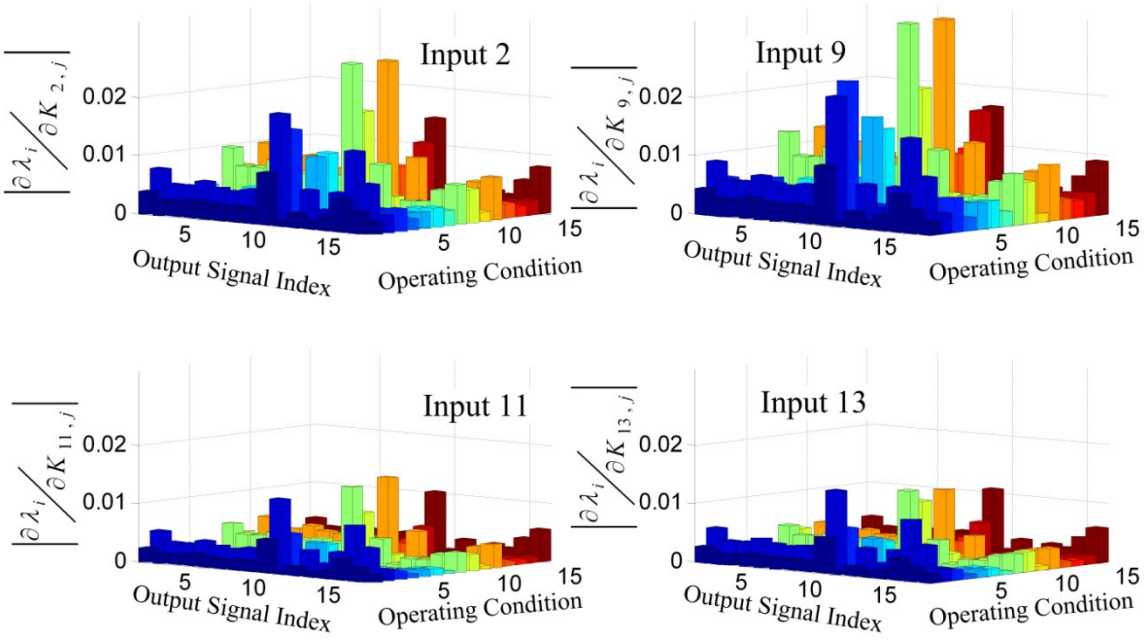

Figure 4.7 Sensitivities of mode A

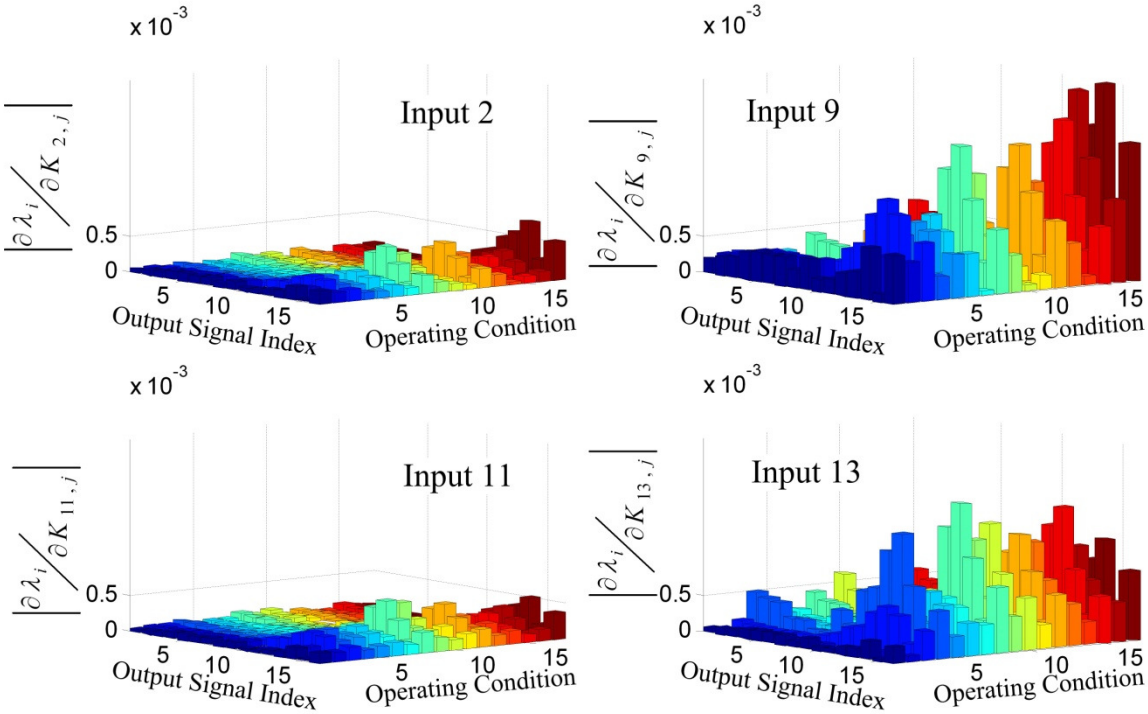

Figure 4.8 Sensitivities of mode B

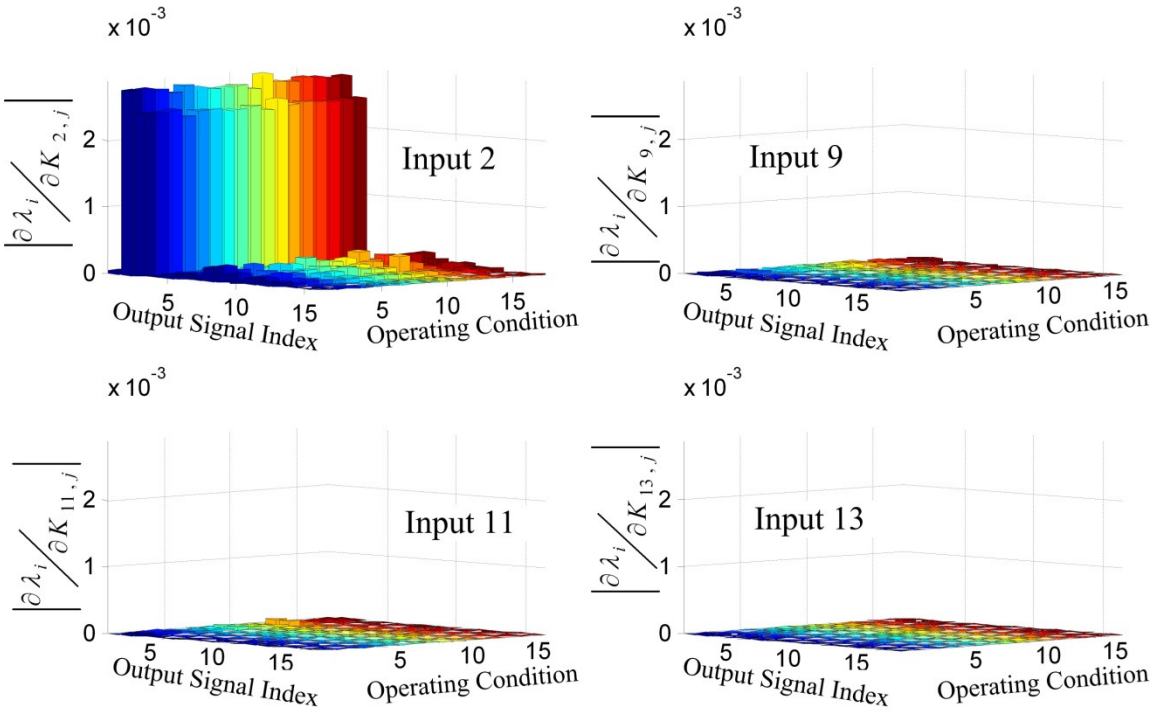

Figure 4.9 Sensitivities of mode C

4.2.3 Observations on the Potential of Holistic Wide-Area Damping Controls

The limitations imposed by low sensitivities of critical eigenvalues can possibly be overcome using holistic damping controls such as those described in Chapter 2. By coordinating the control efforts applied at a large number of input locations instead of only a few, it might be possible to enhance the damping of eigenvalues with low sensitivity without resorting to excessively high feedback gains. As mentioned before, increasing the input/output signal count imposes higher communications requirements, complicates the controller development process, and might have a detrimental effect on reliability. However, if rotor angle stability gains are enough to enhance the operating region of the system significantly, these drawbacks might not prevent the deployment of holistic designs.

4.3 SCALABILITY OF ARTIFICIAL NEURAL NETWORKS-BASED IWADC

The previous section demonstrated some of the limitations of minimalist approaches to power system damping controls. It was also argued that holistic damping controls might provide some of the capabilities needed to overcome those limitations. Among the different approaches to damping control, intelligent damping control using neural networks has shown great promise. However, previous studies of intelligent wide-area damping control (IWADC) have been completed on smaller power system models ([10] and [63]) or have taken the minimalist approach of selecting a low number of global signals ([11]) on medium sized systems. Researchers have shown that appropriate training can make IWADCs robust; however, their ability to scale-up to meet the demands of large-scale power systems is still an open question. This section aims to provide insights into that question.

The learning mechanisms for the forms of IWADC pursued in this dissertation rely on the use of a differentiable dynamical model of the input/output behavior of the power system to be controlled. This model is typically obtained using artificial neural network (ANN)-based dynamical system identification. The system identification step is the first step to complete when implementing an IWADC. Consequently, an IWADC that oversees and manipulates the dynamic behavior of increasingly large portions of a large-scale power system requires an increasingly large and complex dynamical model of that system. The ANN-based system identification mechanisms for deriving such a model and their ability to scale-up are investigated next.

4.3.1 Overview of Artificial Neural Networks-Based System Identification

Proven universal approximation capabilities coupled with the availability of effective parameter adaptation (training) algorithms make ANNs good candidates for non-linear dynamical system identification [77]. The neuro-identification task is illustrated in Figure 4.10 and can be summarized as: given the present inputs and outputs of an unknown plant, provide one-step-ahead predictions of the plant outputs. The ANN model resulting from the system identification process is called the "model network". It is assumed that once the model network is capable of accurately predicting the future outputs, it has "learned" the underlying principles governing the dynamic input/output mapping of the plant.

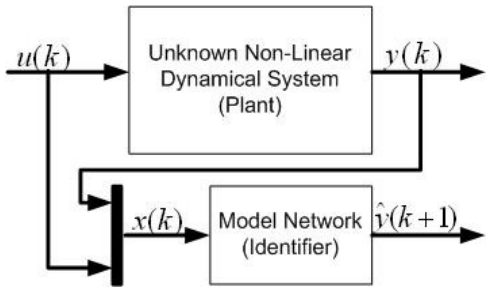

Figure 4.10 Configuration for neural network-based system identification

The globally recurrent neural network (GRNN) topology illustrated in Figure 4.11 is selected in this research and its output equation is defined in (4.1). Note the presence of time-delayed feedback loops between the outputs and inputs of the hidden layer. These loops provide the network with memory, and give it the capability to accurately represent arbitrary dynamical systems as proven in [78].

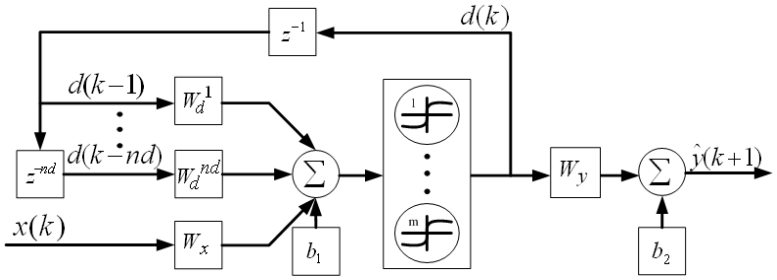

Figure 4.11 Globally recurrent neural network architecture

$$\hat{y}(k+1) = f\left(W_x x(k) + W_d^1 d(k-1) + \cdots + W_d^{nd} d(k-nd) + b_1\right) W_y + b_2 \qquad (4.1)$$

Arguably the most important factor for achieving acceptable performance when using ANNs is the training algorithm. In [79] a discussion of several of the presently available training algorithms is provided, and recommendations are given for the use of conjugate gradient-based methods for training ANNs. A heuristic evaluation completed in [12] confirms these recommendations. The scaled conjugate gradient from [80] is selected. The gradient calculations follow the truncated back-propagation through-time approach outlined in [81]. A C++ library implementing ANNs, gradient calculations, and multiple training algorithms is developed for this research using concepts provided in [82]. A brief description of this library can be found in Appendix E.

In [83] it was demonstrated that model networks for power systems can be made robust by properly designing the dataset used for training them. Training a model network is a parameter estimation process commonly formulated as in (4.2).

$$W^* = \arg\min_W \left\{ \sum_{j=1}^{n_{o.p.}} \left(\frac{1}{n_s} \sum_{k=1}^{n_s} \left\| y_k^j - \hat{y}\left(x_k^j, W\right) \right\|^2 \right) \right\} \qquad (4.2)$$

The optimal set of weights W^* in (4.2) is the set of ANN parameters (weights and biases in Figure 4.11) that minimizes the difference between the dynamical behavior of

the model network and that of the measured plant over n_s samples and $n_{o.p.}$ operating points.

An accurate model network allows the intelligent controller adaptation algorithm to estimate the output sensitivities. The ability of NNs to provide accurate estimates of a function and its sensitivities was demonstrated in [84]. The sensitivities are estimated by calculating the partial derivative of the model network's outputs with respect to the network's inputs via back-propagation. The importance of estimating these sensitivities will become clear in the next chapter.

4.3.2 Scalability of ANN-Based Identification of Power System Models

Results originally reported in [12] show that the artificial neural network (ANN)-based non-linear system identification methodologies described above do not scale-up well enough to cope with the unparalleled complexity of realistically sized power systems. Some of those results are repeated here, but interested readers are pointed to [12] for more detailed explanations. Two system identification approaches illustrated in Figure 4.12 are evaluated: centralized and modular. The study focuses on the growth in size and training times of model networks as the size of the system is increased.

Acceptable accuracy is achievable even for the largest model tested, which identified the dynamics of 16-machines in an interconnected power system. However, the number of ANN parameters and the training times required to achieve that accuracy using the centralized approach rise quickly with the size of the system as shown in Figure 4.13. Clearly, this is not acceptable for a realistically sized system with hundreds or even thousands of machines. The modular approach is more scalable, but it is incapable of

capturing the coupling relationships between the different generating stations in the system and is not acceptable for control purposes.

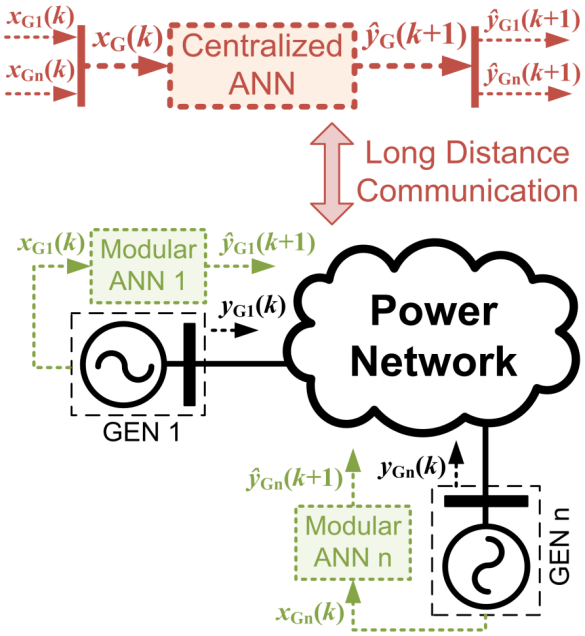

Figure 4.12 Centralized and modular ANN-based system identification approaches

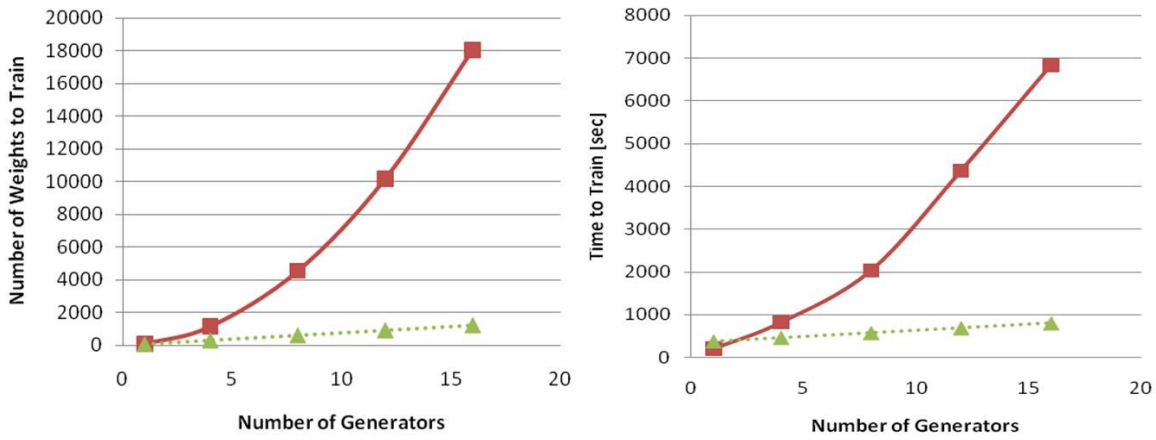

Figure 4.13 Scalability results as the size of the system being identified grows

4.3.3 Implications for Holistic Intelligent Wide-Area Damping Control

Poor scalability during the ANN-based power system identification stage translates directly to poor scalability for the IWADC algorithms currently available in the literature.

The behavior of the training times for the ANNs used for system identification is expected to be representative of the behavior of the training times for the other neural networks that compose the learning algorithms for intelligent control used in the remainder of the dissertation. These other neural networks and the rest of the algorithm for intelligent control will be described in detail in the next chapter.

The observations in this section can be used to infer that state-of-the-art intelligent damping controls for power systems cannot be scaled up to handle the size and complexity of large-scale systems. This makes them impractical for real power systems and will prevent them from ever reaching the application stage. Further development is needed to overcome these limitations.

4.4 SUMMARY

This chapter investigated the importance of scalability and the ability of state-of-the-art intelligent damping controllers to scale-up to handle the size and complexity of large-scale power systems.

An extensive numerical analysis of controllability, observability, and sensitivity for multiple oscillatory modes in a sample system is completed. The results show that minimalist approaches to power system damping controls might not provide the capabilities needed to significantly improve rotor-angle stability over a large number of power system operating conditions. These limitations can potentially be overcome using holistic controls that measure and inject signals at a large number of locations across a power system. However, holistic damping control of large-scale power systems demands highly scalable control methodologies.

A probing study into the scalability of artificial neural networks-based intelligent controls is completed. The results showed that artificial neural network training times become prohibitive as the size of the system is increased. Consequently, state-of-the-art artificial neural network-based intelligent damping controllers do not scale-up well enough to be deployed in real power systems.

The next chapter begins the process of developing scalable intelligent wide-area damping controllers for power systems and provides a detailed description of the intelligent control approach investigated in this dissertation. System aggregation techniques are used to improve scalability such that these controls become more feasible for deployment in large-scale power systems.

CHAPTER 5 AGGREGATION-BASED INTELLIGENT LOCAL-AREA DAMPING CONTROL

5.1 INTRODUCTION

The previous chapter demonstrated that artificial neural network (ANN)-based system identification and consequently intelligent wide-area damping control (IWADC) can be difficult to scale-up to the proportions needed for holistic power system control. A key insight for controlling large-scale systems is offered by system aggregation techniques [85]: it is possible to develop reduced-order models that greatly simplify complex systems while accurately representing their dominant dynamic characteristics.

This chapter presents research efforts aimed at exploiting physical insights into the dynamic behavior of power systems to generate simplified abstract power system models that can be used for real-time closed-loop control. These models simplify the design and implementation of large-scale holistic IWADCs by reducing the size and complexity of the system "seen" by these controllers in real-time while preserving the dominant system characteristics needed for effective damping control. The aggregation ideas in this chapter were first presented in [13] and [86], which introduced the concept of a "virtual generator" (VG) described in section 5.2.

The mechanism that makes the controllers "intelligent" is then described in detail in section 5.3. Finally, an application example used to evaluate the core ideas of the research is given in section 5.4. The design example and simulation studies of this chapter only serve as the starting point for demonstrating the methodologies developed in the dissertation. Therefore, only a medium-size system is used. More representative scalability evaluations are left for Chapter 7.

5.2 VIRTUAL GENERATORS: SIMPLIFIED REPRESENTATIONS OF POWER SYSTEMS

The simplified abstract representations needed to improve scalability rely on the concept of coherency. This section briefly discusses that concept, describes the method used for identifying coherent generators, and outlines how it can be exploited to generate simplified models.

5.2.1 Generator Coherency

Coherency in power systems refers to the tendency of groups of generators to "swing together" after disturbances. Swinging together refers to generators oscillating in phase at the same angular speed and maintaining the same rotor-angle deviation. This tendency has been attributed to a variety of factors such as the stiffness of the interconnection between generators and the ratio between the synchronizing torque coefficients and the inertias of the generators within a group [87].

In [88] and [89] it was demonstrated that, for certain kinds of power system studies, coherent behavior can be exploited to generate simplified dynamic equivalents of portions of power systems while maintaining acceptable simulation accuracy. These equivalents represent a number of coherent generators by a single equivalent generator model, thus greatly reducing the complexity of the simulation.

5.2.2 Coherency Identification

A variety of methods have been developed to identify groups of coherent generators. Three of these methods were evaluated in [90]: weak links (WL), two-time scale (TS), and linear time simulations (LS). The authors of that paper concluded that all three methods produced good generator grouping for creating equivalents. The LS is

considered the classical method to identify coherent generators. It consists of simulating a linearized model of the power system with classical second-order generator models and ignoring non-generator dynamics. Once the generators' swing curves (time-domain waveforms of the rotor-angles) are obtained, clustering algorithms can be used to find groups of generators that exhibit strong similarity in their swing curves. Details of the LS coherency identification algorithm can be found in [88]. More advanced techniques such as the one presented in [91] have also been proposed, but the additional clustering accuracy gains that can result from such approaches are unnecessary for the research in this dissertation.

The approach in this research is similar to the LS method; however, the full order model of the system (not a simplified and linearized version of it) is used to generate the generator swing curves. Hierarchical clustering based on these curves is then completed using tools available in MATLAB's Statistics Toolbox. This approach to generator clustering will be called full simulation hierarchical clustering (FSHC) in this research.

5.2.3 Power System Equivalents and Virtual Generators

One of the methods for creating simplified power system representations is called slow coherency aggregation [92]. It defines the center of angle of a group of coherent machines as a slow variable, and their inter-machine oscillations as a fast variable. The definitions of these for a group of two machines are given in (5.1) and (5.2).

$$\delta_{slow} = \frac{H_1\delta_1 + H_2\delta_2}{H_1 + H_2} \tag{5.1}$$

$$\delta_{fast} = \delta_1 - \delta_2 \tag{5.2}$$

The constant H_i is the per unit inertia of generator i with all generators in the group referred to the same power base. Equation (5.1) can be differentiated to obtain:

$$\dot{\delta}_{slow} = \frac{H_1\dot{\delta}_1 + H_2\dot{\delta}_2}{H_1 + H_2} = \omega_{slow} = \frac{H_1\omega_1 + H_2\omega_2}{H_1 + H_2} \tag{5.3}$$

Generalizing for groups of N coherent generators results in (5.4).

$$\omega_{slow} = \frac{\sum_{i=1}^{N}(H_i\omega_i)}{\sum_{i=1}^{N}(H_i)} \tag{5.4}$$

The coherency assumption and fast decay rates result in the vanishing of the fast variable in (5.2) to a small value that is neglected. Also, the availability of PMU data allows the real-time calculation of (5.4) as the system operates. As a consequence, large portions of the system containing a number of coherent generators can be represented as a single generator for WADC purposes. The resulting "equivalent" generator is called a "virtual generator" (VG) in [13]. The rotor speed of the VG is defined as in (5.5).

$$\omega_{VG} = \omega_{slow} = \frac{\sum_{i=1}^{N}(H_i\omega_i)}{\sum_{i=1}^{N}(H_i)} \tag{5.5}$$

Coupling VG-based simplifications with the ANN-based system identification of Chapter 4 provides a differentiable input/output mapping of the dynamical behavior of an area in the power system in the form of a VG model network.

5.3 Overview of Approximate Dynamic Programming for Intelligent Control

This section overviews the characteristics of approximate dynamic programming (ADP) in the form of heuristic dynamic programming (HDP), a mechanism that allows IWADCs to learn and adapt from interactions with the system and approach optimality as they gain experience. The origins of ADP stem back to the pioneering work by Werbos in [93]. The connections between ADP and classical optimal control can be found in [94]. It is worth mentioning that more advanced and powerful methods exist for implementing ADP. One of such methods is explored further in Chapter 7 .

Heuristic dynamic programming (HDP) is a reinforcement learning mechanism from the family of adaptive critic designs (ACDs) [95]. In addition to a differentiable model of the system to be controlled (the model network), HDP requires two function approximation structures: a critic and an actor ("actor" and "action network" will be used interchangeably). Both are implemented using the GRNN shown in Figure 4.11 and repeated in Figure 5.1. The dynamic equation for the GRNN is also repeated in (5.6).

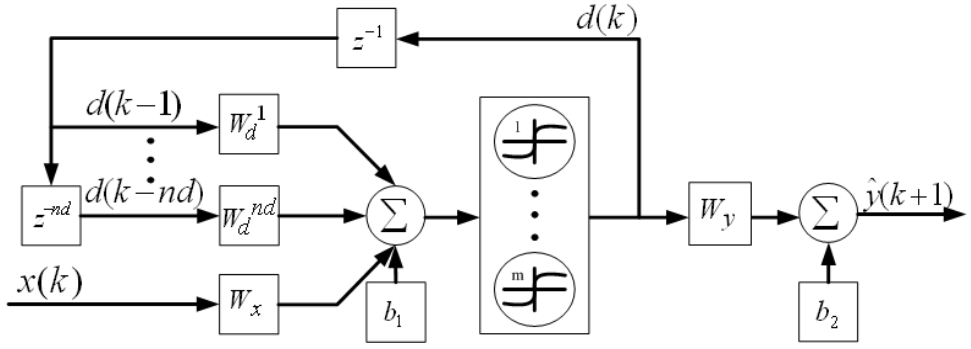

Figure 5.1 Globally recurrent neural network architecture

$$\hat{y}(k+1) = f\left(W_x x(k) + W_d^1 d(k-1) + \cdots + W_d^{nd} d(k-nd) + b_1\right) W_y + b_2 \qquad (5.6)$$

The critic learns to approximate the cost-to-go function in Bellman's equation of dynamic programming, while the actor learns to synthesize the control policy that minimizes the cost-to-go approximated by the critic. The cost-to-go function to be minimized is:

$$J\left(y(k)\right)=\sum_{i=0}^{\infty}\gamma^{i}U\left(y(k+i),u(k+i)\right) \tag{5.7}$$

In (5.7), γ is a scalar discount factor in the ($0<\gamma<1$) interval used for infinite horizon problems, *U(•)* is a utility function to be minimized over time that captures the objectives of the control task, and *u(k)* and *y(k)* are the vectors of inputs and outputs to and from the plant being controlled.

5.3.2 Critic Network Training

The recursive form of Bellman's equation (5.8) enables the training of the critic.

$$J\left(y(k)\right)=U\left(y(k),u(k)\right)+\gamma J\left(y(k+1)\right) \tag{5.8}$$

HDP progressively adapts the critic network parameters to improve the estimate of (5.8) by minimizing the following error measure over time [95]:

$$\sum_{k}\hat{J}\left(y(k)\right)-\left(U\left(y(k),u(k)\right)+\gamma\hat{J}\left(y(k+1)\right)\right) \tag{5.9}$$

Minimization of (5.8) can be achieved incrementally by changing the critic network parameters at each time step according to the following weight update rule (5.10)-(5.11):

$$\Delta w^{C}(k)=-\eta\left(\hat{J}\left(y(k)\right)-U\left(y(k),u(k)\right)-\gamma\hat{J}\left(\hat{y}(k+1)\right)\right)\frac{\partial\hat{J}\left(y(k)\right)}{\partial w^{C}(k)} \tag{5.10}$$

$$w^{C}(k+1)=w^{C}(k)+\Delta w^{C}(k) \tag{5.11}$$

Where η is a small positive learning rate and w^C is the set of critic GRNN parameters ($W_x, W_d^1, \cdots, W_d^{nd}, b_1, b_2, W_y$ in (5.6)). A model network of the form described in Chapter 4 is used to provide the one-step-ahead estimate of the plant output needed to calculate (5.10).

A modified version of the critic weight update algorithm proposed as strategy 4b in [96] is used to improve the convergence of the critic training procedure. The approach is based on sliding data windows and closely follows the developments to be described in section 7.4.4 in Chapter 7 . When the error measure in (5.9) becomes small, the critic is assumed to be capable of providing an estimate of (5.7) that is good enough to be used for guiding the adaptation of the action network. This estimate is given by (5.12).

$$J(y(k)) \approx \hat{J}(\hat{y}(k)) \approx U(y(k), u(k)) + \gamma \hat{J}(\hat{y}(k+1)) \tag{5.12}$$

5.3.3 Action Network Training

The training of the action network modifies the parameters w^A of the action GRNN to improve the performance of the system by minimizing (5.12). This process begins with calculating an estimate of the sensitivity of the cost-to-go (5.13).

$$\frac{\partial J(y(k))}{\partial u(k)} \approx \frac{\partial U(y(k), u(k))}{\partial u(k)} + \gamma \frac{\partial \hat{y}(k+1)^T}{\partial u(k)} \frac{\partial \hat{J}(\hat{y}(k+1))}{\partial \hat{y}(k+1)} \tag{5.13}$$

This sensitivity can be used to adapt the action network according to the following incremental weight update rule:

$$\Delta w^A(k) = -\eta \frac{\partial \hat{J}(y(k))}{\partial w^A(k)} = -\eta \frac{\partial \hat{J}(y(k))^T}{\partial u(k)} \frac{\partial u(k)}{\partial w^A(k)} \tag{5.14}$$

$$w^A(k+1) = w^A(k) + \Delta w^A(k) \tag{5.15}$$

5.4 AGGREGATION-BASED INTELLIGENT LOCAL-AREA DAMPING CONTROL (AB-ILADC)

This section integrates the ideas of ANN-based system identification, coherency analysis, VG-based simplifications, and HDP-based intelligent control to generate a preliminary version of an aggregation-based intelligent wide-area damping controller (AB-IWADC). This integration is shown via a design example on a medium-size power system model. The goal of a holistic controller for a large-scale system mentioned in Chapter 2 using AB-IWADC is postponed until Chapter 7. A slight modification of the terminology is made here to reflect the preliminary nature of the control approach presented in this chapter. The controller is named an aggregation-based intelligent local-area damping controller (AB-ILADC). The terms "local-area" highlight that input and output locations are limited to a relatively small portion of the system: the "local-area". This work was originally presented in [97]. An overview of the system model used for these initial evaluations is presented next.

5.4.1 Modified 68-Bus Benchmark System

The model shown in Figure 5.2 is a modified version of the power system model used in Chapter 2. The modifications were performed to match the system model used for another portion of the larger project of which the research in this dissertation is a part of. The modifications include slight changes of parameters for the excitation systems, the addition of turbine/governor models for each generator, and the placement of PSSs on G14, G15, and G16.

The excitation system and prime mover units at each generating station are modeled as shown in Figure 5.3.

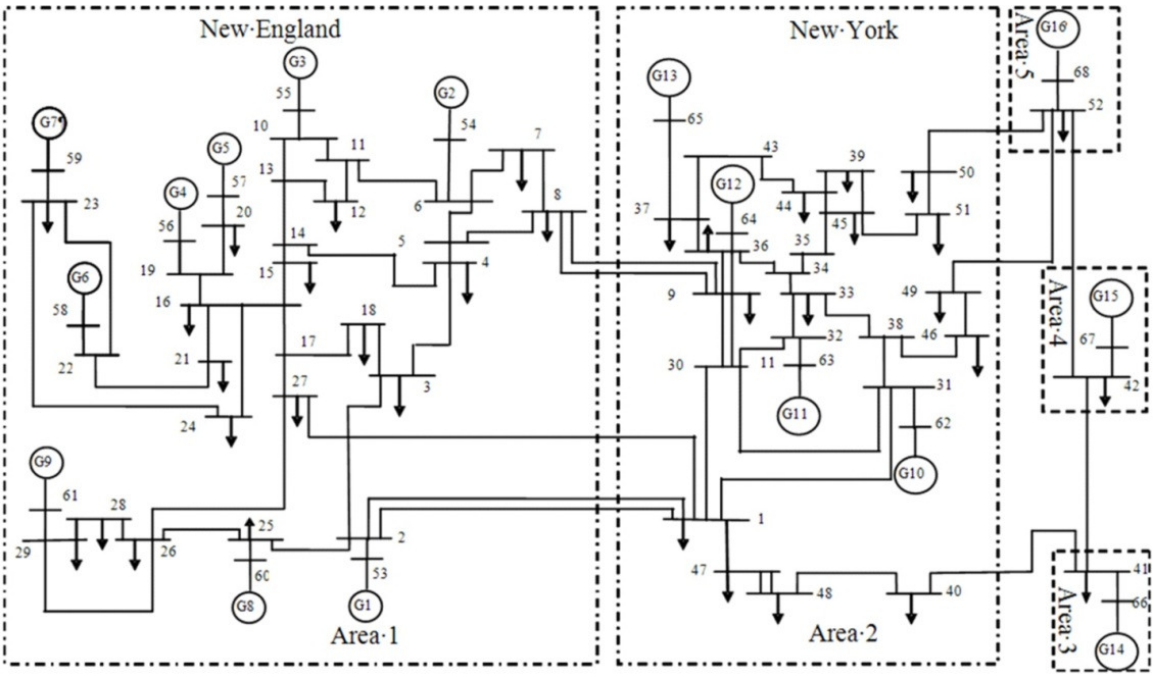

Figure 5.2 Detailed single line diagram of the 68-bus system

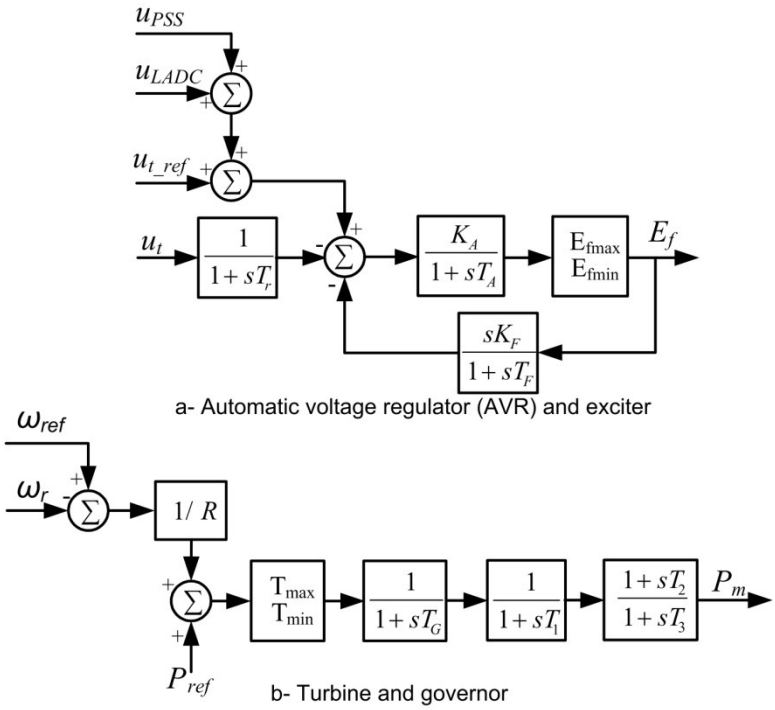

Figure 5.3 Generator controls in 68-bus system

This time, only the New England side of the system is considered accessible; i.e., inputs and output locations are only available for this portion of the system. This assumption is made to reflect the fact that in a real power system, it is unlikely that a single entity would have access to all portions of the system.

5.4.2 Virtual Generator Representations of the 68-Bus System

The first step in designing the aggregation-based intelligent local-area damping controller (AB-ILADC) is to generate the VG representations of the system. Once again, these representations will allow the AB-ILADC to treat large portions of the system as if they were a single machine, thereby improving scalability.

5.4.2.1 Illustration of Coherency Determination

The VG concept assumes that the machines being represented are coherent. Coherent groups are identified using the method described in section 5.2. The response of the system to three-phase faults applied at a number of locations across the system is simulated to generate the swing curves. These curves are then grouped by similarity using hierarchical clustering.

The clustering results are summarized in the dendrogram shown in Figure 5.4. The height of the horizontal links connecting one generator to another is a measure of the dissimilarity between the swing curves.

None of the generators exhibit perfect coherency; however, 4 groups of coherent generators can be formed by selecting the coherency threshold line shown in the figure: {1, 8}, {2, 3}, {4, 5, 6, 7}, and {9}. The selection of an appropriate coherency threshold line is heuristic at this time.

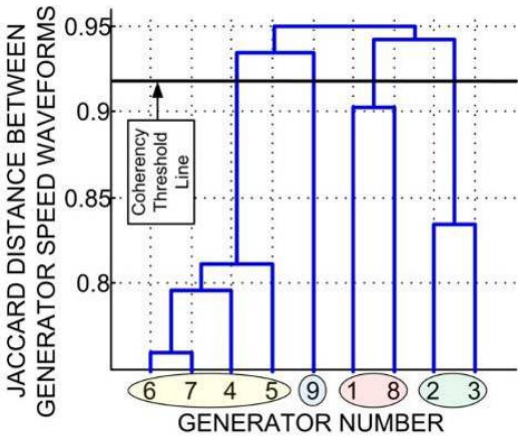

Figure 5.4 Coherent generator clustering dendrogram

5.4.2.2 Virtual Generators for the 68-Bus System

Complementing the information provided by Figure 5.4 with load flow studies allows the partitioning of the 68-bus network into the four sub-networks shown in Figure 5.5. The New York side of the system is now shown as an external power network that cannot be measured nor controlled.

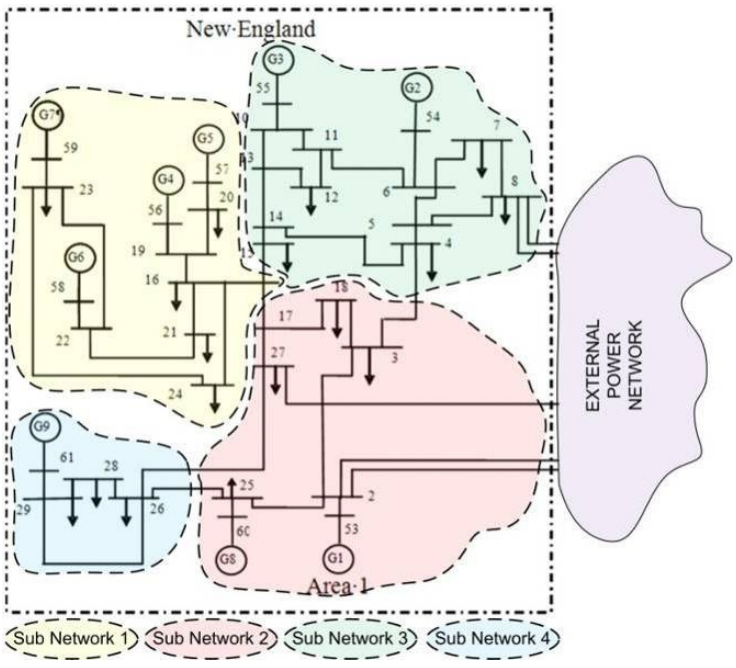

Figure 5.5 Partitioning of the New England side of the 68-bus system

For LADC, the rotor speeds of the generators inside of these sub-networks can be represented using one VG per sub-network. Applying (5.5) to calculate the speeds of the four VGs after a disturbance in the system results in the waveforms shown in Figure 5.6, and the sub networks clearly respond in very different ways.

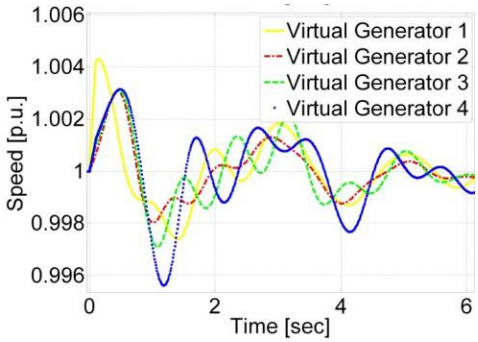

Figure 5.6 VG speeds after a 3-phase short circuit disturbance

For AB-ILADC, the system can now be viewed in its aggregated form as shown in Figure 5.7. There is a significant reduction of system complexity in going from Figure 5.5 and Figure 5.7. However, also note that the simplifications performed so far are a way of interpreting information and measurements about the system. Therefore, in spite of these simplifications, the actual system remains unchanged.

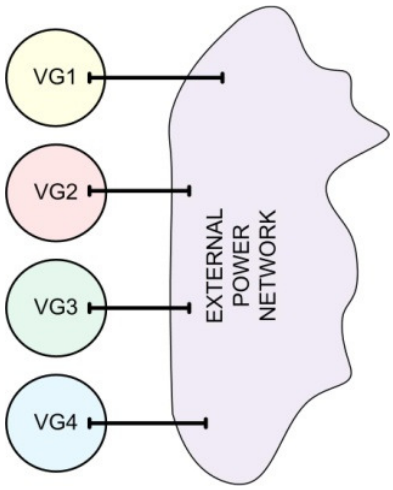

Figure 5.7 VG Representation of the 68-bus system

5.4.2.3 Grouped Generators Don't Always Behave Coherently

The VG representation is based on the assumption that all generators in a group behave coherently. However, this assumption is typically satisfied only for disturbances that occur electrically far away from the coherent group. Figure 5.8 (left) shows the speed deviations of generators G4-G7 and of the VG representing these four generators when a disturbance is applied at a remote location. The speeds of the generators are nearly identical, and the coherency assumption holds. In contrast, when the disturbance is applied electrically close by, the coherency assumption is violated, and the VG representation is no longer accurate as illustrated in Figure 5.8 (right) for the same sub network. Nevertheless, simulation results will show that good damping can be achieved by the AB-ILADC even when coherency is not fully satisfied. Also, more advanced coherency-based clustering methods that provide groupings that are applicable over a wide range of operating conditions and disturbances [98]-[99] are available in case this becomes an issue.

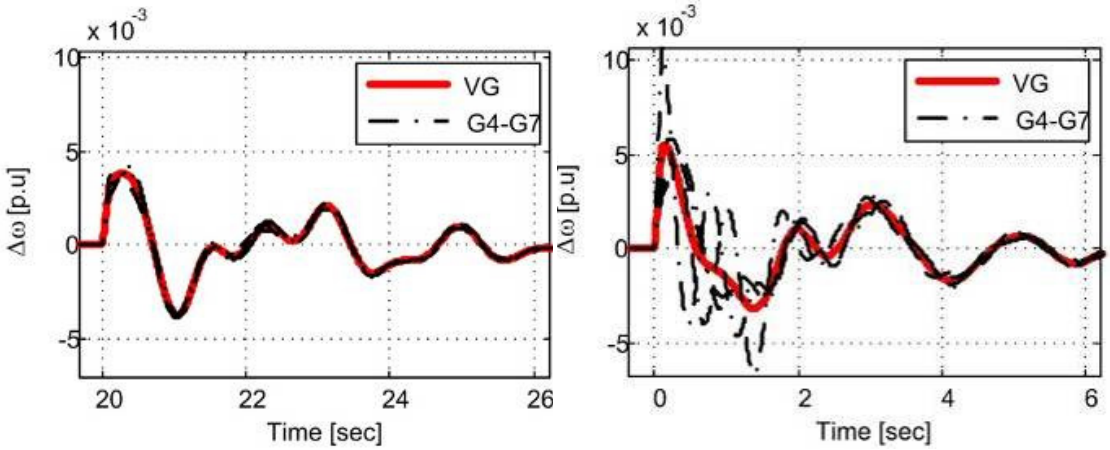

Figure 5.8 Speed deviations for disturbance applied electrically far away (left) and close by (right)

5.4.3 Recurrent Neural Networks-Based Virtual Generator Model Identification

The previous section demonstrated how the VG concept can be used to represent groups of several coherent generators in a power system as a single VG speed. However, knowledge of the dynamical input-output behavior of the VG is critical for the controller adaptation methodology presented in section 5.3.

The fact that the VG is not a real device in the system, but merely a way of interpreting local-area information from PMUs, for example, makes developing an analytical model from first principles difficult at best. However, the neural network of Chapter 4 provides an effective tool for finding a dynamical model of the VG using input/output data. This network is referred to as the Model Network (MN). The process of training a MN was briefly discussed in section 4.3. More detailed steps are given next.

5.4.3.1 Model Network Training

GRNN weight updates are limited to offline training, which is completed in the following sequence:

Pseudo-random binary signals (PRBSs) are injected to each of the generators in the group at the point labeled uLADC in Figure 5.3. Details on how to design appropriate signals for system identification are provided in [100]. Stochastic load changes are also applied at multiple locations to ensure the training data contains information about the behavior of the system at different operating points.

2000 s of input-output pairs (sampled at 10Hz) are collected as training data and are imported into the C++ neural network library in Appendix E. Some de-trending and scaling of the data is performed to improve learning.

The scaled conjugate gradient (SCG) [80] training algorithm generates a set of network weights (W) that minimizes the mean squared error (MSE) over the training data set. The definition of this optimization problem is repeated in (5.16) for completeness.

$$W^* = \arg\min_W \left\{ \sum_{j=1}^{n_{o.p.}} \left(\frac{1}{n_s} \sum_{k=1}^{n_s} \left\| y_k^j - \hat{y}\left(x_k^j, W\right) \right\|^2 \right) \right\} \tag{5.16}$$

5.4.3.2 Model Network Testing and Sensitivity Estimation

The testing stage ensures that the model network has learned the underlying principles driving the input/output relationship of the plant. PRBSs are no longer applied and disturbances not present in the training set are used instead to excite the system. Accurate predictions of the system output under these conditions are considered an indicator of successful system identification. A typical result observed during testing is shown in Figure 5.9-a.

The model network allows the controller adaptation algorithm to estimate the effect of the input signals on the output of the system by providing estimates of the output sensitivities. The ability of NNs to provide accurate estimates of a function and its sensitivities was shown in [84]. The sensitivities are estimated by calculating the partial derivative of the model network's outputs with respect to the network's inputs via back-propagation. Examples of these estimates during a disturbance are shown in Figure 5.9-b.

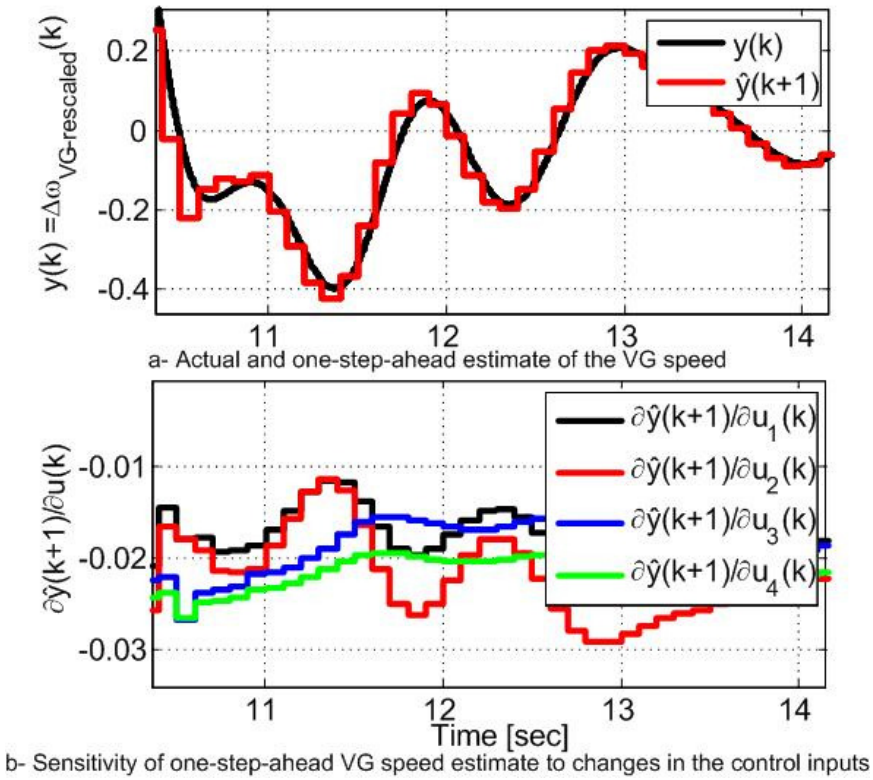

Figure 5.9 Model network's one-step-ahead estimate of VG speed and its sensitivity after a 60 ms 3-phase fault at t = 10 s

5.4.4 Aggregation-Based Intelligent Local-Area Damping Control of the Modified 68-Bus System

The AB-ILADC including the VG, model network, action network, and critic network as well as the critical signals used for controller adaptation are shown in Figure 5.10. The utility function $U(\bullet)$ in (5.7) is chosen as (5.17). The constants C_{CE} and C_{DI} are chosen heuristically to achieve an acceptable tradeoff between control effort and damping improvement.

$$U(y(k),u(k)) = \sum_{i=1}^{N} \left(C_{CE} u_{WADC\_i}(k)^2 \right) + C_{DI} \left(\omega_{VG}(k) - 0.4\omega_{VG}(k-1) - 0.3\omega_{VG}(k-2) \right)^2 \quad (5.17)$$

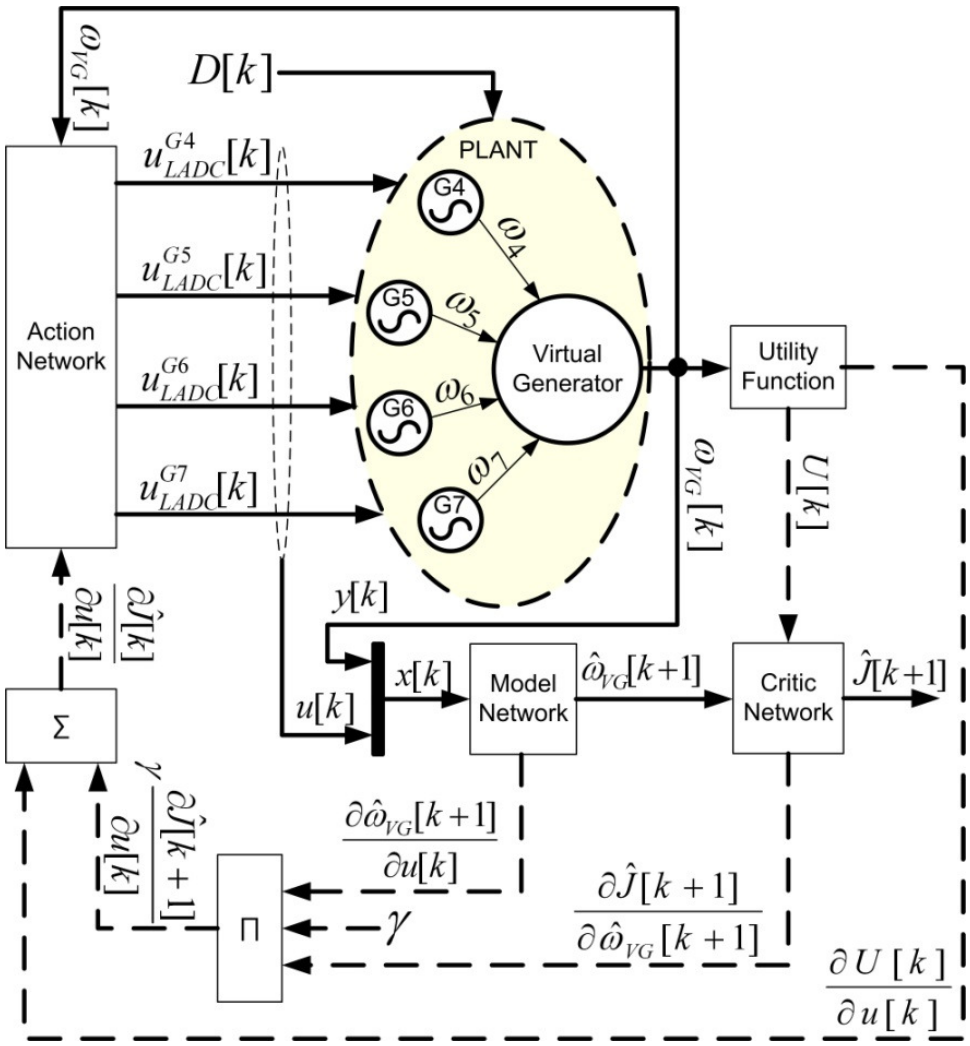

Figure 5.10 VG and HDP-based ILADC

Training of the critic and action networks is completed for 1000 seconds of simulation. At the end of this period the magnitudes of (5.9) and (5.13) are small enough to indicate convergence. During training, large random load disturbances at multiple buses in NE and NY systems disturb the system and cause oscillations of the local area that the action network learns to damp out. These load disturbances also cause significant changes in the steady state power flows, pushing the controller to become robust by learning to perform well at multiple operating points.

5.4.5 Simulation Results

The simulation results shown in this section focus on evaluating the ability of the ILADC to damp low-frequency oscillations resulting from a variety of disturbances applied at different system operating conditions. The disturbances applied and a brief description of them is given in Table 5.1. A graphical representation of these disturbances and the connections between the AB-ILADC and the system are shown in Figure 5.11.

Table 5.1 List of disturbances applied to the system for AB-ILADC evaluation

#	Time [sec]	Description of Disturbance
D1	10	80 ms self-clearing 3-phase fault applied at bus 56. This disturbance excites local oscillations within the sub-network represented by the virtual generator which causes violations of the coherency assumption.
D2	50	100 ms fault in transmission line connecting buses 1 and 2 cleared by opening both lines connecting these two buses. This is an important corridor interconnecting the NE and NY sides of the system. This disconnection of this corridor has a strong impact on inter-area oscillations since it weakens the interconnection between two distant areas.
D3	90	Load in bus 1 increased by 200%. This change increases the transfer from NE to NY. This transfer increase causes further stress in the interconnection between the NE and NY sides of the system and reduces the damping of inter-area oscillations.
D4	130	50 ms self-clearing 3-phase fault at bus 8. This fault excites local and inter-area oscillations when operating under a heavily stressed operating condition.

Disturbances D1-D4 in Table 5.1 were carefully selected to evaluate the performance of the AB-ILADC when the coherency assumption is violated, and as the system is pushed to operate under increasingly stressed conditions known to result in rotor-angle instability.

Comparisons are drawn between three different cases: no stabilizing controls (Base), state-of-the-art PSS4B-type PSSs (PSS4B), and system with one AB-ILADC (ILADC). PSSs were added to generators G4, G5, G6, and G7 in the second case. The PSS4B parameters for setting 2 recommended in [27] were used for the PSS4B case.

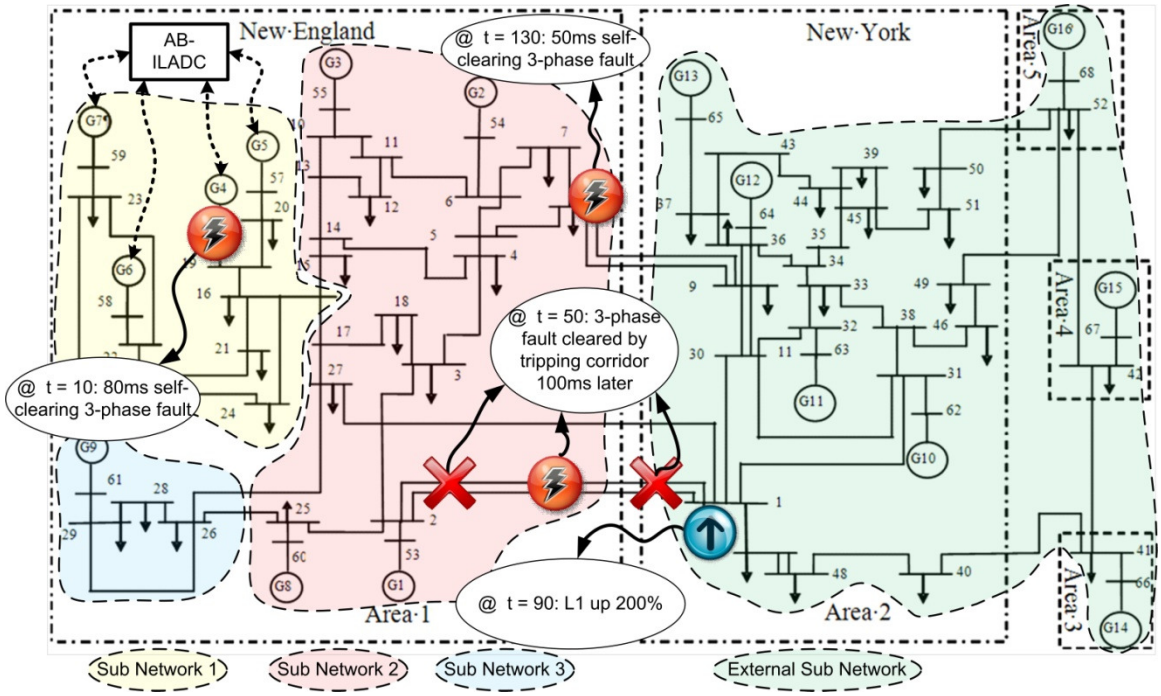

Figure 5.11 ILADC connections to system and disturbance times and locations

Figure 5.12 shows selected eigenvalues obtained from small signal analysis of the base case system before and after disturbances D2 and D3 in Figure 5.11. Only eigenvalues around the frequency range typically associated with electromechanical oscillations (0.1-3Hz) are shown [16]. The diagonal lines define the set of 5% and 10% damping ratio points.

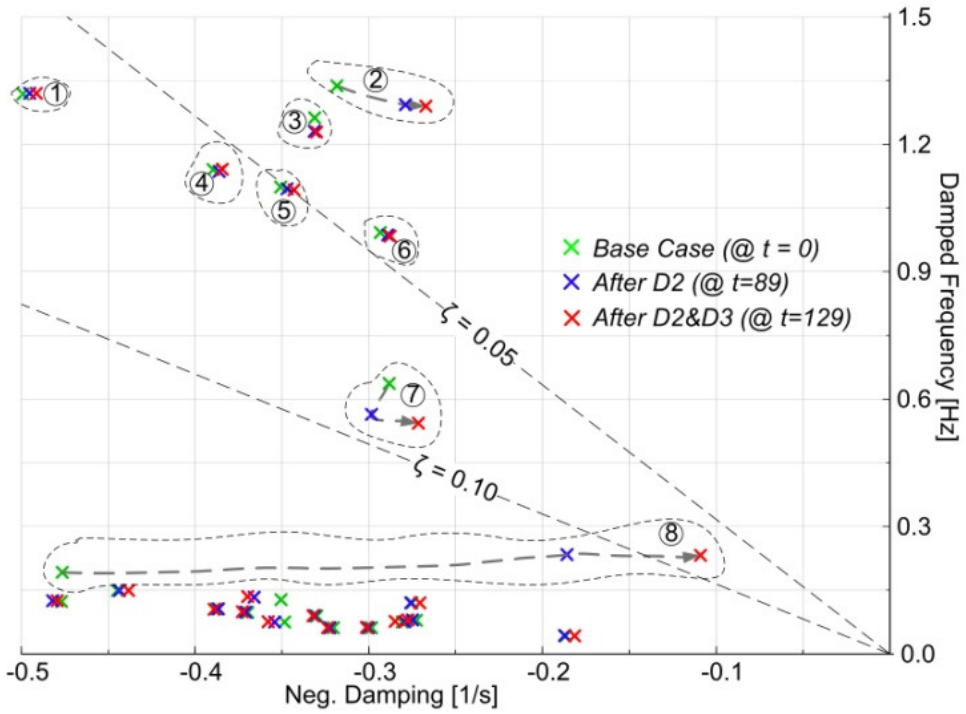

Figure 5.12 Eigenvalues of the base case system at different times

Modes 1-6 show fairly low damping ratios (less than 5-10%), but they are local in nature, can be expected to decay fairly quickly, and are not particularly sensitive to changes in the operating condition. Modes 7 and 8 show low damping and are interarea in nature. Mode 8 in particular will decay slowly when the system gets stressed and needs to be addressed. Mode 8 is also highly sensitive to the system's operating condition as demonstrated by its drastic move towards the right of the plane as the NE-NY interconnection is weakened and as the power interchange increases. The right eigenvectors associated with these modes (calculated at t = 129) are used to analyze the mode shapes. Table 5.2 summarizes the results.

Generators G4-G7 are found to have high participation in the more critical and sensitive mode 8, and some participation in mode 7, indicating that appropriate damping signals at these 4 generators can be effective for damping both of those modes.

Table 5.2 Summary of Modal Analysis of 68-Bus System

#	Eigenvalues	Freq [Hz]	Damping Ratio [%]	Generators Involved
1	-0.492±j8.294	1.320	5.92	G2 vs. G3
2	-0.267±j8.103	1.290	3.30	G10 vs. Rest
3	-0.330±j7.721	1.229	4.27	G1,G8 vs. Rest
4	-0.385±j7.168	1.141	5.34	G12 vs. Rest
5	-0.343±j6.867	1.092	4.99	G2-G3 vs. G4-G7
6	-0.288±j6.182	0.983	4.65	G9 vs. Rest
7	-0.272±j3.415	0.544	7.93	G10-G13 vs. G4-G9
8	-0.109±j1.456	0.232	7.47	G1-G9 vs. G10-G13

The non-linear simulations presented next evaluate the dynamic behavior of the system for the set of disturbances illustrated in Figure 5.11 for three different initial load flows. The load flow is varied such that there is an increase in the active power flow from NE to NY to evaluate the capabilities of the different controllers to improve dynamic stability as the system gets pushed closer to its stability limits. Only certain time periods of the each simulation are shown for simplicity.

Figure 5.13-Figure 5.15 show the following signals (from top to bottom): speeds of generator G4, damping signals injected at generator G4, G4's rotor-angle with respect to G13's (slack generator), and active/reactive power exports from NE to NY. In each case, the speed and control input waveforms for generators G5, G6, and G7 are almost identical to those of G4.

The first set of simulations is completed using load flow A, which is characterized by a 720 MW export from NE to NY. Figure 5.13 shows the stability improvement provided by both damping approaches. The damping of the oscillations corresponding to modes 7

and 8 is increased for all disturbances. Clearly there is no noticeable improvement resulting from the AB-ILADC. This is expected since, when properly designed, conventional stabilizing technology can be robust to some changes in the power system dynamics.

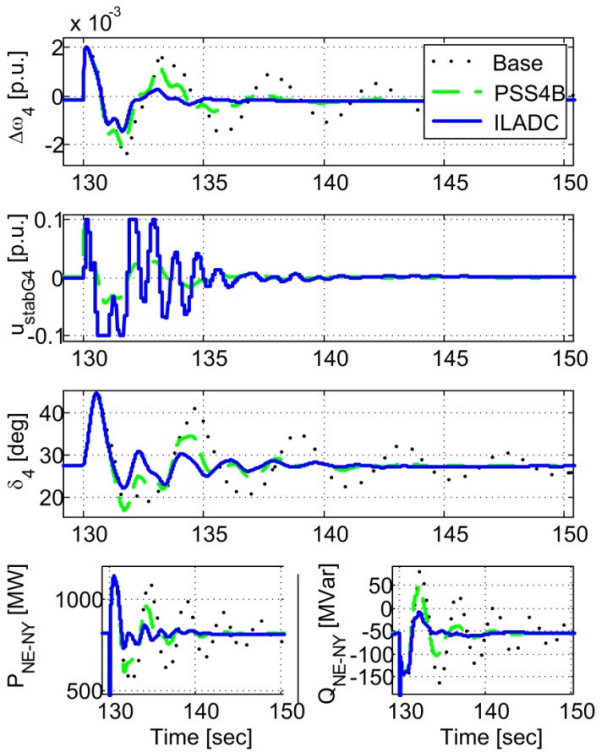

Figure 5.13 Results for disturbance D4 under load flow A

The second set of simulations is completed using load flow B, which is characterized by a 974 MW export from NE to NY. The additional generation in NE is distributed equally (in per unit) among all the generators in that area. Active power balance is achieved by reducing the output of G13 while maintaining all loads unchanged.

The left side of Figure 5.14 shows that the uncontrolled base case becomes unstable after a three-phase fault is cleared by tripping an important transmission corridor between NE and NY at t=50 (D2 in Fig. 11). The PSS4B case is beginning to show poorly damped

low-frequency oscillations, indicating that the performance of the PSS4Bs is degrading. In contrast, these oscillations are well damped in the AB-ILADC case in spite of very similar control effort. The right side of Figure 5.14 shows that once the system gets pushed further by a load increase at t=90 and disturbed by a self-clearing fault at t=130, the PSS4Bs fail to provide appropriate damping signals and sustained low-frequency oscillations emerge. The additional damping provided by the AB-ILADC allows the system to maintain normal operation. This demonstrates the AB-ILADC improvements over conventional control approaches.

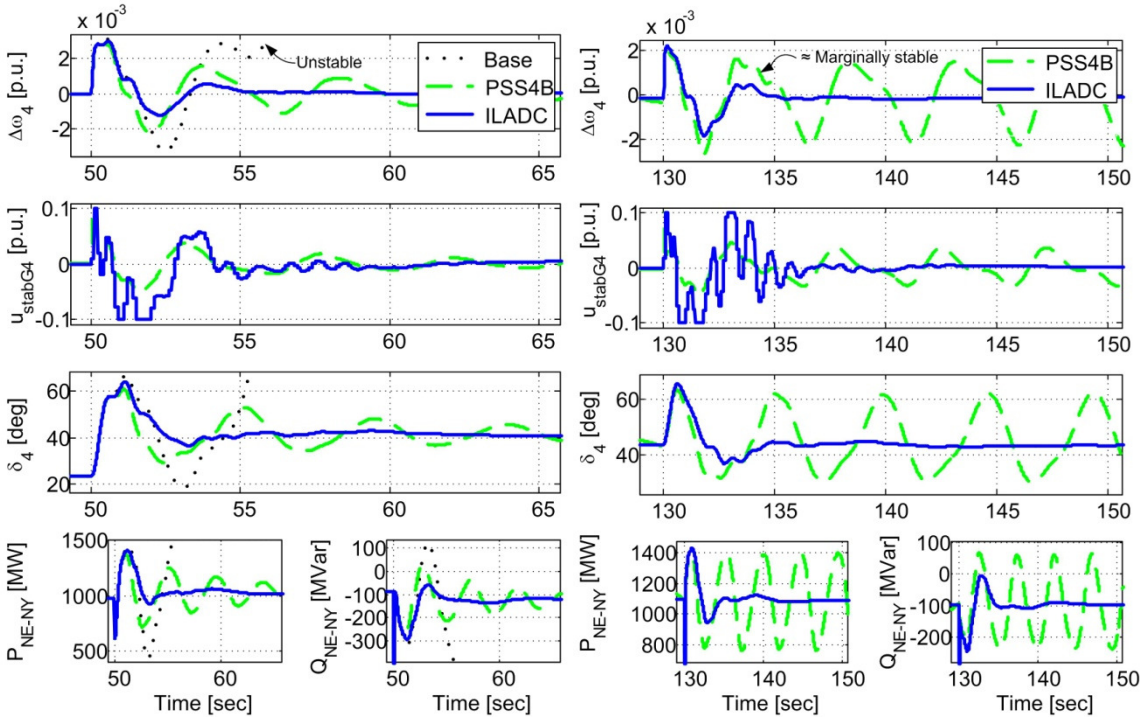

Figure 5.14 Results for disturbances D2 and D4 under load flow B

A third set of simulations is carried out using load flow C, which is characterized by a 1053 MW export from NE to NY. The left side of Figure 5.15 shows that once again the base case system becomes unstable after the events at t=50. This time the PSS4Bs fail to

maintain stability and the ILADC's superiority in damping the low-frequency oscillations becomes obvious. The right side of Figure 5.15 illustrates how the AB-ILADC is able to cope with the load increase at t=90, and provides appropriate damping even under this heavily loaded operating condition with a weakened NE-NY interconnection. Simulations not presented here show that pushing the system further results in non-oscillatory instability for which the type of controls studied in this paper would be ineffective.

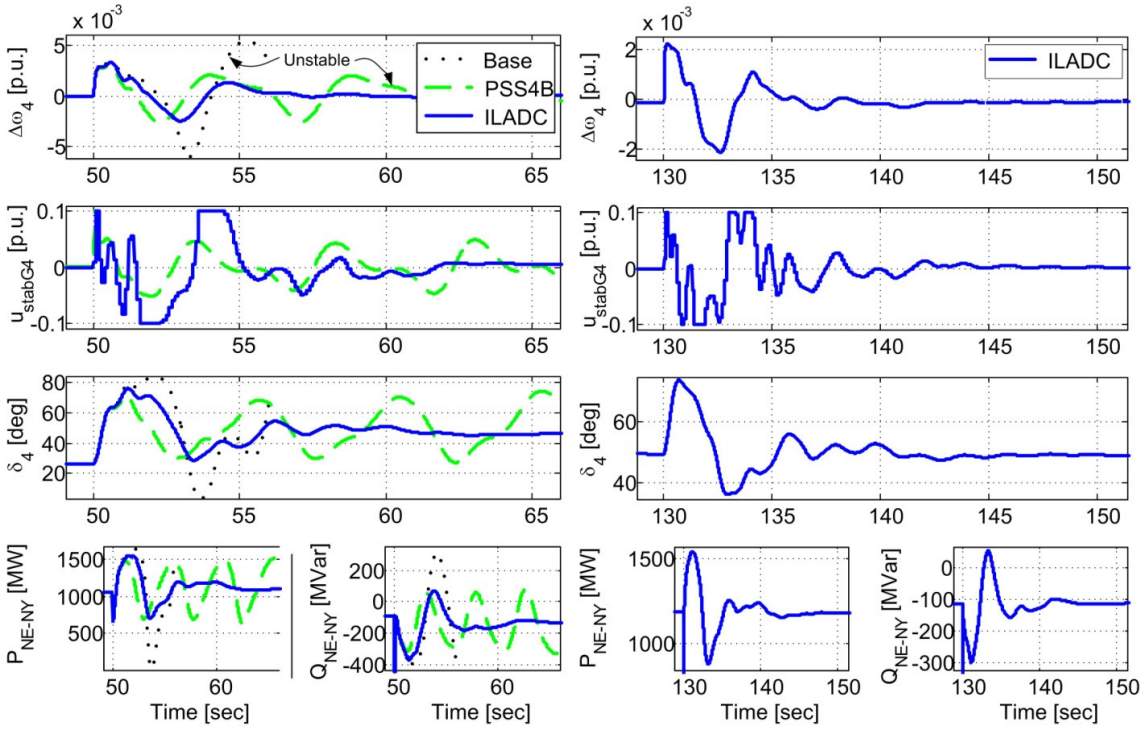

Figure 5.15 Results for disturbance D2 and D4 under load flow C

The time-domain results in Figure 5.13-Figure 5.15 are further confirmed by Prony analysis using the Prony Toolbox for MATLAB available in [101]. G4's rotor angle after the last disturbance (t = 131-160 time period sampled at 10Hz) was analyzed. Figure 5.16 provides the estimates of the settling times for the dominant low-frequency modes (modes 7 and 8). These plots further confirm that, while the conventional controllers

offer acceptable performance for load flow A, once the system gets pushed closer to its limits the performance of those controllers degrades to the point that they can no longer prevent instability. In contrast, the performance degradation of the AB-ILADC is more gradual and the system remains stable and performs better for a wider range of operation conditions.

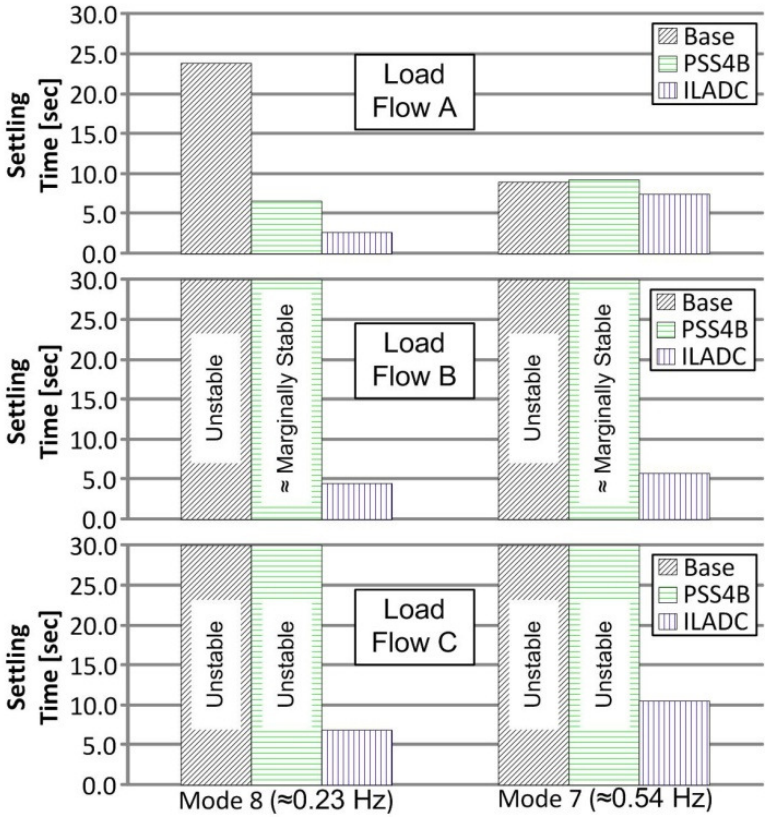

Figure 5.16 Settling time estimates for modes 7 and 8 at each load flow with a 10% criterion (time to decay to 10% of initial amplitude)

These results demonstrate the ability of the AB-ILADC to enhance the operation of the system by enabling power flows that would otherwise result in unstable operation when the system is controlled by more conventional stabilizing technology. Plots of the damping signals at the output of the AB-ILADC illustrate that these enhancements can be

achieved with low control effort if the damping signals injected into the system are appropriately generated.

These results demonstrate that the AB-ILADC can enhance the operation of the system by enabling power flows that would otherwise result in unstable operation under more conventional stabilizing technology.

5.5 SUMMARY

This chapter served as the initial proof of concept for aggregation-based intelligent damping control for power systems. The concept of a virtual generator was used to reduce the dimensionality of the control problem by generating simplified representations of portions of the power system to be controlled. These representations allow intelligent controllers to treat large portions of the system as if they were a single machine. This results in significant dimensionality reductions and consequently scalability is improved.

Approximate dynamic programming in the form of heuristic dynamic programming (HDP) was described. The combination of VGs, ANN-based system identification, and HDP results in an aggregation-based intelligent local-area damping control (AB-ILADC) methodology expected to be able to provide some of the scalability properties needed for holistic control of large-scale power systems.

Simulations on a medium-size power system model demonstrated that an AB-ILADC can outperform conventional damping controllers and enable more extensive utilization of the installed transmission infrastructure. However, in spite of the promising results of this chapter, the scalability of the proposed control approach remains an open question to be answered in Chapter 7 .

The next chapter will describe the characteristics, development, and validation of a realistic large-scale power system model. This model will then be used in Chapter 7 to generate more conclusive results in terms of the applicability of the ideas in this dissertation to real-world power systems.

CHAPTER 6 BRAZILIAN POWER SYSTEM MODEL FOR EVALUATING SCALABILITY

6.1 INTRODUCTION

The results in the previous chapter are encouraging. However, the system used for evaluating the AB-ILADC is not representative of a real large-scale power system and does not provide a valid benchmark to evaluate scalability.

This chapter describes the development of such a benchmark model. A high level overview of the system is given next. Detailed descriptions of the characteristics of the simulation model, its development, and validation follow. Eigenvalue studies are then completed to pinpoint the weaknesses of the system in terms of rotor-angle stability. The result is a large set of challenging yet credible operating conditions in which rotor-angle stability is highly compromised without resorting to unrealistic operating regimes.

The multi-model selection approach developed in Chapter 3 is then used to reduce the redundancy of this large set. The reduced set enables analysis of the behavior of the system over a wide set of operating regimes without incurring unnecessary computational costs characteristic of studies of large-scale systems.

Finally, the shapes of the critical inter-area modes are analyzed in detail using extensive small-signal studies. These mode shapes help identify the oscillatory patterns present in the system, and can be used to guide the controller design and evaluation efforts to be completed in Chapter 7.

6.2 SYSTEM OVERVIEW

The power system modeled for evaluating scalability is a somewhat simplified equivalent of the Brazilian power grid. In spite of the simplifications, the portions of the system servicing the South, Southeast, and Midwest areas of Brazil are modeled in detail. In Brazil, the power system is known as the "Sistema Interligado Nacional" or the "SIN", which translates to the "National Interconnected System". A geographically accurate map of Brazil is presented on the left side of Figure 6.1 below. The right side of Figure 6.1 is an abstracted view of the regions of Brazil serviced by the portions of the SIN simulated in detail. These regions include the most populous areas of the country and the largest generating stations, and thus the model contains the majority of the important load and generation centers of the Brazilian power system.

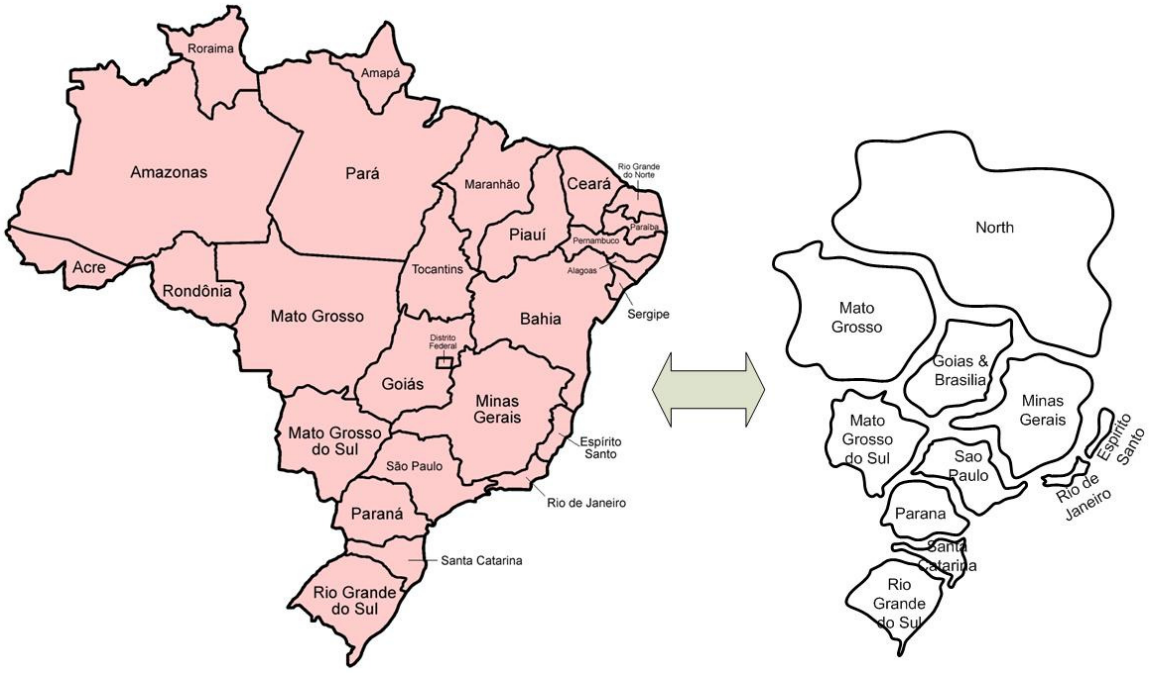

Figure 6.1 Real and abstracted maps of Brazil

The SIN is a large-scale power system that spans over a large and diverse geographical region. The generation mix is dominated by hydroelectric generation. This system is owned and operated by multiple companies in the South, Southeast, Midwest, Northeast, and North regions of Brazil. The planning and operation of the generation and transmission infrastructure in this system is orchestrated by an organization known as the "Operador Nacional do Sistema Eletrico" or "ONS", which translates to the "National Electric System Operator".

A high level view of the different portions of the SIN is depicted in Figure 6.2 to provide the reader with some insights into the inter-area transfers in the SIN. This figure was produced by ONS to illustrate inter-area flows in the SIN and can be found in [102], where it is updated regularly to reflect the transfers occurring in the system. Therefore it was used for the work here to gain insights into the active power inter-area transfer patterns in the system over time.

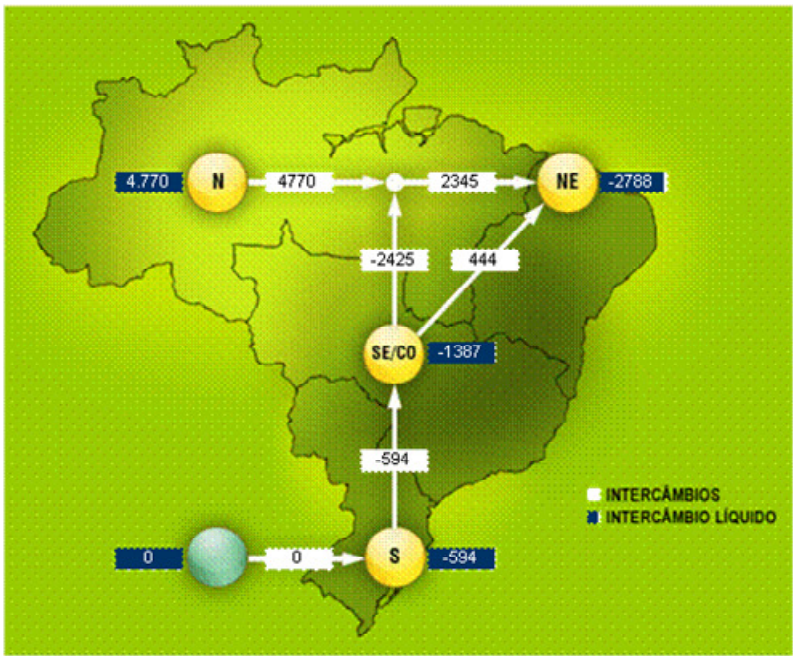

Figure 6.2 Regional configuration of power flow interchanges according to ONS

Power flows in the SIN are heavily influenced by meteorological conditions across Brazil. During unfavorable hydrological conditions, there is a need to transfer large blocks of energy between distant regions of the system. The authors of [103] report how, in a few highly unfavorable cases, the system has been operated with violations of the transient stability criteria, in which a single critical contingency has the potential to push the system towards rotor-angle instability and cause widespread blackouts.

The high variability of the inter-area flows in the SIN is clearly noticeable in the graphs given in Figure 6.3, which depict the median active power interchanges from the South to the Southeast portions of the system from 2007 to 2010 [102].

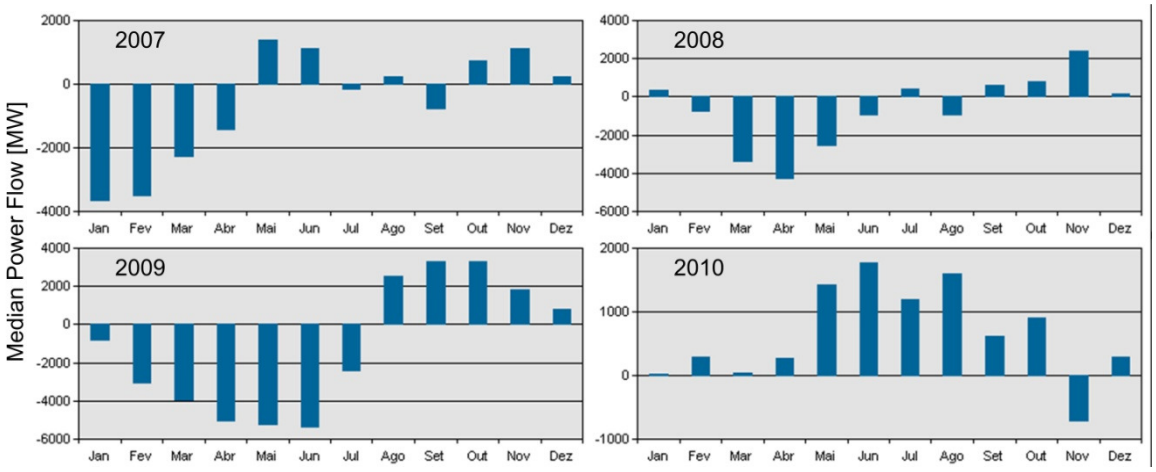

Figure 6.3 Historical active power interchanges from the South to the Southeast-Midwest regions

With this type of highly variable operating regimes, which include large power transfers between distant areas, it becomes even more important to implement damping controllers that can improve rotor-angle stability over a large set of operating conditions.

The next section provides a detailed overview of the simulation model of the SIN developed for the work in this dissertation.

6.3 SIN MODEL DETAILS

The parameters for the simulation correspond to the system configuration for March 2007 operating under heavy load. A simulation model of this system was developed by some of the collaborators in this project using Simulight, a power system simulation program developed at the Federal University of Rio de Janeiro. The Simulight model was found to be reasonably accurate when validated against the actual system some time ago [104]. Significant efforts were spent as part of this dissertation to translate, debug, and validate this model from Simulight to DIgSILENT PowerFactory. The model translation was completed following the steps shown in Figure 6.4. This translation was needed because the Simulight software did not provide the capabilities or flexibility needed to complete the research in this dissertation.

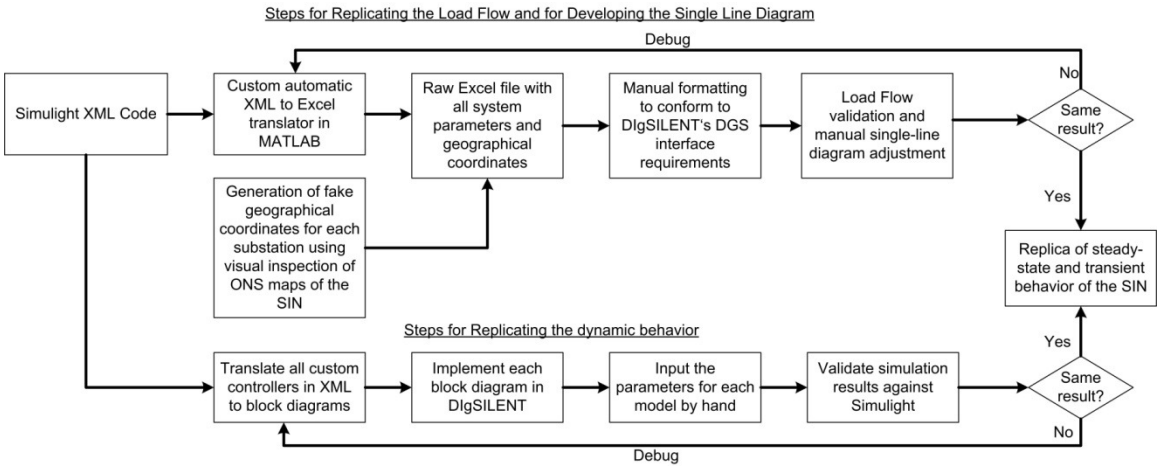

Figure 6.4 Steps for translating Simulight model to DIgSILENT PowerFactory

The single-line diagram of the DIgSILENT model of the SIN is shown in Figure 6.5. This single line diagram is not geographically accurate and follows an operational map of the system provided by ONS instead. However, some geographical reference is provided by drawing and naming the Brazilian states using dashed lines in Figure 6.5.

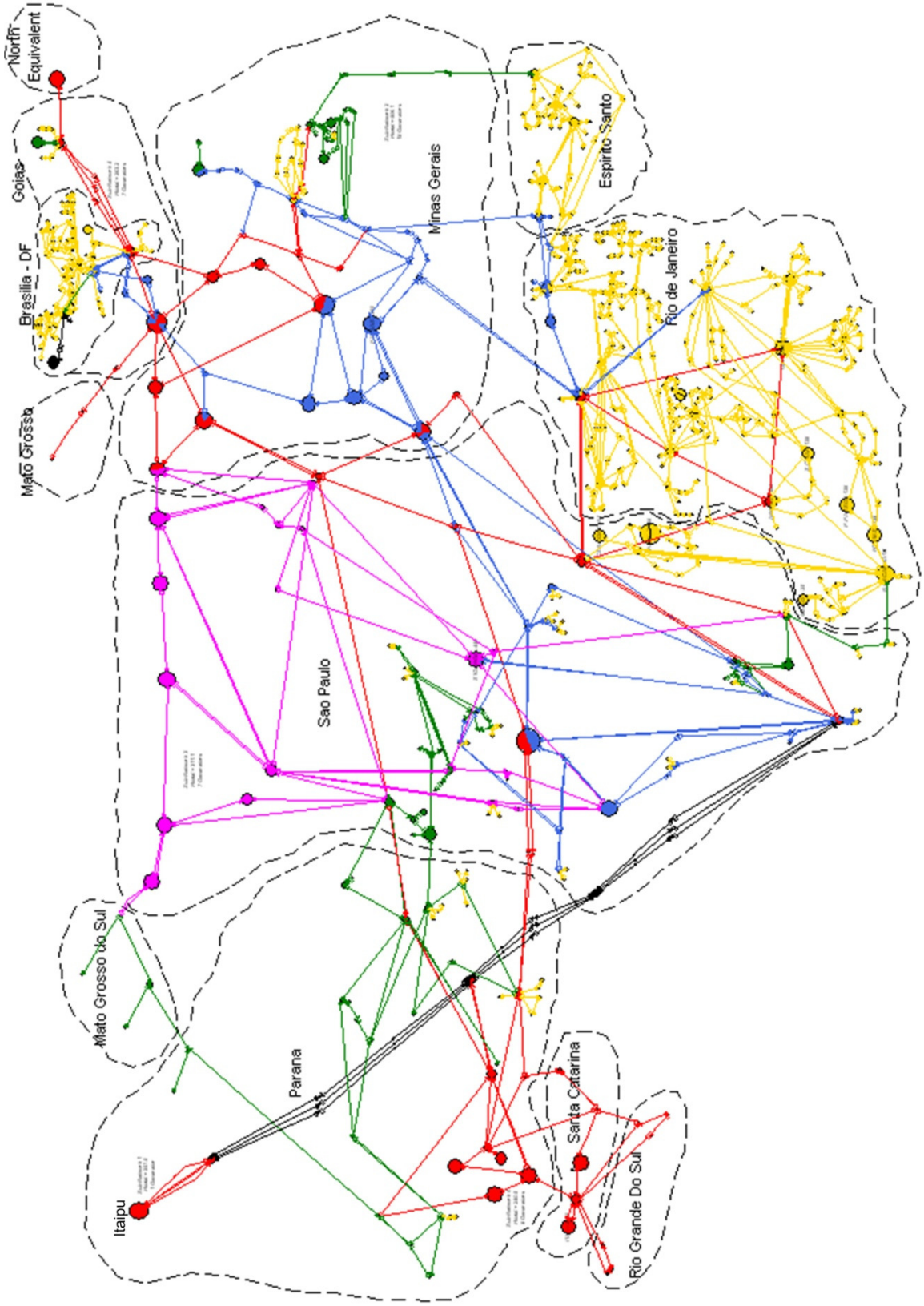

Figure 6.5 Model of the Brazilian SIN in DIgSILENT PowerFactory

The system contains 274 generators. 52 of them are small enough to have a negligible effect on the system dynamics and are modeled as negative impedances. The other 222 are spread across 73 power plants. The available data is not detailed enough to model interplant dynamics, so only 73 synchronous machines are simulated, with many of them representing groups of parallel connected machines at a plant. One of these machines is a large equivalent machine used to represent the Northern portion of the SIN. 72 of these machines are equipped with automatic voltage regulators, 69 of them with prime mover units and speed governors, and 38 with power system stabilizers.

The largest generating station in the SIN is located at the Itaipu dam. Half of the energy from Itaipu is generated at 50 Hz and transmitted via two HVDC links to the Southeast region of the system. Lack of detailed data forced this generation and HVDC transmission elements to be modeled as constant current injections neglecting any dynamics.

Customized realistic models are used for the devices and their controls at each electric power generation plant. Accurate load modeling is critical when studying inter-area oscillations in large-scale power systems. Therefore, loads are modeled using polynomial ZIP models consisting of constant power, constant current, and constant impedance components with coefficients determined on an area-by-area basis by ONS.

The transmission network is modeled using algebraic equations as is customary for large power system simulation studies. The interconnection consists of 1006 buses and 1008 transmission and distribution lines with voltages ranging from 765 kV to 138 kV and below. These voltage levels are depicted by the different colors in Figure 6.5.

Each circle in Figure 6.5 depicts a substation in the system. Larger circles mark substations with relatively large generators. Multiple loads, transformers, reactor/capacitor banks, busses, generators, etc, are located inside of each of those substations. An example of one of the substation diagrams (the Serra da Mesa substation) is shown in Figure 6.6.

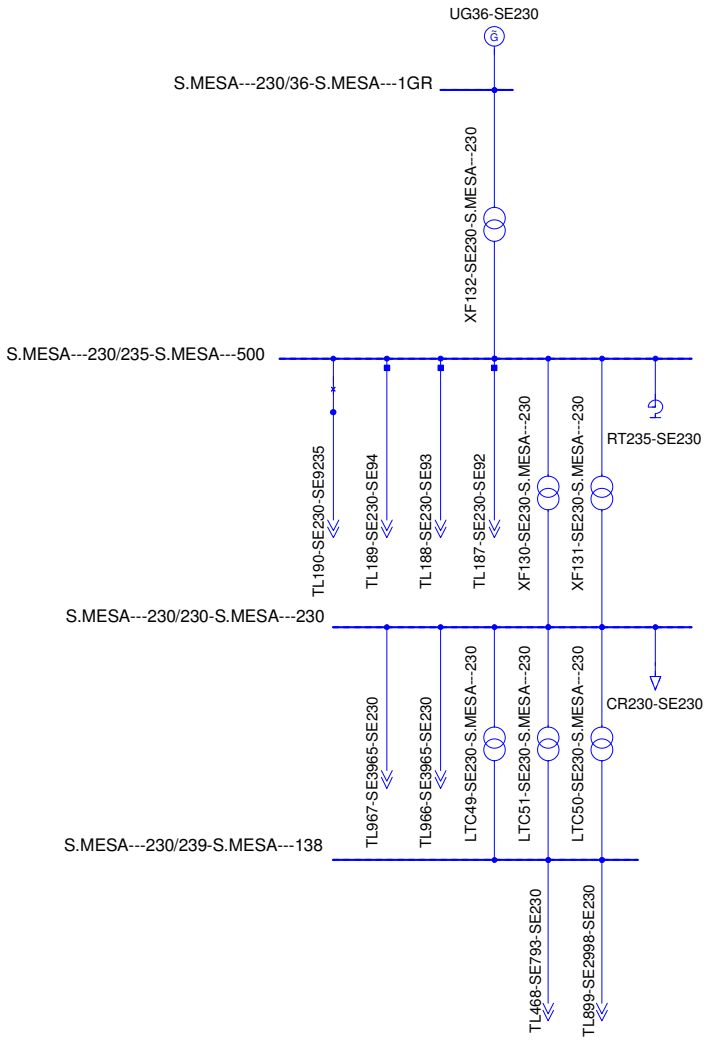

Figure 6.6 Sample substation diagram – Serra da Mesa substation

The total installed capacity of the system is 51.3 GW, total generation is 43.0 GW, total load is 41.2 GW, and total loss is 1.8 GW. The model has a total of 1378 state

variables. The validation of this model assumes the Simulight model developed in Brazil to be sufficiently accurate and that it can therefore be used in lieu of real measured data. The validation results are summarized next.

6.4 SIN MODEL VALIDATION

As mentioned in the previous section, the translation of the model from Simulight to DIgSILENT followed the steps illustrated in Figure 6.4. Multiple rounds of debugging were required to achieve acceptable matching between the DIgSILENT PowerFactory and Simulight models of the SIN. Several factors make the perfect matching between the models impossible. Some of those factors include: the machine models in each software package are not identical, some PV buses in Simulight had to be converted to PQ in DIgSILENT, integration algorithms are different, etc. In spite of these differences, the load flows (terminal voltages, angles, and active and reactive power flows) match closely, indicating that the translation process was effective.

The validation of the dynamic behavior was completed using time-domain simulations of the response of the system to several disturbances at different locations across the system. The validation was limited to visual inspection of multiple variables at a number of locations across the system. Figure 6.7 provides some typical results obtained at the end of the debugging process. Only electrical power outputs, terminal voltages, and reactive power outputs from 4 machines are shown. Brief descriptions of the variables in Figure 6.7 are given in Table 6.1. The 4 machines are spread across the system, so these graphs provide a comprehensive view of what is occurring in the simulation. Though the matching is not perfect, the agreement between the Simulight model developed in Brazil and the DIgSILENT model developed here is acceptable.

Table 6.1 List of some of the signals used for model validation of the SIN model

Signal	Description of Signal
A1	Active power output of large generator in Sao Paulo in per unit
A2	Active power output of large generator in Sao Paulo (distant from that in A1) in per unit
A3	Active power output of Itaipu plant in per unit
A4	Active power output of medium generator in Minas Gerais in per unit
B1	Voltage of 500 kV bus in Rio de Janeiro in per unit
B2	Terminal voltage at Itaipu plant in per unit
B3	Voltage of 440 kV bus in Sao Paulo in per unit
B4	Voltage of 138 kV bus in Rio de Janeiro (far from that in B1) in per unit
C1	Reactive power output of large generator in Sao Paulo in MVar
C2	Reactive power output of large generator in Sao Paulo (distant from that in A1) in MVar
C3	Reactive power output of Itaipu plant in MVar
C4	Reactive power output of medium generator in Minas Gerais in MVar

As a side note, at the time of this writing, the 10 sec simulation shown in Figure 6.7 took 40 sec to complete in DIgSILENT PowerFactory using a fixed step-size of 0.005 seconds. Simulation speeds can be increased using larger step sizes or the variable step-size algorithm available in the software, but it was chosen to be small and fixed to ease the comparisons used for validation. This selection minimizes the potential impact that discrepancies between integration algorithms could have on the simulation results.

Now that the model has been validated, it is possible to study the behavior of the electromechanical oscillations in the SIN using linear analysis techniques similar to those used in previous chapters. That study is completed next. The results are used in Chapter 7 to guide the controller development and validation process.

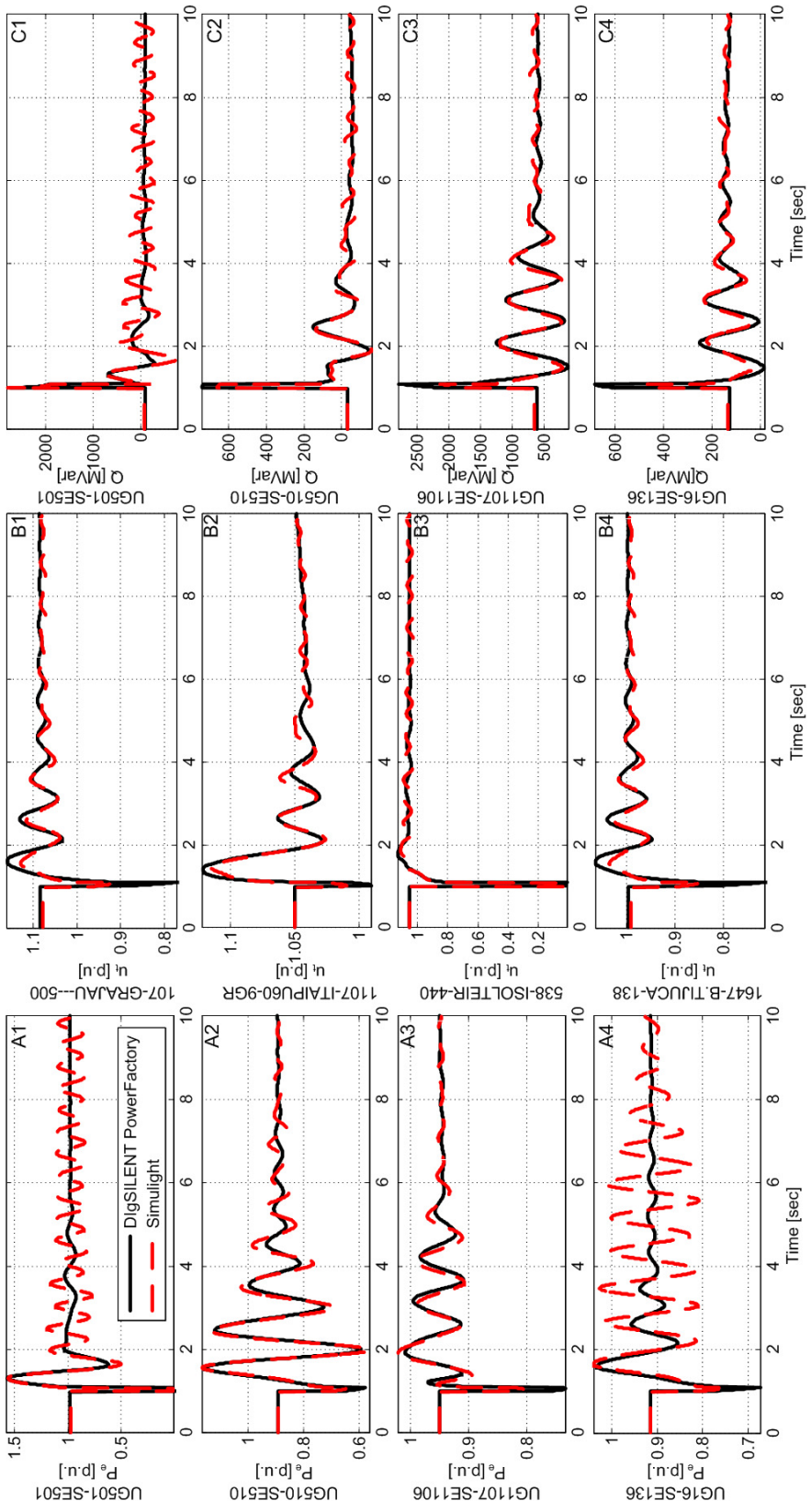

Figure 6.7 Time-domain waveforms for validation of SIN model

6.5 SMALL SIGNAL ANALYSIS

In practice, the analysis of real power systems and the development of controllers for them are guided by operational experience developed over many years of real observations and planning. This is not the case for the work here. This section attempts to compensate for this lack of operational experience by extensive analysis using linearized models of the power system over a large set of operating conditions. The goal is to pinpoint some of the weaknesses of the SIN model in terms of rotor-angle stability, and to gain a clear understanding of their characteristics. These weaknesses can then be eliminated, or at least mitigated, using the control algorithms developed throughout the dissertation.

6.5.1 Pinpointing Rotor-Angle Stability Weaknesses of the SIN

Real power systems are operated such that their dynamic behavior is acceptable and that stability is virtually guaranteed over a fairly large set of possible operating conditions. The low occurrence of blackouts is proof of this. Consequently, using a power system model that closely resembles a real power system, such as the SIN model in this chapter, means that the dynamic performance and stability properties of the model are acceptable over a relatively large set of conditions. Designing controllers for a system with these characteristics can only result in negligible dynamic performance gains that are not substantial enough justify the efforts in this dissertation.

One of the goals of this section is therefore to find a set of critical operating conditions that degrade rotor angle stability significantly without resorting to unrealistic operating regimes, e. g., opening a large number of transmission lines simultaneously, increasing loads beyond credible levels, etc. This set would provide an appropriate

benchmark to test the adequacy and effectiveness of advanced damping controls of the type sought throughout this dissertation.

The set of all possible operating conditions, disturbances, contingencies, etc, for a system such as the SIN model in this chapter is extremely large at best. Therefore, finding the set of critical operating conditions that significantly reduce rotor-angle stability is a complex task in itself. Thankfully, the search for this set of operating conditions can be guided by knowledge of the fundamental phenomena causing the emergence of power system oscillations.

As was mentioned in previous chapters, for the most part low frequency inter-area oscillations tend to emerge or worsen when large blocks of power are transferred between distant areas in a power system, and when the interconnection between distant areas is weak. An automated search is thus completed by modifying the generation schedules such that the active power interchange between the South and the Southeast regions of the SIN is increased in a stepwise manner. Single-line contingencies are applied to important transmission corridors all across the system at each interchange level to weaken the interconnection between areas. Only lines carrying the most power in the pre-contingency state are considered. This is done to reduce the number of cases to a more manageable level, since considering all 1006 single-line contingencies would be computationally challenging. It is argued here that disconnection of the lines carrying the largest blocks of power has the largest impact in the system's post-contingency state, so this approach provides a worst-case scenario perspective at each interchange level.

The studies are based on the multi-operating point small-signal analysis approach from Chapter 3. The flow chart in Figure 6.8 reintroduces the steps involved in this

analysis. This approach consists of calculating linearized models of the power system at each operating condition. These linearized models can then be used to determine the oscillatory behavior of the system at each foreseeable operating condition.

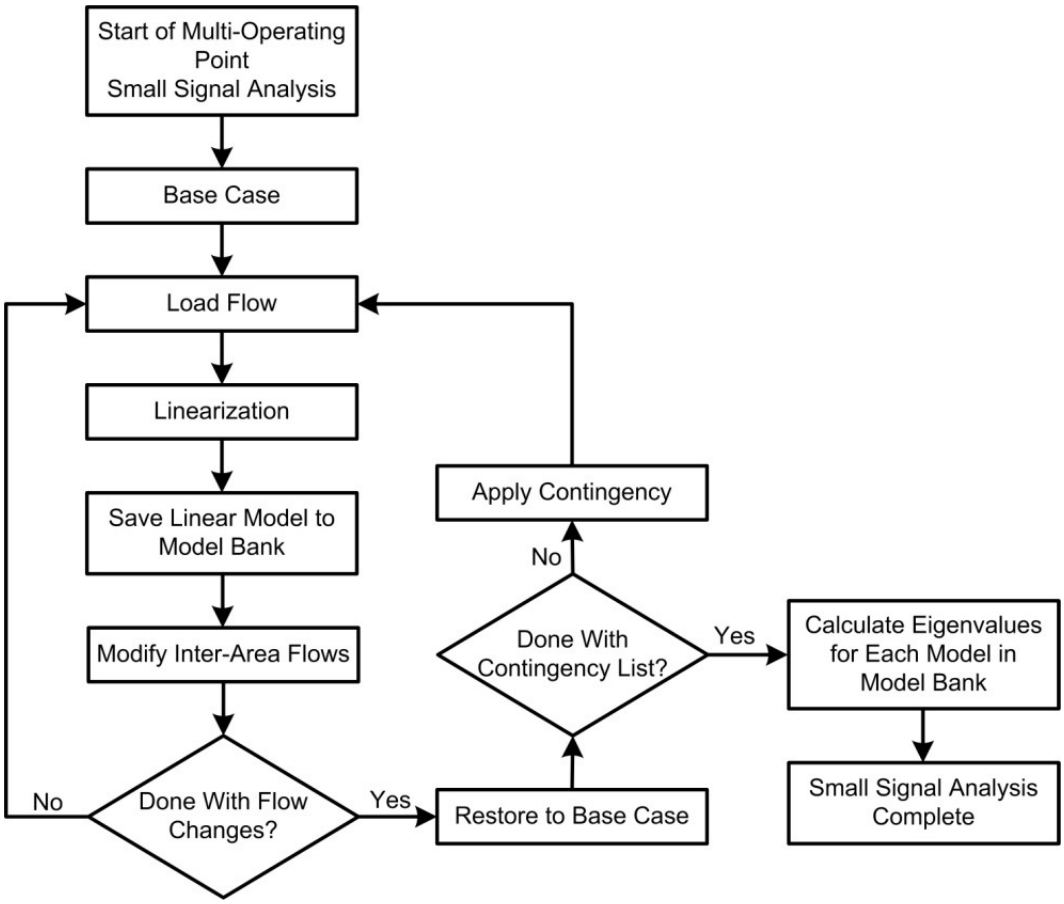

Figure 6.8 Flow chart of approach to multi-operating point small signal analysis

In all, 5 active power interchange levels are evaluated: 3.4 GW (base case), 4 GW, 4.6 GW, 5.2 GW, and 5.8 GW. Closer inspection of Figure 6.3 proves that, although high in the last instance (5.8 GW), these interchange levels are not unrealistic. 50 line contingencies are evaluated at each level, for a total of 250 possible operating conditions. Two of them result in non-convergent power flow conditions and are not considered further. Therefore, a total of 248 operating conditions are considered henceforth.

While varying the system's load flow settings, special attention has been given to making the resulting operating conditions as realistic as possible. However, loading constraints for the transmission system were not considered because thermal limits were unavailable. Therefore, loading violations are likely in many of the cases under analysis.

The interchange levels were varied by controlling the active power output of all machines in the South to result in a given interchange level. Power balance was achieved by controlling all machines in the Southeast and Midwest under frequency control. The power of the equivalent machine used to represent the North side of the system was held constant. Active power variations were distributed evenly (in per unit) among all machines in each area. The maximum active power limits for all generators were upheld. All loads were held constant, so the actual power demand and overall system loading level is the same throughout the studies.

The plot in Figure 6.9 illustrates the movement of the system's eigenvalues over the resulting set of operating conditions. Only eigenvalues with a damping ratio lower than 0.5 are plotted. Special attention is given to the lower frequency range of the complex plane, since it is typically associated with poorly damped inter-area modes. The damping of all modes is acceptable for all contingency cases when operating at the base interchange level. This demonstrates that the PSSs already in place (recall that more than half of the generators have PSSs installed) are relatively effective and robust. However, poorly damped oscillations with damping ratios close to 3% appear once the interchange reaches 5.2 GW. With interchanges of 5.8 GW the system begins to operate in violation of stability constraints, where a single critical contingency can push the system to lose rotor-angle stability in the small-signal sense.

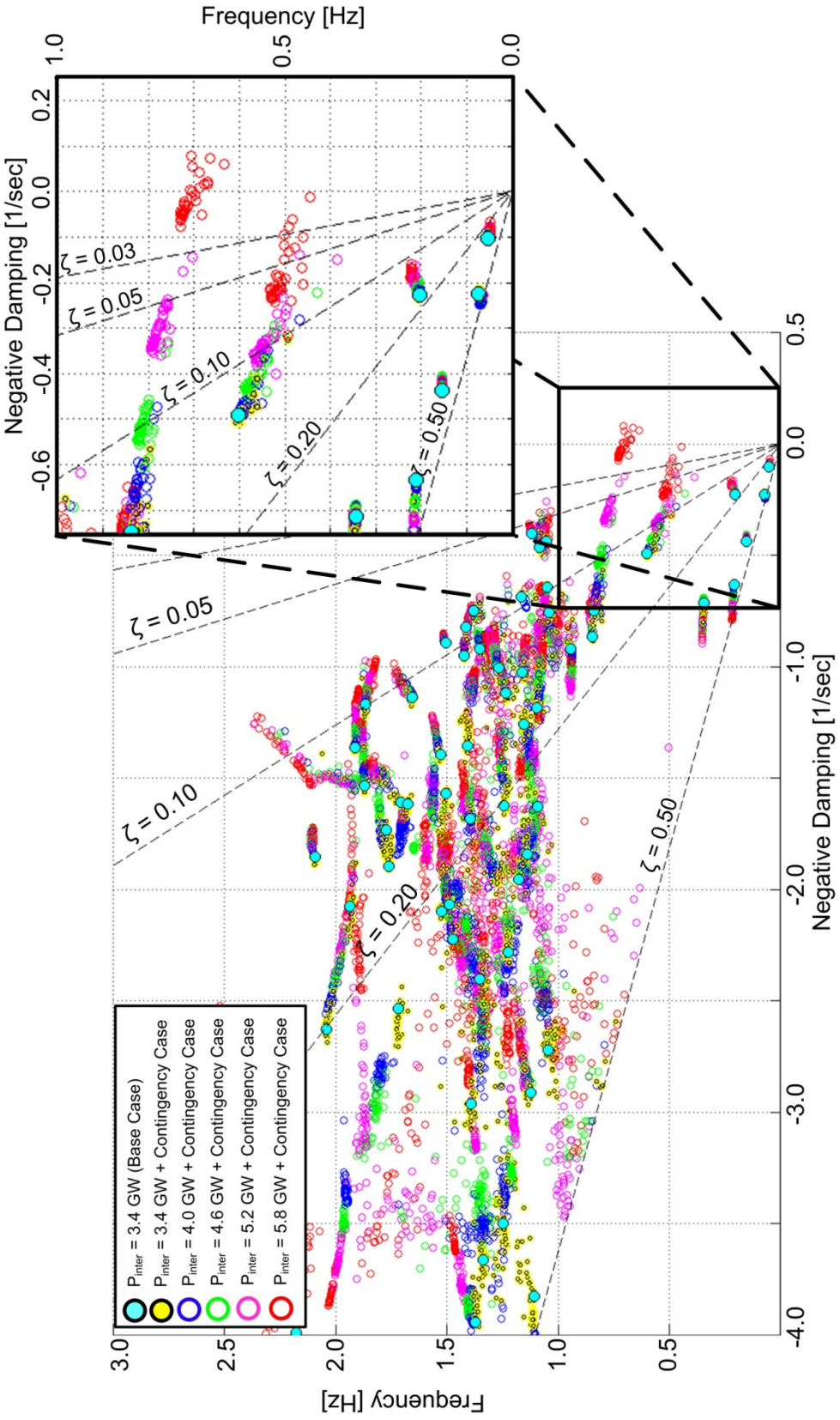

Figure 6.9 Eigenvalue movements for the SIN over 250 operating conditions

Advanced intelligent controllers might prevent these oscillations from emerging and improve the dynamic performance of the SIN. This could allow for higher utilization of the transmission infrastructure, and keep the system from operating under risky regimes that can eventually result in widespread blackouts. Such controllers could allow the system to operate reliably even under highly unfavorable hydrological conditions.

By design, the set of 248 operating conditions just described encompasses operating regimes in which credible contingencies can severely degrade rotor-angle stability. Consequently, the set provides a realistic and challenging benchmark to evaluate the aggregation-based intelligent damping control approach to be proposed in the next chapter. However, analysis over a set of 248 operating conditions can be time consuming and cumbersome. Time-domain simulations of the full non-linear model to be completed in Chapter 7 are computationally intensive (particularly for a model of order 1348), making the analysis over all 248 conditions highly undesirable. The next section discards redundant operating conditions using ideas from Chapter 3.

6.5.2 Reducing the Number of Operating Conditions Analyzed

The gap metric and hierarchical clustering-based operating point selection method introduced in Chapter 3 can be used to reduce the set of operating conditions to consider for analysis, design, and evaluation. The goal is to derive a small subset of conditions by minimizing redundancy without significantly reducing the richness of the information contained in the retained set.

The steps for completing the operating point selection are depicted in Figure 6.10. The selection process utilizes the 248 linearized models from the previous section. Each of these models is reduced using balanced realization truncation to minimize the

computational burden of calculating the gap metric, which is found to be highly time consuming for high order models. The order of the reduced models is chosen heuristically as 200 (out of the original 1348). Bode plot comparisons not shown here demonstrate that these reduced models are highly accurate over the frequency range of interest (0.1-2 Hz).

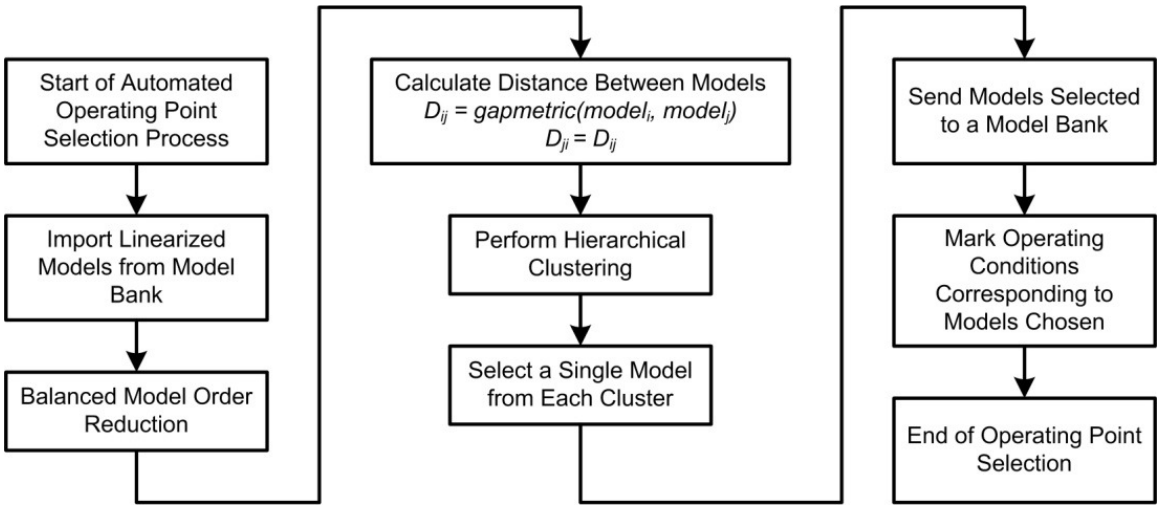

Figure 6.10 Automated selection of small set of operating points

The dendrogram in Figure 6.11 illustrates the results of the operating point selection step. 38 clusters of operating conditions are selected by cutting the dendrogram as shown by the dashed line. A single operating condition is then used to represent each of those clusters. Consequently, the original set of 248 operating conditions is now reduced to 38.

From here onwards, the discussion assumes that these 38 operating conditions provide a comprehensive picture of the behavior of the system at all critical operating conditions of interest. This assumption is justified if the original set of 248 is considered to cover all operating conditions of interest. However, this set can become significantly larger if a wider set of conditions beyond the original 248 is considered.

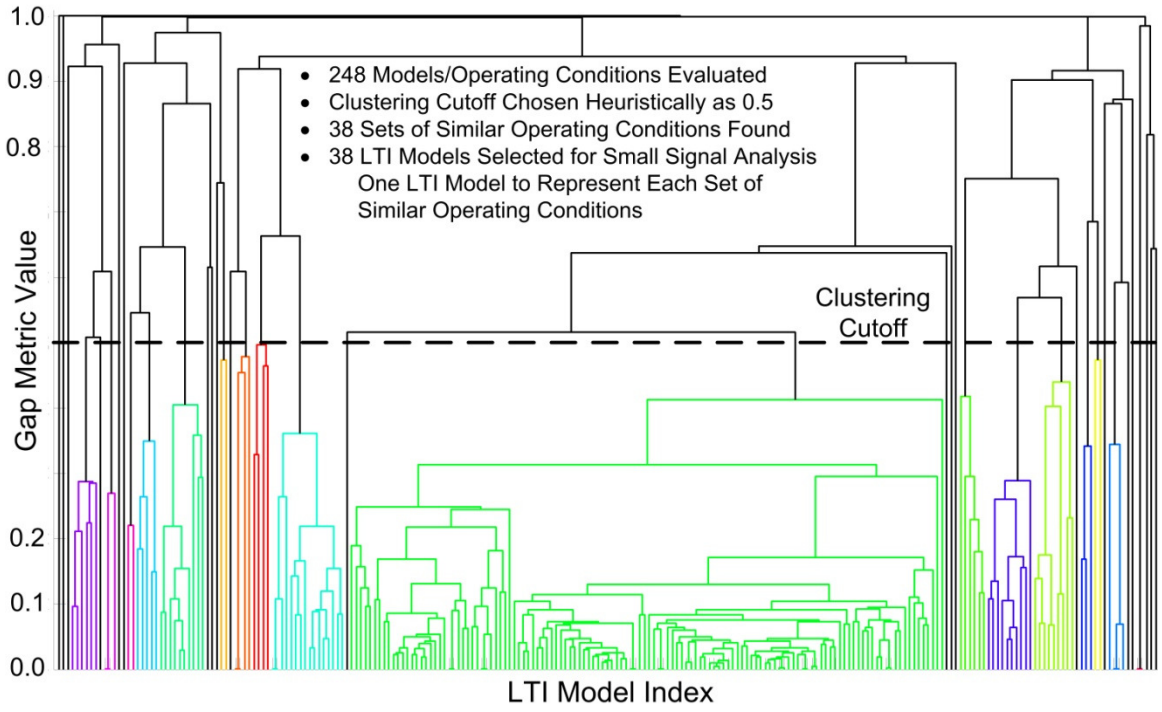

Figure 6.11 Dendrogram of dissimilarities between 248 different operating conditions of the SIN

6.5.3 Analysis of Critical Inter-Area Modes

Now that the system's operating envelope has been determined, it is possible to probe deeper into system's dynamic behavior to obtain a comprehensive picture of the oscillatory patterns in the system. The eigenvalues for the SIN over the envelope of 38 operating conditions of interest are shown in Figure 6.12.

Four different inter-area modes, labeled A, B, C, and D respectively, are highlighted in red. For convenience, the locations of these are encircled by the green/dashed lines in Figure 6.12.

Modes B and C become highly sensitive to a number of contingencies once the active power interchange from the Southeast to the South of the SIN reaches 5.2 GW or higher. Their average frequencies are 0.53 Hz and 0.72 Hz respectively. These modes have the tendency to become poorly damped and even unstable for a number of contingencies.

This tendency makes them the focus of the remainder of this chapter. The aggregation-based intelligent wide-area damping controller proposed in Chapter 7 will be dedicated to improving the damping of these modes such that rotor-angle stability is maintained over the range of operating conditions considered.

Modes A and D are not as sensitive and remain well damped at all times. Therefore, they do not require additional damping and are not given further special attention.

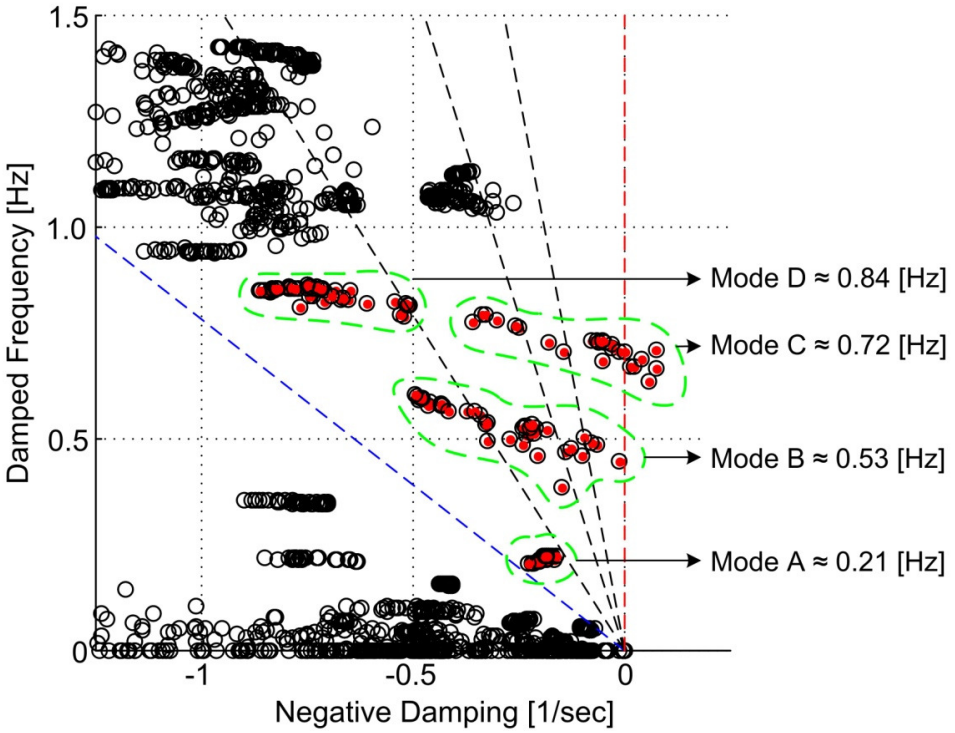

Figure 6.12 Inter-area modes of the SIN over chosen set of operating conditions

The mode shapes of modes B and C are illustrated in the left sides of Figure 6.13 and Figure 6.14 respectively. Colors have been assigned depending on the geographical area of Brazil where each generator is located. The size of each circle is defined by the inertia of each machine. The shapes for all 38 operating conditions are plotted. Therefore, these

two figures give a comprehensive view of the oscillatory patterns in the system by depicting the shapes of all generators at all operating conditions.

The right side of Figure 6.13 provides an average geographical interpretation of the shape of mode B. The dashed line in the figure depicts the "mode interface", and indicates that mode B results in oscillations in which one half of the system oscillates against the other.

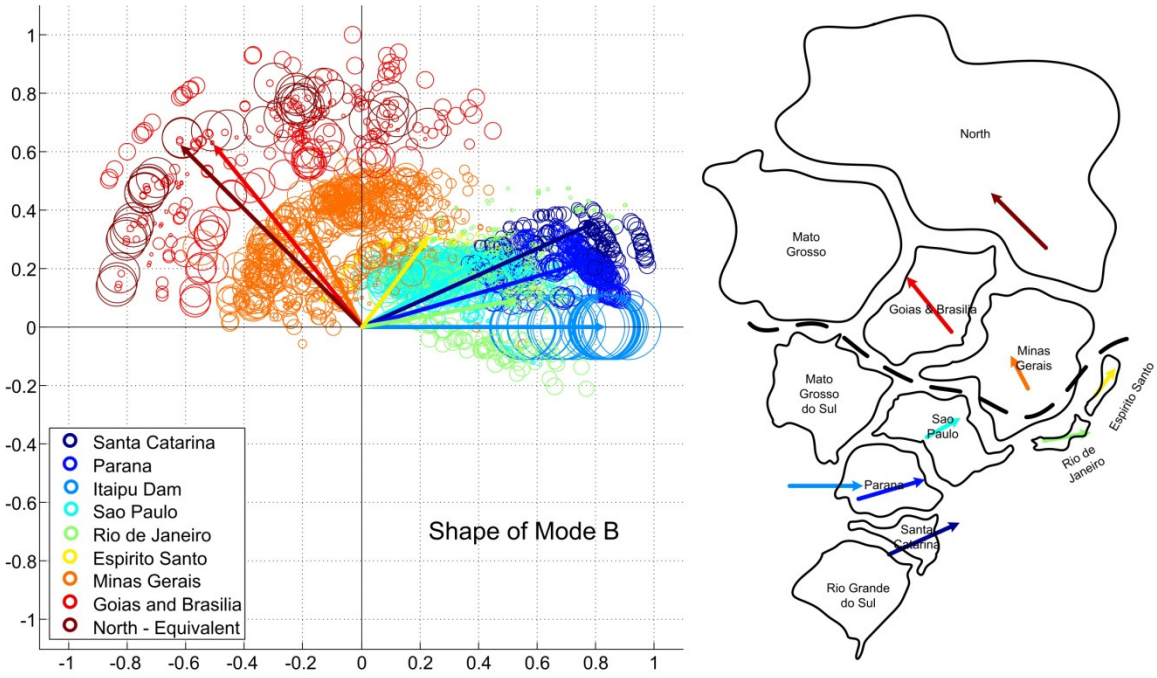

Figure 6.13 Normalized shape of mode B over 38 operating conditions

The right side of Figure 6.14 provides the same average geographical representation for mode C. The mode interface indicates that mode C involves all machines in Sao Paulo and some in Minas Gerais oscillating against the rest of the system. The rest of the system can be further split in two other portions, South and Midwest, as indicated in the figure.

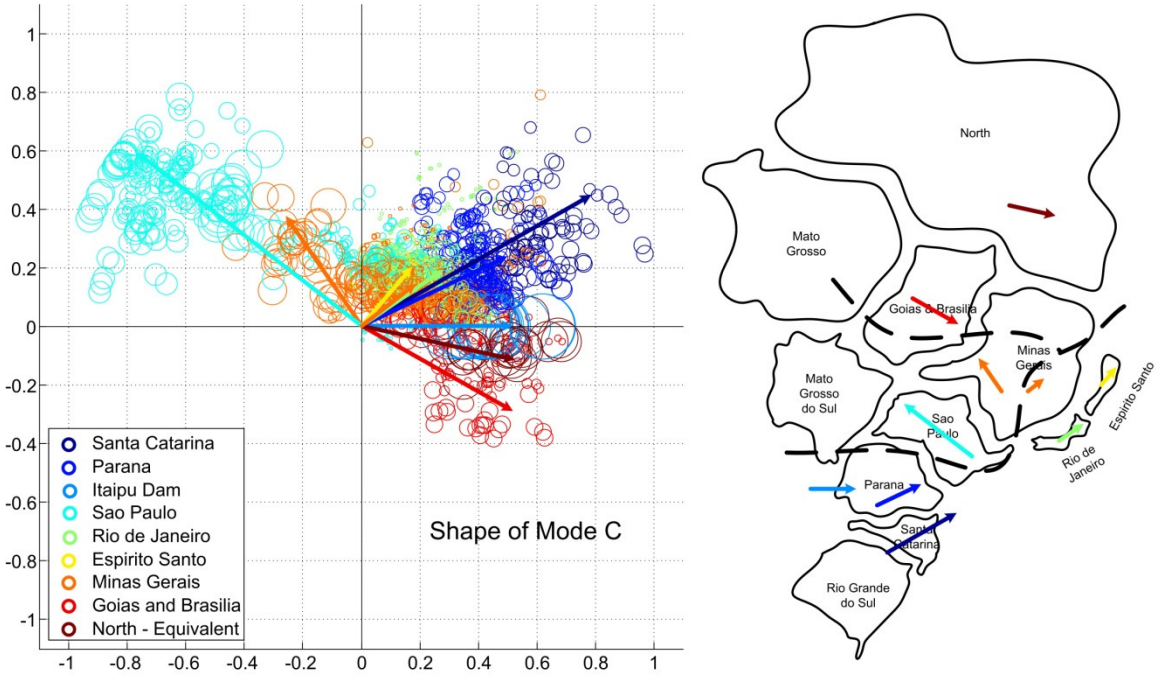

Figure 6.14 Normalized shape of mode C over 38 operating conditions

The extensive eigenvalue and mode shape analysis of this section provide significant insights into the oscillatory patterns in the SIN model. Figure 6.12 indicates that the damping of two critical inter-area modes, both of which involve large portions of the system oscillating against each other, as illustrated in Figure 6.13 and Figure 6.14, are very sensitive to changes of the system's operating condition. These modes even become unstable for a number of operating conditions and need damping improvement.

Mode shapes in Figure 6.13 and Figure 6.14 indicate that the oscillatory patterns are not as sensitive and their distribution across the system's geography remains relatively constant regardless of the operating condition. Also, for the critical inter-area modes, generators within the same geographical region tend to behave coherently. Therefore, aggregation-based control based on the geographical location of the generators within the system is a promising approach. This can be used to replace the time-domain waveform-

based coherency clustering approach taken in Chapter 5. Consequently, a virtual generator can be used to represent all generators within a geographical portion of the power system, allowing each area to be controlled as a single unit. This observation will be exploited in Chapter 7.

6.6 SUMMARY

This chapter described the characteristics, development, and validation of a large-scale power system model that can be used as a benchmark to evaluate the approaches proposed in the dissertation. The model represents a large portion of the Brazilian power system and hence can be considered a large-scale power system model.

Extensive analysis of the system over a large number of credible operating conditions highlighted some of the weaknesses of this system in terms of rotor-angle stability. Two critical inter-area modes were found to be highly sensitive to changes in the system operating condition. Specifically, the damping of these two modes decays and eventually they become unstable when the transfers between two distant regions in the system become large enough. This system is known to require such transfers during adverse hydrological conditions due to the dominance of hydroelectric generation in Brazil. During highly adverse conditions, this system has been operated in violation of transient stability constraints. Under such operating regimes, a single contingency can lead to rotor-angle instability and possibly widespread blackouts. A controller capable of significantly improving the damping of all critical inter-area modes under all operating conditions can improve the system's dynamic performance, enhance inter-area transfer capabilities, and improve the reliability of the system.

In contrast to the high variability of the damping of the critical inter-area modes, their mode shapes remain relatively constant as the system's operating conditions change. Also, there is a strong correspondence between geographical location of generators and their tendency to swing together in the inter-area modes. The mode shapes showed that generators that are close to each other tend to swing together in these modes. This is not unexpected, since geographical nearness can be expected to result in strong electrical coupling, known to be a key driver of coherent behavior. Therefore, aggregation-based control guided by the geographical location of generators is a promising approach that can replace the time-domain-waveform-based coherency-clustering approach taken in Chapter 5.

The next chapter will combine all the ideas explored throughout the dissertation to develop a scalable holistic aggregation-based intelligent wide-area damping controller capable of significantly improving the rotor-angle stability of the large-scale power system model in this chapter at all operating conditions under consideration.

CHAPTER 7 SCALABLE HOLISTIC AGGREGATION-BASED INTELLIGENT WIDE-AREA DAMPING CONTROL

7.1 INTRODUCTION

The preliminary results in Chapter 5 served as a proof of concept for aggregation-based intelligent control for enhancing rotor-angle stability in power systems. However, the 68-bus/16-machine power system model used was not representative of a realistically sized power system. Therefore, although the results were encouraging, it was not possible to assert whether the virtual generator-based simplifications provided the improvements needed to overcome the scalability challenges highlighted in Chapter 4 . Consequently, the ability of intelligent controllers to scale-up to real power systems was left as an open question. That question is answered in this chapter. The complex and realistic power system model developed in Chapter 6 is utilized to explore the adequacy of aggregation-based intelligent control for improving rotor-angle stability of large-scale power systems.

Some enhancements are made to the control approach described in Chapter 5 . First, the time-domain-based partitioning using swing curves is replaced by mode shape-based partitioning in section 7.2. This allows the determination of groupings of coherent generators that remain coherent over a large set of disturbances and operating conditions, i.e. robust coherent groups. Second, the ANN-based non-linear system identification approach to obtain a differentiable model of the aggregate system is enhanced by exploiting the availability of linearized models of the power system in section 7.3. The use of linearized models guides the structure, size, and initial set of weights for the ANN used as a model network, thus significantly reducing the complexity of the model network training process. Third, the heuristic dynamic programming (HDP)

implementation of approximate dynamic programming (ADP), is replaced by the more advanced and powerful dual heuristic programming (DHP) in section 7.4. This enhancement improves the online adaptation capabilities of the intelligent controller. The integration of system aggregation and intelligent control techniques to form an aggregation-based intelligent wide-area damping controller (AB-IWADC) is given in section 7.5.

Section 7.6 presents simulation results illustrating the effectiveness and robustness of the AB-IWADC. The AB-IWADC allows the system to remain stable over a larger set of operating conditions, makes the system more resilient to contingencies, and increases the potential for beneficial inter-area power transfers. A cohesive framework for designing aggregation-based wide-area damping controllers is then described in section 7.7.

7.2 MODE-SHAPE-BASED VIRTUAL GENERATOR REPRESENTATIONS OF THE SIN

The aggregation-based simplified power system representations introduced in Chapter 5 are based on the tendency of certain generators in an interconnected system to behave coherently. The validity of these representations hinges on having appropriate groupings of coherent generators. These representations allowed the controllers proposed in Chapter 5 to control all generators within a group as if they were a single machine. This approach can only be applied if all generators in a group behave coherently. Therefore, the robustness of the controls is tied to the robustness of the coherency-based groupings.

In Chapter 5, coherent generators were grouped using clustering of time-domain swing curves. There are several drawbacks to this method. First, the swing curves used for clustering are obtained by simulating the system's response to one or multiple disturbances. Consequently, the clustering results become dependent on the type and

location of the disturbance applied. Applying a large number of disturbances at multiple locations can mitigate this dependence at the cost of higher computational expense. Second, the system's time-domain response is dependent on the system's operating condition. Consequently, the robustness groupings obtained considering a single operating condition is questionable. Increased robustness can be achieved by simulating the system's response at multiple operating conditions. However, once the set of disturbances applied and the number of operating conditions become large, the computational demands become substantial and even prohibitive.

Coherent groups can also be determined using linearized models of the system as proposed in [105]. Using linearized models instead of time-domain waveforms eliminates the dependence of the groupings on disturbance type and location, but the dependence on operating conditions remains. Again, one can reduce this dependence and generate robust coherent groupings by performing the analysis over a large set of operating conditions. Such an analysis imposes the need for calculating a linearized model of the system at each operating condition, which can be time consuming for large-scale systems. Here, those models are already available as a by-product of the analysis in Chapter 6.

The mode shapes from Chapter 6 are thus used here to determine the coherent groupings to be used for aggregation-based control. Figure 7.1 illustrates the average mode shapes for the two critical inter-area modes in the SIN identified by the analysis in Chapter 6. The length of the arrows in the figure represents the degree to which a particular oscillatory mode is visible in the rotor speed measurement of generators in a particular area, i.e., the longest arrows indicate the areas where an oscillation is most visible. The direction of the arrows represents the phase displacement of the oscillations

in generators with respect to each other, i.e., arrows pointing in opposite directions indicate areas with generators oscillating against each other. The arrows in magenta indicate areas that are not considered for grouping. These areas either do not swing significantly in the inter-area modes, or correspond to the North equivalent. This equivalent does swing significantly in the inter-area modes, but is assumed to not be measurable or uncontrollable for the analysis here.

These average mode shapes were obtained over a large set of operating conditions. Consequently, generator groups determined using these results are robust to changes in the system's operating condition. Figure 7.2 is a rough geographical representation of such a grouping. The system is sub-divided into four sub-networks (SN), each enclosing a set of coherent generators. The groups are selected by visual inspection of the mode shapes. A more sophisticated approach to mode shape-based grouping can be found in [105], but the potential accuracy gains by this method are found unnecessary here.

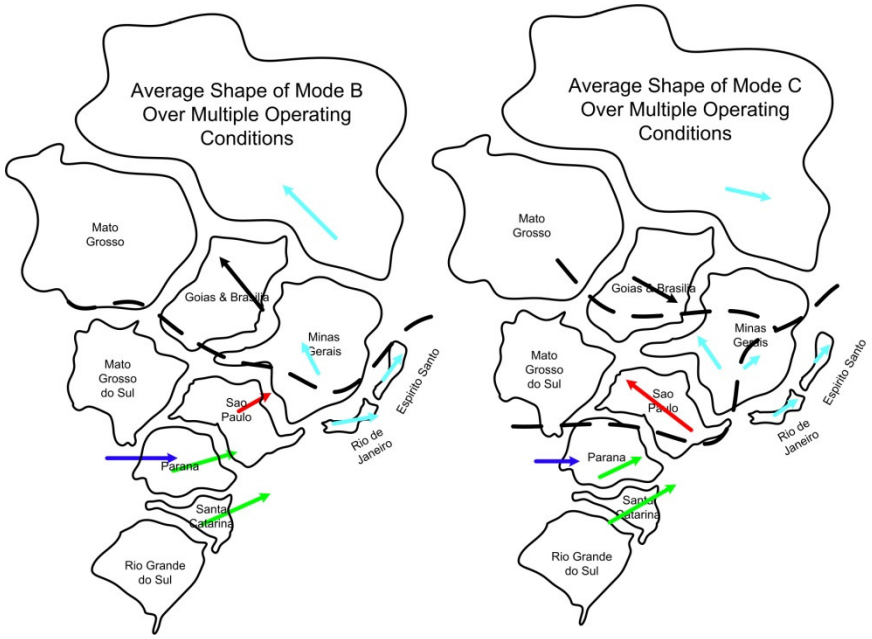

Figure 7.1 Geographical representation of average mode shapes for the two critical inter-area modes in the SIN

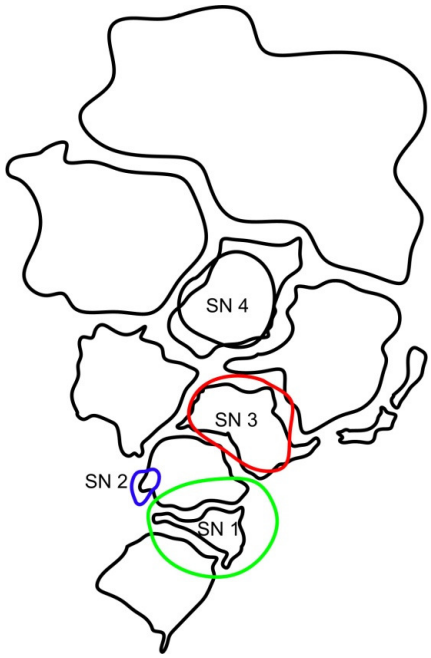

Figure 7.2 Geographical representation of average mode-shape-based robust generator groupings

The groups in Figure 7.2 are then utilized to generate aggregate system representations using the VG concept from Chapter 5. Four VGs are calculated, one for each sub-network, using the configuration depicted in Figure 7.3.

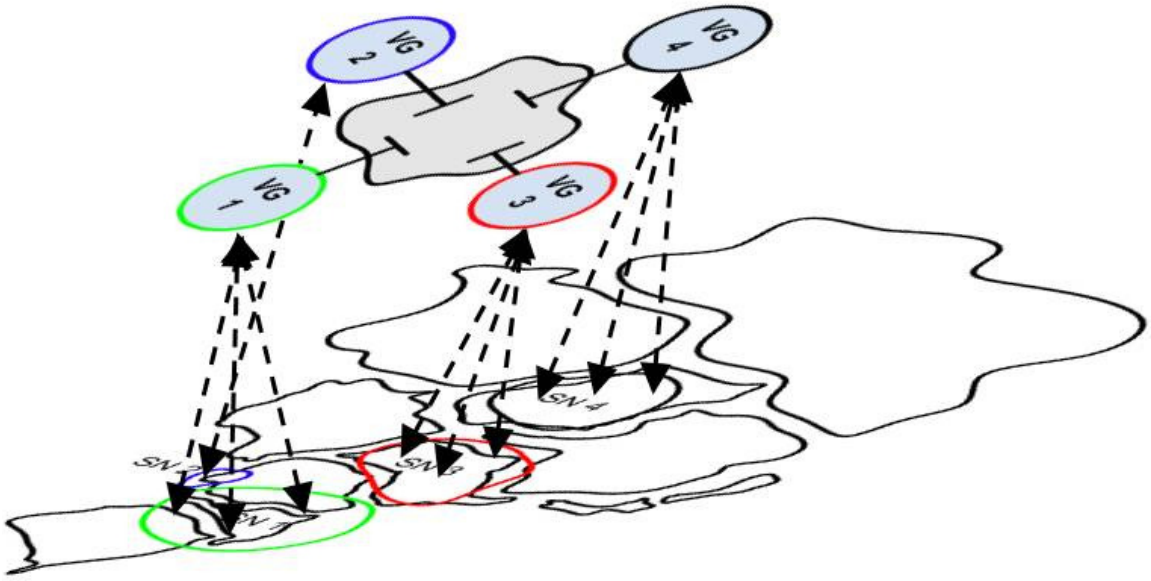

Figure 7.3 VG implementation for the SIN

Since the groupings are generated using linearized models of the system, it is necessary to validate them using time-domain simulations of the non-linear power system model. Visual inspection of waveforms not shown here allows further refinements of the generator groups. Generators with small inertia with respect to other generators in their group are discarded from the VG calculations. This can be done with minimal information loss since the contribution of generators with low relative inertia to the VG speed is small. VG2 corresponds to a single large equivalent generator used to represent multiple generators located at the Itaipu dam. Refer to section 6.3 for more details. The speed of VG2 is thus the actual measured speed of a generator and not an equivalent.

Figure 7.4 illustrates typical time-domain simulation results. The operating condition is selected such that mode C is poorly damped. The actual speed of each generator in a group and the VG speed used to represent them are shown for a generic disturbance. As expected, generators within a group swing together in the inter-area modes, indicating that the grouping results are suitable. VG speeds are also plotted at the bottom of the figure to highlight the oscillatory patterns in the system. Since mode C is poorly damped, it dominates the system response. Figure 7.1 showed that this mode involves machines in Sao Paulo (SN3 and VG3 Figure 7.3) oscillating against the rest of the system. This is verified by the time-domain response, which shows VG3 oscillating against VG1, VG2, and VG4.

The tendency to swing together does not hold when considering local oscillations. Figure 7.5 shows the response of generators in SN1 (12 coherent generators) and of VG1 to small continuous load variations across the system. The weighted averaging effect of the VG-based aggregate representation discards faster local oscillations and retains

slower phenomena. This allows a controller which only sees the aggregate representation to ignore faster local oscillations, known to be controllable using conventional local controls such as PSSs, and to focus on improving dynamic performance in terms of the troublesome and more difficult-to-control inter-area oscillations instead.

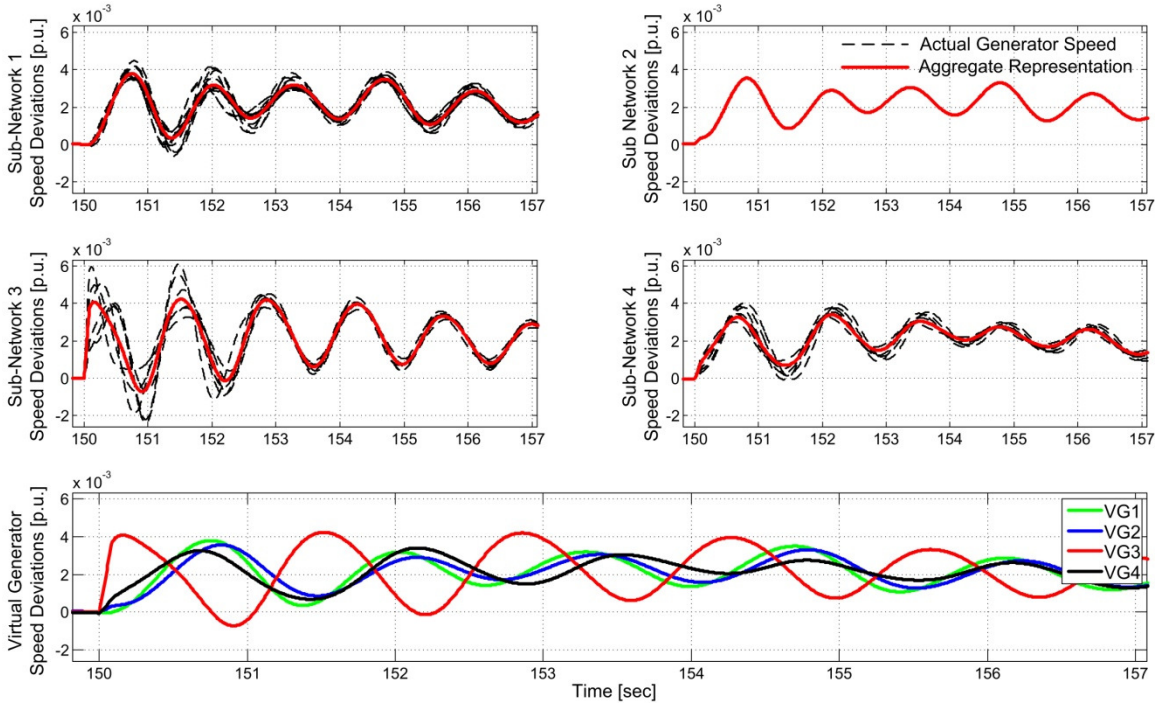

Figure 7.4 Time-domain results for validating generator groups and VG representations

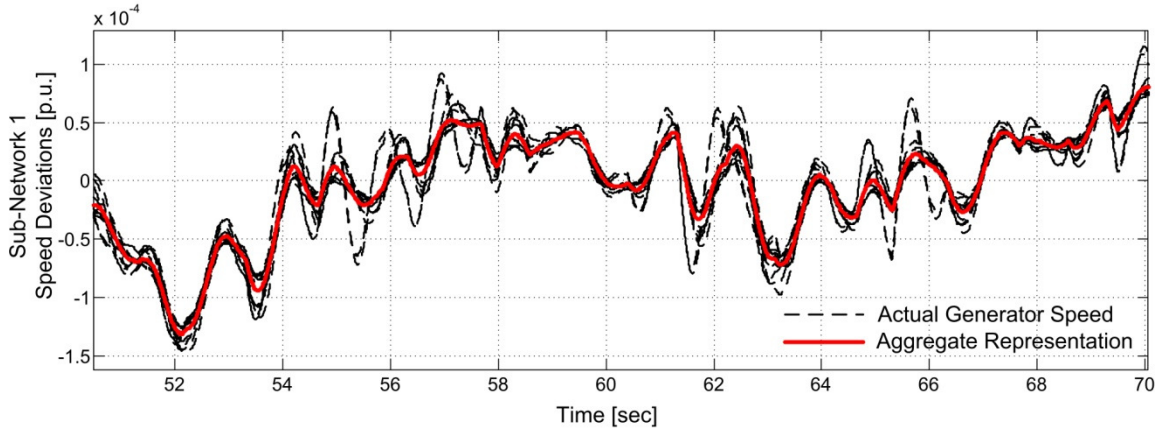

Figure 7.5 Effect of aggregation on perception of local oscillations

As in Chapter 5, calculating the VG-speed is only part of the aggregation procedure. Once the coherency-based generator clusters and the VG speeds are available, it is necessary to obtain accurate models that capture the dynamical input-output relationship of the VGs. An improved approach to obtain such models is provided next.

7.3 IDENTIFICATION OF VG DYNAMICS USING NEURAL NETWORKS

As discussed in Chapter 5, ANNs can be used to identify and capture the behavior of arbitrary and unknown dynamical systems using input-output data pairs. Such a network is called a model network. Model networks are flexible enough to represent complex non-linear dynamical systems; however, when the dynamics of the system to be modeled are complex, and/or when the system is large, the process of training a model network can require large and rich input-output data sets, be computationally complex, and become time-consuming. This is the case here. This section illustrates how to utilize linearized power system models to aid in the process of designing a model network.

The VG-based representations from the previous section significantly reduce the size and complexity of the system to be controlled. However, there is no clear path for developing an appropriate model network for the resulting aggregated system. The linearized system models obtained in Chapter 6 can provide useful insights. As a bi-product of the analysis in Chapter 6, a linear model of the form in (7.1) is available for each operating condition. In (7.1), the output vector $y(k)$ corresponds to the rotor speeds of the 73 generators in the Brazilian system, and the input vector $u(k)$ corresponds to the 73 wide-area damping control signals as defined in (7.2). These output and input signals are connected to the power system at the locations shown in Figure 7.6.

$$x(k+1) = Ax(k) + Bu(k)$$
$$y(k) = Cx(k) \tag{7.1}$$

$$y(k) = \left[\Delta\omega_{G1}(k) \quad \cdots \quad \Delta\omega_{G73}(k)\right]^T$$
$$u(k) = \left[u_{WADC}^{G1}(k) \quad \cdots \quad u_{WADC}^{G73}(k)\right]^T \tag{7.2}$$

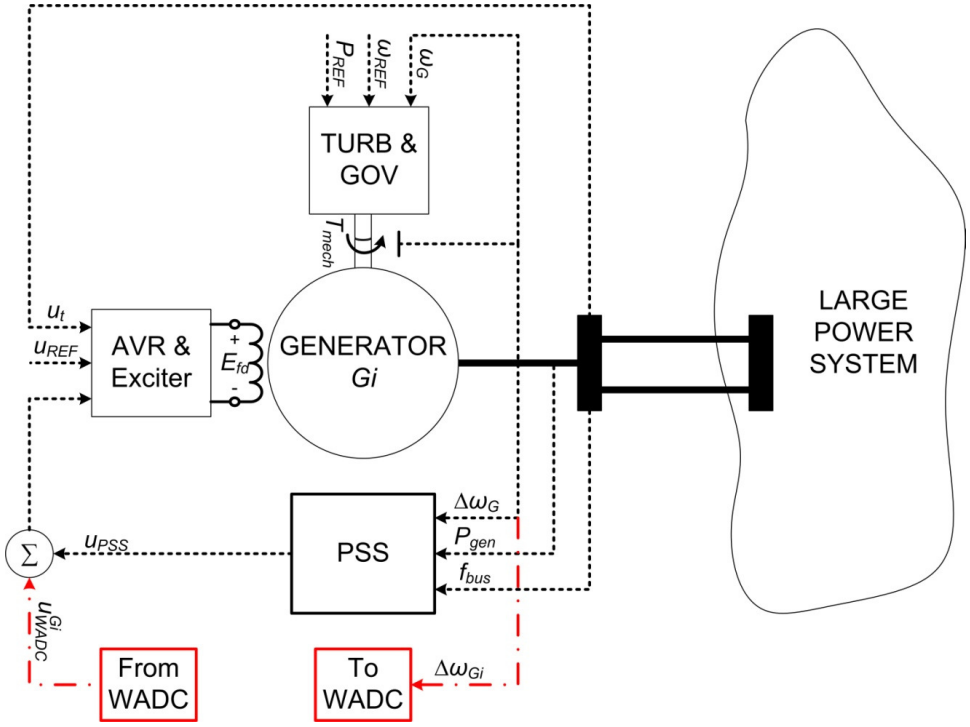

Figure 7.6 Connections of a WADC to a generating plant selected to participate in wide-area damping enhancement

By definition, an accurate linear model of a non-linear dynamical system can provide an accurate approximation of the system's behavior in response to small disturbances when operating "close" to the condition used for linearization. How close is not trivial to determine. The accuracy of the linear model is guaranteed when the model is obtained by direct linearization of the non-linear dynamic equations of the system. A model network whose small-signal behavior matches that of an accurate linear model of the system can, at the very least, represent the system's behavior over a small operating region.

Therefore, models of the form in (7.1) can become the "template" for creating an acceptable model network. How to use such a template will become clear shortly.

Linear models obtained by direct linearization are known to be accurate; however, they are of the same order as the original non-linear system. Clearly, the order is bound to be high for large-scale power systems. Soon it will become clear that using a high-order linear model as the template to create the model network adds significant complexity. Model order reduction techniques can be used to derive simple yet relatively accurate linear models that can be used to guide the development of the model network. This is illustrated next.

7.3.2 Simplified Linear Models for Model Network Design

The linear models from Chapter 6 result from direct linearization of the full non-linear dynamical model of the system. Consequently, they are of the same order as the original system, i.e., 1348. Accurate reduced order models of order 200 can be obtained using the balanced realization truncation method, which allows the elimination of states that contribute the least to the input-output behavior of the full-order system [106]. As a side note, once model order reductions are performed, the connection between the state variables and the actual system variables is lost, making the state vector an abstract mathematical construct with no direct physical connection to the power system.

For control purposes and for guiding the development of a VG model network, a model of order 200 is still large and further reductions are needed. However, such reductions must be completed in a sensible way to ensure that important dynamical behaviors in terms of inter-area oscillations are preserved.

The VG-based aggregations from the previous section can be applied to the linearized reduced-order models. The formula for calculating the VG speeds is repeated in (7.3) for convenience, where $\sum_{j \in SNi}$ indicates summation over all generators in sub-network *i*.

$$\Delta\omega_{VGi} = \frac{\sum_{j \in SNi} H_j \Delta\omega_j}{\sum_{j \in SNi} H_j} \tag{7.3}$$

For aggregation-based control, the VG speeds are assumed to be the outputs of the system. The output vector for the four sub-networks from the last section can then be defined as in (7.4). The superscript *a* is used to indicate an aggregate variable.

$$y^a(k) = \left[\Delta\omega_{VG1}(k) \quad \Delta\omega_{VG2}(k) \quad \Delta\omega_{VG3}(k) \quad \Delta\omega_{VG4}(k)\right]^T \tag{7.4}$$

In Chapter 5, the local-area damping controller (LADC) generated a different signal for each generator, so there was no input-aggregation and the LADC generated four different auxiliary damping control signals. This approach severely limits the dimensionality reductions obtained by the aggregation stage and is avoided here due to the higher complexity of the Brazilian system. For realistically sized systems, groups are expected to contain large numbers of generators, and so output measurement aggregation using VGs alone does not suffice. An input disaggregation scheme is thus needed to further improve scalability. The disaggregation scheme should be designed in a way that enhances coordination. The PSO controller design techniques from Chapter 3 can potentially be adapted to be used to this end. However, that approach has not been developed at this point. Consequently, the same aggregated input signal is sent to all generators within the same group. Obviously this choice is not optimal; however,

simulations shown later indicate that acceptable control performance is attainable in spite of this rudimentary scheme. The inputs into the system can then be defined as in (7.5).

$$u^a(k) = \left[u_{WADC}^{VG1}(k) \quad u_{WADC}^{VG2}(k) \quad u_{WADC}^{VG3}(k) \quad u_{WADC}^{VG4}(k) \right]^T \tag{7.5}$$

The relation between the aggregated inputs and the original u_{WADC} inputs into the group of generators within sub-network i (SNi) is defined in (7.6). Again, all generators within a group receive identical auxiliary wide-area damping control signals.

$$u_{WADC}^{Gj}(k) = u_{WADC}^{VGi}(k) \qquad (\forall j \mid Gj \in SNi) \tag{7.6}$$

An aggregated linear model following the assumptions above can be described as in (7.7). The state matrix A remains the same as in (7.1), while the input and output matrices B and C are replaced by the aggregated matrices B^a and C^a defined in (7.8).

$$\begin{aligned} x(k+1) &= Ax(k) + B^a u^a(k) \\ y^a(k) &= C^a x(k) \end{aligned} \tag{7.7}$$

$$\begin{aligned} B^a &= \left[\sum_{j \in SN1} (B(:,j)) \quad \cdots \quad \sum_{j \in SN4} (B(:,j)) \right] \\ C^a &= \left[\frac{\sum_{j \in SN1} (H_j C(j,:))}{\sum_{j \in SN1} (H_j)} \quad \cdots \quad \frac{\sum_{j \in SN4} (H_j C(j,:))}{\sum_{j \in SN4} (H_j)} \right] \end{aligned} \tag{7.8}$$

Figure 7.5 provided a pictorial representation of the tendency of the VG-based aggregation stage to discard local oscillations from the VG speeds (the outputs) while preserving the inter-area ones. Balanced realization truncation allows the elimination of state variables with a low influence on the system's input-output behavior. Consequently, when the aggregated model in (7.7) is reduced using balanced realization truncation, state

variables associated with local oscillations are discarded, while the ones associated with inter-area ones are preserved.

Figure 7.7 depicts the Hankel singular values of one of the linearized systems before and after the aggregation step. Hankel singular values can be interpreted as the relative contribution of a particular state variable to the input-output behavior of a linear system. More detailed explanations can be found in [106]. The tendency of the aggregation stage to eliminate certain oscillatory modes from the input-output behavior of the system is made obvious by the fact that the system's response after aggregation is dominated by only a few state variables. The Hankel singular values in Figure 7.7 indicate that a 20^{th} order model is complex enough to capture the essential dynamic input-output properties of the aggregate system. The original 1348^{th} order model is thus reduced and a 20^{th} order model is obtained. The complexity of this model is significantly lower than that of the full order of 1348 or the initial reduced order of 200 from Chapter 6.

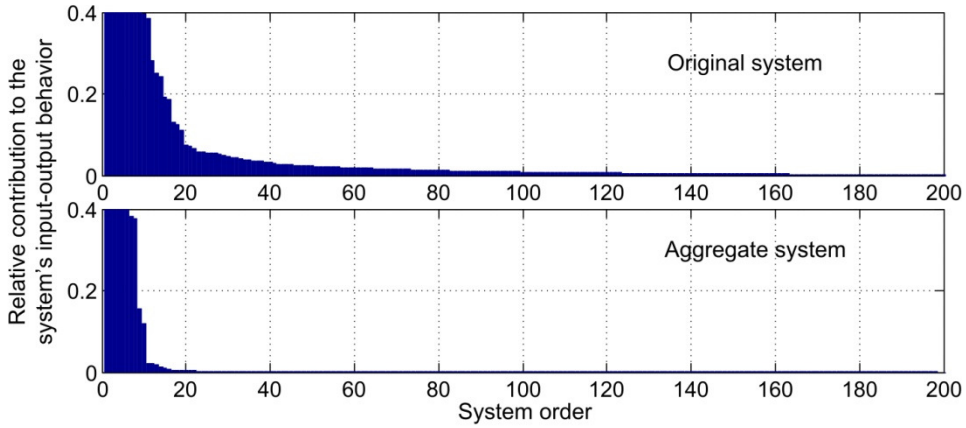

Figure 7.7 Hankel singular values of linearized model before and after aggregation

The motivation behind developing simple yet accurate linear models of the system is to guide the development of an acceptable VG model network. For the application at

hand, the model network can be viewed as a non-linear state observer of the power system. This perspective allows the utilization of powerful techniques for designing state observers when developing the model network. A brief detour into one of those techniques is taken next.

7.3.3 Brief Detour into Linear State Observers

Assume that the reduced order model from the previous section is the true plant to be controlled. The discrete-time dynamic equation of the plant is then given by (7.9).

$$\begin{aligned} x(k+1) &= Ax(k) + Bu(k) \\ y(k) &= Cx(k) \end{aligned} \tag{7.9}$$

A full-order Luengberger observer for this linear plant has the form in (7.10). The goal of the observer is to estimate the state *x(k)* of the system using measurable inputs and outputs (*u(k)* and *y(k)*). This state estimate can then be used for feedback control. The observer design task consists of selecting an appropriate gain *L* that will drive the error between the state estimate and the true state of the plant in (7.11) to zero as time progresses.

$$\begin{aligned} \hat{x}(k+1) &= A\hat{x}(k) + Bu(k) + L\left(y(k) - C\hat{x}(k)\right) \\ \hat{y}(k) &= C\hat{x}(k) \end{aligned} \tag{7.10}$$

$$e(k) = x(k) - \hat{x}(k) \tag{7.11}$$

The observer error's dynamic behavior is given by (7.12).

$$e(k+1) = (A - LC)e(k) \tag{7.12}$$

If the system is observable, then the eigenvalues of the matrix *(A – LC)* in (7.12) can be placed at arbitrary locations in the complex plane. If these eigenvalues are chosen to

be stable (inside the unit circle) the observer error will converge to zero over time, and the state estimate will be accurate. A thorough treatment of the theory on observer design can be found in [107], and an instructive discussion on how to select appropriate pole locations for acceptable observer performance appears in [108].

A graphical representation of the observer equation in (7.10) is provided in Figure 7.8. This block diagram and observer parameter set (matrices *A*, *B*, *C*, and *L*) can now be used as a template to create the VG model using the approach presented next.

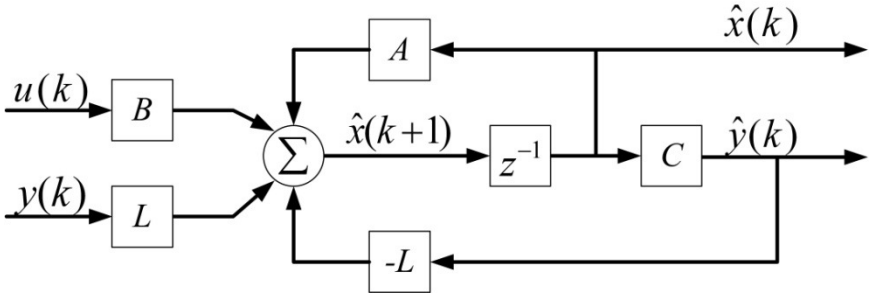

Figure 7.8 Block diagram of linear full-order observer

7.3.4 From Linear State Observers to Model Networks

As mentioned earlier, model networks are flexible enough to represent complex non-linear dynamical systems; however, when the dynamics of the system to be modeled are complex, and/or when the system is large, the process of training a model network can require large and rich input-output data sets, be computationally complex, and become time-consuming.

The design of an appropriate model network is further complicated by the fact that there are no clear indicators to guide the selection of the structure, size, parameters, etc., of the ANN to be used. Thankfully, the model network can be viewed as a non-linear

state observer. From this perspective, one can draw inspiration from the state observer in the previous section to guide the design of the model network.

The idea is to initialize the non-linear model network such that its small-signal behavior replicates that of an accurate linear state observer. A model network initialized in this way is capable of generating accurate state estimates over a region near the point for which the linear observer was designed even before training occurs. This perspective provides useful insights into acceptable choices of ANN structure, size, and initial parameter sets, significantly reducing the complexity of designing a model network.

The ANN structure in Figure 7.9 is created such that its small-signal behavior can replicate the full-order observer in Figure 7.8. The number of hidden layer neurons (*nm* in Figure 7.9) is chosen to be the same as the order of the state observer from the last section, i.e. 20.

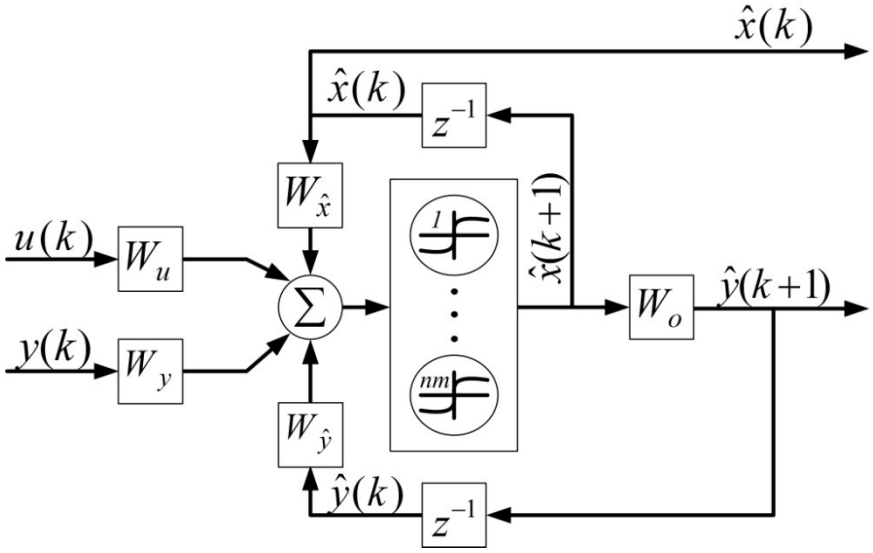

Figure 7.9 Full-order observer-inspired VG model network

The dynamic equation of the ANN in Figure 7.9 is given in (7.13). The non-linear elements in the hidden layer neurons are chosen as the hyperbolic tangent. This ensures

linear behavior at points near the origin, since the derivative of the hyperbolic tangent around the origin is 1.

$$\begin{aligned} \hat{x}(k+1) &= \hat{f}\left(W_{\hat{x}}\hat{x}(k) + W_u u(k) + W_y y(k) + W_{\hat{y}}\hat{y}(k)\right) \\ \hat{y}(k+1) &= W_o \hat{x}(k+1) \end{aligned} \tag{7.13}$$

The small-signal behavior of this model network around the origin is given by (7.14). If the weights of the network are initialized as prescribed in (7.15), then the small-signal behavior of the model network at initialization is guaranteed to match that of the linear observer in the previous section.

$$\begin{aligned} \Delta\hat{x}(k+1) &= W_{\hat{x}}\Delta\hat{x}(k) + W_u \Delta u(k) + W_y \Delta y(k) + W_{\hat{y}}\Delta\hat{y}(k) \\ \Delta\hat{y}(k+1) &= W_o \Delta\hat{x}(k+1) \end{aligned} \tag{7.14}$$

$$W_{\hat{x}} = A \qquad W_u = B \qquad W_y = L \qquad W_{\hat{y}} = -L \qquad W_o = C \tag{7.15}$$

This ANN structure and parameter initialization approach is an improvement over the heuristic ANN structure selection and random ANN parameter initialization approach taken in Chapters 4 and 5.

Non-linearities have not been accounted for, so the observer-based initialization proposed in this section only provides the starting point for the development of the model network. To account for non-linearities, the model network can be tuned further by solving the parameter optimization problem given by (7.16) and (7.17), which involves the minimization of the model network error over multiple operating conditions using time-domain data.

$$w^m = \left\{W_{\hat{x}}, W_u, W_y, W_{\hat{y}}, W_o\right\} \tag{7.16}$$

$$w^{m^*} = \underset{w^m}{\operatorname{argmin}} \left\{ \sum_{j=1}^{n_{o.p.}} \left(\frac{1}{n_s} \sum_{k=1}^{n_s} \left\| y_k^j - \hat{y}_k^j \right\|^2 \right) \right\} \tag{7.17}$$

Additional hidden layer neurons, feedback connections, etc, can potentially be added to enhance the capabilities of the model network. In such cases, it is possible to initialize all additional weights to be "very small" to preserve the small-signal properties of the model network at startup. Those additional weights would then be adjusted as the optimization in (7.17) progresses. In spite of these potential enhancements, the intelligent controller adaptation mechanism in the next section is known for being robust to modeling errors. Consequently, the model network does not need to be highly accurate and further tuning and modifications are postponed until later (if needed).

Figure 7.10 illustrates typical results obtained during time-domain simulations of the non-linear power system and the model network for a generic fault. Visual inspection of the one-step-ahead and five-step-ahead predictions provides insights into the ability of the model network to capture the input-output behavior of the VG-based representation of the system. During and shortly after the fault, the network is incapable of accurately estimating the system state, which results in poor estimates of the output. This is illustrated by the difference between the outputs of the model network and that of the actual system at 150 seconds in Figure 7.10. However, after the initial transients decay, the state estimate becomes accurate and the output estimates match the actual outputs from the system. This is the desired result, so the model network design stage can be considered successful.

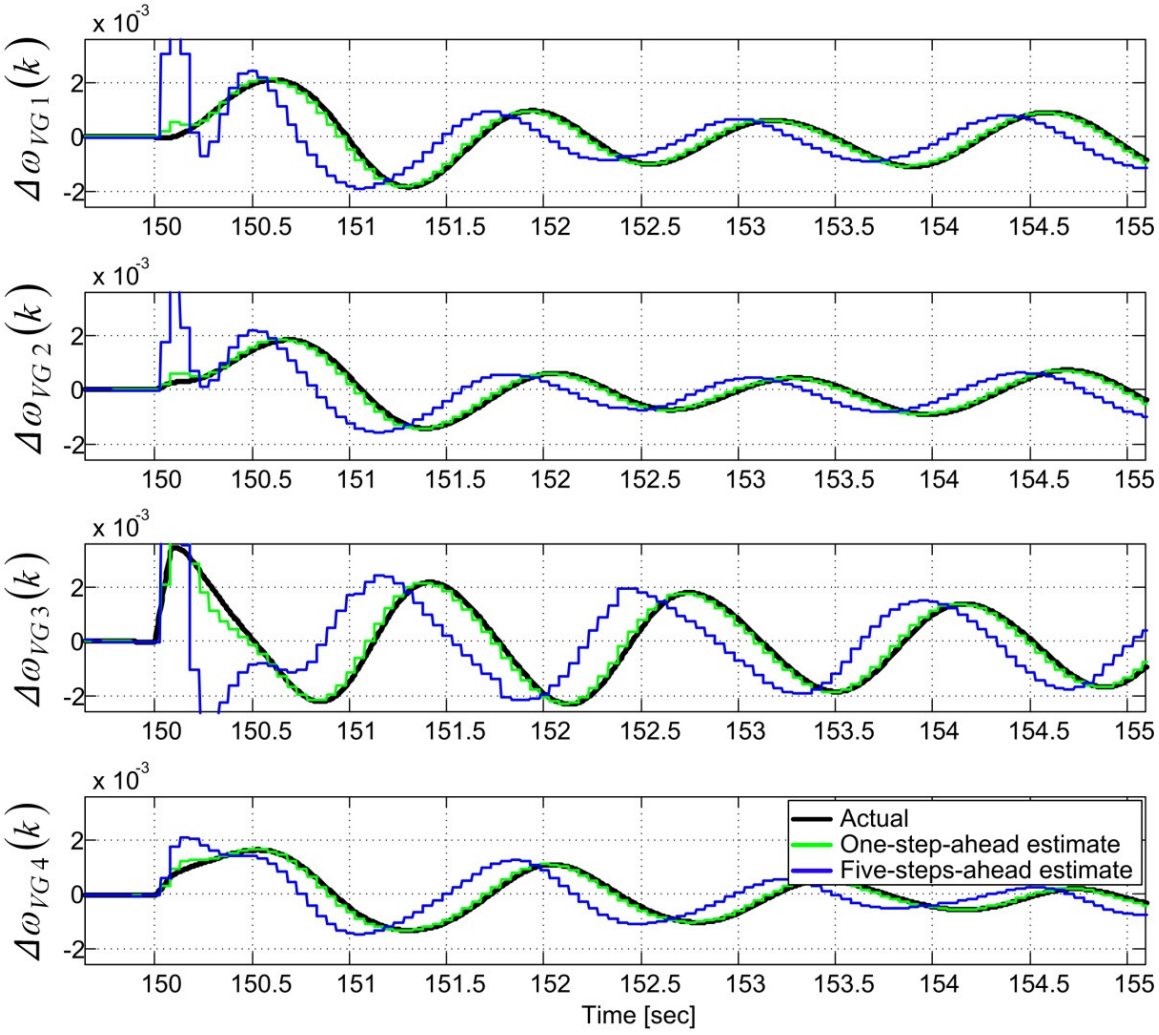

Figure 7.10 Time-domain waveforms of calculated VG speed deviations and step-ahead estimates for a generic disturbance

In the next section, the system to be controlled will be assumed to satisfy (7.18). Errors introduced by linearization, model-order reduction, system aggregation, imperfect measurements, etc, prevent this assumption from ever being satisfied. In fact, since the order of the full non-linear system is 1348 and that of the model network is 20, a match between the state estimate and the actual state is impossible. Recall that the state vector *x(k)* being estimated is an abstract construct with no direct relation to the real state variables in the power system. However, coherency-based aggregation ensures that this

abstract state vector captures the inter-area behaviors needed for wide-area damping control. Clearly, (7.18) represents a significant approximation and introduces substantial errors. However, results shown later in the chapter demonstrate that acceptable results can be obtained in spite of these modeling shortcomings.

$$\begin{aligned} \hat{x}(k) &\approx x(k) \\ \hat{x}(k+1) &= \hat{f}\left(\hat{x}(k), u(k), w^m\right) \approx f\left(x(k), u(k)\right) \end{aligned} \tag{7.18}$$

7.4 ADVANCED APPROXIMATE DYNAMIC PROGRAMMING

As mentioned in Chapter 5 , the intelligent control approaches pursued in this dissertation are based on approximate dynamic programming (ADP). There are multiple different approaches to implement ADP, but all of them share the goal of enabling controllers to "learn" from interactions with the system and approach optimality over time as they gain experience. This learning capability makes ADP-based controllers attractive to the application at hand, since it allows the controllers to adapt and remain effective even as the operating conditions of the power system change. In addition, the ability to adapt effectively in real-time can allow intelligent controllers to damp oscillations more aggressively in comparison to non-adaptive control schemes without sacrificing robustness, thereby avoiding the tradeoff between effectiveness and robustness illustrated in Chapter 3 (section 3.6).

ADP in the form of heuristic dynamic programming (HDP) was utilized in Chapter 5 . HDP is one of the most basic and simpler mechanisms to implement ADP, which justified its use in the preliminary investigations of Chapter 5 . However, there are other forms of ADP known to be more powerful and provide more effective controller adaptation compared to HDP. The increased effectiveness comes at the cost of higher

computational burden and complexity of implementation. A discussion of the different possibilities for implementing ADP can be found in [93]-[95]. Among them, dual heuristic programming (DHP) has been recognized as one that often strikes an appropriate compromise between complexity and effectiveness [95]. Therefore, in this chapter the HDP approach used in Chapter 5 is replaced by the DHP approach described next.

7.4.1 Overview of Dual Heuristic Dynamic Programming (DHP)

The goal of ADP is to enable controllers to "learn" from interactions with the system and approach optimality over time as they gain experience. A family of designs known as the adaptive critic designs (ADC) was developed by Werbos for this task in [93]. ACDs provide methods for obtaining on-line solutions of optimal control problems, with information that becomes available incrementally over time. The design equations for implementing DHP are reviewed next. The derivations shown next borrow heavily from [94]. Note that there is some overlap between the developments here and those shown in section (5.3).

DHP is a model-based approach, and so its development starts with the assumption that a sufficiently accurate model of the system to be controlled is available. The system's dynamic behavior is assumed to be governed by the discrete-time dynamic equation in (7.19). The index k corresponds to the discrete-time step.

$$x(k+1) = f(x(k), u(k)) \tag{7.19}$$

Clearly, the order and complexity of (7.19) for a large-scale power system are high. However, as mentioned in chapter 5 and in the previous section, it is possible to develop reduced-order models that greatly simplify complex systems while accurately

representing their dominant dynamic characteristics. Employing the VG and ANN-based abstract representations of the previous section significantly reduce the complexity of (7.19) without losing information necessary for effective wide-area damping control. With this approach, (7.19) becomes a differentiable model network of moderate complexity capable of representing the system's inter-area dynamics with acceptable accuracy as shown in the previous section. The internal state of this model network is then used as the state *x(k)* in (7.19). As a side note, it is worth mentioning that, in practice, researchers have found that ADP is capable of achieving acceptable control in spite of imperfect models in a variety of applications ranging from power system damping and dynamic power flow control to aircraft landing control [8]-[11], [109], [13], [48], [49], [63], [83], [95], [97].

Optimal control problems consist of minimizing a performance metric subject to the system dynamics. The metric to be minimized in the case of ADP is known as the cost-to-go function *J* and is defined in (7.20).

$$J(k) = \sum_{i=0}^{\infty} \gamma^i U\left(x(k+i), u(k+i)\right) \tag{7.20}$$

Solving this optimal control problem consists of finding a control policy such that the cost-to-go is minimized for all possible values of the state *x(k)*. An arbitrary control policy can be defined as in (7.21).

$$u(k) = \pi\left(x(k)\right) \tag{7.21}$$

Given a control policy, the cost-to-go function associated with it can be written as in (7.22), which can also be written in its recursive form as in (7.23).

$$J(x(k),\pi)=\sum_{i=0}^{\infty}\gamma^{i}U(x(k+i),\pi(x(k+i))) \tag{7.22}$$

$$J(x(k),\pi)=U(x(k),\pi(x(k)))+\gamma J(x(k+1),\pi) \tag{7.23}$$

Richard Bellman's principle of optimality [110] states that the optimal cost-to-go satisfies (7.24). Consequently, the optimal control policy satisfies (7.25) for all possible values of the state. The optimal cost-to-go results from the application of the optimal control policy as defined in (7.26).

$$J^{*}(x(k))=\min_{u(k)}\left\{U(x(k),u(k))+\gamma J^{*}(x(k+1))\right\} \tag{7.24}$$

$$u^{*}(k)=\pi^{*}(x(k))=\operatorname*{argmin}_{u(k)}\left\{U(x(k),u(k))+\gamma J^{*}(x(k+1))\right\} \tag{7.25}$$

$$J^{*}(x(k))=J(x(k),\pi^{*}) \tag{7.26}$$

Adaptive critic designs (ACDs) utilize two function approximation structures: a critic and an actor. Recall from Chapter 5 (section 5.3) that in HDP the critic is used to approximate the value of the cost-to-go *J*. In contrast, in DHP the critic is used to approximate the sensitivities of *J* to changes in the value of the state as defined in (7.27).

$$\lambda(x(k),\pi)=\frac{\partial J(x(k),\pi)}{\partial x(k)} \tag{7.27}$$

The actor is used to implement an appropriate control policy to be optimized over time. The mechanism to enable appropriate real-time adaptation of the critic network is presented next. The mechanism for adapting the action network follows.

7.4.2 Critic Network Equations – Cost-To-Go Estimation

An estimate of (7.27) given by the critic network is calculated as in (7.28). The critic network $c(x(k),\pi,w_l^c)$ is a differentiable ANN. The parameters (or weights) w_l^c of the

critic network are yet to be determined. The training iteration index l and the time interval index k are not necessarily equal. The goal during training iteration l is to improve the parameters of the critic network such that the estimates of the sensitivities of the cost-to-go at iteration $l+1$ are a better approximation of (7.27).

$$c\left(x(k),\pi,w_l^c\right)=\hat{\lambda}_l\left(x(k),\pi\right)\approx\lambda\left(x(k),\pi\right)\equiv\frac{\partial J\left(x(k),\pi\right)}{\partial x(k)} \tag{7.28}$$

Using the recursive form of the cost-to-go, (7.27) can also be written as in (7.29).

$$\begin{aligned}\lambda\left(x(k),\pi\right)&=\frac{\partial\left(U\left(x(k),u(k)\right)+\gamma J\left(x(k+1),\pi\right)\right)}{\partial x(k)}\\ \lambda\left(x(k),\pi\right)&=\frac{\partial\left(U\left(x(k),\pi(x(k))\right)+\gamma J\left(x(k+1),\pi\right)\right)}{\partial x(k)}\end{aligned} \tag{7.29}$$

Taking the partial derivatives prescribed in (7.29) results in (7.30) which can be used to guide the adaptation of the critic network in DHP. For convenience, (7.27) can be substituted into (7.30) to obtain (7.31).

$$\begin{aligned}\lambda\left(x(k),\pi\right)=&\frac{\partial U\left(x(k),u(k)\right)}{\partial x(k)}+\left[\frac{\partial\pi\left(x(k)\right)}{\partial x(k)}\right]^T\frac{\partial U\left(x(k),u(k)\right)}{\partial u(k)}\\ &+\gamma\left[\frac{\partial f\left(x(k),u(k)\right)}{\partial x(k)}\right]^T\frac{\partial J\left(x(k+1),\pi\right)}{\partial x(k+1)}\\ &+\left[\frac{\partial\pi\left(x(k)\right)}{\partial x(k)}\right]^T\left[\frac{\partial f\left(x(k),u(k)\right)}{\partial u(k)}\right]^T\frac{\partial J\left(x(k+1),\pi\right)}{\partial x(k+1)}\end{aligned} \tag{7.30}$$

$$\begin{aligned}\lambda\left(x(k),\pi\right)=&\frac{\partial U\left(x(k),u(k)\right)}{\partial x(k)}+\left[\frac{\partial\pi\left(x(k)\right)}{\partial x(k)}\right]^T\frac{\partial U\left(x(k),u(k)\right)}{\partial u(k)}\\ &+\gamma\left[\frac{\partial f\left(x(k),u(k)\right)}{\partial x(k)}\right]^T\lambda\left(x(k+1),\pi\right)\\ &+\left[\frac{\partial\pi\left(x(k)\right)}{\partial x(k)}\right]^T\left[\frac{\partial f\left(x(k),u(k)\right)}{\partial u(k)}\right]^T\lambda\left(x(k+1),\pi\right)\end{aligned} \tag{7.31}$$

In (7.31), the function *f(x(k),u(k))* governing the system dynamics is assumed known and differentiable. Also, the control policy *π(x(k))* is known, differentiable, and (at least for now) constant. The system model (model network), control policy (action network), and an initially random critic network (at $l = 0$) can be used to calculate an improved estimate of (7.27) using (7.32). This improved estimate becomes the target value used to improve the parameters of the critic network at each training iteration.

$$\begin{aligned}\hat{\lambda}_l^{\text{target}}\left(x(k),\pi\right) = &\frac{\partial U\left(x(k),u(k)\right)}{\partial x(k)} + \left[\frac{\partial \pi\left(x(k)\right)}{\partial x(k)}\right]^T \frac{\partial U\left(x(k),u(k)\right)}{\partial u(k)} \\ &+ \gamma\left[\frac{\partial f\left(x(k),u(k)\right)}{\partial x(k)}\right]^T \hat{\lambda}_l\left(x(k+1),\pi\right) \\ &+ \left[\frac{\partial \pi\left(x(k)\right)}{\partial x(k)}\right]^T \left[\frac{\partial f\left(x(k),u(k)\right)}{\partial u(k)}\right]^T \hat{\lambda}_l\left(x(k+1),\pi\right)\end{aligned} \tag{7.32}$$

The new set of critic network parameters is obtained by solving the parameter optimization problem defined in (7.33). A window of M data points is used for updating the critic parameters. For real-time adaptation, researchers typically set M to 1 and the optimization is completed at each time step. In such cases, the training iteration index l and the time step index k are the same. In contrast, in this research the size of the training window is selected heuristically to be between 10 to 50 samples long, and the optimization is not completed at each time-step but in regularly spaced intervals. The spacing of these intervals ensures that the training window is filled with M new data points each time the optimization routine is called. This setup improved learning during the simulation studies presented later in this chapter; however, no mathematical proofs have been completed at this time to support/justify this observation/selection.

$$w_{l+1}^{c} = \underset{w^{c}}{\operatorname{argmin}} \left\{ \sum_{i=1}^{M} \left\| \hat{\lambda}_{l}^{\text{target}}\left(x(k-M+i),\pi\right) - c\left(x(k-M+i),\pi,w^{c}\right) \right\|^{2} \right\} \tag{7.33}$$

The parameter optimization problem in (7.33) is solved using the scaled conjugate gradient algorithm from [80].

The critic adaptation algorithm based on (7.32) results in estimates of (7.27) that become more accurate over time. When coupled with the model of the system, these estimates can be used to generate control policies that improve over time and approach optimality. The mechanism for generating these control policies is described next.

7.4.3 Action Network Equations – Control Policy Optimization

The control policy is implemented as an ANN called the action network as defined in (7.34). The parameters (or weights) w_l^a of the action network are yet to be determined. The training iteration index *l* is the same as for the critic network. Starting from random initial weights (at *l = 0)*, the goal during training iteration *l* is to improve the parameters of the action network such that the control policy at iteration *l+1* moves closer towards optimality as defined in (7.25).

$$a\left(x(k), w_l^a\right) = \pi_l\left(x(k)\right) \tag{7.34}$$

The estimates of the cost-to-go sensitivities provided by the critic network are used to guide the adaptation of the action network. The cost-to-go resulting from an active sub-optimal control policy can be improved following the formulation in (7.35).

$$J_l^{improved}\left(x(k),\pi_l\right) = \min_{u(k)} \left\{ U\left(x(k),u(k)\right) + \gamma J\left(x(k+1),\pi_l\right) \right\} \tag{7.35}$$

This improved value of the cost-to-go is achieved by implementing the control action defined in (7.36). This control action can be used as the target for optimizing the parameters of the action network.

$$u_l^{\text{target}}(k) = \pi_l^{\text{target}}(x(k)) = \underset{u(k)}{\operatorname{argmin}} \{U(x(k), u(k)) + \gamma J(x(k+1), \pi_l)\} \tag{7.36}$$

The first order necessary condition for attaining the minimum in (7.35) and (7.36) at state *x(k)* is defined by (7.37). However, the exact sensitivities of the cost-to-go to variations in the state vector are not available, so the estimates provided by the critic are used instead as given in (7.38).

$$\frac{\partial J(x(k), \pi_l)}{\partial u(k)} = \frac{\partial U(x(k), u(k))}{\partial u(k)} + \gamma \left[\frac{\partial f(x(k), u(k))}{\partial u(k)}\right]^T \frac{\partial J(x(k+1), \pi_l)}{\partial x(k+1)} = 0 \tag{7.37}$$

$$\frac{\partial J(x(k), \pi_l)}{\partial u(k)} \approx \frac{\partial U(x(k), u(k))}{\partial u(k)} + \gamma \left[\frac{\partial f(x(k), u(k))}{\partial u(k)}\right]^T \hat{\lambda}_l(x(k+1), \pi_l) = 0 \tag{7.38}$$

Assuming critic estimates are accurate, (7.38) can be used in conjunction with an iterative numerical optimization algorithm such as gradient descent to find approximate solutions of (7.36). Here, this optimization is performed by updating the target action vector $u_l^{\text{target}}(k)$ iteratively along the gradient direction until (7.38) is approximately satisfied (sensitivities are close to zero). These solutions become the targets for training the action networks. A window of M data points is used for updating the action network parameters by solving the parameter optimization problem in (7.39). The scaled conjugate gradient algorithm is used again here to perform this optimization. The configuration of the data windows used for training the actor mirrors that used for the critic.

$$w_{l+1}^{a} = \underset{w^{a}}{\operatorname{argmin}} \left\{ \sum_{i=1}^{M} \left\| u_{l}^{\text{target}}\left(x(k-M+i)\right) - a\left(x(k-M+i), w^{a}\right) \right\|^{2} \right\} \tag{7.39}$$

Equations (7.32), (7.33), (7.36), (7.38), and (7.39) form the basis for the DHP intelligent controller adaptation algorithm. The details of the implementation of these equations for the work in this dissertation are given next.

7.4.4 DHP Implementation Details

The ANNs used to implement the critic and action networks are chosen to have the multi-layer perceptron (MLP) structure depicted in Figure 7.11 and Figure 7.12. MLPs are known to be universal function approximators, are differentiable, and effective training algorithms are available. These factors make them an acceptable choice for implementing the critic and action networks in DHP.

Each line in Figure 7.11 and Figure 7.12 corresponds to a weight (or parameter) to be updated at each training iteration. The inputs into these networks correspond to the state estimates generated by the model network from the last section. The number of hidden layer neurons for the critic and action networks (*nc* and *na* in Figure 7.11 and Figure 7.12 respectively) are design choices that define the complexity of the critic and action networks. More hidden layer neurons allow the networks to represent more complex functions, but result in higher computational complexity and can make the networks more difficult to train. Therefore, there is a tradeoff to be made in selecting these parameters. These are selected by intuition to be equal to the order of the model network here. The "correctness" of this choice is questionable, but simulation results shown in upcoming sections support it.

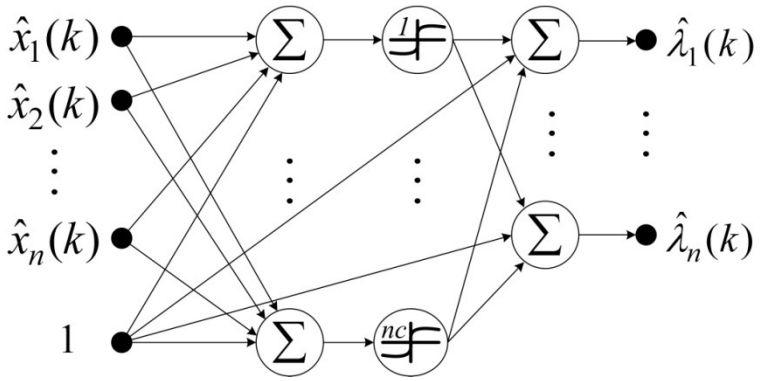

Figure 7.11 ANN implementing the critic network

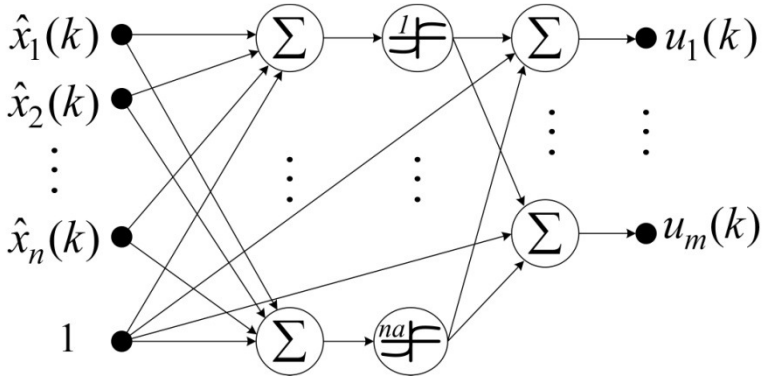

Figure 7.12 ANN implementing the action network

The iterative optimization of the critic and action networks is performed online following the approach given in Figure 7.13. Observe that the parameter optimization routines for solving (7.33) and (7.39) are not called at each iteration. Instead, they are called after training windows have been filled with "appropriate" sets of new data. An "appropriate" set of new data for the critic network is one generated using a single control policy. An "appropriate" set of new data for the action network is one generated using a single cost-to-go function. Consequently, the critic network is trained using M targets corresponding to a time interval during which the action network is held constant. Similarly, the action network is trained using M targets corresponding to a time interval during which the critic network is held constant.

Figure 7.13 assumes M = 10 for illustration purposes, but M = 20 was used to generate the results in this chapter. Anecdotal experience obtained throughout the course of this research supports the use of "data window-based" approaches over incremental ones which update networks at each iteration to improve the intelligent adaptation process. As mentioned before, no mathematical proofs have been completed at this time to support/justify this observation/selection.

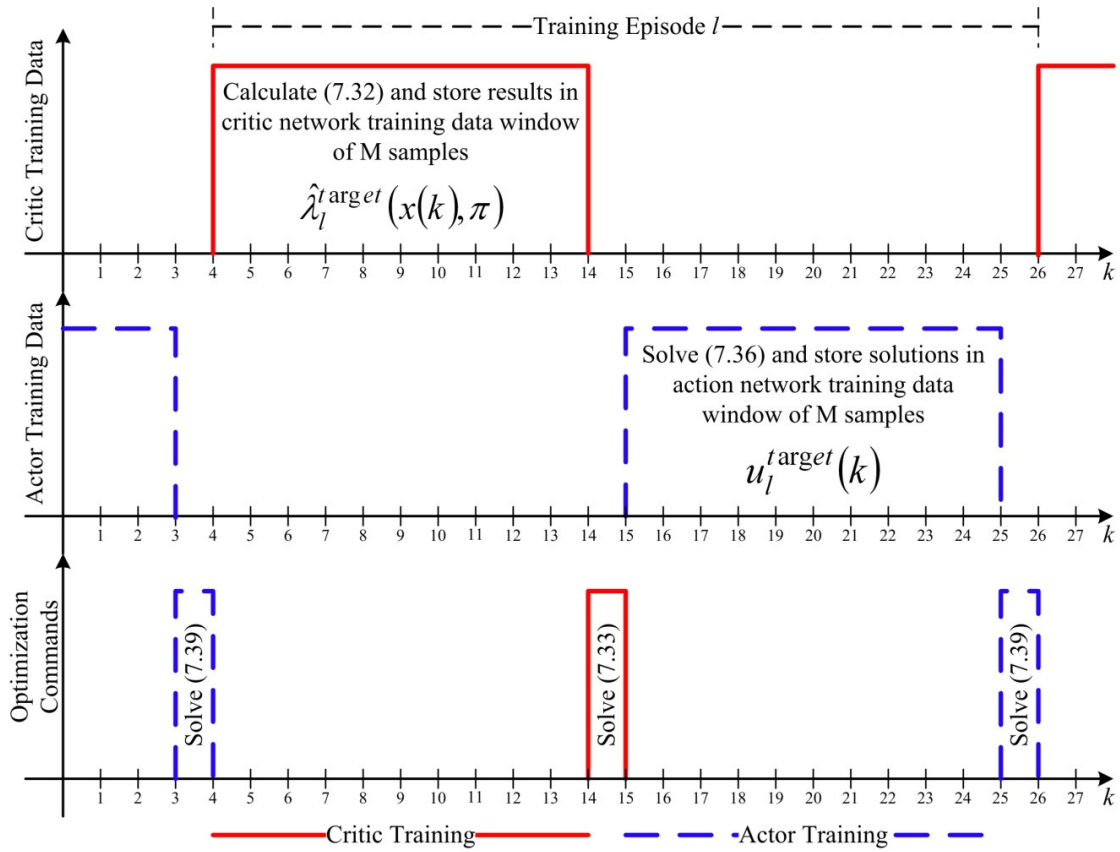

Figure 7.13 Data window-based online implementation of DHP

The DHP-based intelligent controller adaptation approach in this section provides the capability to generate control policies that improve over time and approach optimality by learning from experience. The details of the control approach resulting from combining aggregation techniques and intelligent control are summarized next.

7.5 FINAL AGGREGATION-BASED INTELLIGENT WIDE-AREA DAMPING CONTROLLER

The full aggregation-based intelligent wide-area damping controller (AB-IWADC) that results from integrating the VG-based power system representation with the DHP intelligent controller adaptation mechanism is illustrated in Figure 7.14. The model network estimates the system state using measurements from the system and the input signals generated by the action network. The action network utilizes this state estimate to calculate the control action needed to damp any oscillations at the output. The critic network utilizes the same state estimate to estimate the sensitivities of the cost-to-go function to changes in the state.

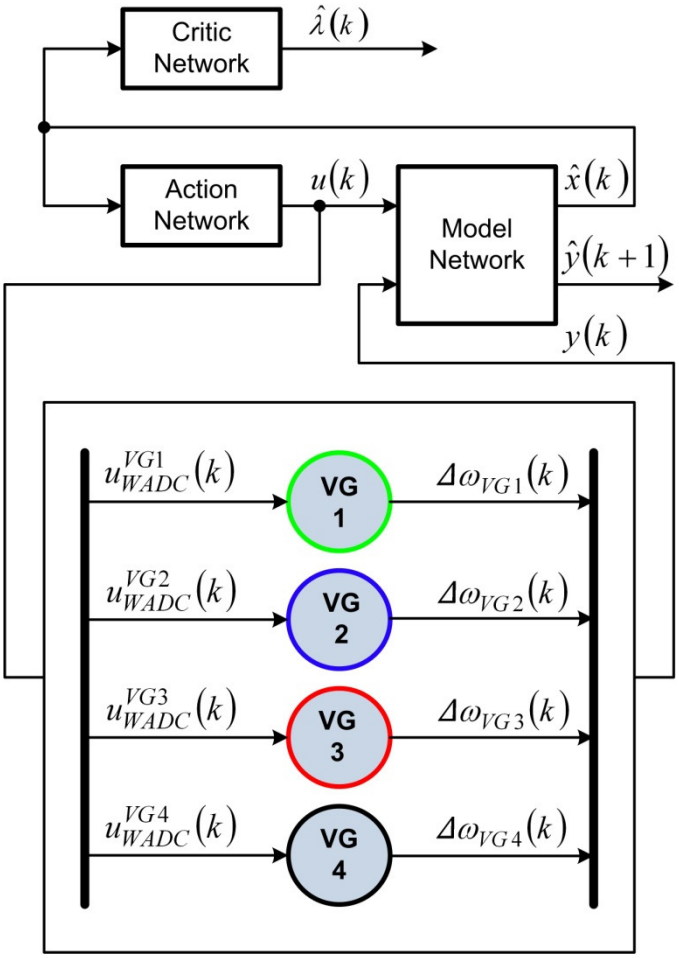

Figure 7.14 Coupling DHP and VG-based aggregate model to form an AB-IWADC

The ANN structures implementing the model, action, and critic networks are as described throughout this chapter. The parameters of these networks are provided in Table 7.1. The data window size for online adaptation of the critic and action networks was selected heuristically via simulation studies.

Table 7.1 ANN configuration for implementing the AB-IWADC

Parameter	**Model**	**Critic**	**Actor**
ANN Structure	Figure 7.9	Figure 7.11	Figure 7.12
Input signals	$u(k)$ $y(k)$	$\hat{x}(k)$	$\hat{x}(k))$
Number of inputs	8	20	20
Output signals	$\hat{x}(k)$ $\hat{y}(k+1)$	$\hat{\lambda}(k)$	$u(k)$
Number of outputs	24	20	4
Hidden neurons	20	20	20
Sampling rate	20 Hz	20 Hz	20 Hz
Non-linear element	Hyperbolic tangent	Hyperbolic tangent	Hyperbolic tangent
Calculations involved	(7.13) and (7.17)	(7.28), (7.32), and (7.33)	(7.34), (7.36), and (7.39)
Parameter initialization	Observer-based	Random	Random
Training approach	Parameter optimization using time-domain data	Real-time using data windows as in Figure 7.13	Real-time using data windows as in Figure 7.13
Online adaptation	None	Every 2 seconds	Every 2 seconds
Training data points	None	20 samples (1 second worth of data)	20 samples (1 second worth of data)
Conditions for training	None	Small random load variations and larger disturbances	Small random load variations and larger disturbances

The interface between the controller and the system is made through the virtual generators following the configuration in Figure 7.15. The output aggregation stage consists of the VG calculation. An advanced input disaggregation stage has not been developed at this time, so each generator within a group receives an identical wide-area damping control signal instead.

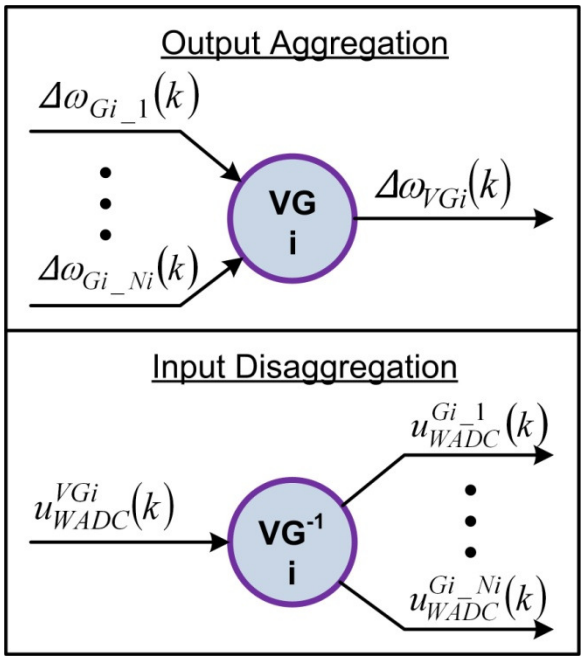

Figure 7.15 Output aggregation and input disaggregation using a VG

The utility function $U(\cdot)$ in (7.20) to be minimized over time follows the definitions in (7.40). The matrix C is the output matrix of the linearized model used to initialize the model network. A controller that minimizes (7.40) over time minimizes deviations of the VG speeds without excessive control action. Minimizing these deviations also minimizes inter-area oscillations, since the VG-speeds highlight inter-area oscillations and discards local ones. The VG-speeds are passed through a washout filter stage to ensure that the AB-IWADC does not respond to constant or very slow speed deviations not associated

with oscillatory stability. The input signals generated by the action network are passed through a low-pass filter stage prior to being sent to the excitation system at generators. This eliminates high frequency (20 Hz) components introduced by sampling from entering the system. The scalar weights c_y and c_u are selected by trial and error. The dimensions of the identity matrix I are selected appropriately.

$$\begin{gathered} U(x(k),u(k)) = x(k)^T Qx(k) + u(k)^T Ru(k) = y(k)^T Q' y(k) + u(k)^T Ru(k) \\ Q = C^T Q' C \\ Q' = c_y I \\ R = c_u I \\ c_y = 100 \qquad c_u = 1 \qquad I = \begin{bmatrix} 1 & \cdots & 0 \\ \vdots & \ddots & \vdots \\ 0 & \cdots & 1 \end{bmatrix} \\ \gamma = 0.95 \end{gathered} \tag{7.40}$$

With this choice of utility function, the parameters of the critic and action networks can be initialized in a fashion similar to that used for the model network. Optimal control theory can be used to calculate a full-state feedback linear quadratic regulator for the linear system used to design the model network as illustrated in Appendix F. The gain of this controller and the solution of the Ricatti equation associated with it can then be used to initialize the action and critic networks respectively. This was not done in this dissertation, but it can be useful for control applications where starting with random initial action and critic networks is not acceptable. The steps for completing this improved initialization are provided in Appendix F.

The effectiveness and robustness of the AB-IWADC is demonstrated next using time-domain simulations.

7.6 EVALUATION OF THE EFFECTIVENESS OF THE AB-IWADC

This section has two main objectives. First, it evaluates whether the AB-IWADC proposed in this dissertation can significantly enhance the rotor-angle stability of a large-scale power system. Second, it evaluates whether the online learning mechanism discussed earlier is effective enough to make the AB-IWADC robust to significant changes in the system dynamics. These two objectives are accomplished by the procedure outlined below.

7.6.1 Evaluation Procedure

The non-linear and time-varying nature of the system and the AB-IWADC together require the use of time-domain simulations to complete these objectives above. The flow chart in Figure 7.16 illustrates the steps followed to complete these evaluations.

Robustness must be evaluated using extensive time-domain simulation studies involving different disturbances over a large set of operating conditions. However, time-domain simulations of large-scale non-linear systems are time consuming and complex. The relatively small set of 38 operating conditions obtained in section 6.5 is thus used. This set consists of critical single-line contingencies, inter-area power flow changes, and combinations thereof, and spans the system's behavior over a larger set of 250 critical operating conditions designed specifically to reduce rotor-angle stability. The set of disturbances consisted of 50 ms self-clearing three-phase faults, one at a time, at multiple locations across the system. The locations chosen span the geography of the system, so they can be expected to excite all oscillations present in the system. Evaluating the performance of the AB-IWADC over this set of operating conditions and disturbances gives a relatively broad perspective of its robustness and effectiveness.

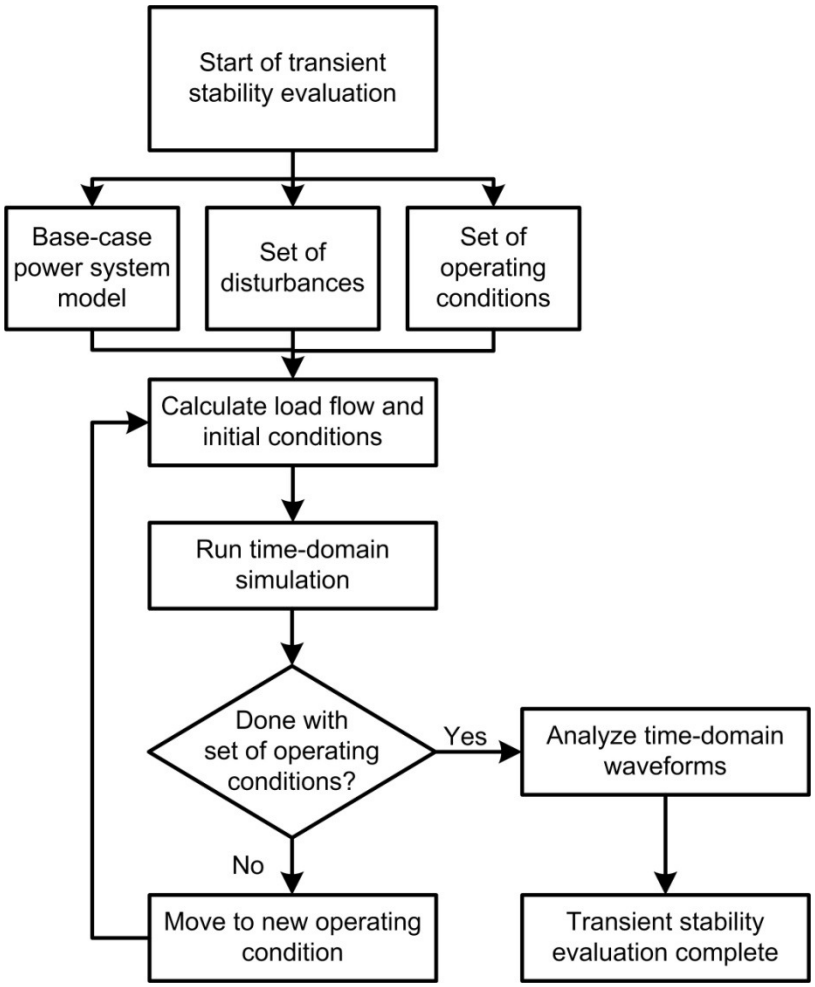

Figure 7.16 Steps for multi-operating transient stability evaluation

7.6.2 Benchmark Linear Controller for Comparisons

Comparisons are made against an aggregation-based linear quadratic regulator (AB-LQR) designed considering 38 reduced-order linearized models corresponding to each of the operating conditions discussed above. The design of this AB-LQR controller is discussed in Appendix F. Similarly to the designs in Chapter 3, a compromise has to be made between effectiveness and robustness. Eigenvalue plots in Appendix F demonstrate that this AB-LQR has been properly designed to be robust and effective, at least in the linear sense, since it is capable of providing adequate damping for the critical inter-area

modes for all 38 linearized models. This makes the AB-LQR an adequate benchmark to evaluate the effectiveness of the AB-IWADC. Often, robust damping controllers designed using linearized models of power systems require further tuning once deployed in the full non-linear system [60]. However, there is no clear path to complete such tuning and so this step is not completed for the AB-LQR here.

Some important additional details about the time-domain simulations are given next for the interested reader. The simulation results follow.

7.6.3 Additional Details on the Time-Domain Simulation Studies

Load variations are added to 5 geographical areas across the system: Sao Paulo, Goias/Brasilia, Minas Gerais, Rio de Janeiro, and Parana/Santa Catarina. The variations consist of pseudo-random injections at the 5 highest loads in each area, and each load varies ±2% of its initial load flow value. A total of 25 random loads are therefore added to the power system model. Different random signals are added at each location. These random loads simulate the continuous load and generation variations characteristic of real-world power systems, and excite oscillations across the system which the AB-IWADC learns to damp out. These learning opportunities will undoubtedly be available in real power systems, so acceptable online learning under these conditions would illustrate the effectiveness of DHP for implementing adaptive power system damping controls.

The simulation is completed using a fixed integration time-step of 5 ms and the random sequences added to each load are repeated each time the simulation is run. This allows better comparison and interpretation of results and makes the simulations reproducible.

The effects of measurement delays and noise have not been considered, but will need to be evaluated prior to real-world deployment of an AB-IWADC.

The weights of the action and critic networks are set to small random values at the start of each simulation run. Therefore, the AB-IWADC is forced to learn an appropriate set of actor and critic parameters at each operating condition. The results can therefore demonstrate the learning capabilities of the controller and prove that acceptable damping performance can be achieved by online learning alone.

7.6.4 Simulation Results

The simulation results in this section are provided for the following 3 cases:

1. *Case 1 – base case (BC):* Original model presented in Chapter 6 with no additional damping controls. The model for this case does contain a large number of conventional power system stabilizers across the system.
2. *Case 2 – aggregation-based linear quadratic regulator case (AB-LQR):* Original model modified to include the AB-LQR designed in Appendix F.
3. *Case 3 – aggregation-based intelligent wide-area damping controller case (AB-IWADC):* Original model modified to include the AB-IWADC designed in this chapter.

The number of signals, variables, etc., for the Brazilian national interconnected system (SIN) is large; therefore, providing all encompassing sets of plots of the time-domain response of the system is not an option. Consequently, only a few carefully selected plots are shown. A much larger set of variables than shown here were monitored during all the simulation studies. The signals chosen provide good insights into the

behavior of the system as a whole. A total of 38 time domain simulations are run for each case above, i.e. a total of 114 simulations.

As mentioned in Chapter 2, rotor-angle stability can be sub-divided into two main categories: small-signal stability, and transient stability. Small-signal stability refers to the response of the system to small perturbations such as the random load changes described before. Typically, this form of stability is studied using eigenvalue. However, at this point there is no clear approach to complete such an analysis once the AB-LQR or the AB-IWADC are added. Therefore, simulations of the system's time-domain response to small perturbations are used instead. Transient stability refers to the response of the system to large disturbances such as faults and transmission line openings. These are typically studied using time-domain simulations as in this section.

The inter-area active power flow from the Southeast to the South of the SIN is chosen to illustrate the small-signal performance of the AB-LQR and the AB-IWADC. Figure 7.17 shows the direction and boundary that defines this flow.

The time-domain behavior of this flow for the 38 operating conditions is plotted in Figure 7.18. Only the inter-area active power flow defined above is plotted in the Figure 7.18. Each different waveform corresponds to a different operating condition. The colors indicate different flow levels: normal (green), medium (blue), and high (red).

The BC system with no contingencies is stable at all flow levels tested. However, once the contingencies are considered, the BC system develops growing inter-area oscillations and eventually synchronism is lost. Consequently, the system is not capable of surviving all possible single contingencies when the inter-area flows are high. This makes rotor-angle stability a limiting factor for the system operator if the system is

operated under an N-1 contingency criterion, under which the system must be capable of surviving all possible single contingencies. In contrast, these oscillations remain sufficiently damped with the AB-LQR and with the AB-IWADC and rotor-angle stability is maintained for all line contingencies considered. The AB-LQR and AB-IWADC are therefore capable of enhancing the safe operating region of the system and have the potential to enable increased utilization of transmission assets.

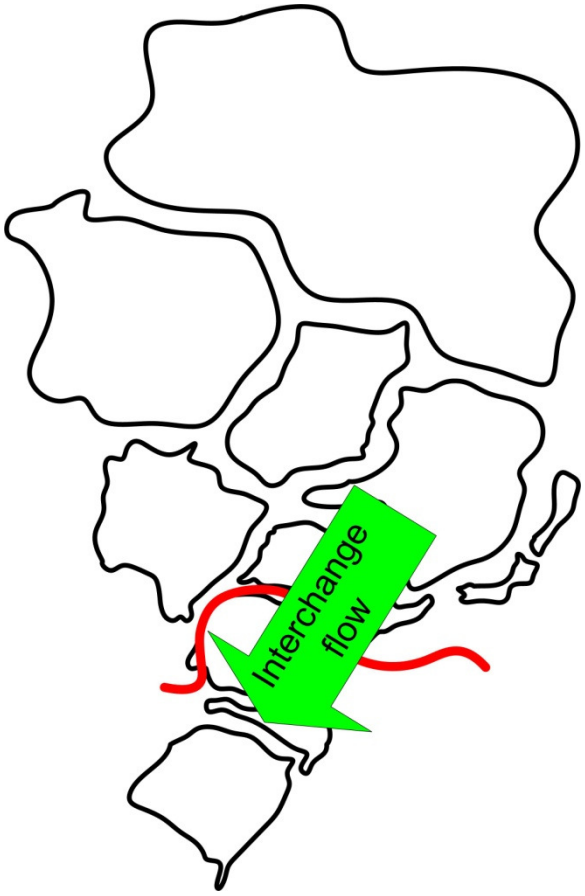

Figure 7.17 Direction and boundaries of active power interchange flow signal

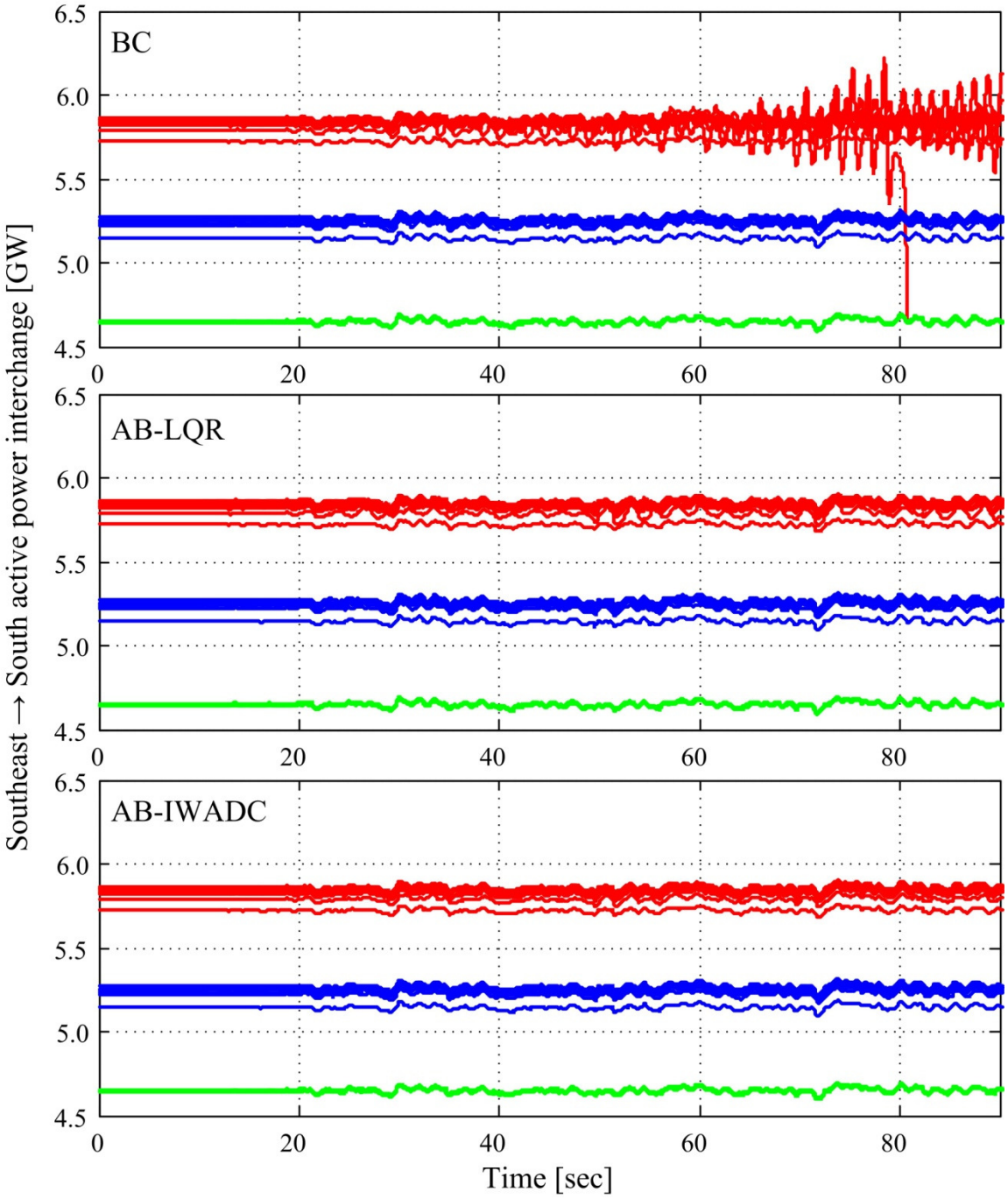

Figure 7.18 Power interchange from the Southeast to the South with small random load variations at critical operating conditions

The speeds of the 4 virtual generators from section 7.2 are chosen to illustrate the performance of the controllers in terms of transient stability. Simulations are run for all

38 operating conditions; however, only two sets of simulation results showing different tendencies observed during the study are reviewed next.

The system's oscillatory behavior in response to a self-clearing three-phase fault in a long line interconnecting two areas is illustrated in Figure 7.19. For this operating condition, the system is operating under medium flow (blue in Figure 7.18) and it is stable with or without wide-area damping controls. However, oscillations decay faster with the AB-LQR and with the AB-IWADC.

The system's response to the same disturbance while operating with a high flow is illustrated in Figure 7.20. This time the system becomes unstable without additional control and synchronism is eventually lost due to growing inter-area oscillations. In contrast, the AB-LQR and the AB-IWADC are both capable of damping these oscillations and the system remains stable. Similar results were obtained for all 38 operating conditions tested, which demonstrates the effectiveness of these controllers. The performance of the AB-LQR is comparable to that of the AB-IWADC and the damping of inter-area oscillations is similar with both control schemes. This is a testament of the robustness of the AB-LQR and the AB-IWADC.

These results confirm the effectiveness of DHP for online adaptation of an aggregation-based damping controller. Also, by considering a relatively small but appropriately chosen set of operating conditions during the design stage, conventional linear controllers can be made effective and robust. However, it is impossible to consider all or even most of the operating conditions a power system might experience. Consequently, once controllers get deployed in an actual system, they are almost guaranteed to enter into operating regimes not considered during the design stage.

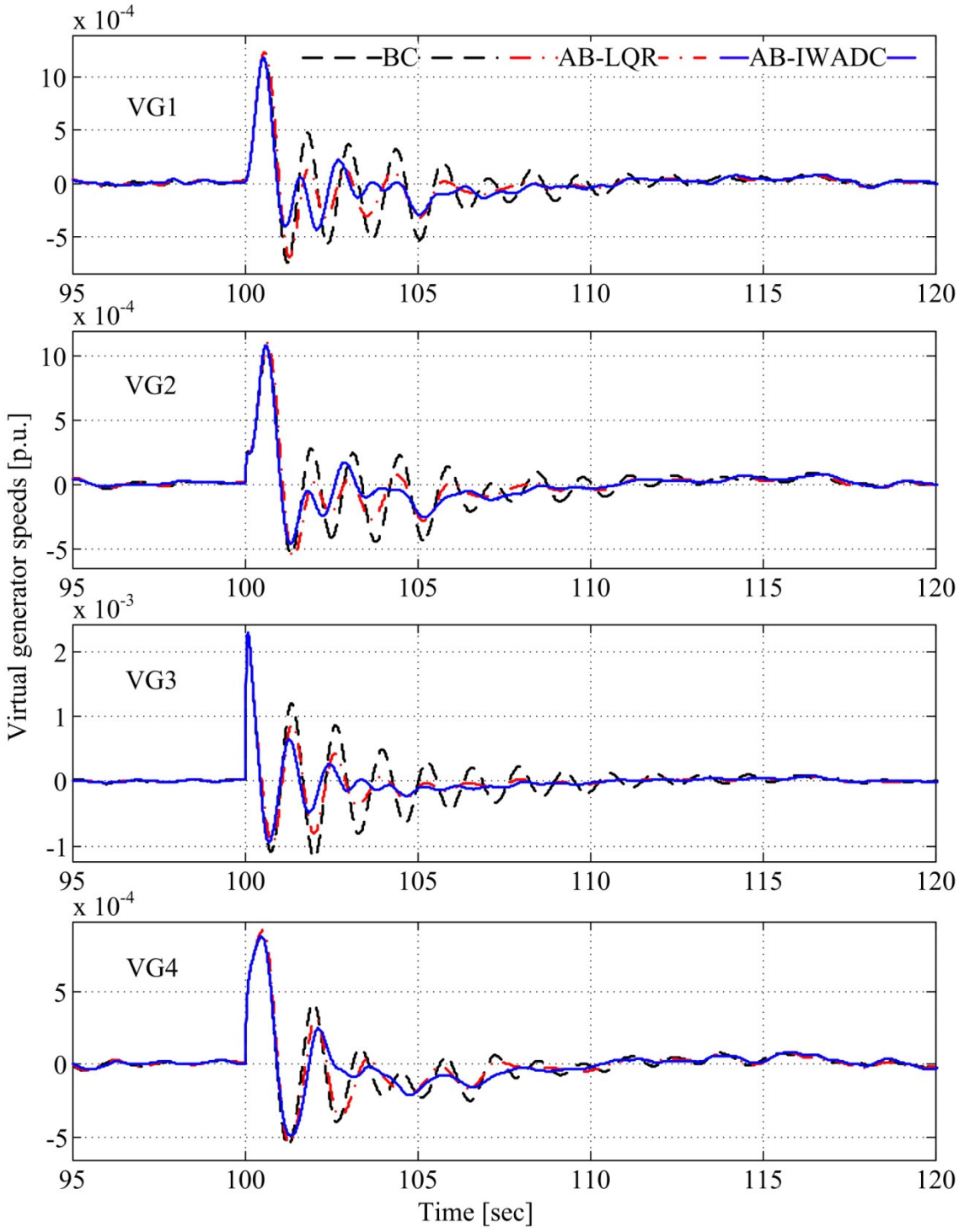

Figure 7.19 Comparisons of virtual generator speeds for a 50 ms self-clearing three-phase fault while operating without a critical line and with medium inter-area transfers

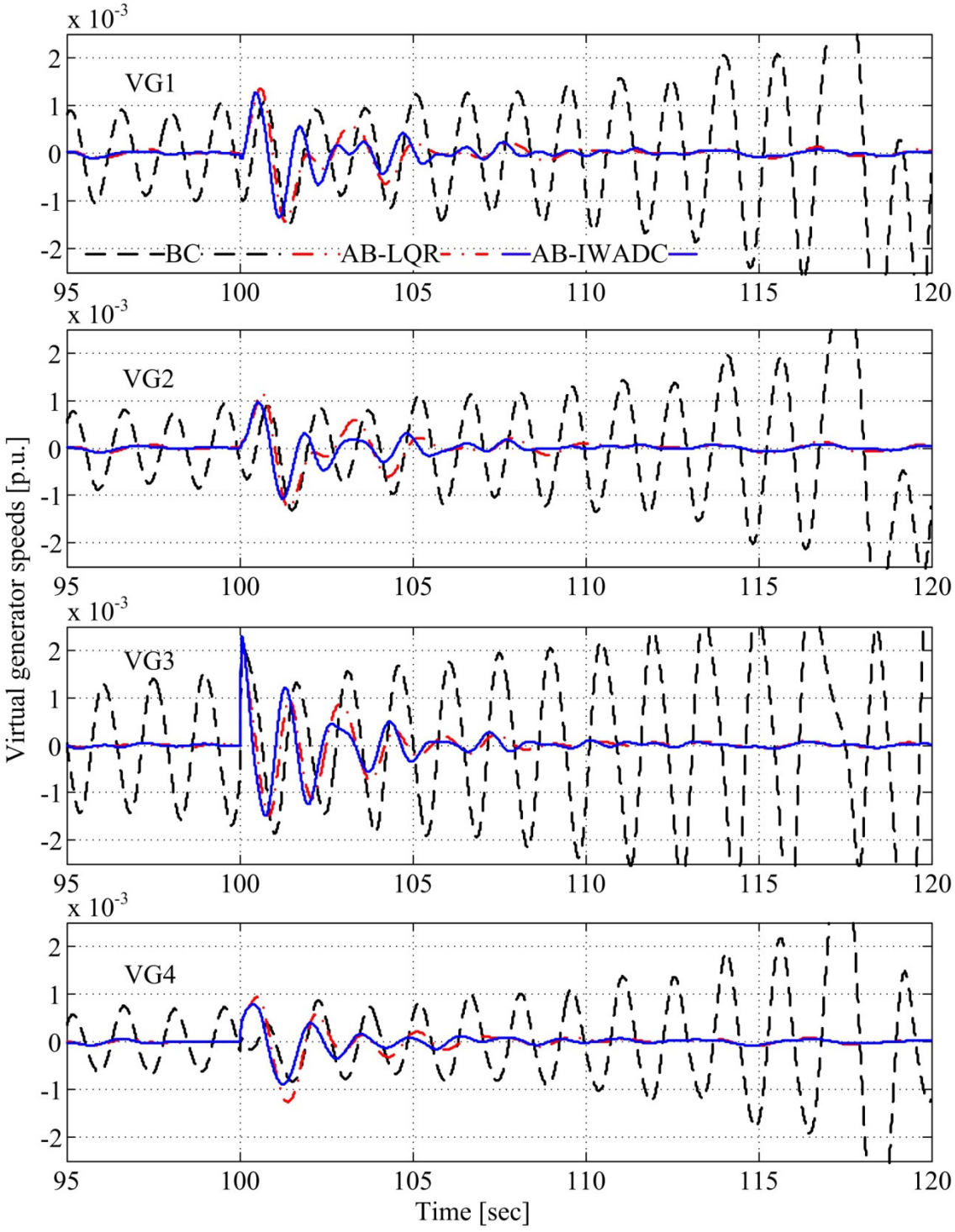

Figure 7.20 Comparisons of virtual generator speeds for a 50 ms self-clearing three-phase fault while operating without a critical line and with high inter-area transfers

A small set of additional operating conditions not considered during the design of the AB-LQR and the AB-IWADC was developed to illustrate the importance of controller adaptation. These conditions were designed to be even more challenging than those used before in terms of rotor-angle stability. The set includes some critical double-line contingencies. The parameters of the AB-LQR were left unchanged during these additional evaluations. The only parameter changes for the AB-IWADC consisted of online adaptation of the weights of the action and critic networks. No other tuning/modifications were made to the DHP algorithm or to the ANNs implementing the model, action, and critic networks.

The system response to two of these additional operating conditions is illustrated in Figure 7.21 and Figure 7.22. The performance degradation suffered by the AB-LQR is clear. In Figure 7.21, the AB-LQR provides additional damping after an initial single-line contingency at time 100 seconds. Once a second contingency occurs at time 120 seconds, this controller becomes detrimental to oscillatory stability, increases the amplitude of some of the oscillations and reduces their damping. This is the opposite of the desired effect. In contrast, the AV-IWADC maintains a similar level of performance and enhances stability even after the second contingency. In Figure 7.22, the AB-LQR is unable to help the system reach a new stable operating condition and synchronism is lost. Once again, the AB-IWADC adapts to the new operating condition and helps the system remain stable. These simulations serve as a clear indicator of the importance of adaptation and demonstrate the effectiveness of DHP for intelligent damping control.

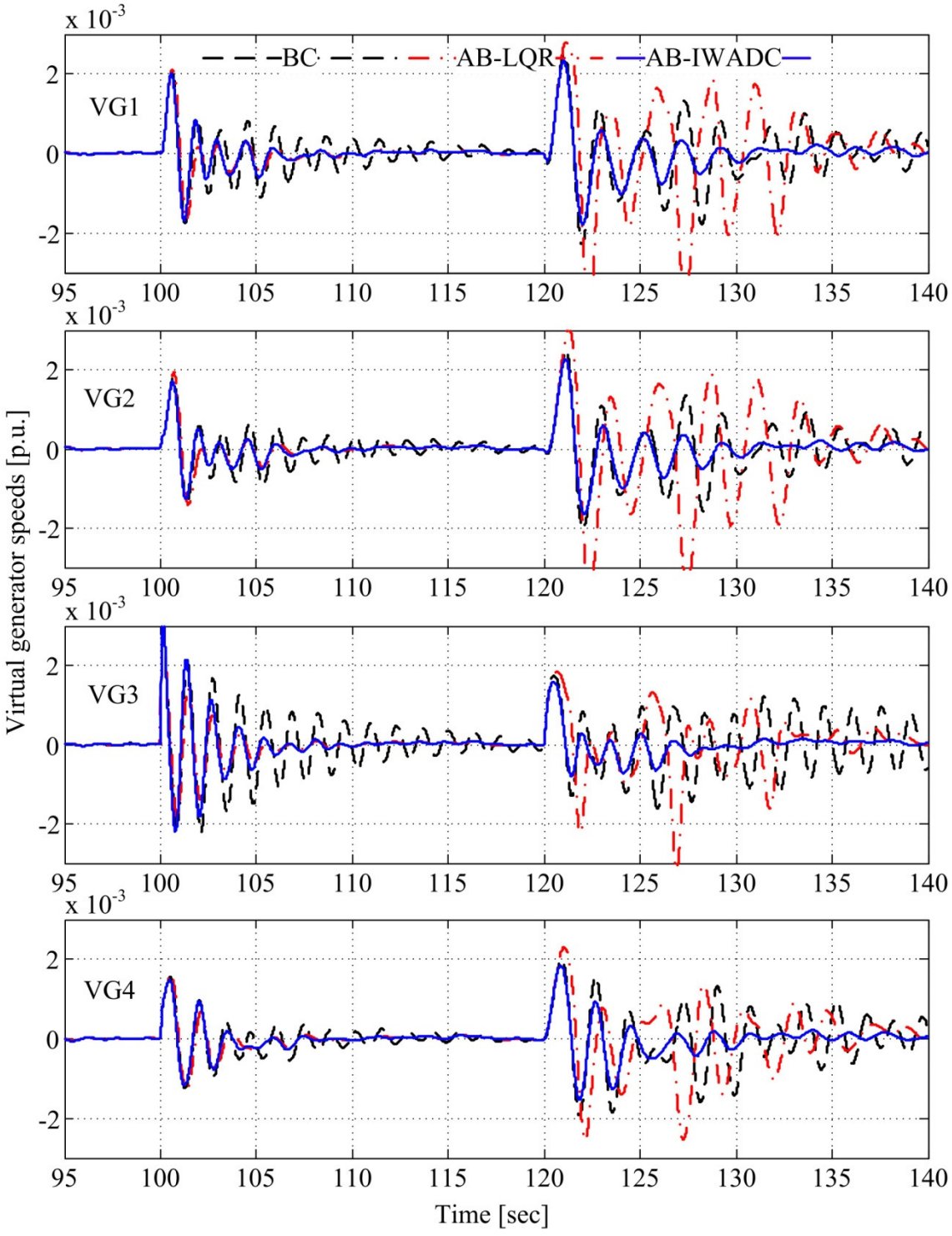

Figure 7.21 Comparisons of virtual generator speeds for a 80 ms three-phase fault cleared by opening a critical line followed by an additional opening of a parallel line (double-line contingency)

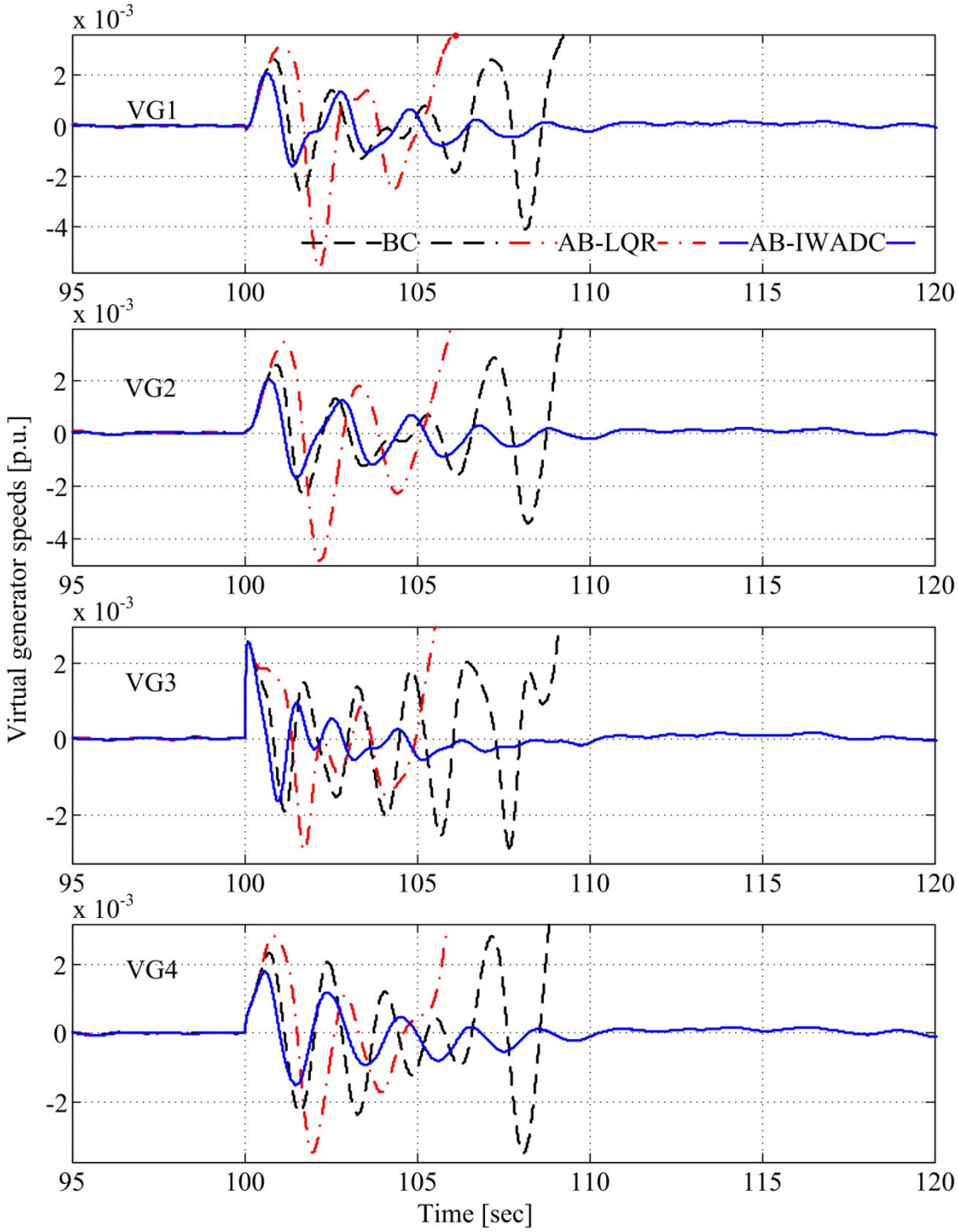

Figure 7.22 Comparisons of virtual generator speeds for an 80 ms three-phase fault cleared by opening two critical parallel lines while operating with high inter-area transfers

At this point it is possible to summarize the framework for designing holistic aggregation-based intelligent wide-area damping controllers for large-large scale power systems.

7.7 PROPOSED AB-WADC DESIGN FRAMEWORK

The ideas explored throughout this dissertation can be integrated into a cohesive framework for designing aggregation-based wide-area damping controllers for large-scale power systems. The proposed framework is illustrated in Figure 7.23.

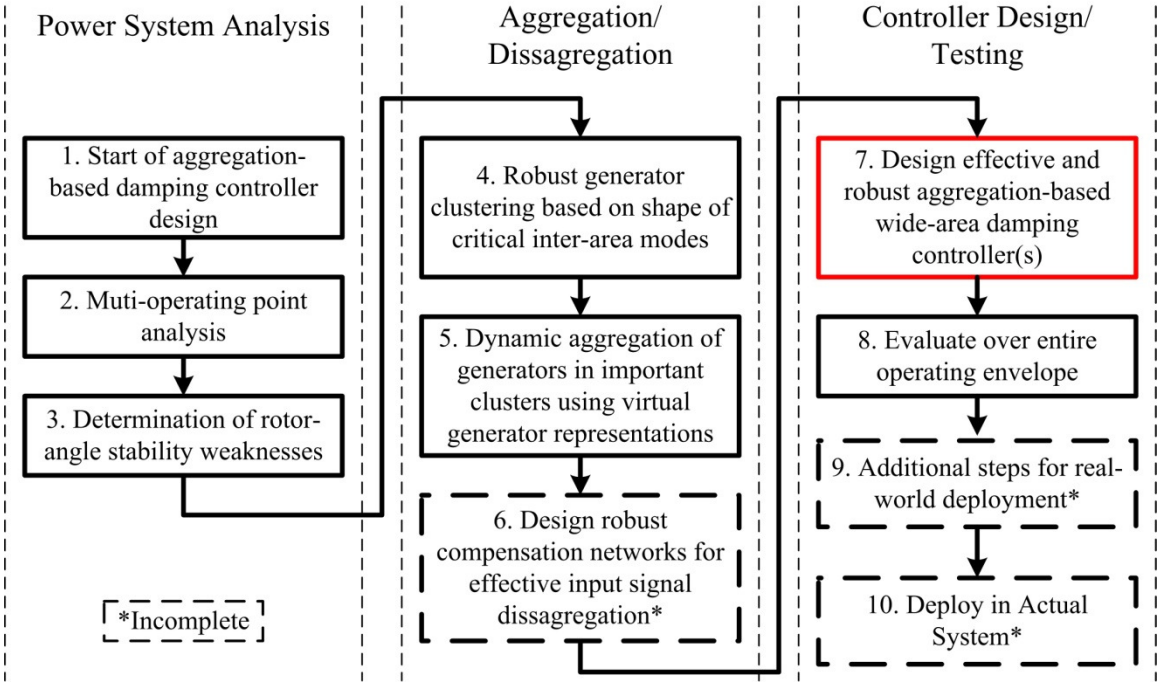

Figure 7.23 Framework for designing AB-WADC for large-scale power systems

The steps composing the framework have been described in detail throughout the dissertation and are summarized here:

1. Start with a full non-linear model of the power system to be controlled. The system is assumed to present poor rotor-angle stability in the form of poorly damped inter-area oscillations at certain operating conditions.
2. Obtain linearized models of the system in 1 at a large number of credible operating conditions. The number of operating conditions considered must span the actual or desirable set of operating conditions for the actual system. Experience obtained during actual operation and through planning studies should be exploited while selecting the operating conditions to analyze. The chosen set can become extremely large. The gap-metric-based automatic operating point selection scheme can be used to eliminate operating conditions that are "redundant" in terms of rotor angle stability.
3. Utilize the linearized models from step 2 to determine the weaknesses of the system in terms of rotor angle stability. The focus is on determining conditions that result in poorly-damped inter-area oscillations. The set of critical inter-area modes is determined in this step using eigenvalue plots and mode shapes.
4. Utilize the mode shapes of the critical inter-area modes from step 3 to determine robust clusters of generators that invariably swing together in the inter-area modes.
5. Utilize the generator cluster from step 4 to create VG-based aggregate representations of the power system. These aggregate representations can also be applied one or more of the linearized models from step 2 to initialize the model network. Further training/tuning of the model network can be

completed if deemed necessary. The resulting aggregate linear models can also be used for designing other types of controllers (optimal, robust, etc.) in the step 7.

6. Design robust compensation networks to improve input disaggregation and enhance the effectiveness of aggregation-based controls. This step has not been developed at this point, but more details on will be provided when discussing future research directions.
7. Design a robust aggregation-based controller capable of damping the critical inter-area oscillations in the system. This design is completed using ADP in the form of DHP in this dissertation, but other control design schemes can also be applied. An example of more classical yet effective design methodology is given in Appendix F.
8. Evaluate the controller designed in step 7 over the operating conditions determined in step 3 and ensure that appropriate improvements are obtained. If the performance is unsatisfactory, it might be necessary to return to steps 4-7 to improve the design. Some of the possible causes for poor performance include: poor generator clustering and erroneous dynamic aggregation, poor modeling of the aggregate system, lack of robust disaggregation networks, or poor controller design. Poor model and controller designs are most likely to result in poor performance.
9. Consider effects such as the effect of time delays, loss of communications, noise, etc., on the performance of the closed loop system. This step is critical

and not trivial when considering real-world deployment, but remains incomplete at this time.

10. Actual deployment. This step can be expected to be the most difficult and will only be pursued if substantial economic benefits are expected. Increased transfer capabilities and higher reliability are the most likely sources of such benefits. An exhaustive economical analysis would need to be completed to determine if the costs/benefit relation justify deployment. This analysis has not been considered in this dissertation.

The details of steps 1-3 are provided in Chapter 6. Steps 4-8 are described in this chapter. Simulation results in the previous section illustrate that intelligent damping controllers designed using this framework are effective and robust. These can significantly improve rotor-angle stability in large scale power systems over a large set of operating conditions.

7.8 SUMMARY

This chapter refined the ideas of aggregation-based control, artificial neural network-based modeling, and approximate dynamic programming-based intelligent adaptive control from previous chapters. These ideas where then integrated into a step-by-step framework for designing controllers capable of significantly improving the rotor-angle stability of large-scale power systems over a large set of operating conditions.

The generator coherency-based grouping and aggregation step was enhanced by improving the coherency identification mechanism. By considering multiple operating points and mode shapes instead of time-domain simulations, it was possible to group generators based on their tendency to swing together over the critical inter-area modes at

all operating conditions considered. This makes the grouping robust, a feature needed for robust coherency aggregation-based control.

The artificial neural network modeling step was enhanced using linearized models of the power system. Reduced-order input-output linear models of the system were used to determine an appropriate size and structure for the model network and to initialize its weights. This improved initialization simplifies the development of the model network.

The heuristic dynamic programming (HDP) approach followed in the preliminary application in Chapter 5 was upgraded to dual heuristic programming (DHP). DHP is known to be a more effective parameter adaptation mechanism and strikes an acceptable compromise between complexity and effectiveness.

The simulation results in this chapter clearly showed the improvements in rotor-angle stability that can be achieved using aggregation-based wide-area damping control. Extensive time-domain simulations over a large set of operating conditions showed that these controllers can be highly effective and robust. A linear controller designed using classical optimal control theory demonstrated the flexibility of the design framework proposed. Arguably, any controller design approach (robust, optimal, non-linear, adaptive, etc.) could be integrated into the framework with little difficulty. The simulations also illustrated how intelligent adaptation can be used to tackle the need for robustness.

Multiple critical steps are still missing and will need to be resolved for an aggregation-based power system damping controller to be deployed in a real power system. A brief discussion on some of these missing steps and the conclusion of this dissertation are provided in the next chapter.

CHAPTER 8 CONCLUSIONS, CONTRIBUTIONS, AND RECOMMENDATIONS FOR FUTURE WORK

8.1 CONCLUSIONS

The work in this dissertation resulted in a framework for designing wide-area damping controllers capable of improving rotor-angle stability of large-scale power systems. Controllers designed using this framework can be expected to be robust and highly effective at damping low-frequency inter-area oscillations known to emerge when power systems are operated under stressed conditions. These oscillations can limit economically beneficial power transfers among distant areas in large interconnected systems, and if left unchecked, they can result in wide-spread blackouts.

A review of the literature in Chapter 2 pointed to wide-area damping control (WADC) as a more effective way to damp inter-area oscillations compared to conventional power system stabilizer (PSS) technology. WADCs are controllers that utilize input and output signals to and from distant locations across a power system. Among the different possibilities for WADC, holistic designs were suggested to offer higher potential for damping control. A holistic controller was characterized as having a high input and output signal count compared to the minimalist designs typically pursued in the literature. It was argued that taking a higher number of measurements and injecting a higher number of signals from and into the system would allow controllers to be highly effective. The review also pointed to the need for robustness when designing wide-area damping controls WADCs, and to the importance of having a control approach that makes controllers less susceptible to communication delays and signal loss.

A design methodology capable of optimizing the parameters of multiple "conventional" PSSs and minimalist WADCs in a coordinated fashion was proposed in Chapter 3. Preliminary investigations using that methodology pointed to the compromise in damping performance that often needs to be made for WADCs to become robust to changes in a power system's operating condition.

Chapter 4 explored the potential improvements to be obtained by pursuing holistic designs. Observability, controllability, and sensitivity measures were calculated for critical inter-area modes in a sample system over a large number of operating conditions. The results pointed that minimalist approaches to WADC might not provide the capabilities needed to significantly improve rotor-angle stability over a large number of power system operating conditions. These limitations can potentially be overcome using holistic controls.

Multiple works in the literature have demonstrated that intelligent WADCs (IWADCs) based on artificial neural networks (ANNs) and approximate dynamic programming (ADP) can be highly effective and robust, and can avoid the compromise mentioned earlier. However, investigations in Chapter 4 demonstrated that the ANN topologies typically used to implement ADP do not scale-up well. Therefore, implementing an intelligent holistic controller for a large-scale system is not feasible unless appropriate enhancements are made.

An approach to create simplified abstract representations of the system that can be used for control was proposed in Chapter 5. The idea of creating aggregate representations based on generator coherency was introduced in the form of a "virtual generator" (VG). VGs are simplified representations of large groups of generators that

have the tendency to swing together. This tendency can be exploited to control multiple generators as if they were a single machine, thereby reducing the complexity of the system from a control perspective. VGs essentially discard local oscillations which are not critical for WADC, while preserving inter-area ones that are. Preliminary studies on a 16-machine/68-bus power system simulation model showed that VGs can be coupled with ANN-based dynamic system identification and intelligent control to significantly improve rotor-angle stability. Comparisons against relatively conventional PSS-based stabilizing technology demonstrated the superiority of a preliminary aggregation-based intelligent local area damping control (AB-ILADC). Although the results were encouraging, the system utilized during the evaluations was not representative of a large-scale power system. Therefore, the ability to scale-up to large-scale systems remained an open question.

A large-scale power system simulation model was developed in Chapter 6. The model is a detailed representation of a large portion of the Brazilian power system. Extensive linear analysis over a large number of operating conditions pinpointed the weaknesses of this system in terms of rotor angle stability.

The design of a holistic aggregation-based intelligent wide-area damping controller (AB-IWADC) for the Brazilian system was illustrated in Chapter 7. Mode-shapes-based coherency identification over multiple operating conditions was used to determine robust generator groupings. VGs were then calculated in real-time from these groupings. A reduced-order linear observer for the system was then used to guide the design and initialization of an ANN-based model of the VG aggregated system. The dual heuristic programming (DHP) form of ADP was then implemented for online controller

adaptation. A step-by-step design framework was described in detail. Time-domain simulations over a large number of operating conditions and for a large number of small and large disturbances were used to evaluate the effectiveness and robustness of the resulting designs. An aggregation-based linear quadratic regulator (AB-LQR) was also developed to study the importance of online adaptation. Evaluations showed that linear controllers can be made relatively robust by considering multiple operating conditions during the design stage. However, once the operating condition deviates far away from those used for control design, the performance of the AB-LQR begins to degrade to the point that it becomes detrimental to rotor-angle stability. In contrast, the online learning capabilities of the AB-IWADC allow it to remain effective at all operating conditions tested.

A summary of the contributions made throughout this dissertation is provided next. Although the current state of the development is encouraging, there are a number of open questions and missing steps that will need to be completed before an AB-IWADC is ready for deployment in a real power system. These are discussed in section 8.3.

8.2 CONTRIBUTIONS

The contributions from the work in this dissertation can be summarized as follows:

1. A technique for optimizing the parameters of multiple local and wide-area damping controllers using particle swarm optimization has been proposed and validated. The gap metric and hierarchical clustering are used to select a small set of power system operating conditions to use for control design and evaluation.
2. Extensive linear analysis of a sample system have been completed to probe into the limitations of local and wide-area damping controls. This analysis sheds some light on the potential limitations of minimalist wide-area damping controllers in terms of mode controllability and observability once multiple operating points are considered.

3. An analysis of scalability of ANNs and their suitability for control of large-scale systems has been carried out. This analysis shed some light on the difficulties of training neural networks as they grow to match the complexity of large-scale power systems.
4. A C++ based flexible artificial neural network software library capable of simulating and training a wide variety of static and recurrent network topologies has been completed.
5. The concept of a virtual generator and a demonstration of its ability to provide simplified representations of groups of coherent generators in an interconnected system. These representations allow damping controllers to treat groups of multiple generators as if they were a single machine.
6. DIgSILENT PowerFactory models of a 16-machine/68-bus power system and of a large portion of the Brazilian power system.
7. A step-by-step framework to design scalable, effective, and robust aggregation based wide-area damping controllers for large-scale power systems. Examples of the use of this framework to design linear optimal controllers and intelligent controllers were given.
8. Extensive evaluations of the small-signal and transient stability improvements obtained by holistic damping controls. These evaluations included a demonstration of the importance of adaptation to maintain stability over a large set of operating conditions.

The publications derived from the work in this dissertation are summarized next.

8.2.1 Publications

1. **D. Molina**, G. K. Venayagamoorthy, and R. G. Harley, "Aggregation-based intelligent wide-area damping control for power systems," *IEEE Transactions on Power Systems*, *in preparation.*
2. **D. Molina**, J. Seuss, G. K. Venayagamoorthy, and R. G. Harley, "Robust design of local and wide-area damping controls using particle swarm optimization and

improved operating point selection," 17th International Conference on Intelligent System Applications to Power Systems, Tokyo, Japan, July 1-4, 2013.

3. **D. Molina**, G. K. Venayagamoorthy, R. G. Harley, "Coordinated design of local and wide-area damping controls using particle swarm optimization," 2013 Power and Energy Society General Meeting, Vancouver, Canada, July 21-25, 2013.
4. **D. Molina**, G. K. Venayagamoorthy, J. Liang, and R. G. Harley, "Intelligent local area signals-based damping control of power systems," *IEEE Transactions on Smart Grids*, vol. 4, no. 1, pp. 498-508, March 2013
5. **D. Molina**, J. Liang, R. G. Harley, and G. K. Venayagamoorthy, "Virtual generators: simplified online power system representations for wide-area damping control," 2012 Power and Energy Society General Meeting, San Diego, USA, July 22-26, 2012.
6. **D. Molina**, R. G. Harley, G. K. Venayagamoorthy, D. Falcao, G. N. Taranto, and T. M. L. Assis, "Coherency based partitioning of a power system for intelligent wide-area damping control", 12th Symposium of Specialists in Electrical Operation and Expansion Planning (SEPOPE), Rio de Janeiro, Brazil, May 20-23, 2012.
7. **D. Molina**, J. Liang, G. K. Venayagamoorthy, and R. G. Harley, "Comparison of TDNN and RNN performances for neuro-identification on small to medium-sized power systems," 2011 IEEE Symposium on Computational Intelligence Applications in Smart Grid, Paris, France, April 11-15, 2011.

8.3 RECOMMENDATIONS FOR FUTURE WORK

The work in this dissertation can be used as the starting point for multiple research directions. Some of those potential directions are summarized next.

8.3.1 Evaluation of the Effect of Communication Delays and Signal Loss

The detrimental effect that communication delays can have on the performance of a wide-area damping controller and some of the methods researchers have used to mitigate these effects were discussed in section 2.2.3. Those effects have not been considered in this dissertation and need to be investigated in the next stage of this work. This will help

ensure that aggregation-based damping controllers can provide acceptable results once deployed in real power systems.

8.3.2 Scheme for Compensating for Communication Delays and Signal Loss

If the effect of delays becomes significant, then it will be necessary to enhance the approach in this dissertation by adding a delay and signal loss compensation scheme. Schemes capable for dealing with this issue have already been developed for ANN-based intelligent control [10], but their ability to work well with an aggregation-based controller has not been demonstrated. The ability of the model network to generate step-ahead-predictions of the state could also be exploited to implement a network predictive controller [111]. This has also not been investigated at this time.

8.3.3 Evaluation of Other Control Design Techniques within the Proposed Design Framework

As was demonstrated by the design of the AB-LQR, the proposed framework does not demand the use of intelligent control techniques or artificial neural networks. The ability of the proposed framework to work in conjunction with other control methodologies such as linear robust control, linear adaptive control, etc, should be investigated.

8.3.4 Collaborative Aggregation-Based Wide-Area Damping Control

The framework proposed in this dissertation results in centralized wide-area damping controllers. Enhancements could be made to allow for the design of multiple controllers, one for each generator group, such that communication requirements are reduced. Such a collaborative approach could also improve reliability, since the damping effort would be

distributed among multiple locations/devices. This would reduce the effect of a single controller failure on overall system stability. Admittedly, attaining these enhancements would likely not be trivial.

8.3.5 Cost-Benefit Evaluation of the Enhanced Rotor-Angle Stability

The economics of implementing a holistic wide-area damping controller such as the ones proposed in this dissertation have not been investigated. Clearly, deploying such controllers will only be justified if the economic and reliability gains justify the expense and effort. At this time there is no clear path to make such an evaluation, so research along this direction would provide the tools needed to make justifiable decisions regarding wide-area damping control schemes.

8.3.6 Analyze the Equipment Requirements and Architecture for Field Deployment

The work in this dissertation is based on simulations alone. Therefore, the difficulties in terms of hardware deployment and the methods to do so have not been explored. This effort is unavoidable if a wide-area damping controller is to be deployed in a real power system. A relatively small laboratory implementation including a number of synchronous machines, lines, loads, etc., and an implementation of an intelligent damping controller in a stand-alone processor such as a DSP could provide a starting point. The laboratory test system, however, must be designed such that its dynamic behavior is relatively similar to that of a large-scale system. A fundamental problem with such a setup is that aggregation-based control cannot be tested, since only a few machines would be present in the system.

APPENDIX A PARAMETERS OF THE 68-BUS POWER SYSTEM MODEL

This appendix provides the details of the base case 16-machine/68-bus power system model used in multiple occasions throughout the dissertation. A detained single-line diagram of the system is provided in Figure A.1. This diagram corresponds to the actual model as implemented in DIgSILENT PowerFactory.

The parameters for the 16 generators in the system are provided in Table A.1 and Table A.2. Two voltage levels were used: 22 kV and 345 kV. These two voltage levels are chosen arbitrarily, as the original system data is typically found in per unit. All generators were modeled as round rotor machines and no mechanical damping was added.

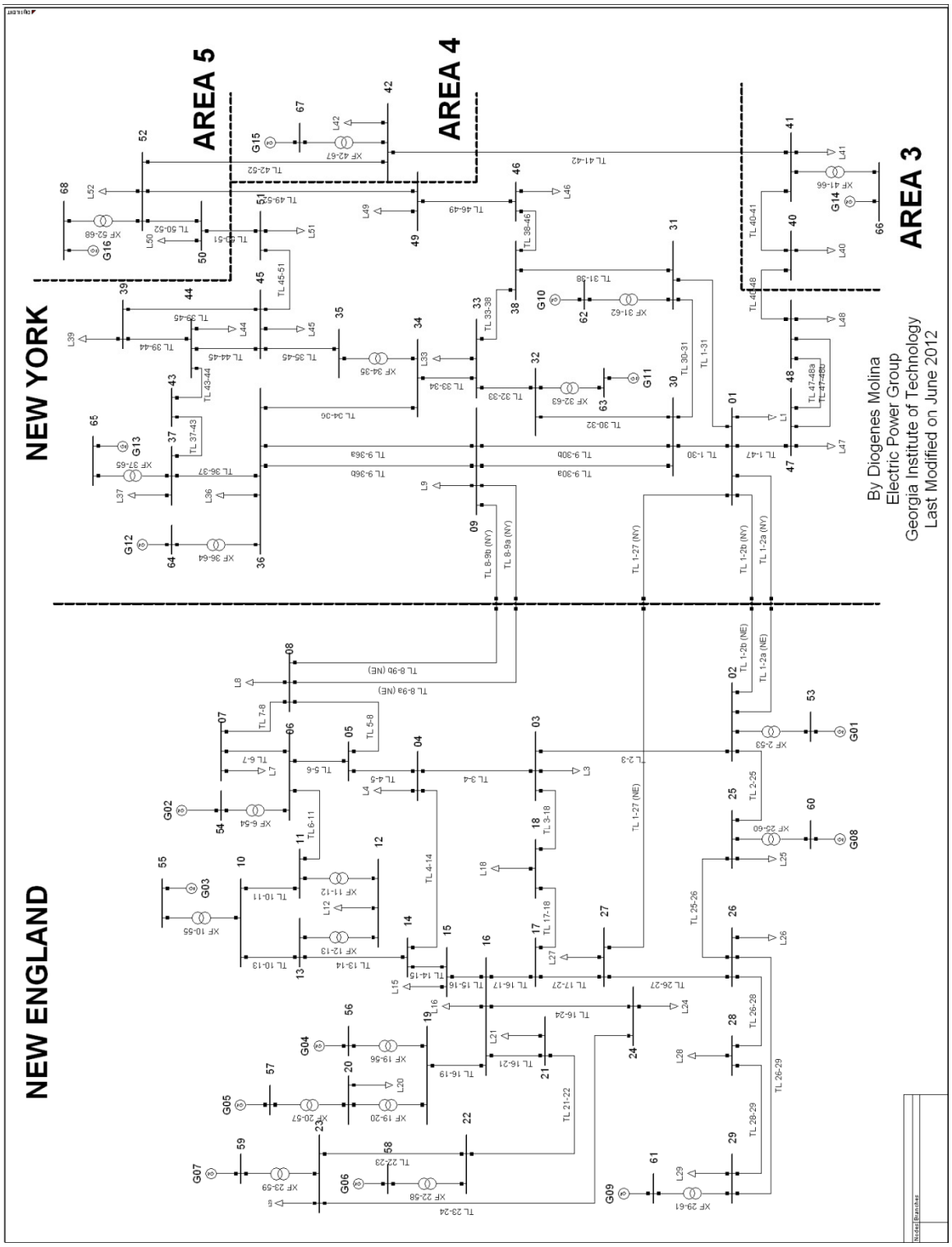

Figure A.1 Detailed single-line diagram of the 68-bus/16 machine power system model

Table A.1 Parameters for generators in the 68-bus/16-machine power system

Gen	Rated Power	Nominal Voltage	H	rstr	xl	xrl	xd	xq
	MVA	kV	sec	p.u.	p.u.	p.u.	p.u.	p.u.
G01	800	22	5.25	0.002	0.1	0	0.8	0.552
G02	850	22	3.553	0.002	0.298	0	2.508	2.397
G03	1000	22	3.58	0.002	0.304	0	2.495	2.37
G04	800	22	3.575	0.002	0.236	0	2.096	2.064
G05	750	22	3.467	0.002	0.203	0	2.475	2.325
G06	1000	22	3.48	0.002	0.224	0	2.54	2.41
G07	750	22	3.52	0.002	0.242	0	2.213	2.19
G08	700	22	3.471	0.002	0.196	0	2.03	1.96
G09	1000	22	3.45	0.002	0.298	0	2.106	2.05
G10	875	22	3.543	0.002	0.174	0	1.479	1.006
G11	1300	22	2.169	0.002	0.134	0	1.664	1.599
G12	2000	22	4.615	0.002	0.44	0	2.02	1.9
G13	10000	345	4.96	0.002	0.15	0	1.48	1.43
G14	10000	345	3	0.002	0.17	0	1.8	1.73
G15	10000	345	3	0.002	0.17	0	1.8	1.73
G16	10000	345	4.5	0.002	0.205	0	1.78	1.67

Table A.2 Parameters for generators in the 68-bus/16-machine power system (continued)

Gen	Td0'	Tq0'	Td0''	Tq0''	xd'	xq'	xd''	xq''
	sec	sec	sec	sec	p.u.	p.u.	p.u.	p.u.
G01	10.2	1.5	0.05	0.035	0.248	0.224	0.2	0.2
G02	6.56	1.5	0.05	0.035	0.592	0.51	0.425	0.425
G03	5.7	1.5	0.05	0.035	0.531	0.5	0.45	0.45
G04	5.69	1.5	0.05	0.035	0.349	0.32	0.28	0.28
G05	5.4	0.44	0.05	0.035	0.495	0.45	0.375	0.375
G06	7.3	0.4	0.05	0.035	0.5	0.45	0.4	0.4
G07	5.66	1.5	0.05	0.035	0.368	0.338	0.3	0.3
G08	6.7	0.41	0.05	0.035	0.399	0.35	0.315	0.315
G09	4.79	1.96	0.05	0.035	0.57	0.5	0.45	0.45
G10	9.37	1.5	0.05	0.035	0.4	0.394	0.35	0.35
G11	4.1	1.5	0.05	0.035	0.234	0.195	0.156	0.156
G12	7.4	1.5	0.05	0.035	0.62	0.56	0.5	0.5
G13	5.9	1.5	0.05	0.035	0.275	0.25	0.2	0.2
G14	4.1	1.5	0.05	0.035	0.285	0.25	0.23	0.23
G15	4.1	1.5	0.05	0.035	0.285	0.25	0.23	0.23
G16	7.8	1.5	0.05	0.035	0.355	0.3	0.275	0.275

All machines were equipped with identical automatic voltage regulators (AVRs) of the form in Figure A.2.

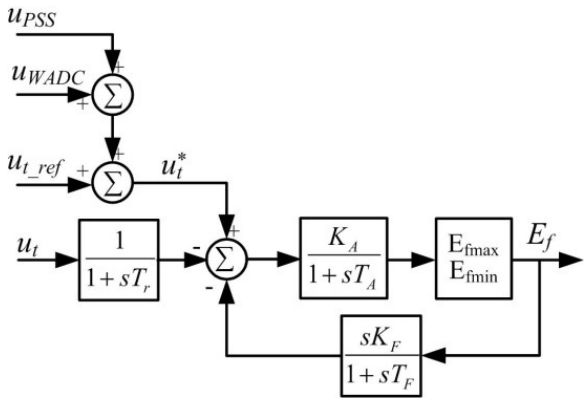

Figure A.2 Automatic voltage regulator model for the 68-bus/16-machine power system model

This model corresponds to a simplified IEEE type ST1A static excitation system with transient gain reduction in the feedback path and ignoring under/over excitation limiters (UEL and OEL). The parameters for each of the AVRs are provided in Table A.3.

Table A.3 Parameters for automatic voltage regulators in the 68-bus/16-machine power system

Name	**E_{fmax}**	**E_{fmin}**	**K_A**	**K_F**	**T_A**	**T_F**	**T_r**
	p.u.	**p.u.**	**p.u.**	**p.u.**	**sec**	**sec**	**sec**
G01 AVR	4	-4	50	0.1	0.02	0.5	0.01
G02 AVR	4	-4	25	0.1	0.02	0.5	0.01
G03 AVR	4	-4	25	0.15	0.02	0.5	0.01
G04 AVR	4	-4	20	0.15	0.02	0.5	0.01
G05 AVR	4	-4	20	0.15	0.02	0.5	0.01
G06 AVR	4	-4	20	0.15	0.02	0.5	0.01
G07 AVR	4	-4	20	0.15	0.02	0.5	0.01
G08 AVR	4	-4	50	0.1	0.02	0.5	0.01
G09 AVR	4	-4	50	0.1	0.02	0.5	0.01
G10 AVR	4	-4	25	0.15	0.02	0.5	0.01
G11 AVR	4	-4	50	0.1	0.02	0.5	0.01
G12 AVR	4	-4	50	0.1	0.02	0.5	0.01
G13 AVR	4	-4	20	0.2	0.02	0.5	0.01
G14 AVR	4	-4	25	0.15	0.02	0.5	0.01
G15 AVR	4	-4	25	0.15	0.02	0.5	0.01
G16 AVR	4	-4	25	0.15	0.02	0.5	0.01

There are a number of transformers and transmission lines in the system as illustrated in Figure A.1. The parameters for those transformers and transmission lines are provided in Table A.4 and 0. All parameters are given in a format compatible with DIgSILENT PowerFactory. Consequently, line parameters are given as a function of line length. Setting the length of each line to 1 Km eliminates this dependency. Only generators and transformer are connected to the 22 kV voltage levels; therefore, all lines are rated to 345 kV.

Table A.4 Parameters for transformers in the 68-bus/16-machine power system

From Bus	To Bus	Rated Power	Primary Voltage	Secondary Voltage	Short Circuit Voltage	Copper Loss
		MVA	kV	kV	%	kW
10	55	100	345	22	2	0
12	11	100	345	345	4.35	160
12	13	100	345	345	4.35	160
19	20	100	345	345	1.38	70
19	56	100	345	22	1.42	70
2	53	100	345	22	1.81	0
20	57	100	345	22	1.8	90
22	58	100	345	22	1.43	0
23	59	100	345	22	2.72	50
25	60	100	345	22	2.32	60
29	61	100	345	22	1.56	80
31	62	100	345	22	2.6	0
32	63	100	345	22	1.3	0
34	35	100	345	345	0.74	10
36	64	100	345	22	0.75	0
37	65	100	345	345	0.33	0
41	66	100	345	345	0.15	0
42	67	100	345	345	0.15	0
52	68	100	345	345	0.3	0
6	54	100	345	22	2.5	0

Lines are modeled as lumped-parameter PI modes as shown in Figure A.3.

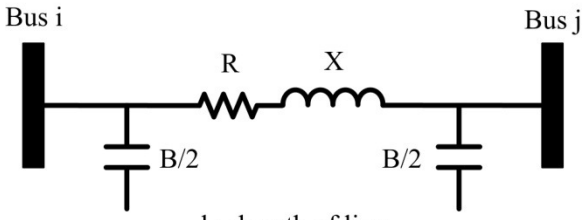

Figure A.3 Transmission line model

Table A.5 Parameters for transmission lines in the 68-bus/16-machine power system

From Bus	To bus	Rated Voltage	Rated Current	R' (20°C)	X'	B'
		kV	kA	Ohm/km	Ohm/km	uS/km
1	2	345	0.16735	8.33	97.84	293.51
1	2	345	0.16735	8.33	97.84	293.51
1	27	345	0.16735	38.09	380.88	344.47
1	30	345	0.16735	0.95	8.81	403.28
1	31	345	0.16735	1.90	19.40	210.04
1	47	345	0.16735	1.55	22.38	1100.61
10	11	345	0.16735	0.48	5.12	61.25
10	13	345	0.16735	0.48	5.12	61.25
13	14	345	0.16735	1.07	12.02	144.76
14	15	345	0.16735	2.14	25.83	307.50
15	16	345	0.16735	1.07	11.19	143.67
16	17	345	0.16735	0.83	10.59	112.75
16	19	345	0.16735	1.90	23.21	255.41
16	21	345	0.16735	0.95	16.07	214.07
16	24	345	0.16735	0.36	7.02	57.13
17	18	345	0.16735	0.83	9.76	110.82
17	27	345	0.16735	1.55	20.59	270.20
2	25	345	0.16735	8.33	10.24	122.66
2	3	345	0.16735	1.55	17.97	216.09
21	22	345	0.16735	0.95	16.66	215.50
22	23	345	0.16735	0.71	11.43	155.09
23	24	345	0.16735	2.62	41.66	303.30
25	26	345	0.16735	3.81	38.45	446.12
26	27	345	0.16735	1.67	17.50	201.30
26	28	345	0.16735	5.12	56.42	655.49
26	29	345	0.16735	6.78	74.39	864.52
28	29	345	0.16735	1.67	17.97	209.20
3	18	345	0.16735	1.31	15.83	179.63

From Bus	To bus	Rated Voltage	Rated Current	R' (20°C)	X'	B'
		kV	kA	Ohm/km	Ohm/km	uS/km
3	4	345	0.16735	1.55	25.35	186.01
30	31	345	0.16735	1.55	22.26	279.77
30	32	345	0.16735	2.86	34.28	410.00
31	38	345	0.16735	1.31	17.50	207.52
32	33	345	0.16735	0.95	11.78	141.15
33	34	345	0.16735	1.31	18.69	169.71
33	38	345	0.16735	4.28	52.85	582.23
34	36	345	0.16735	3.93	13.21	1218.23
35	45	345	0.16735	0.83	20.83	1167.82
36	37	345	0.16735	0.60	5.36	268.85
37	43	345	0.16735	0.60	32.85	0.00
38	46	345	0.16735	2.62	33.80	361.27
39	44	345	0.16735	0.00	48.92	0.00
39	45	345	0.16735	0.00	99.86	0.00
4	14	345	0.16735	0.95	15.35	116.11
4	5	345	0.16735	0.95	15.24	112.75
40	41	345	0.16735	7.14	99.98	2646.50
40	48	345	0.16735	2.38	26.19	1075.40
41	42	345	0.16735	4.76	71.42	1890.36
42	52	345	0.16735	4.76	71.42	1890.36
43	44	345	0.16735	0.12	1.31	0.00
44	45	345	0.16735	2.98	86.89	0.00
45	51	345	0.16735	0.48	12.50	604.91
46	49	345	0.16735	2.14	32.61	226.84
47	48	345	0.16735	2.98	31.90	336.06
47	48	345	0.16735	2.98	31.90	336.06
49	52	345	0.16735	9.05	135.81	974.59
5	6	345	0.16735	0.24	3.09	36.46
5	8	345	0.16735	0.95	13.33	124.01
50	51	345	0.16735	1.07	26.30	1361.06
50	52	345	0.16735	1.43	34.28	1730.73
6	11	345	0.16735	0.83	9.76	116.70
6	7	345	0.16735	0.71	10.95	94.94
7	8	345	0.16735	0.48	5.48	65.53
8	9	345	0.16735	5.48	86.41	159.80
8	9	345	0.16735	5.48	86.41	159.80
9	30	345	0.16735	2.26	21.78	243.65
9	30	345	0.16735	2.26	21.78	243.65

From Bus	To bus	Rated Voltage	Rated Current	R' (20°C)	X'	B'
		kV	kA	Ohm/km	Ohm/km	uS/km
9	36	345	0.16735	2.62	23.33	285.65
9	36	345	0.16735	2.62	23.33	285.65

All loads in the system were modeled as constant impedance loads. The load and generation at each bus, together will all other data needed to recreate and validate the load flow are provided in Table A.6. Clearly, this load flow was varied significantly throughout the dissertation to evaluate robustness and other phenomena. Providing the data for each of the cases tested would be impractical and is avoided here.

Table A.6 Base-case load flow data

Bus Number	Nominal Voltage	Bus Voltage	Bus Angle	Active Load at Bus	Active Generation at Bus	Reactive Load at Bus	Reactive Generation at Bus
	kV	p.u.	deg	MW	MW	MVar	MVar
1	345	1.01	14.41	256.86	0.00	120.51	0.00
2	345	1.00	20.91	0.00	0.00	0.00	0.00
3	345	1.00	19.09	320.95	0.00	1.99	0.00
4	345	1.00	19.90	198.11	0.00	72.91	0.00
5	345	1.00	20.33	0.00	0.00	0.00	0.00
6	345	1.00	20.99	0.00	0.00	0.00	0.00
7	345	0.99	18.51	229.36	0.00	82.33	0.00
8	345	0.99	17.86	204.29	0.00	69.27	0.00
9	345	0.99	8.95	102.21	0.00	122.85	0.00
10	345	1.01	23.60	0.00	0.00	0.00	0.00
11	345	1.01	22.71	0.00	0.00	0.00	0.00
12	345	1.01	22.75	9.09	0.00	88.91	0.00
13	345	1.01	22.94	0.00	0.00	0.00	0.00
14	345	1.00	21.42	0.00	0.00	0.00	0.00
15	345	0.99	20.67	311.90	0.00	149.13	0.00
16	345	1.00	21.99	327.01	0.00	31.81	0.00
17	345	1.00	20.41	0.00	0.00	0.00	0.00
18	345	1.00	19.45	157.20	0.00	29.85	0.00
19	345	1.01	27.06	0.00	0.00	0.00	0.00
20	345	0.99	25.72	669.13	0.00	101.35	0.00
21	345	0.99	24.86	269.78	0.00	113.23	0.00
22	345	1.01	29.94	0.00	0.00	0.00	0.00

Bus Number	Nominal Voltage	Bus Voltage	Bus Angle	Active Load at Bus	Active Generation at Bus	Reactive Load at Bus	Reactive Generation at Bus
	kV	p.u.	deg	MW	MW	MVar	MVar
23	345	1.00	29.62	249.08	0.00	85.37	0.00
24	345	1.00	22.18	309.75	0.00	-92.22	0.00
25	345	1.01	22.31	229.65	0.00	48.19	0.00
26	345	1.01	21.08	143.14	0.00	17.51	0.00
27	345	1.00	19.39	282.81	0.00	76.49	0.00
28	345	1.01	24.22	212.00	0.00	28.81	0.00
29	345	1.02	27.03	292.82	0.00	27.84	0.00
30	345	1.00	13.24	0.00	0.00	0.00	0.00
31	345	1.01	16.16	0.00	0.00	0.00	0.00
32	345	1.00	17.59	0.00	0.00	0.00	0.00
33	345	1.00	13.42	113.00	0.00	0.00	0.00
34	345	1.01	7.04	0.00	0.00	0.00	0.00
35	345	1.01	7.05	0.00	0.00	0.00	0.00
36	345	0.99	2.46	100.77	0.00	-19.23	0.00
37	345	1.00	-5.59	5943.74	0.00	297.19	0.00
38	345	1.01	15.87	0.00	0.00	0.00	0.00
39	345	0.98	-5.31	255.82	0.00	12.07	0.00
40	345	1.03	23.11	69.15	0.00	24.79	0.00
41	345	1.00	53.20	997.35	0.00	249.34	0.00
42	345	1.00	47.34	1147.71	0.00	249.50	0.00
43	345	0.98	-5.21	0.00	0.00	0.00	0.00
44	345	0.98	-5.19	259.36	0.00	4.69	0.00
45	345	1.00	7.11	208.37	0.00	21.04	0.00
46	345	0.99	16.97	147.52	0.00	27.90	0.00
47	345	1.02	14.87	213.18	0.00	34.20	0.00
48	345	1.03	16.79	255.59	0.00	2.33	0.00
49	345	0.98	20.47	155.95	0.00	27.58	0.00
50	345	0.99	25.81	98.39	0.00	-144.63	0.00
51	345	1.00	11.63	338.40	0.00	-122.51	0.00
52	345	0.99	46.65	2421.78	0.00	120.60	0.00
53	22	1.00	23.50	0.00	250.00	0.00	-0.78
54	22	0.98	29.54	0.00	545.00	0.00	216.73
55	22	0.98	31.66	0.00	650.00	0.00	240.17
56	22	1.00	32.27	0.00	632.00	0.00	98.68
57	22	1.01	30.89	0.00	505.20	0.00	159.37
58	22	1.02	35.59	0.00	700.00	0.00	197.33
59	22	1.02	38.16	0.00	560.00	0.00	98.22
60	22	1.00	29.49	0.00	540.00	0.00	9.05

Bus Number	Nominal Voltage	Bus Voltage	Bus Angle	Active Load at Bus	Active Generation at Bus	Reactive Load at Bus	Reactive Generation at Bus
	kV	p.u.	deg	MW	MW	MVar	MVar
61	22	1.01	34.06	0.00	800.00	0.00	38.09
62	22	1.00	23.58	0.00	500.00	0.00	5.07
63	22	1.00	25.03	0.00	1000.00	0.00	39.57
64	22	1.00	8.30	0.00	1350.00	0.00	149.34
65	345	1.01	0.00	0.00	2909.67	0.00	1220.81
66	345	1.00	54.74	0.00	1785.00	0.00	112.18
67	345	1.00	48.20	0.00	1000.00	0.00	73.90
68	345	1.00	53.61	0.00	4000.00	0.00	570.26

APPENDIX B AUTOMATED CALCULATION OF LINEAR POWER SYSTEM MODELS FOR ROBUSTNESS EVALUATION AND CONTROL DESIGN IN DIGSILENT POWERFACTORY

This appending illustrates how to obtain linearized input-output linear models of power systems modeled using DIgSILENT PowerFactory. PowerFactory offers built-in tools to perform small-signal stability analysis. For this analysis, the program first calculates a linearized model of the system of the form in (B.1).

$$\frac{dx(t)}{dt} = Ax(t) \tag{B.1}$$

The eigenvalues of the A matrix in (B.1) and their corresponding left and right eigenvectors are then calculated within the software. By default, the software does not grant access to the A matrix. However, it does provide access to all of the eigenvalues and eigenvectors of the system. These can be used to retrieve the original A matrix. The process begins with the definition of the two matrices of eigenvalues and right eigenvectors in (B.2).

$$\begin{aligned} \Lambda &= \begin{bmatrix} \lambda_1 & 0 & \dots & 0 \\ 0 & \lambda_2 & 0 & \vdots \\ \vdots & 0 & \ddots & 0 \\ 0 & \dots & 0 & \lambda_n \end{bmatrix} \\ \Phi &= \begin{bmatrix} \phi_1 & \cdots & \phi_1 \end{bmatrix} \end{aligned} \tag{B.2}$$

From the software documentation in [70] and utilizing theory from [16] equation (B.3) is found, which allow the calculation of the system matrix A.

$$\begin{aligned} A\Phi &= \Phi\Lambda \\ A &= \Phi\Lambda\Phi^{-1} \end{aligned} \tag{B.3}$$

The models used throughout this dissertation for analysis and control design have the form in (B.4), so it is necessary to manipulate the calculation of the *A* matrix such that this form can be obtained.

$$\begin{aligned} \frac{dx(t)}{dt} &= Ax(t) + Bu(t) \\ y(t) &= Cx(t) \end{aligned} \tag{B.4}$$

This manipulation is best explained with a generic example. The process starts with a generic power system model such as that in Figure B.1 for which an input-output linearized model of the form in (B.4) is to be calculated. The input and output signals $u_i(t)$ and y_i(t) are pre-determined.

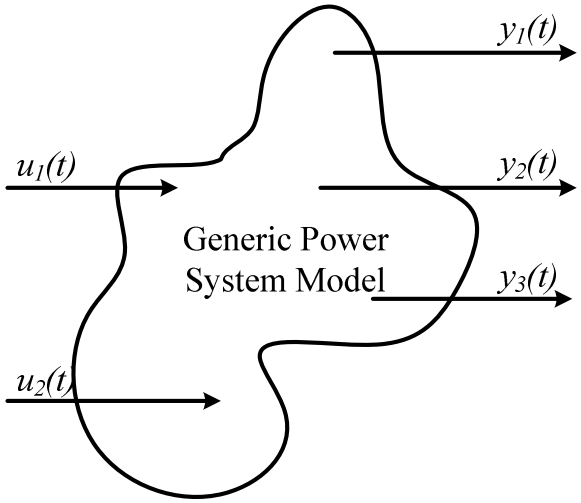

Figure B.1 Generic power system model for which a 2 input-3 output linearized model is to be obtained

The full non-linear power system model is then augmented using integrator blocks at each of the input locations as shown in Figure B.2. If the outputs are state variables in the original system, e.g. generator speeds or angles, no further augmentation is needed. If the outputs are not state variables in the original system, e.g., active power trough a line or

voltage at a particular bus, then the system is further augmented with an integrator block for each non-state-variable output signal.

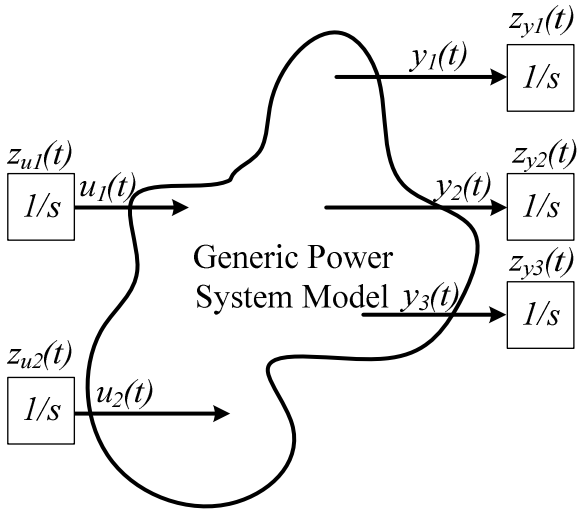

Figure B.2 Augmented generic power system model. Integrator blocks are added to augment the system state vector

A linearized model of the form in (B.1) is then calculated using the small-signal analysis tool in PowerFactory. The resulting augmented *A'* matrix is obtained as described previously. The A, B, and C matrix for the model in (B.4) can then be extracted from the augmented *A'* matrix following (B.5).

$$\frac{dx'(t)}{dt} = A'x'(t)$$
$$x' = \begin{bmatrix} x \\ z_u \\ z_y \end{bmatrix} \tag{B.5}$$
$$A' = \begin{bmatrix} A & B & C \end{bmatrix}$$

The only difficulty with this approach stems from the ordering of the variables in the state vector from PowerFactory, which is not as neatly organized as in (B.5). However, by assigning unique variable names to the state variables in the integrator blocks used to

augment the system, the proper ordering for extracting the *B* and *C* matrices as prescribed in (B.5) can be identified.

It is worth noting that some versions of PowerFactory (version 14.1 was used here) provide a command to extract the A matrix in (B.1) directly, circumventing the need for the calculations in (B.2) and (B.3). This command was intended for debugging purposes by the software developers at DIgSILENT, and not for typical user applications. However, it was found useful throughout the course of this dissertation.

The command is given in (B.6). The user inputs this command in the "Input Window" in PowerFactory's "data manager". This command causes the system A matrix to be printed to the "Output Window" when the user completes a "Modal Analysis" run. The "Output Window" can then be saved as a text file which is then imported to a software tool such as MATLAB for further analysis and manipulation.

$$\textit{\_test/Amat} \tag{B.6}$$

This process can be automated such that a large number of linearized models are created with relative ease.

APPENDIX C UNDERSTANDING MODE SHAPES

This appendix provides a brief primer on the meaning of mode shapes, how they can be calculated, and how they can be interpreted and plotted. It is not meant to be a rigorous explanation, since it is only expected to provide readers with enough insights to better understand the contents of this dissertation. The explanations here borrow heavily from [16] and [105].

Assume that the behavior of the power system within a small region of the state-space can be described using (C.1). The state vector *x(t)* is composed of all the state variables in the power system and is of length *n*. The matrix *A* is thus an *n x n* matrix.

$$\begin{aligned} \frac{dx(t)}{dt} &= Ax(t) + Bu(t) \\ y(t) &= Cx(t) \end{aligned} \tag{C.1}$$

The unforced response of this system is given by (C.2). This is the portion of the response that is of interest when analyzing mode shapes, so the B and C matrices are ignored in what follows.

$$\frac{dx(t)}{dt} = Ax(t) \tag{C.2}$$

The eigenvalues of the A matrix in (C.2) are the set of scalars (either real or complex) that satisfy (C.3). A right eigenvector is a column vector of *n* components that satisfies (C.4) for a particular eigenvalue of *A*. Therefore, an eigenvector always corresponds to a particular eigenvalue.

$$\begin{aligned} \det(A - \lambda I) &= 0 \\ \lambda &= \lambda_1, \lambda_2, \cdots, \lambda_n \end{aligned} \tag{C.3}$$

$$A\phi_i = \lambda_i \phi_i$$
$$\phi_i = \begin{bmatrix} \phi_{1i} \\ \vdots \\ \phi_{ni} \end{bmatrix} \tag{C.4}$$

The eigenvalues and eigenvectors can be collected into *n x n* matrices of the form in (C.5) and (C.6) for convenience. Using these matrices, it is possible to write equation (C.4) as in (C.7), from which (C.8) follows directly.

$$\Lambda = \begin{bmatrix} \lambda_1 & 0 & \dots & 0 \\ 0 & \lambda_2 & 0 & \vdots \\ \vdots & 0 & \ddots & 0 \\ 0 & \dots & 0 & \lambda_n \end{bmatrix} \tag{C.5}$$

$$\Phi = \begin{bmatrix} \varphi_{11} & \varphi_{12} & \cdots & \varphi_{1n} \\ \varphi_{21} & \varphi_{12} & \cdots & \varphi_{2n} \\ \vdots & \vdots & \dots & \vdots \\ \varphi_{n1} & \varphi_{n2} & \cdots & \varphi_{nn} \end{bmatrix} \tag{C.6}$$

$$A\Phi = \Phi\Lambda \tag{C.7}$$

$$\Phi^{-1} A \Phi = \Lambda \tag{C.8}$$

Using these derivations, it is possible to transform the original linear system in (C.2) to a form that is more amenable to the study of oscillations in the system. The transformed representation of the system's small-signal behavior is given in (C.9).

$$\begin{gathered} x = \Phi z \\ z = \Phi^{-1} x \\ \dot{z} = \Phi^{-1} \dot{x} = \Phi^{-1} A x = \Phi^{-1} A \Phi z \\ \dot{z} = \Lambda z \end{gathered} \tag{C.9}$$

Since the eigenvalue matrix Λ is diagonal, the response of the transformed system in (C.9) corresponds to the system of *n* decoupled first-order differential equations in (C.10). The solution for this system of equations is known to be (C.11).

$$\begin{aligned} \dot{z}_1 &= \lambda_1 z_1 \\ &\vdots \\ \dot{z}_n &= \lambda_n z_n \end{aligned} \tag{C.10}$$

$$z_i(t) = z_i(0) \times e^{\lambda_i t} \tag{C.11}$$

Assuming that at time zero all eigenvalues are excited equally and with unity excitation ($z_i(0) = 1$),then (C.11) becomes:

$$z_i(t) = e^{\lambda_i t} \tag{C.12}$$

This response can be transformed back to the original state vector using (C.4) and (C.9), resulting in (C.13) and (C.14).

$$x(t) = \Phi z(t) = \begin{bmatrix} \phi_1 & \cdots & \phi_n \end{bmatrix} \times \begin{bmatrix} e^{\lambda_1 t} \\ \vdots \\ e^{\lambda_n t} \end{bmatrix} \tag{C.13}$$

$$x(t) = \phi_1 \times e^{\lambda_1 t} + \ldots + \phi_n e^{\lambda_n t} \tag{C.14}$$

Close inspection of (C.14) reveals the effect of each individual eigenvalue on the state variables of the original system. The effect of each eigenvalue on the ith state variable of the original system is determined by the right eigenvectors as in (C.15).

$$x_i(t) = \phi_{i1} \times e^{\lambda_1 t} + \ldots + \phi_{in} e^{\lambda_n t} \tag{C.15}$$

The components of the right eigenvectors (ϕ_{ij}) can therefore be used to analyze the effect of a particular eigenvalue on different state variables in the system. In general, the ϕ_{ij} components are complex numbers.

With the developments presented so far, it is now possible to describe the meaning of the mode shapes presented throughout this dissertation.

First, note that a mode shape corresponds to a single oscillatory mode. This oscillatory mode, in turn, corresponds to a pair of complex conjugate eigenvalues. The eigenvectors of complex conjugate eigenvalues are also complex conjugates of each other. A single eigenvector can thus be used to analyze the shape of an oscillatory mode corresponding to a pair of complex conjugate eigenvalues.

The mode shapes used in this dissertation are derived by extracting the eigenvector components corresponding to *generator speed state variables* in the linearized system. These components are further normalized to a maximum amplitude of unity. The components are also rotated such that the largest lies on the positive-real-axis in the complex plane.

An example is given next to provide further insights into the interpretation of the resulting mode shapes. Once again, the system under study is given by the dynamic equation in (C.2). For this example, the state matrix A is defined as in (C.16). The goal of studying mode shapes is to gain insights into the oscillatory patterns in the system, since such insights cannot be obtained by mere observation of (C.2) and (C.16).

$$A = \begin{bmatrix} -0.0833 & 6.2832 & 0.0333 & -1.5708 & 1.5625 \\ -4.0888 & -0.1000 & 4.1888 & 0 & -0.4189 \\ 0.0167 & -3.1416 & -0.0667 & -1.5708 & -3.1499 \\ 0.5236 & 0 & 1.0472 & -0.0500 & -0.2118 \\ 0 & 0 & 0 & 0 & -0.1 \end{bmatrix} \quad \text{(C.16)}$$

The five eigenvalues (always the same as the order of the system) and their corresponding eigenvectors of (C.16) can be calculated using linear analysis packages such as MATLAB. The model matrices in (C.5) and (C.6) for (C.16) are given in (C.17) and (C.18). Complex pairs of eigenvalues correspond to oscillatory modes, which are of interest for the work in this dissertation. The imaginary component of a complex

eigenvalue corresponds to the frequency of oscillations. Its real component corresponds to the decay rate of the oscillation. Two complex pairs are found in (C.17). The first corresponds to an oscillation frequency of 1 Hz (6.28 divided by 2π). The second corresponds to an oscillation frequency of 0.25 Hz. Each has a negative real part, so they can be expected to decay over time.

$$\Lambda = \begin{bmatrix} -0.1 + j6.28 & 0 & 0 & 0 & 0 \\ 0 & -0.1 - j6.28 & 0 & 0 & 0 \\ 0 & 0 & -0.05 + j1.57 & 0 & 0 \\ 0 & 0 & 0 & -0.05 - j1.57 & 0 \\ 0 & 0 & 0 & 0 & -0.1 \end{bmatrix} \quad \text{(C.17)}$$

$$\Phi = \begin{bmatrix} -j0.6667 & -0.6667 & 0.5774 & 0.5774 & 0.0659 \\ 0.6667 & 0.6667 & 0 & 0 & -0.3297 \\ j0.3333 & -j0.3333 & 0.5774 & 0.5774 & 0.1319 \\ 0 & 0 & -j0.5774 & j0.5774 & -0.6594 \\ 0 & 0 & 0 & 0 & 0.6594 \end{bmatrix} \quad \text{(C.18)}$$

For this example, it is assumed that the first and third components of the state vector correspond to the speed states variables of a 2-machine linearized power system model. This assumption is made only for illustration purposes, as the matrices used in this example do not correspond to an actual power system model.

The oscillatory patterns of the 1 Hz and 0.25 Hz modes are now analyzed in more detail. Eigenvectors corresponding to these two modes are extracted from (C.18) by taking the first and third columns of that matrix, and only their components corresponding to the "speed states" x_1 and x_3 are retained. This step results in the two speed eigenvectors in (C.19). As mentioned before, a single eigenvector is considered for each complex conjugate pair. The selection of which of the two eigenvectors to consider is not important.

$$\phi_{1Hz} = \begin{bmatrix} \phi_{11} \\ \phi_{31} \end{bmatrix} = \begin{bmatrix} -j0.6667 \\ j0.3333 \end{bmatrix}$$
$$\phi_{0.25Hz} = \begin{bmatrix} \phi_{13} \\ \phi_{33} \end{bmatrix} = \begin{bmatrix} 0.5774 \\ 0.5774 \end{bmatrix} \quad \text{(C.19)}$$

The speed eigenvectors ϕ_{1Hz} and $\phi_{0.25Hz}$ in (C.19) are normalized by dividing their components by *-j0.6667* and *0.5774* respectively, resulting in (C.20).

$$\hat{\phi}_{1Hz} = \begin{bmatrix} \hat{\phi}_{11} \\ \hat{\phi}_{31} \end{bmatrix} = \begin{bmatrix} 1.0 \\ -0.5 \end{bmatrix}$$
$$\hat{\phi}_{0.25Hz} = \begin{bmatrix} \hat{\phi}_{13} \\ \hat{\phi}_{33} \end{bmatrix} = \begin{bmatrix} 1 \\ 1 \end{bmatrix} \quad \text{(C.20)}$$

These normalized mode shapes can now be used to understand the oscillatory patterns in the system. The 1 Hz oscillation can be expected to be reflected in x_1 oscillating against x_3, since their mode shapes $\hat{\phi}_{11} = 1.0$ and $\hat{\phi}_{31} = -0.5$ are 180º apart (they have opposite signs). Also, this oscillation will be twice as visible in x_1 compared to x_3, since its mode shape has twice the magnitude with respect to the shape of x_3. In contrast, the 0.25 Hz oscillation will be reflected equally in x_1 and x_3 (since $\hat{\phi}_{13} = \hat{\phi}_{33}$) and the two can be expected to oscillate in-phase with each other since they have equal magnitude and angle. Visual inspection of the simulated time-domain response in Figure C.1 of the system confirms these insights. As expected, x_1 and x_3 oscillate against each other in the 1 Hz oscillation, and the oscillation is most visible in x_1. Also, x_1 and x_3 oscillate in phase with each other and with the same amplitude in the lower frequency 0.25 Hz oscillation. Mode shapes are powerful tools for understanding the oscillatory behavior of power systems.

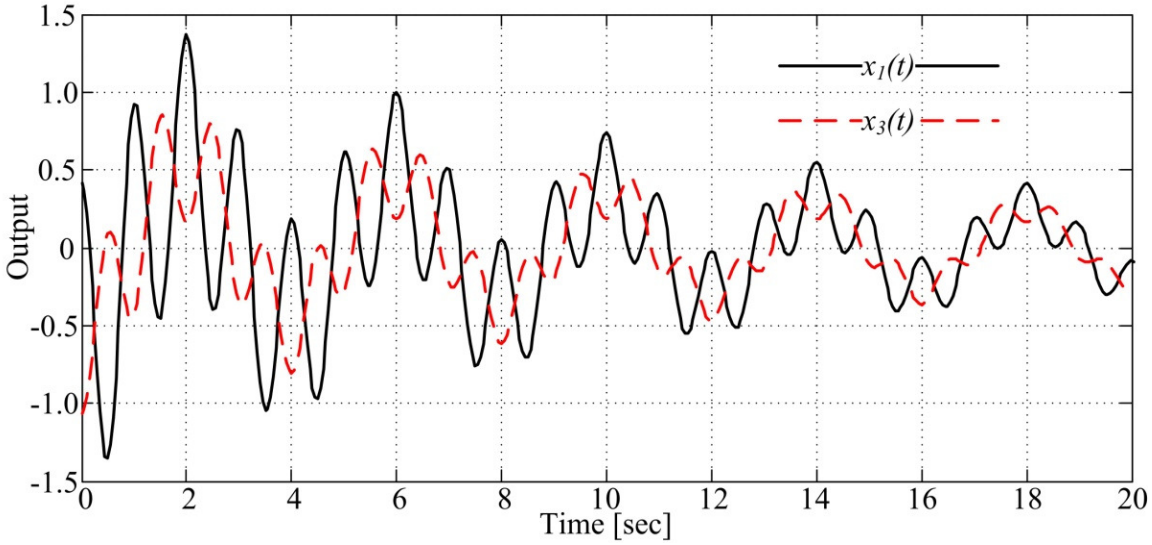

Figure C.1 System response to an arbitrary initial condition

APPENDIX D DERIVATION OF EIGENVALUE SENSITIVITIES

This appendix presents the derivation of eigenvalues sensitivities utilized in Chapter 4. This derivation applies to linear systems of the form in (D.1). Note that the feedback controller corresponds to an output-feedback control law. The goal of the derivation here is to find the effect on a particular eigenvalue of changing parameters (gains) in the controller.

$$\begin{aligned} \dot{x} &= Ax + Bu \\ y &= Cx \\ u &= Ky \end{aligned} \tag{D.1}$$

Closing the loop results in the system in (D.2). The derivation begins by finding the sensitivity of an eigenvalue to changes in a parameter in the closed-loop system matrix A_c in (D.3).

$$\begin{aligned} \dot{x} &= \left(A + BKC\right)x \\ A_c &= \left(A + BKC\right) \\ \dot{x} &= A_c x \end{aligned} \tag{D.2}$$

$$A_c = \begin{bmatrix} a_{11} & \cdots & a_{1n} \\ \vdots & \ddots & \vdots \\ a_{n1} & \cdots & a_{nn} \end{bmatrix} \tag{D.3}$$

The process begins by calculating an eigenvalue of interest and its corresponding eigenvectors. An eigenvalue λ_i and its corresponding right and left eigenvectors e_i and f_i satisfy (D.4), (D.5), and (D.6).

$$\left(A_c + \lambda_i I\right) = 0 \tag{D.4}$$

$$A_c e_i = \lambda_i e_i \tag{D.5}$$

$$f_i^T A_c = f_i^T \lambda_i \tag{D.6}$$

The left and right eigenvectors are orthogonal to each other and can be normalized such that they satisfy (D.7).

$$\begin{aligned} f_i^T e_i &= 1 \qquad \forall i = j \\ f_i^T e_i &= 0 \qquad \forall i \neq j \end{aligned} \tag{D.7}$$

Equation (D.8) derives directly from (D.5) and can be used to derive (D.9). Multiplying both sides of (D.9) by the transpose of the left eigenvector as in (D.10) results in (D.11).

$$\frac{\partial A_c e_i}{\partial a_{kl}} = \frac{\partial \lambda_i e_i}{\partial a_{kl}} \tag{D.8}$$

$$\left.\begin{aligned} \frac{\partial A_c e_i}{\partial a_{kl}} &= \frac{\partial A_c}{\partial a_{kl}} e_i + A_c \frac{\partial e_i}{\partial a_{kl}} \\ \frac{\partial \lambda_i e_i}{\partial a_{kl}} &= \frac{\partial \lambda_i}{\partial a_{kl}} e_i + \lambda_i \frac{\partial e_i}{\partial a_{kl}} \end{aligned}\right\} \frac{\partial A_c}{\partial a_{kl}} e_i + A_c \frac{\partial e_i}{\partial a_{kl}} = \frac{\partial \lambda_i}{\partial a_{kl}} e_i + \lambda_i \frac{\partial e_i}{\partial a_{kl}} \tag{D.9}$$

$$f_i^T \left(\frac{\partial A_c}{\partial a_{kl}} e_i + A_c \frac{\partial e_i}{\partial a_{kl}} \right) = f_i^T \left(\frac{\partial \lambda_i}{\partial a_{kl}} e_i + \lambda_i \frac{\partial e_i}{\partial a_{kl}} \right) \tag{D.10}$$

$$f_i^T \frac{\partial A_c}{\partial a_{kl}} e_i + f_i^T A_c \frac{\partial e_i}{\partial a_{kl}} = f_i^T \frac{\partial \lambda_i}{\partial a_{kl}} e_i + f_i^T \lambda_i \frac{\partial e_i}{\partial a_{kl}} \tag{D.11}$$

Right-multiplying $\frac{\partial e_i}{\partial a_{kl}}$ by both sides of (D.6) results in (D.12).

$$f_i^T A_c \frac{\partial e_i}{\partial a_{kl}} = f_i^T \lambda_i \frac{\partial e_i}{\partial a_{kl}} \tag{D.12}$$

This allows further simplification of (D.11) which results in (D.13).

$$f_i^T \frac{\partial A_c}{\partial a_{kl}} e_i = f_i^T \frac{\partial \lambda_i}{\partial a_{kl}} e_i \tag{D.13}$$

Since $\frac{\partial \lambda_i}{\partial a_{kl}}$ is a scalar value, it is possible to re-write (D.13) as (D.14), which can be simplified using (D.7) to obtain (D.15). Equation (D.15) defines the sensitivity of an eigenvalue to changes in the closed-loop system matrix A_c.

$$f_i^T \frac{\partial A_c}{\partial a_{kl}} e_i = \frac{\partial \lambda_i}{\partial a_{kl}} f_i^T e_i \tag{D.14}$$

$$\frac{\partial \lambda_i}{\partial a_{kl}} = f_i^T \frac{\partial A_c}{\partial a_{kl}} e_i \tag{D.15}$$

The sensitivity to changes to parameters in the output-feedback gain matrix follows directly and is given in (D.16) and (D.17).

$$\begin{aligned} A_c &= (A + BKC) \\ \frac{\partial A_c}{\partial K_{kl}} &= \frac{\partial (A + BKC)}{\partial K_{kl}} = \frac{\partial (BKC)}{\partial K_{kl}} = B \frac{\partial K}{\partial K_{kl}} C \end{aligned} \tag{D.16}$$

$$\frac{\partial \lambda_i}{\partial K_{kl}} = f_i^T B \frac{\partial K}{\partial K_{kl}} C e_i \tag{D.17}$$

APPENDIX E FLEXIBLE C++ ARTIFICIAL NEURAL NETWORK LIBRARY

All artificial neural networks (ANNs) in this dissertation were implemented using a flexible ANN library coded using C++ in the Microsoft Visual Studio 2010 Ultimate programming environment and object oriented programming. The development of this library was guided by theory and algorithms available in [79]-[82]. Only a brief overview of the library is given in this appendix, as the full documentation is yet to be written.

At the core of the library is the "neuron" object. A rough depiction of this object is shown in Figure E.1. The neuron object is composed of a list of connections indicating which other neurons in the network are connected to it and their time delays, a set of weights corresponding to each connection in the list, and miscellaneous indicators dictating the characteristics of the neuron such as activation function type, neuron identification number, etc. The neuron object is generic in the sense that it can be defined to contain an arbitrary activation function, number of connections/weights, connection list, and delays.

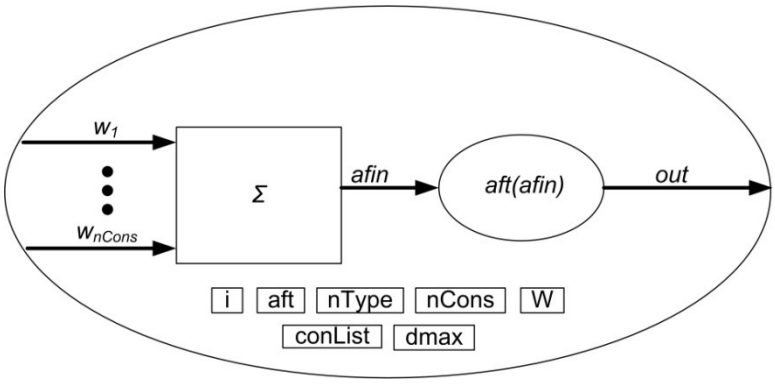

Figure E.1 Generic neuron object

The library is implemented such that an ANN is just a collection of generic neurons. Each neuron in an ANN contains its own weights, connection list, etc. A generic ANN with 6 neurons is shown in Figure E.2. All neurons in an ANN are identical to Figure E.1.

A large number of methods for creating/training/simulating/storing/loading/etc generic ANNs have been implemented. All training algorithms are gradient based, so it is important to have smooth differentiable activation functions in all neurons in an ANN.

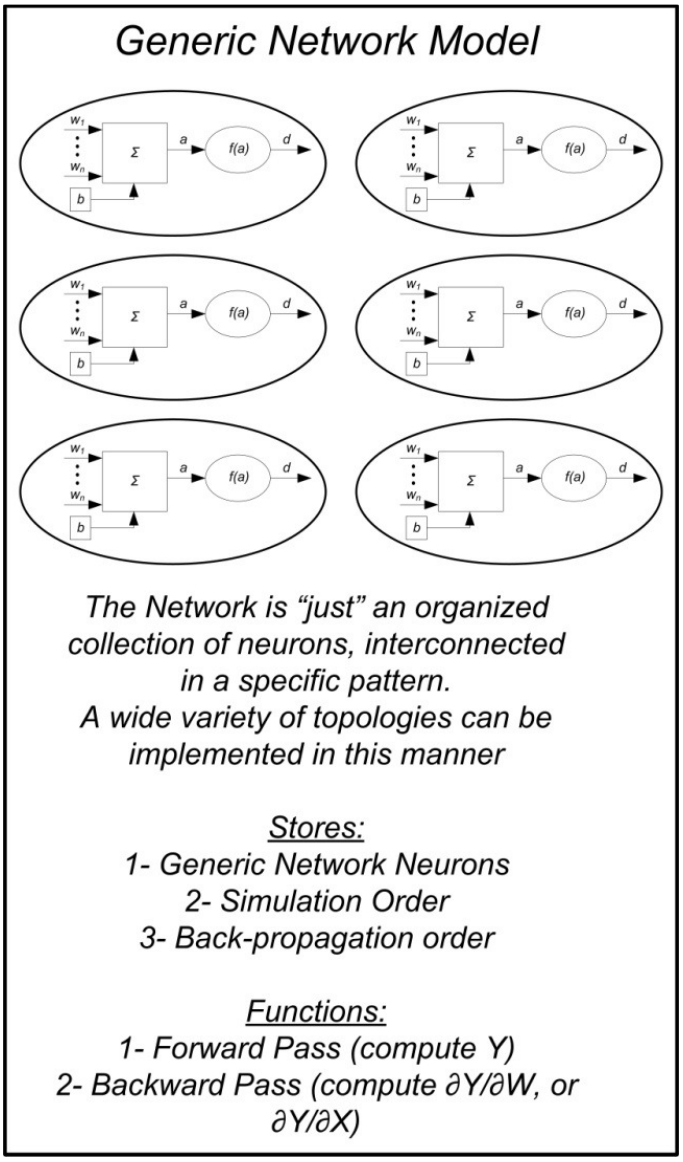

Figure E.2 Generic ANN

By specifying the right connection list, neuron type, etc, it is possible to create a wide variety of ANN topologies. Static and recurrent ANNs can be implemented seamlessly. An example of a recurrent network is given in Figure E.3.

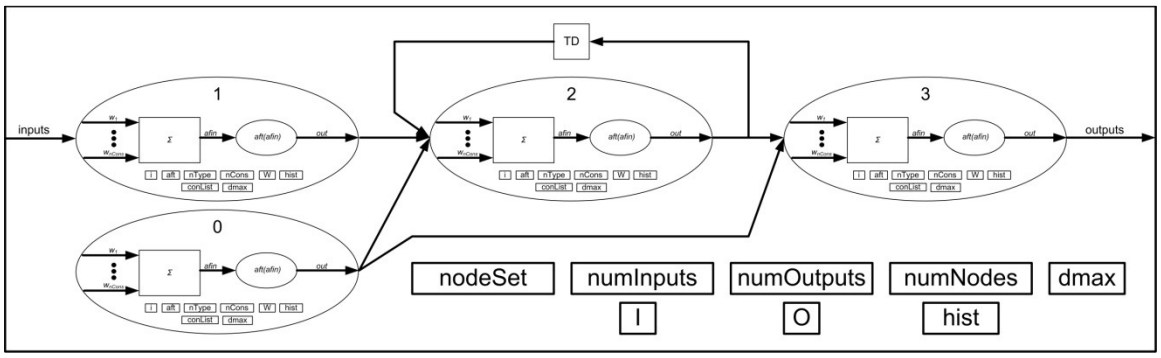

Figure E.3 Network diagram accounting for neuron connection pattern

Static (classical) back-propagation and truncated back-propagation-trough-time (BPTT) have been implemented for calculating the sensitivities of the ANN outputs to changes in network weights and inputs. The truncation depth for BPTT is a user defined parameter.

Training algorithms include incremental and batch gradient descent, and the scaled conjugate gradient. Sliding-window-based versions of these algorithms were implemented for real-time identification and control. Other training algorithms could also be added without much additional effort.

Multiple activation function types have been implemented, and other ones can be added without significant effort.

If the proper formatting requirements are followed, it is possible to import ANNs trained using other software packages. Also, networks obtained through the library can be exported for use by other software programs. All import/export is completed using text files.

Communication between the library and DIgSILENT PowerFactory for closed-loop control is made using Dynamic Link Libraries (DLLs) following the approach depicted in Figure E.4. This is an efficient way of implementing the ANNs needed for the power system applications in this dissertation and results in minimal communication overhead and memory consumption. This interface involves complex mechanisms internal to PowerFactory and could only be developed after some interactions with the support team from DIgSILENT.

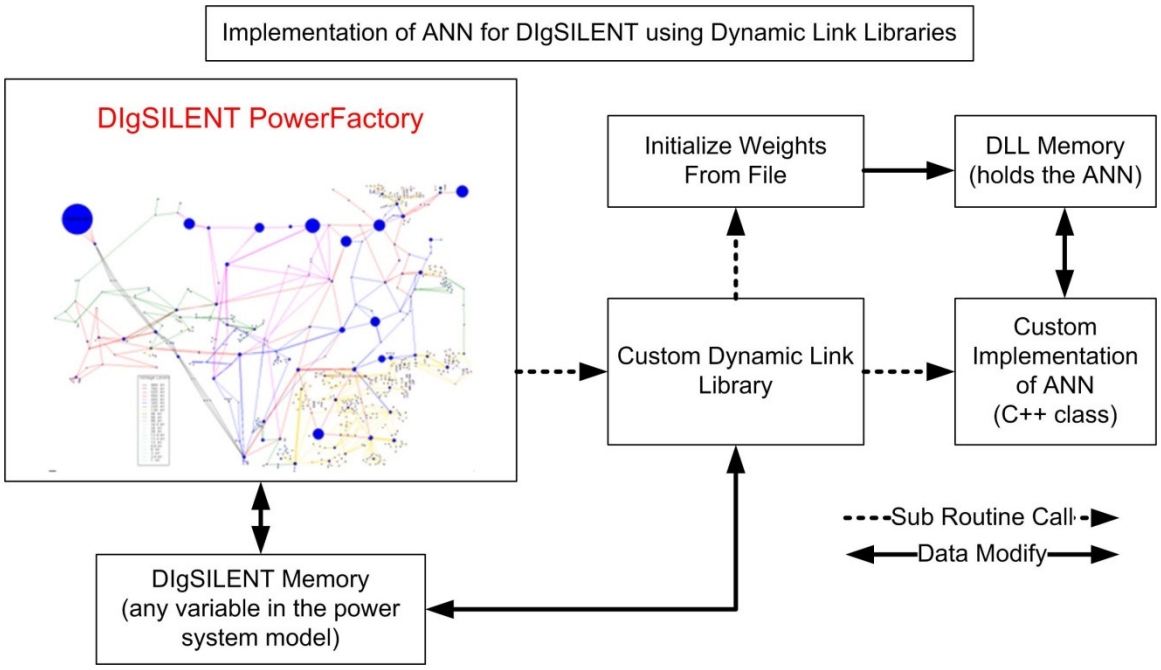

Figure E.4 ANN library-DIgSILENT PowerFactory interface

All results are collected within DIgSILENT PowerFactory and exported to excel and text files. This data extraction step is not affected by the implementation of the ANN library discussed here, and follows the normal procedures available in DIgSILENT PowerFactory.

APPENDIX F DESIGN OF AN AGGREGATION-BASED LINEAR QUADRATIC REGULATOR

This appendix describes the design of the aggregation-based linear quadratic regulator (AB-LQR) used for comparisons in Chapter 7. The descriptions here borrow heavily from classical control design theory found in references such as [108] and [112].

The process of designing an AB-LQR assumes the availability of a linear time-invariant model of the aggregate system of the form in (F.1). The model used here is identical to the 20th order aggregate model developed for enhancing the initialization of the model network in Chapter 7.

$$\begin{aligned} x(k+1) &= Ax(k) + Bu(k) \\ y(k) &= Cx(k) \end{aligned} \tag{F.1}$$

The controller to be designed is a state feedback controller of the form in (F.2).

$$u(k) = Kx(k) \tag{F.2}$$

The goal of the control design stage is to find the controller gain K in (F.2) that minimizes a pre-determined performance index (PI). The performance index is chosen to be the same as that used for the AB-IWADC in Chapter 7 for ease of comparisons. The PI is thus composed of a single-stage-cost function $U(\cdot)$ to be minimized over time and defined as in (F.3), (F.4), and (F.5).

$$U(x(k), u(k)) = x(k)^T Qx(k) + u(k)^T Ru(k) \tag{F.3}$$

$$
\begin{gathered}
Q = C^T Q' C \\
Q' = c_y I \\
R = c_u I \\
c_y = 100 \qquad c_u = 1 \qquad I = \begin{bmatrix} 1 & \cdots & 0 \\ \vdots & \ddots & \vdots \\ 0 & \cdots & 1 \end{bmatrix}
\end{gathered}
\tag{F.4}
$$

$$
U\left(x(k), u(k)\right) = y(k)^T Q' y(k) + u(k)^T R u(k) \tag{F.5}
$$

The PI to be minimized consists of the summation of all single-stage-cost starting from a given value of the state to all future time-steps and is formulated as in (F.6). Note that this PI is almost identical to the cost-to-go function minimized by the AB-IWADC in Chapter 7.

$$
\begin{aligned}
J\left(x(k)\right) &= \sum_{n=0}^{\infty} U\left(x(k), u(k)\right) \\
J\left(x(k)\right) &= \sum_{n=0}^{\infty} y(k)^T Q' y(k) + u(k)^T R u(k)
\end{aligned}
\tag{F.6}
$$

Given the control law in (F.2), the performance objective can also be written as in (F.7) to highlight that the value of the PI is a function of the controller gain *K*. The optimal controller gain is that which minimizes *J(·)* for all possible values of the state. The optimal cost and gain are defined as in (F.8) and (F.9) respectively.

$$
J\left(x(k), K\right) = \sum_{n=0}^{\infty} x(k)^T C^T Q' C x(k) + x(k)^T K^T R K x(k) \tag{F.7}
$$

$$
J^{opt}\left(x(k)\right) = \min_{K} \left\{ J\left(x(k), K\right) \right\} \tag{F.8}
$$

$$K^{opt} = \underset{K}{\operatorname{argmin}}\{J(x(k), K)\} \tag{F.9}$$

From classical control theory, $J^{opt}(\cdot)$ is known to satisfy (F.10). This fact will be useful when discussing an improved critic network initialization scheme introduced later.

$$J^{opt}(x(k)) = x(k)^T S^{opt} x(k) \tag{F.10}$$

This optimization problem can be solved numerically in an efficient manner using control design software tools available in programs such as MATLAB. MATLAB's "*lqr*" function was thus used here to obtain the optimal controller gain K^{opt} in (F.9). The cost gain S^{opt} in (F.10) is also obtained as a by-product of the optimization routine. The optimal controller so obtained is a full-state-feedback controller, since it utilizes measurements of all state variables in the system to generate the inputs. However, recall that the model used for AB-LQR design is an aggregated and reduced order model of the system. As such, the states cannot be fed back for control. Consequently, a state "observer" is needed. The state-observer from Chapter 7 is used for implementing the AB-LQR.

The control feedback gain and the state observer are integrated into the closed-loop control law shown in Figure F.1. A washout stage is added to the system outputs *y(t)* (virtual generator speeds) to prevent the AB-LQR from responding to steady-state deviations in virtual generator speeds. A low-pass stage is added to the controller outputs *u(k)* to avoid exciting fast system dynamics due to the discrete nature of the controller, which results in generator stair-step waveforms (each step-transition contains high-frequency components). The washout and low-pass filtering stages are added to the linear

models prior to the balanced-realizations and truncation based-model-order-reduction process discussed in Chapter 7.

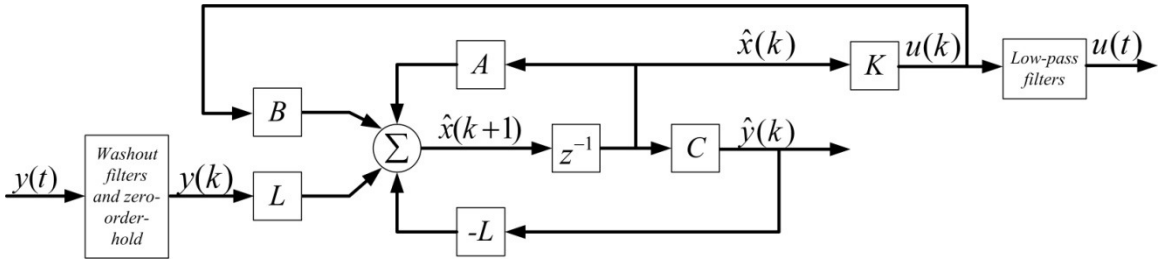

Figure F.1 AB-LQR structure including feedback gain and state observer

Robustness is evaluated prior to implementing the AB-LQR in the non-linear simulation model. This evaluation is completed in a similar way to that used in Chapter 3, where the eigenvalues of the closed-loop system where evaluated using a large number of linearized models. The bank of 38 linearized models from Chapter 6 is used during the evaluations. It is not clear which of the 38 models to use for control design, and the choice is found to be critical. A heuristic trial-and-error approach is thus followed. Multiple iterations of the control design stage are completed until desired damping is observed for all 38 linear models. The main variation during the iterative process corresponds to the model used for control design.

Figure F.2 the eigenvalues at each operating point before and after adding the first iteration of the AB-LQR. Clearly, selecting the wrong model for control design can result in poor performance and instability as illustrated by the unstable eigenvalues in the plot.

Figure F.3 the eigenvalues at each operating point before and after adding the AB-LQR at the end of the design process. All eigenvalues remain well damped for all operating conditions. This is a clear indication that the AB-LQR is relatively robust and effective.

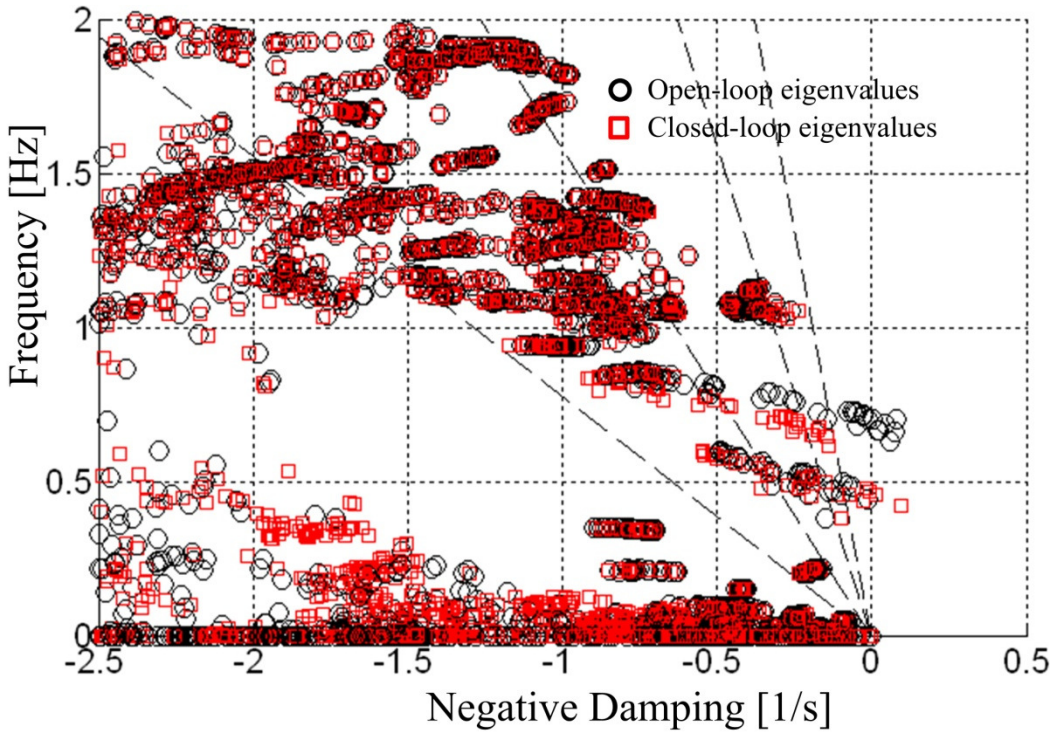

Figure F.2 Closed-loop system eigenvalues with initial AB-LQR design

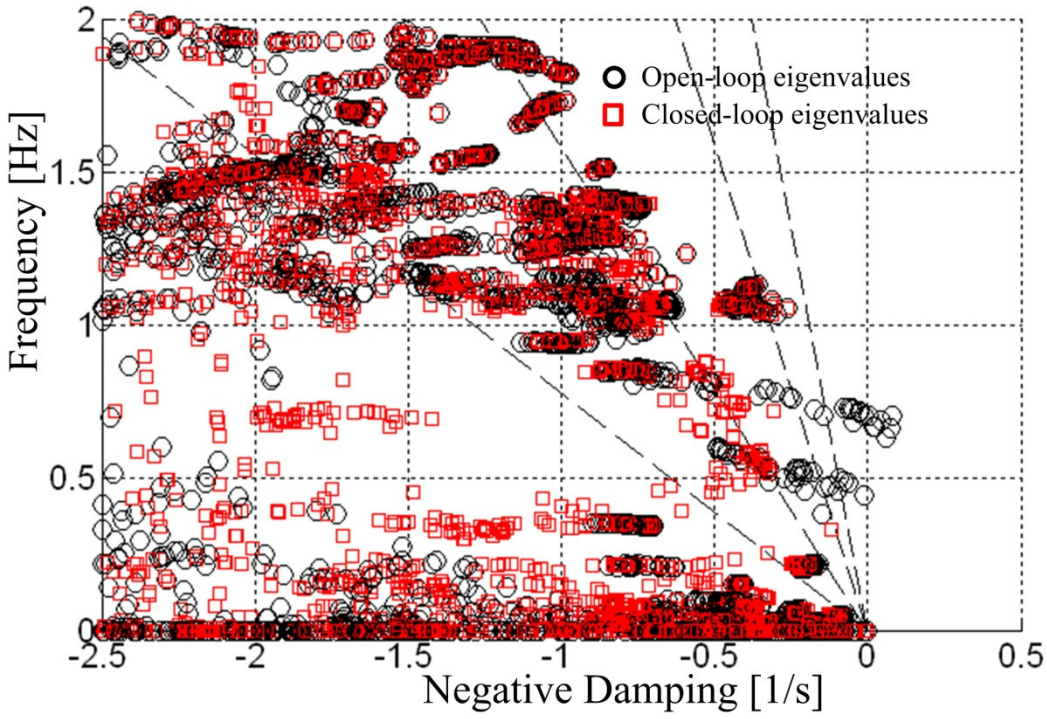

Figure F.3 Closed-loop system eigenvalues with final AB-LQR design

The literature review in Chapter 2 pointed to robust control design approaches with a higher degree of sophistication. These can be used to design an aggregation-based controller following many of the same steps as described in Chapter 7 but were not pursued here to avoid unnecessary complications.

The AB-LQR design process results in an optimal controller gain matrix K^{opt} and its corresponding S^{opt} as defined in (F.9) and (F.10). These matrices can be used to initialize the action and critic networks in an intelligent controller of the form in Chapter 7. This initialization procedure can be useful in control applications where starting with random parameters is unacceptable due to stability and/or performance considerations. The action and critic networks are implemented using ANNs of the form in Figure F.4 and Figure F.5 respectively.

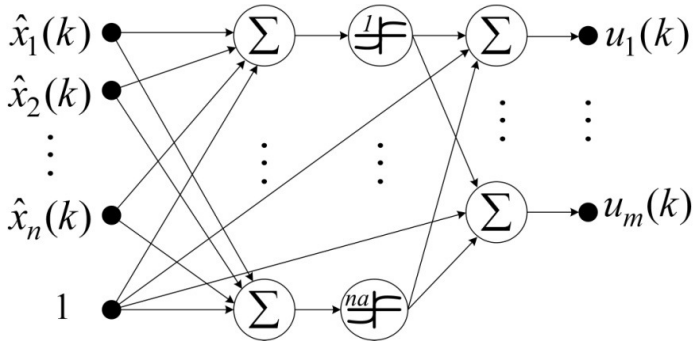

Figure F.4 ANN implementing the action network

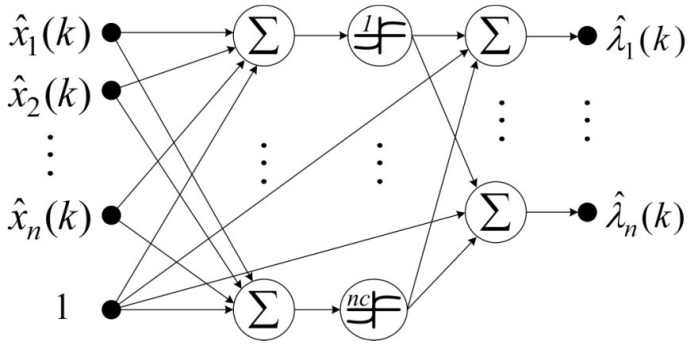

Figure F.5 ANN implementing the critic network

The output equation of the action network (assuming the input and output bias weights are set to zero and that activation functions are hyperbolic tangents) is defined as in (F.11). The linear behavior of this network when operating around the origin is defined as in (F.12).

$$a\left(x(k), w_0^a\right) = \pi_0\left(x(k)\right) = u\left(x(k)\right) = V_0^a \tanh\left(W_0^a x(k)\right) \tag{F.11}$$

$$\Delta a\left(\Delta x(k), w_0^a\right) = \Delta u\left(x(k)\right) = V_0^a W_0^a \Delta x(k) \tag{F.12}$$

Performing QR factorization of the optimal feedback matrix obtained previously, this gain can be written as in (F.13). The QR algorithm is readily available in software packages such as MATLAB. By setting the input and output weights of the action network as in (F.14), it is possible to guarantee that the action network behaves the same as the optimal controller designed previously. The state estimates needed to implement this control law are provided by the model network from Chapter 7.

$$K^{opt} = K_q^{opt} K_r^{opt} \tag{F.13}$$

$$V_0^a = K_q^{opt} \qquad W_0^a = K_r^{opt} \tag{F.14}$$

A similar approach can be taken to initialize the critic network. The output equation and its linearization are given in (F.15) and (F.16).

$$c\left(x(k), \pi_0, w_0^c\right) = \hat{\lambda}_0\left(x(k), \pi_0\right) = V_0^c \tanh\left(W_0^c x(k)\right) \tag{F.15}$$

$$\Delta c\left(\Delta x(k), w_0^c\right) = \Delta \hat{\lambda}\left(x(k)\right) = V_0^c W_0^c \Delta x(k) \tag{F.16}$$

Given that the optimal cost is defined as in (F.17), its derivative can be taken with respect to the state vector to obtain (F.18).

$$J^{opt}\left(x(k)\right) = x(k)^T S^{opt} x(k) \tag{F.17}$$

$$\lambda^{opt}\left(x(k)\right) = \frac{\partial J^{opt}\left(x(k)\right)}{\partial x(k)} = 2S^{opt}x(k) \tag{F.18}$$

Equation (F.19) results from applying QR factorization of the gain matrix ($2S^{opt}$) in (F.18). This allows the critic's input and output matrices to be initialized as in (F.20).

$$2S^{opt} = S_q^{opt} S_r^{opt} \tag{F.19}$$

$$V_0^c = S_q^{opt} \qquad W_0^c = S_r^{opt} \tag{F.20}$$

These improved action and critic initializations can be expected to improve the performance of the DHP algorithm at startup.

REFERENCES

[1] J.-M. Saugrain, "Banishing blackouts," *Power Engineer*, vol. 21, no. 2, pp. 36-41, April-May 2007

[2] P. Panciatici, G. Bareux, and L. Wehenkel, "Operating in the fog: security management under uncertainty," *IEEE Power and Energy Magazine*, vol. 10, no. 5, pp. 40-49, September-October, 2012

[3] X. Xie, Y. Xin, J. Xiao, J. Wu, and Y. Han, :WAMS applications in Chinese power systems," *IEEE Power and Energy Magazine*, vol. 4, no. 1, pp. 54-63, January-February 2006

[4] M. Jonsson, M. Begovic, and J. Daalder, "A new method suitable for real-time generator coherency determination," *IEEE Transactions on Power Systems*, vol. 19, no. 3, pp. 1473-1482, August 2004

[5] Western Systems Coordinating Council (WSCC), *Disturbance report for the power system outage that occurred on the Western interconnection on August 10th, 1996 at 1548 PAST*, October 1996.

[6] C. Y. Chung, L. Wang, F. Howell, and P. Kundur, "Generation rescheduling methods to improve power transfer capability constrained by small-signal stability," *IEEE Transactions on Power Systems*, vol. 19, no. 1, pp. 524-530, February 2004.

[7] D. Bailey, "Experience with power systems oscillations," IEEE Colloquium on Power System Dynamics Stabilization (Digest No. 1998/196 and 1998/278), February, 1998

[8] G. K. Venayagamoorthy, R. G. Harley, and D. C. Wunsch, "Dual heuristic programming excitation neurocontrol for generators in a multimachine power system," *IEEE Transactions on Industry Applications*, vol. 39, no. 2, pp. 382-394, March/April 2003.

[9] J.-W. Park, R. G. Harley, and G. K. Venayagamoorthy, "Adaptive-critic-based optimal neurocontrol for synchronous generators in a power system using MLP/RBF neural networks," *IEEE Transactions on Industry Applications*, vol. 39, no. 5, pp. 1529-1540, September-October 2003

[10] S. Mohagheghi, G. Venayagamoorthy, and R. Harley, "Optimal wide area controller and state predictor for a power system," *IEEE Transactions on Power Systems*, vol. 22, no. 2, pp. 693-705, May 2007

[11] S. Ray, G. Venayagamoorthy, B. Chaudhuri, and R. Majumder, "Comparison of adaptive critic-based and classical wide-area controllers for power systems," I*EEE Transactions on Systems, Man, and Cybernetics – Part B: Cybernetics*, vol. 38, no. 4, pp. 1002-1007, August 2008

[12] D. Molina, J. Liang, G. K. Venayagamoorthy, and R. Harley, "Comparison of TDNN and RNN performances for neuro-identification on small to medium-sized power systems," Proceedings of the 2011 IEEE Symposium on Computational Intelligence in Smart Grids, Paris, France, April 2011.

[13] D. Molina, J. Liang, G. K. Venayagamoorthy, and R. G. Harley, "Virtual generators: simplified online power system representations for wide-area damping control," 2012 IEEE Power and Energy Society General Meeting, San Diego, USA, July 2012.

[14] IEEE/CIGRE Joint Task Force on Stability Terms and Definitions, "Definition and classification of power system stability," *IEEE Transactions on Power Systems*, vol. 19, no. 2, pp. 1387-1401, May 2004

[15] C. P. Steinmetz, "Power control and stability of electric generating stations," *Transactions of the AIEE*, vol. XXXIX, no. 2, pp. 1215–1287, July 1920.

[16] P. Kundur*, Power system stability and control*. New York: McGraw-Hill, 1993

[17] P. Sauer and M. Pai, Power system dynamics and stability, Upper Saddle River, NJ: Prentice Hall, 1998

[18] G. Rogers, Power System Oscillations. Norwell, MA: Kluwer, 2000

[19] P. Kundur, M. Klein, G. J. Rogers, and M. S. Zywno, Application of power system stabilizers for enhancement of overall system stability," *IEEE Transactions on Power Systems*, vol. 4, no. 2, pp. 614-626, May 1989

[20] Western Electricity Coordinating Council, *WECC policy statement on power system stabilizers*, April 2002. Available online: http://www.wecc.biz/library/default.aspx. Last accessed: October 11, 2012

[21] F. R. Schleif and J. White, "Damping for the northwest-southwest tieline oscillations – an analog study," IEEE Transactions on Power Apparatus and Systems, vol. PAS-85, no. 12, pp. 1239-1247, December, 1966.

[22] F. R. Schleif, H. D. Hunkins, G. E. Martin, and E. E. Hattan, "Excitation control to improve powerline stability," *IEEE Transactions on Power Apparatus and Systems*, vol. PAS-87, no. 6, pp. 1426-1434, June 1968.

[23] F. P. DeMello and C. Concordia, "Concepts of synchronous machine stability as affected by excitation control," *IEEE Transactions on Power Apparatus and Systems*, vol. PAS-88, no. 4, pp. 316-329, April 1969.

[24] E. V. Larsen and D. A. Swann, "Applying power system stabilizers, part I: general concepts," *IEEE Transactions on Power Apparatus and Systems*, vol. PAS-100, no. 6, pp. 3017-3024, June 1981.

[25] E. V. Larsen and D. A. Swann, "Applying power system stabilizers, part II: performance objectives and tuning process," *IEEE Transactions on Power Apparatus and Systems*, vol. PAS-100, no. 6, pp. 3025-3033, June 1981.

[26] E. V. Larsen and D. A. Swann, "Applying power system stabilizers, part III: practical considerations," *IEEE Transactions on Power Apparatus and Systems*, vol. PAS-100, no. 6, pp. 3034-3046, June 1981.

[27] I. Kamwa, R. Grondin, and G. Trudel, "IEEE PSS2B versus PSS4B: the limits of performance of modern power system stabilizers," *IEEE Transactions on Power Systems*, vol. 20, no. 2, pp. 903-915, May 2005

[28] W. G. Heffron and R. A. Phillips, "Effect of a modern amplidyne voltage regulator on underexcited operation of large turbine generators," *Transactions of the AIEE – Part III: Power Apparatus and Systems*, vol. 71, no. 1, pp. 692-697, January 1952.

[29] Western Electricity Coordinating Council, *WECC white paper on power system stabilizer tuning*, May 2002. Available online: http://www.wecc.biz/library/default.aspx. Last accessed: October 11, 2012.

[30] S. Chen and O. P. Malik, "Power system stabilizer design using μ synthesis," *IEEE Transactions on Energy Conversion*, vol. 10, no. 1, pp. 175-181, March 1995.

[31] S. Chen and O. P. Malik, "H∞ optimization-based power system stabilizer design," *IEE Proceedings on Generation, Transmission, and Distribution*, vol. 142, no. 2, pp. 179-184, March 1995.

[32] C. Zhu, M. Khammash, V. Vittal, and W. Qiu, "Robust power system stabilizer design using H∞ loop shaping approach," *IEEE Transactions on Power Systems,* vol. 18, no. 2, pp. 810-818, May 2003.

[33] H. Werner, P. Korba, and T. C. Yang, Robust tuning of power system stabilizers using LMI-techniques," IEEE Transactions on Control Systems Technology, vol. 11, no. 1, pp. 147-152, January 2003.

[34] G. P. Chen, O. P. Malik, G. S. Hope, Y. H. Qin, and G. Y. Xu, "An adaptive power system stabilizer based on the self-optimizing pole shifting control strategy," *IEEE Transactions on Energy Conversion*, vol. 8, no. 4, pp. 639-645, December 1993.

[35] O. P. Malik, C. X. Mao, K. S. Prakash, G. S. Hope, and G. C. Hancock, "Tests with a microcomputer based adaptive synchronous machine stabilizer on a

400MW thermal unit," *IEEE Transactions on Energy Conversion*, vol. 8, no. 1, pp. 6-12, March 1993.

[36] M. A. Abido, "Optimal design of power-system stabilizers using particle swarm optimization," *IEEE Transactions on Energy Conversion*, vol. 17, no. 3, pp. 406-413, September 2002.

[37] M. A. Abido, "Robust design of multimachine power system stabilizers using simulated annealing," *IEEE Transactions on Energy Conversion*, vol. 15, no. 3, pp. 297-304, September 2000.

[38] Y. LL. Abdel-Magid and M. A. Abido, "Optimal multiobjective design of robust power system stabilizers using genetic algorithms," *IEEE Transactions on Power Systems*, vol. 18, no. 3, pp. 1125-1132, August 2003.

[39] A. L. B. do Bomfim, G. N. Taranto, and D. Falcao, "Simultaneous tuning of power system damping controllers using genetic algorithms," *IEEE Transactions on Power Systems*, vol. 15, no. 1, pp. 163-169, February 2000.

[40] R. A. Jabr, B. C. Pal, and N. Martins, "A sequential conic programming approach for the coordinated and robust design of power system stabilizers," *IEEE Transactions on Power Systems*, vol. 25, no. 3, pp. 1627-1637, August 2010.

[41] T. K. Das, G. K. Venayagamoorthy, and U. O. Aliyu, "Bio-inspired algorithms for the design of multiple optimal power system stabilizers: SPPSO and BFA," *IEEE Transactions on Industry Applications*, vol. 44, no. 5, pp. 1445-1457, September/October 2008.

[42] A. Elices, L. Rouco, H. Bourles, and T. Margotin, "Physical interpretation of state feedback controllers to damp power system oscillations," *IEEE Transactions on Power Systems*, vol. 19, no. 1, pp. 436-443, February 2004.

[43] K. A. El-Metwually and O. P. Malik, "Fuzzy logic power system stabilizer," IEE Proceedings on Generation, Transmission and Distribution, vol. 142, no. 3, pp. 277-281, May 1995.

[44] S. K. Yee and J. V. Milanovic, "Fuzzy logic controller for decentralized stabilization of multimachine power systems," *IEEE Transactions on Fuzzy Systems*, vol. 16, no. 4, pp. 971-981, August 2008.

[45] T. Hiyama, S. Oniki, and H Nagashima, "Evaluation of advanced fuzzy logic PSS on analog network simulator and actual installation on hydro generators," *IEEE Transactions on Energy Conversion*, vol. 11, no. 1, pp. 125-131, March 1996.

[46] J. W. Park, R. G. Harley, and G. K. Venayagamoorthy, "Indirect adaptive control for synchronous generator: comparison of MLP/RBF neural networks approach with Lyapunov stability analysis," *IEEE Transactions on Neural Networks*, vol. 15, no. 2, pp. 460-464, March 2004.

[47] D. K. Chaturvedi and O. P. Malik, "Experimental studies with a generalized neuron-based power system stabilizer," *IEEE Transactions on Power Systems*, vol. 19, no. 3, pp. 1445-1453, August 2004.

[48] W. Liu, G. K. Venayagamoorthy, D. C. Wunsch, "A heuristic-dynamic-programming-based power system stabilizer for a turbogenerator in a single-machine power system," *IEEE Transactions on Industry Applications*, vol. 41, no. 5, pp. 1377-1385, September/October, 2005.

[49] G. K. Venayagamoorthy, R. G. Harley, and D. C. Wunsch, "Implementation of adaptive critic-based neurocontrollers for turbogenerators in multimachine power system," *IEEE Transactions on Neural Networks*, vo. 14, no. 5, pp. 1047-1064, September 2003.

[50] X. Yang and A. Feliachi, "Stabilization of inter-area oscillation modes through excitation systems," *IEEE Transactions on Power Systems*, vol. 9, no. 1, pp. 494-502, February 1994.

[51] M. Aboul-Ela, A. Sallam, J. McCalley, and A. Fouad, "Damping controller design for power system oscillations using global signals," *IEEE Transactions on Power Systems*, vol. 11, no. 2, pp. 767-773, May 1996.

[52] M. J. Gibbard, D. J. Vowles, and R. Pourbeik, "Interactions between, and effectiveness of, power system stabilizers and FACTS device stabilizers in multimachine systems," *IEEE Transactions on Power Systems*, vol. 15, no. 2, pp. 748-755, May 2000.

[53] W. Juanjuan, F. Chang, and Z. Yao, "Design of WAMS-based multiple HVDC damping control system," *IEEE Transactions on Smart Grid*, vol. 2, no. 2, pp. 363-374, June 2011.

[54] A. G. Phadke and R. M. de Moraes, "The wide world of wide-area measurement," *IEEE Power and Energy Magazine*, vol. 6, no. 6, pp. 52-65, September-October 2008.

[55] I. Kamwa, A. Heniche, G. Trudel, M. Dobrescu, R. Grondin, and D. Lefebvre, "Assessing the technical value of FACTS-based wide-area damping control loops," 2005 IEEE Power and Energy Society General Meeting, San Francisco, USA, June 2005.

[56] A. M. Almutari and J. V. Milanovic, "Comparison of different methods for input/output signal selection for wide area power system control," IEEE Power and Energy Society General Meeting, Calgary, Canada, July 2009.

[57] A. M. A. Hamdam and A. M. Alabdalla, "Geometric measures of model controllability and observability of power system models," *Electric Power Systems Research*, vol. 15, no. 2, pp. 147-155, October 1988.

[58] I. Kamwa, R. Grondin, and Y. Hebert, "Wide-area measurement based stabilizing control of large power systems – A descentralized/hierarchical approach," *IEEE Transactions on Power Systems*, vol. 16, no. 1, pp. 136-153, February 2001.

[59] D. P. Ke and C. Y. Chung, "An inter-area mode oriented pole-shifting method with coordination of control efforts for robust tuning of power oscillation damping controllers," *IEEE Transactions on Power Systems*, vol. 27, no. 3, pp. 1422-1432, August 2012.

[60] Y. Zang and A. Bose, "Design of wide-area damping controllers for interarea oscillations," *IEEE Transactions on Power Systems*, vol. 23, no. 3, pp. 1136-1143, August 2008.

[61] H. Ni, G. T. Heydt, and L. Mili, "Power system stability agents using robust wide area control," *IEEE Transactions on Power Systems*, vol. 17, no. 4, pp. 1123-1131, November 2002.

[62] F. Okou, L.-A. Dessaint, and O. Akhrif, "Power systems stability enhancement using a wide-area signals based hierarchical controller," *IEEE Transactions on Power Systems*, vol. 20, no. 3, pp. 1465-1477, August 2005.

[63] S. Mohagheghi, "Adaptive critic designs based neurocontrollers for local and wide area control of a multimachine power system with a static compensator," Ph.D. dissertation, School of Electrical and Computer Engineering, Georgia Institute of Technology, Atlanta, 2006.

[64] H. Wu, K. S. Tsakalis, and G. T. Heydt, "Evaluation of time delay effects to wide-area power system stabilizer design," *IEEE Transactions on Power Systems*, vol. 19, no. 4, pp. 1935-1941, November 2004.

[65] S. Wang, X. Meng, and T. Chen, "Wide-area control of power systems through delayed communication network," *IEEE Transactions on Control Systems Technology*, vol. 20, no. 2, pp. 495-503, March 2012.

[66] D. Dotta, A. S. e Silva, and I. C. Decker, "Wide-area measurements-based two-level control design considering signal transmission delay," *IEEE Transactions on Power Systems*, vol. 24, no. 1, pp. 208-216, February 2009.

[67] D. Molina, G. K. Venayagamoorthy, and R. G. Harley, "Coordinated design of local and wide-area damping controllers for power systems using PSO," 2013 IEEE Power and Energy Society General Meeting, Vancouver, Canada, July 2013

[68] D. Molina, J. Seuss, G. K. Venayagamoorthy, and R. G. Harley, "Robust design of local and wide-area damping controls using particle swarm optimization and improved operating point selection," 17th International Conference on Intelligent Systems Applications to Power Systems, Tokyo, Japan, July, 2013.

[69] IEEE Power and Energy Society, "IEEE Std 421.5™-2005, IEEE recommended practice for excitation system models for power system stability studies," New York: IEEE, 2006.

[70] DigSILENT GmbH , *DigSILENT PowerFactory version 14 user manual*, Gomaringen, Germany, 2008.

[71] J. Kennedy and R. Eberhart, "Particle swarm optimization," *in Proc. of the IEEE ICNN*, vol. 4, pp. 1042-1948, November 1995

[72] Y. del Valle, G. K. Venayagamoorthy, S. Mohagheghie, J. C. Hernandez, and R. G. Harley, "Particle swarm optimization: basic concepts, variants and applications in power systems," *IEEE Transactions on Evolutionary Computation*, vol. 12, no. 2, pp. 171-195, April 2008

[73] B. Chaudhurri, S. Ray, and R. Majumder, "Robust low-order controller design for multi-modal power oscillation damping using flexible AC transmission systems devices," *IET Generation, Transmission, and Distribution*, vol. 3, is. 5, pp. 448-459, 2009

[74] A. K. El-Sakkary, "The gap metric: robustness of stabilization of feedback systems," *IEEE Transactions on Automatic Control*, vol. AC-30, no. 3, March 1985.

[75] O. Galan, J. A. Romagnoli, Y. Arkun, and A. Palazoglu, "On the use of the gap metric for model selection in multi-linear model-based control," Proceedings of the American Control Conference, June, 2009.

[76] M. Klein, G. J. Rojers, and P. Kundur, "A fundamental study of inter-area oscillations in power systems," *IEEE Transactions on Power Systems*, vol. 6, no. 3, pp. 914-921, August, 1991

[77] K. S. Narendra, K. Parthasarathy, "Identification and control of dynamical systems using neural networks," *IEEE Transactions on Neural Networks*, vol.1, no.1, pp. 4-27, March 1990.

[78] L. Jin, P. Nikiforuk, and M. Gupta, "Approximation of Discrete-Time State-Space Trajectories Using Dynamic Recurrent Neural Networks," *IEEE Transactions on Automatic Control*, vol. 40, no. 7, pp. 1266-1270, July 1995.

[79] T. Masters, "Advanced Algorithms for Neural Networks: a C++ sourcebook," London: Academic Press, 1993.

[80] M. F. Moller, "A scaled conjugate gradient algorithm for fast supervised learning", Neural Networks, vol. 6, no. 4, pp. 525-533, 1993.

[81] D. Prokhorov, G. Puskorius, and L. Feldkamp, "Dynamical neural networks for control," in J. Kolen and S. Kremer (Eds.), "A Field Guide to Dynamical Recurrent Networks," IEEE Press, 2001.

[82] J. Rogers, *Object-oriented neural networks in C++*. London: Academic Press, 1997.

[83] J.-W. Park, G. K. Venayagamoorthy, and R. G. Harley, "MLP/RBF neural-networks-based online global model identification of synchronous generator," *IEEE Transactions on Industrial Electronics*, vol. 52, no. 6, pp. 1685-1695, December 2005.

[84] H. White and A. Gallant, "On learning the derivatives of an unknown mapping with multilayer feedforward networks," *Neural Networks*, vol. 5, pp. 129-138, 1992.

[85] M. S. Mahmoud, M. F. Hassan, and M. G. Darwish, *Large-scale control systems: theories and techniques*, Marcel Dekker, New York, 1985.

[86] D. Molina, R. G. Harley, G. K. Venayagamoorthy, D. Falcao, G. N. Taranto, and T. M. L. Assis, "Coherency based partitioning of a power system for intelligent wide-area damping control", 12th Symposium of Specialists in Electrical Operation and Expansion Planning (SEPOPE), Rio de Janeiro, Brazil, May 2012

[87] J. Dorsey, and R. Shlueter, "Structural archetypes for coherency: a framework for comparing power system equivalents," *Automatica*, vol. 20, no. 3, pp. 349-352, 1984.

[88] R. Podmore, "Identification of coherent generators for dynamic equivalents," *IEEE Transactions on Power Apparatus and Systems*, vol. PAS-97, no. 4, pp. 1344-1354, July/August 1978.

[89] A. Germond, and R. Podmore, "Dynamic aggregation of generating unit models," *IEEE Transactions on Power Apparatus and Systems*, vol. PAS-97, no. 4, pp. 1060-1069, July/August 1978.

[90] L. Wang, M. Klein, S. Yirga, and P. Kundur, "Dynamic reduction of large power systems for stability studies," *IEEE Transactions on Power Systems*, vol. 12, no. 2, pp. 889-895, May 1997.

[91] S.-K. Joo, C. Liu, L. Jones, and J. Choe, "Coherency and aggregation techniques incorporating rotor and voltage dynamics," *IEEE Transactions on Power Systems*, vol. 19, no. 2, pp. 1068-1075, May 2004

[92] J. Chow, R. Galarza, P. Accari, and W. Price, "Inertial and slow coherency aggregation algorithms for power system dynamic model reduction," *IEEE Transactions on Power Systems*, vol. 10, no. 2, pp. 680-685,May 1995

[93] P. Werbos, “Advanced forecasting methods for global crisis warning and models of intelligence,” *General Systems Yearbook*, vol, 22, pp. 25-38, 1977

[94] S. Ferrari, and R. F. Stengel, “Model-based adaptive critic designs,” J. Si, A. Barto, W. Powell, D. Wunsch (Eds.), “Handbook of learning and approximate dynamic programming”, New York: Wiley, July 2004

[95] D. Prokhorov, and D. Wunsch, “Adaptive critic designs,” *IEEE Transactions on Neural Networks*, vol. 8, no. 5, Sept. 1997

[96] G. G. Lendaris, and C. Paintz, “Training strategies for critic and action neural networks in dual heuristic dynamic programming method,” Proceedings of the 1997 Int. Conf. on Neural Networks, vol. 2, pp. 712-717, Houston, USA, June 1997.

[97] D. Molina, G. K. Venayagamoorthy, J. Liang, R. G. Harley, “Intelligent local area signal-based damping of power systems using virtual generators and approximate dynamic programming,” *IEEE Transactions on Smart Grid*, vol. 4, no. 1, pp. 498-508, March 2013.

[98] I. Kamwa, A. K. Pradhan, and G. Joos, “Automatic segmentation of large power system into fuzzy coherent areas for dynamic vulnerability assessment,” *IEEE Transactions on Power Systems*, vol. 22, no. 4, pp. 1974-1985, November 2007

[99] I. Kamwa, A. K. Pradhan, G. Joos, and S. R. Samantaray, “Fuzzy partitioning of a real power system for dynamic vulnerability assessment,” *IEEE Transactions on Power Systems*, vol. 24, no. 3, pp. 1356-1365, August 2009

[100] Y. Zhu, *Multivariable system identification for process control*, Oxford, UK: Elsevier, 2010

[101] S. Singh, J. C. Hamann, “Prony Toolbox,” available online: http://www.mathworks.com/matlabcentral/fileexchange/3955, last accessed on August 29, 2012.

[102] Operador Nacional do Sistema Electrico, “Intercambio entre as regioes,” available online: http://www.ons.org.br/historico/intercambio_entre_regioes.aspx, last accessed on May 9, 2013.

[103] N. Martins, A. A. Barbosa, J. C. R. Ferraz, M. G. Dos Santos, A. L. B. Bergamo, C. S. Yung, V. R. Oliveira, N. J. P. Macedo, “Retuning stabilizers for the north-south Brazilian interconnection,” IEEE Power and Energy Society Summer Meeting, vol. 1, vol. 1, pp. 58-67, July, 1999.

[104] G. N. Taranto, D. M. Falcão, A. Manzoni, and T. M. L. Assis, “Dynamic Performance of Distributed Generation Considering Disturbances in the Brazilian Interconnected Power System and Switching at the Distribution Grid”, Technical

Report – COPPETEC: PEE8729, Federal University of Rio de Janeiro, Brazil, 2007.

[105] S. Geeves, "A modal-coherency technique for deriving dynamic equivalents," *IEEE Transactions on Power Systems*, vol. 3, no. 1, pp. 44-51, February 1988.

[106] G. Obinata, and B. D. O. Anderson, *Model reduction for control system design*. London: Springer, 2000.

[107] Bernard Friedland, "Observers," *in The Control Handbook*, William S. Levine, Ed., Boca Raton: CRC Press, 1996.

[108] K. Dutton, S. Thompson, and B. Barraclough, *The art of control engineering*, Essex, England: Addison Wesley Longman, 1997.

[109] J. Liang, D. Molina, G. K. Venayagamoorthy, and R. G. Harley, "Two-level dynamic stochastic optimal power flow control for smart grids with intermittent renewable generation," *IEEE Transactions on Power Systems,* vol. 28, no. 3, pp. 2670-2678, August 2013.

[110] R. E. Bellman and S. E. Dreyfus, *Applied dynamic programming*, Princeton: Princeton University Press, 1962.

[111] P. LoonTang and C. de Silva, "Compensation for transmission delays in an Ethernet-based control network using variable-horizon predictive control," *IEEE Transactions on Control Systems Technology*, vol. 14, no. 4, pp. 707-718, July 2006.

[112] L. Lublin and M Athans, "Linear Quadratic Regulator Control," *in The Control Handbook*, William S. Levine, Ed., Boca Raton: CRC Press, 1996.